

AN ABSTRACT OF THE DISSERTATION OF

Douglas N. Woods for the degree of Doctor of Philosophy in Nuclear Engineering
presented on June 4, 2018.

Title: Discrete Ordinates Radiation Transport using High-Order Finite Element
Spatial Discretizations on Meshes with Curved Surfaces

Abstract approved:

Todd S. Palmer

We spatially discretize the S_N transport equation using the high-order (HO) discontinuous finite element method (DFEM) on HO meshes. Previous work provided a proof-of-concept for this spatial discretization method in X - Y geometry. Included in the present work, we derive a spatial discretization for the S_N transport equation in both X - Y and R - Z geometries using HO DFEMs on HO meshes. We characterize the behavior of these methods by solving several numerical test problems. In X - Y geometry, we determine that the spatial error dominates the errors introduced by the approximate integrals on the surface term on problems with curved surfaces that are both incident and outgoing. We also conclude, that for an optically thick and diffusive problem, that these *highly* curved meshes may propagate the boundary layer oscillations into the problem interior. In R - Z geometry, we conclude that the spatial discretization error is dependent upon the angular discretization, that the spatial error converges at $O(p + 1)$ on problems with smooth solutions, that the spatial error degrades for solutions with less regularity, and that preserving a particular spherical symmetry problem is primarily a function of finite element order and spatial mesh resolution.

This work also implements the modified interior penalty (MIP) diffusion synthetic acceleration (DSA) method and investigates the sensitivities of the spectral radius to

several parameters, including finite element order, mesh curvature, and a user-defined constant. We conclude that the spectral radius is especially dependent upon the finite element order and the user defined constant. We also derive and implement a Robin boundary condition for the MIP DSA method to accelerate the source iteration. The testing we perform reveals substantially faster convergence rates in the optically thin and intermediate regimes, while degrading the convergence rates in optically thick regimes when compared to the original MIP DSA equations. Also, we conclude that the Robin boundary condition method reduces the dependence of the spectral radius ~~upon~~ changes in both the finite element order and the user defined constant.

©Copyright by Douglas N. Woods

June 4, 2018

All Rights Reserved

Discrete Ordinates Radiation Transport using High-Order Finite Element Spatial
Discretizations on Meshes with Curved Surfaces

by
Douglas N. Woods

A DISSERTATION

submitted to

Oregon State University

in partial fulfillment of
the requirements for the
degree of

Doctor of Philosophy

Presented June 4, 2018
Commencement June 2018

Doctor of Philosophy dissertation of Douglas N. Woods presented on June 4, 2018.

APPROVED:

Major Professor, representing Nuclear Engineering

Head of the School of Nuclear Science and Engineering

Dean of the Graduate School

I understand that my dissertation will become part of the permanent collection of Oregon State University libraries. My signature below authorizes release of my dissertation to any reader upon request.

Douglas N. Woods, Author

ACKNOWLEDGMENTS

I first want to thank my Lord and Savior for the opportunities and gifts I've been given. I want to thank my major advisor, Dr. Todd Palmer, for piquing my interest in transport discretizations during the advanced courses he taught. He found and presented the opportunity to work on this project, brought immense knowledge, and has been encouraging throughout this entire project. Thank you to Dr. Tom Brunner for serving as my mentor during a summer at Lawrence Livermore National Laboratory and giving me an inordinate amount of time, patience, and attention throughout this degree process. He provided countless edits and comments to my papers, including this dissertation, and once provided comments during his vacation in the Caribbean. I must thank my parents for being so encouraging, supportive, and loving during my life. All of my friends and family have been so patient with me – I too often neglected visiting them despite my relatively close proximity at Oregon State.

TABLE OF CONTENTS *(use “\conheading” in .toc)*

	<u>Page</u>
1 Introduction	1
1.1 Radiation Transport	3
1.2 Discretization	4
1.2.1 Direction of Travel Discretization	7
1.2.2 Spatial Discretization	9
1.2.3 High-Order Finite Elements	9
1.2.4 Meshes	11
1.2.5 <i>R-Z</i> Geometry	12
1.3 Spherical Symmetry in <i>R-Z</i> Geometry	15
1.4 Diffusion Limit	16
1.5 Source Iteration Acceleration	18
1.6 Research Objectives	22
1.7 Outline	22
2 Methods	23
2.1 High-Order Finite Elements Spatial Discretization	23
2.2 Meshes with Curved Surfaces	29
2.3 Solution Method	31
2.4 <i>R-Z</i> Geometry	33
2.4.1 Angular Discretization	34
2.4.1.1 Reflecting Boundary at $r = 0$	37
2.4.2 Spatial Discretization	38
2.5 Modified Interior Penalty DSA	42

TABLE OF CONTENTS (Continued)

	<u>Page</u>
2.6 MIP DSA with Robin Boundary Conditions	44
3 Results	46
3.1 <i>X-Y</i> Geometry	46
3.1.1 Uniform Infinite Medium	46
3.1.2 Spatial convergence on a highly curved mesh	47
3.1.3 Alternating Incident angular flux Boundary Conditions	49
3.1.4 Sensitivities on a highly curved mesh	51
3.2 <i>R-Z</i> Geometry	54
3.2.1 Uniform Infinite Medium	54
3.2.2 Angular Dependence Study	54
3.2.3 Spatial Convergence Studies	59
3.2.3.1 Smooth Manufactured Solution	59
3.2.3.2 Reduced Regularity Manufactured Solution	63
3.2.4 Spherical Symmetry Preservation	64
3.2.4.1 Low-Order Mesh	67
3.2.4.2 High-Order Mesh	92
3.2.4.3 Axisymmetry Summary and Discussion	115
3.2.5 Strong Scatter with Alternating Boundaries Test	118
3.2.6 Material Discontinuity Stress Test	122
3.3 Modified Interior Penalty Diffusion Synthetic Acceleration	126
3.3.1 MIP DSA with Homogeneous Dirichlet Boundary Conditions .	126
3.3.1.1 Spectral Radius Sensitivity to Constant C	126

3.3.1.2	Sensitivity of the Spectral Radius to the Scattering Ratio c	131
3.3.1.3	Infinite Medium MIP DSA Results	132
3.3.2	MIP DSA with Homogeneous Robin Boundary Conditions	134
3.3.2.1	Accuracy	134
3.3.2.2	Sensitivity Study of the Spectral Radius	136
4	Conclusions	139
4.1	X - Y Geometry Conclusions	140
4.2	R - Z Geometry Conclusions	140
4.3	MIP DSA Conclusions	142
4.4	FutureWork	143
A	Implementation in MFEM	152
A.1	Transport Operators	153
A.2	MIP DSA Operators	154
B	Alternative Implementations for DSA with Robin Boundary Conditions	159
C	Mathematica Scripts	162
C.1	Mass Matrix Entries for RZ BLD Gauss-Legendre on Quadrilaterals	162
C.2	Angular Redistribution Matrix Entries for RZ BLD Gauss-Legendre on Quadrilaterals	164
C.3	r-Leakage Matrix Entries for RZ BLD Gauss-Legendre on Quadrilaterals	167
C.4	z-Leakage Matrix Entries for RZ BLD Gauss-Legendre on Quadrilaterals	170
C.5	z-Leakage Matrix Entries for RZ BLD Gauss-Legendre on Quadrilaterals	172
C.6	r Surface-Integral Matrix Entries for RZ BLD Gauss-Legendre on Quadri- lateral	175

C.7	z Surface-Integral Matrix Entries for RZ BLD Gauss-Legendre on Quadrilaterals	177
C.8	Linear Form Angular Redistribution Matrix Entries for RZ BLD Gauss-Legendre on Quadrilaterals	179
C.9	Linear Form Scattering/Fixed Source Matrix Entries for RZ BLD Gauss-Legendre on Quadrilaterals	182

LIST OF FIGURES use “\contlofheading” in .lof

<u>Figure</u>	<u>Page</u>
1 Flow diagram for solution process. This research is focused on the processes boxed by the dashed line.	6
2 The positive octant for S_6 level-symmetric angular quadrature.	8
3 Cylindrical space-angle coordinate system showing the position (r, z) and direction of travel Ω .	13
4 Example of an incident and outgoing surface.	25
5 Example of mapping the reference element to a physical element.	30
6 Angular discretization showing (ξ, μ) pairs; adapted from [1]	34
7 Uniform infinite medium scalar flux solution.	47
8 MMS solution on a <i>highly</i> curved mesh.	48
9 Errors between the manufactured and DFEM solutions. Reference lines depict order of spatial convergence $O(n) \equiv O((N_{\text{zones}})^{n/2})$.	49
10 Scalar flux solution for Test Problem 3.	50
11 4 th -order mesh with surfaces that are both incident and outgoing.	52
12 Error for various surface numerical integration order schemes, where p is the finite element order, g is the mesh order, and $d = 2$ is the spatial dimension of the problem.	52
13 Error for various S_N orders.	53
14 Uniform infinite medium solution.	55
15 MMS solution for Equation 99.	57
16 MMS solution for Equation 107.	59
17 MMS solution to Equation 116.	61

LIST OF FIGURES (Continued)

<u>Figure</u>		<u>Page</u>
18 L ² -norm of the errors from the manufactured solution and reference lines computed from a least squares fit, where $N_{\text{unknowns}} = N_{\text{cells}}(p + 1)^2$.		62
19 DGFEM scalar flux solution to Equation 124.		63
20 L ² -norm of the errors from the manufactured solution and reference line, where $N_{\text{unknowns}} = N_{\text{cells}}(p + 1)^2$.		64
21 Example scalar flux solution using 1 st -order finite elements, S_8 level-symmetric angular quadrature, 2 nd -order mesh, and refined mesh with 8128 mesh zones.		68
22 Relative asymmetry for 1 st -order finite elements on a 1 st -order mesh for given order of level-symmetric angular quadrature.		70
23 Measure of the asymmetry for each finite element node for the given level-symmetric angular quadrature order for 1 st -order DFEM and 1 st -order mesh with 120 zones (see Figure 22).		71
24 Accuracy of solutions for given angular quadrature using $p = 1$ on a 1 st -order mesh with 120 zones.		71
25 Relative asymmetry for 2 st -order finite elements on a 1 st -order mesh for given order of level-symmetric angular quadrature.		73
26 Measure of the asymmetry for each finite element node for the given level-symmetric angular quadrature order for 2 nd -order DFEM and 1 st -order mesh with 120 zones (see Figure 25).		74
27 Accuracy of solutions for given angular quadrature using $p = 2$ on a 1 st -order mesh with 120 zones.		74

28	Relative asymmetry for 4 st -order finite elements on a 1 st -order mesh for given order of level-symmetric angular quadrature.	76
29	Measure of the asymmetry for each finite element node for the given level-symmetric angular quadrature order for 4 th -order DFEM and 1 st -order mesh with 120 zones (see Figure 28).	77
30	Accuracy of solutions for given angular quadrature using $p = 4$ on a 1 st -order mesh with 120 zones.	77
31	Relative asymmetry for 8 st -order finite elements on a 1 st -order mesh for given order of level-symmetric angular quadrature.	79
32	Measure of the asymmetry for each finite element node for the given level-symmetric angular quadrature order for 8 th -order DFEM and 1 st -order mesh with 120 zones (see Figure 31).	80
33	Accuracy of solutions for given angular quadrature using $p = 8$ on a 1 st -order mesh with 120 zones.	80
34	Relative asymmetry for $p = \{1, 2, 4\}$ finite elements on a 1 st -order mesh with 120 zones for S_8 level-symmetric angular quadrature.	82
35	Measure of the asymmetry for each finite element node for the given finite element order using S_8 level-symmetric angular quadrature on a 1 st -order mesh with 120 zones (see Figure 34).	83
36	Accuracy of solutions for given finite element order using S_8 level-symmetric angular quadrature on a 1 st -order mesh with 120 zones.	83
37	Relative asymmetry for $p = 1$ finite elements on a 1 st -order mesh for S_8 level-symmetric angular quadrature for $N_{\text{zones}} = \{6, 28, 120\}$	85
38	Relative asymmetry for $p = 1$ finite elements on a 1 st -order mesh for S_8 level-symmetric angular quadrature for $N_{\text{zones}} = \{496, 2016, 8128\}$; mesh overlay may be removed for clarity.	86

39	Measure of the asymmetry for each finite element node for 1 th -order finite elements using S_8 level-symmetric angular quadrature on a 1 st -order mesh with various number of zones (see Figures 37-38)	87
40	Accuracy of solutions for given mesh refinement for $p = 1$ using S_8 level-symmetric angular quadrature on a 1 st -order mesh.	87
41	Relative asymmetry for $p = 4$ finite elements on a 1 st -order mesh for S_8 level-symmetric angular quadrature for $N_{\text{zones}} = \{6, 28, 120\}$	89
42	Relative asymmetry for $p = 4$ finite elements on a 1 st -order mesh for S_8 level-symmetric angular quadrature for $N_{\text{zones}} = \{496, 2016, 8128\}$; mesh overlay may be removed for clarity.	90
43	Measure of the asymmetry for each finite element node for 4 th -order finite elements using S_8 level-symmetric angular quadrature on a 1 st -order mesh with various number of zones (see Figures 41-42).	91
44	Accuracy of solutions for given mesh refinement for $p = 4$ using S_8 level-symmetric angular quadrature on a 1 st -order mesh.	91
45	Relative asymmetry for 1 st -order finite elements on a 2 nd -order mesh for given order of level-symmetric angular quadrature.	93
46	Measure of the asymmetry for each finite element node for the given level-symmetric angular quadrature order for 1 st -order DFEM and 2 nd -order mesh with 120 zones (see Figure 45).	94
47	Accuracy of solutions for given angular quadrature using $p = 1$ on a 2 nd -order mesh with 120 zones.	94
48	Relative asymmetry for 2 nd -order finite elements on a 2 nd -order mesh for given order of level-symmetric angular quadrature.	96

49	Measure of the asymmetry for each finite element node for the given level-symmetric angular quadrature order for 2 nd -order DFEM and 2 nd -order mesh with 120 zones (see Figure 48).	97
50	Accuracy of solutions for given angular quadrature using $p = 2$ on a 2 nd -order mesh with 120 zones.	97
51	Relative asymmetry for 4 th -order finite elements on a 2 nd -order mesh for given order of level-symmetric angular quadrature.	99
52	Measure of the asymmetry for each finite element node for the given level-symmetric angular quadrature order for 4 th -order DFEM and 2 nd -order mesh with 120 zones (see Figure 51).	100
53	Accuracy of solutions for given angular quadrature using $p = 4$ on a 2 nd -order mesh with 120 zones.	100
54	Relative asymmetry for $p = \{1, 2, 4\}$ finite elements on a 2 nd -order mesh for S_8 level-symmetric angular quadrature.	102
55	Measure of the asymmetry for each finite element node for the given finite element order using S_8 level-symmetric angular quadrature on a 2 nd -order mesh with 120 zones (see Figure 54).	103
56	Accuracy of solutions for given angular quadrature using S_8 level-symmetric angular quadrature on a 2 nd -order mesh with 120 zones.	103
57	Relative asymmetry for $p = 1$ finite elements on a 2 nd -order mesh for S_8 level-symmetric angular quadrature.	105
58	Relative asymmetry for $p = 1$ finite elements on a 2 nd -order mesh for S_8 level-symmetric angular quadrature; mesh overlay may be removed for clarity.	106

59	Measure of the asymmetry for each finite element node for 1 st -order finite elements using S_8 level-symmetric angular quadrature on a 2 nd -order mesh with various number of zones (see Figures 57-58)	107
60	Accuracy of solutions for mesh refinement study using $p = 1$, S_8 level-symmetric angular quadrature, on a 2 nd -order mesh.	107
61	Relative asymmetry for $p = 4$ finite elements on a 2 nd -order mesh for S_8 level-symmetric angular quadrature.	109
62	Relative asymmetry for $p = 4$ finite elements on a 2 nd -order mesh for S_8 level-symmetric angular quadrature; mesh overlay may be removed for clarity.	110
63	Measure of the asymmetry for each finite element node for 4 th -order DFEM, S_8 level-symmetric angular quadrature, and 2 nd -order mesh with various number of zones (see Figures 61 - 62).	111
64	Accuracy of solutions for mesh refinement study using $p = 4$, S_8 level-symmetric angular quadrature, on a 2 nd -order mesh.	111
65	Relative asymmetry for $p = 1$ finite elements on a 2 nd -order mesh with 8128 zones; mesh overlay may be removed for clarity.	113
66	Measure of the asymmetry for each finite element node for the given level-symmetric angular quadrature order for 1 st -order DFEM and 2 nd -order mesh with 8128 zones.	114
67	Accuracy of solutions for given angular quadrature using $p = 4$ on a 2 nd -order mesh with 8128 zones.	114
68	Measure of the asymmetry for each finite element node for the given level-symmetric angular quadrature order for 1 st -order DFEM on the given mesh with 120 zones.	115

69	Measure of the asymmetry for each finite element node for the given level-symmetric angular quadrature order for 4 th -order DFEM on the given mesh with 120 zones.	116
70	Measure of the asymmetry for each finite element node for 4 th -order DFEM, S_8 level-symmetric angular quadrature, on the given mesh with various number of zones.	116
71	Analytic representation of each term of the transport equation using the manufactured solution, Equation 127, for $(\mu, \xi) \approx (0.218, 0.951)$. The complicated shapes of the streaming and source terms are typical of the other Ω directions.	118
72	Strong scatter with discontinuous BCs with MIP DSA problem geometry; gray boundaries indicate incident boundary locations.	119
73	Solution to strong scatter with discontinuous boundary conditions with $p = 1$ finite elements and S_4 level-symmetric angular quadrature. White regions indicate negative scalar fluxes.	120
74	Solution to strong scatter with discontinuous boundary conditions with $p = 4$ finite elements and S_8 level-symmetric angular quadrature. White regions indicate negative scalar fluxes.	121
75	Solution to strong scatter with discontinuous boundary conditions with $p = 4$ finite elements and S_{12} level-symmetric angular quadrature on a 2 nd -order mesh. White regions indicate negative scalar fluxes.	122
76	Material discontinuity stress test with MIP DSA problem geometry; materials defined in Table 3.	123
77	Solution to multi-material stress test. White regions indicate negative scalar fluxes.	125

78	Spectral radius data for varying p with $C = 2$ on an orthogonal mesh with homogeneous Dirichlet boundary conditions in the DSA solve; plot reproduced from Woods et al. [2].	127
79	Spectral radius data for varying p with $C = 4$ on an orthogonal mesh with homogeneous Dirichlet boundary conditions in the DSA solve; plot reproduced from Woods et al. [2].	129
80	Spectral radius data for varying p with $C = 6$ on an orthogonal mesh with homogeneous Dirichlet boundary conditions in the DSA solve; plot reproduced from Woods et al. [2].	130
81	Spectral radius data for various scattering ratios c using 4 th -order finite elements, constant $C = 4$, and orthogonal mesh.	132
82	Spectral radius data for various scattering ratios c using 4 th -order finite elements, constant $C = 4$, and 3 rd -order mesh.	132
83	Spectral radius data for varying p with $C = 2$ on a periodic orthogonal mesh.	133
84	Spectral radius data for varying p with $C = 4$ on a periodic orthogonal mesh.	133
85	Spectral radius data for varying p with $C = 6$ on a periodic orthogonal mesh.	134
86	Spectral radius data for varying p with $C = 2$ on an orthogonal mesh using the vacuum boundary MIP DSA method.	137
87	Spectral radius data for varying p with $C = 4$ on an orthogonal mesh using the zero incident current DSA method.	138
88	Spectral radius data for varying p with $C = 6$ on an orthogonal mesh using the zero incident current DSA method.	139

LIST OF TABLES

<u>Table</u>	<u>Page</u>
1 Gaussian quadrature locations.	28
2 Summary of discretizations and determination of whether they reduce the asymmetry.	117
3 Material discontinuity stress test with MIP DSA material properties.	122
4 L_2 norm of the errors between the diffusion equation using the given boundary condition method and the reference solution (1-D analytic solution) using 3 rd -order elements, $C = 4$, on an orthogonal mesh with 2304 zones.	135
5 MFEM transport operator function calls where the arguments have been dropped.	155
6 MFEM R - Z transport operator function calls where the arguments have been dropped.	156
7 MFEM default integration orders for transport operators. The notation for the finite element order is p , mesh order is g , and problem spatial dimension is d	157
8 MFEM diffusion equation function calls.	158
9 L_2 norm of the errors between the diffusion equation using the given boundary condition method and the reference solution (1-D analytic solution) using 3 rd -order elements, $C = 4$, on an orthogonal mesh with 2304 zones.	160

1 Introduction

The solution to the radiation transport equation is valuable in the design and analysis of many ~~physical~~ systems. A few examples are nuclear reactors [3], medical radiation treatments [4], and high energy density physics systems like those found in astrophysics or inertial confinement fusion (ICF) [5]. ICF experiments are being performed at facilities such as the National Ignition Facility¹ (NIF) and the Omega Laser Facility². Nuclear fusion occurs in the high energy-density physics (HEDP) regime where the energy-density of a material is very high [5, 6]. If material temperatures are very high, materials emit black body radiation (also called thermal radiation) in tremendous quantities and ~~deposit~~ energy back to the material influencing the material internal energy, momentum, temperature, and density. This complicated system of thermal radiation transport with hydrodynamics is ~~studied in~~ radiation hydrodynamics. While all of the forces in these HEDP systems are important, we can develop some of the computational models independently. For instance, we may develop hydrodynamics model~~s~~ (and software tools) separately from those for radiation transport.

Lawrence Livermore National Laboratory (LLNL) is developing a hydrodynamics code called BLAST³ [7]. BLAST solves the Euler equations using a general finite element method (FEM) on meshes with curved surfaces for the conservation of mass, energy, and momentum of a fluid [8]. Novel features include higher-order elements to represent the thermodynamic and kinematic variables~~s~~ and meshes with curved surfaces. Compared to the most common method, ~~staggered~~ grid hydrodynamics, Dobrev et al. [8] demonstrated that BLAST can more accurately model flow geometry,

¹<https://lasers.llnl.gov>

²http://www.lle.rochester.edu/omega_facility/omega/

³<https://computation.llnl.gov/project/blast/>

symmetry of radial flow, ~~and an increased resolution~~ of a shock front — observing that the FEM approach has the ability to model the shock within a single mesh element. These improvements have reduced some of the numerical errors that have been exhibited by previous methods.

BLAST employs the Modular Finite Element Methods Library⁴ (MFEM) [9], a general finite element library also being developed at LLNL, to spatially discretize using the high-order (HO) FEM on meshes with curved surfaces. To become an effective radiation hydrodynamics package, BLAST ~~will need to integrate~~ with a radiation transport package that is able to model the radiation field in these HEDP regimes in ~~the same geometries and spatial discretizations as the hydrodynamics being modeled~~. That is, ~~the radiation transport must be solved using the spatial discretizations that BLAST uses to solve the hydrodynamics equations~~. The main topic of this thesis is rooted in the spatial discretization of the radiation transport equation using HO finite elements on HO meshes.

This chapter introduces the radiation transport equation and establishes the motivation for using the HO methods. In Section 1.1, we give a brief introduction to the radiation transport equation and nomenclature. In Section 1.2, we describe various discretization methods used to solve the radiation transport equation. In Section 1.3, we further the *R-Z* geometry discussion by motivating a need for solving a spherically symmetric system using *R-Z* geometry. In Section 1.4, we describe the diffusion limit and its application to optically thick problems found in HEDP regimes. In Section 1.5, we discuss some of the research conducted for accelerating the source iteration method. In Section 1.6, we state the research objectives for this dissertation. Finally, in Section 1.7, we outline the remainder of this dissertation.

⁴mfem.org

1.1 Radiation Transport

The time- and energy-dependent radiation transport equation,

$$\begin{aligned} & \frac{1}{u} \frac{\partial \psi(\mathbf{x}, \boldsymbol{\Omega}, E, t)}{\partial t} + \boldsymbol{\Omega} \cdot \nabla \psi(\mathbf{x}, \boldsymbol{\Omega}, E, t) + \sigma_t(\mathbf{x}, \boldsymbol{\Omega}, E, t) \psi(\mathbf{x}, \boldsymbol{\Omega}, E, t) \\ &= \frac{1}{4\pi} \int_{4\pi} \int_0^\infty \sigma_s(\mathbf{x}, \boldsymbol{\Omega}' \rightarrow \boldsymbol{\Omega}, E' \rightarrow E, t) \psi(\mathbf{x}, \boldsymbol{\Omega}', E', t) dE' d\boldsymbol{\Omega}' + S_0(\mathbf{x}, \boldsymbol{\Omega}, E, t), \end{aligned} \quad (1)$$

describes the angular flux distribution, $\psi(\mathbf{x}, \boldsymbol{\Omega}, E, t)$, as a function of position, \mathbf{x} , direction of travel, $\boldsymbol{\Omega}$, energy, E , and time, t . We also define the scalar flux by

$$\phi(\mathbf{x}, E, t) = \int_{4\pi} \psi(\mathbf{x}, \boldsymbol{\Omega}, E, t) d\boldsymbol{\Omega}, \quad (2)$$

that describes the density of particles traveling in all directions at each spatial position \mathbf{x} . Both the angular and scalar fluxes describe a particle density in a phase space denoted by their dependent variables. The angular flux has units $\text{cm}^{-2} \text{ s}^{-1} \text{ ster}^{-1}$. The scalar flux is integrated over all directions and has units $\text{cm}^{-2} \text{ s}^{-1}$. In general, the total macroscopic cross section, $\sigma_t(\mathbf{x}, \boldsymbol{\Omega}, E, t) = \varsigma_t(\mathbf{x}, \boldsymbol{\Omega}, E, t) N(\mathbf{x}, t)$, is a property of the microscopic total cross section, $\varsigma_t(\mathbf{x}, \boldsymbol{\Omega}, E, t) \text{ cm}^2$, and the number density of the material, $N(\mathbf{x}, t) \text{ cm}^{-3}$. The absorption and scattering cross sections are related to the total cross section by $\sigma_t(\mathbf{x}, \boldsymbol{\Omega}, E, t) = \sigma_a(\mathbf{x}, \boldsymbol{\Omega}, E, t) + \sigma_s(\mathbf{x}, \boldsymbol{\Omega}, E, t)$. The value $\sigma_s(\mathbf{x}, \boldsymbol{\Omega}' \rightarrow \boldsymbol{\Omega}, E' \rightarrow E, t)$ denotes scattering from direction $\boldsymbol{\Omega}'$ into $\boldsymbol{\Omega}$ and from energy E' into E at position \mathbf{x} and time t . Additionally, the volumetric source, $S_0(\mathbf{x}, \boldsymbol{\Omega}, E, t)$, is some radiation emitting external source (e.g., fission neutrons or blackbody radiation).

There are only a few specific cases where the radiation transport equation can be solved exactly. Problems of interest typically fall outside of this subset and numerical methods must be employed to obtain approximate solutions. There are two general categories of methods used to solve this equation: stochastic and deterministic

methods.

Stochastic methods take a statistical approach. In any particular source region, a single particle is emitted and tracked through its “random walk”, traversing the problem domain until it is either absorbed or escapes the domain. One can tally the number of particles that get absorbed into a region of interest. This method is rooted in the physics of the stochastic particle-material interactions. If enough particles are simulated, a statistically significant conclusion can be drawn about the particle density in a region of interest. For simple problems (absent of nonlinear effects like particle-particle collisions), this can be very accurate but also computationally demanding because of the large number of particles required to be simulated.

Alternatively, deterministic methods solve the radiation transport equation for the angular and scalar fluxes by discretizing the equation in each of the dependent variables (i.e., space and direction of travel). The discretized equation results in a linear system of equations that can be solved with linear algebra techniques. Deterministic methods are generally faster than stochastic methods but involve discretization or truncation errors. However, employing certain discretizations can reduce the impact of these errors.

1.2 Discretization

Physically, particles can be distributed continuously in three-dimensional space. Numerically, we discretize the spatial domain into a smaller subset of discrete locations. Similarly, a particle’s direction of travel can be distributed continuously so we approximate it traveling in only a few discrete directions. It is common to discretize the direction of travel into a finite number of directions by using the discrete ordinates (S_N) method [10]. Particles with various energies may behave or interact with material differently. It is common to approximate the continuum of particle ener-

gies by grouping them into a finite number of energy groups. If a problem evolves through time, we discretize the time continuum with discrete time steps. Ideally, we would model the continuous phase space because it describes the physical behavior of neutral particles. Since we cannot numerically account for a continuum of variables, we must make these discrete approximations. In this light, we discretize each of the continuous variables to approximate each as closely as practical. In general, this can mean refining the discretization, e.g., refining the spatial mesh or using a higher order discrete ordinates approximation. However, the cost of higher accuracy is increased computational time that may become prohibitively expensive.

The transport equation discretized in time, energy, and direction can be written

$$\begin{aligned} & \frac{1}{u} \frac{\partial \psi(\mathbf{x}, \boldsymbol{\Omega}_m, E_g, t_\tau)}{\partial t} + \boldsymbol{\Omega} \cdot \nabla \psi(\mathbf{x}, \boldsymbol{\Omega}_m, E_g, t_\tau) \\ & \quad + \sigma_t(\mathbf{x}, \boldsymbol{\Omega}_m, E_g, t_\tau) \psi(\mathbf{x}, \boldsymbol{\Omega}_m, E_g, t_\tau) \\ & = \frac{1}{4\pi} \int_{4\pi} \int_0^\infty \sigma_s(\mathbf{x}, \boldsymbol{\Omega}' \rightarrow \boldsymbol{\Omega}_m, E' \rightarrow E_g, t_\tau) \psi(\mathbf{x}, \boldsymbol{\Omega}', E', t_\tau) dE' d\boldsymbol{\Omega}' \\ & \quad + S_0(\mathbf{x}, \boldsymbol{\Omega}_m, E_g, t_\tau), \quad (3) \end{aligned}$$

and

$$\phi(\mathbf{x}, E_g, t_\tau) = \int_{4\pi} \psi(\mathbf{x}, \boldsymbol{\Omega}', E_g, t_\tau) d\boldsymbol{\Omega}', \quad (4)$$

A flow chart of the general solution algorithm is shown in Figure 1. Discretizing the transport equation in all of phase space, we first advance through each time step ($t_\tau = t_0, t_1, \dots$). Within each time-step, we loop through each energy group ($g = 1, \dots, G$). Within each energy group, we loop through all discrete ordinate directions ($m = 1, \dots, M$). Within the angular discretization loop, we spatially discretize the transport equation, solve it, and obtain a scalar flux. We perform a source iteration until the scalar flux is converged.

This research is concerned with the innermost loop (boxed in Figure 1 with a

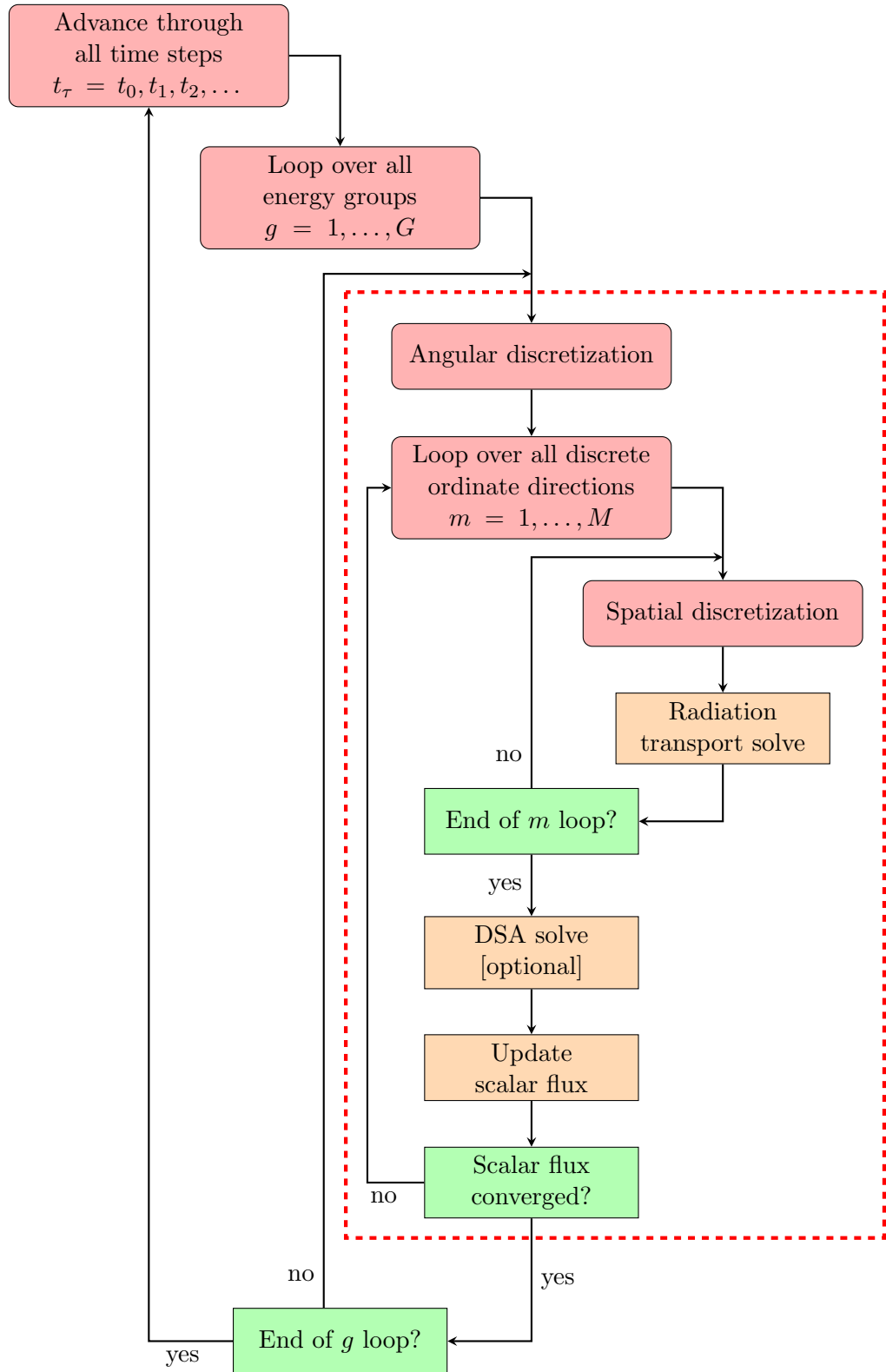


Figure 1: Flow diagram for solution process. This research is focused on the processes boxed by the dashed line.

dashed line) over discrete ordinate directions until the scalar flux converges. We assume the solution of the transport equation has reached steady-state (or is being solved at a single time-step), making the problem time independent. We also assume there is only one energy group (or we are solving for one of many energy groups), thereby making the problem energy independent. We discretize the two remaining dependent variables (space and direction of travel) where the spatial discretization is the main focus of this dissertation. The steady-state, mono-energetic radiation transport equation,

$$\boldsymbol{\Omega} \cdot \nabla \psi(\mathbf{x}, \boldsymbol{\Omega}) + \sigma_t(\mathbf{x})\psi(\mathbf{x}, \boldsymbol{\Omega}) = \frac{1}{4\pi}\sigma_s(\mathbf{x}) \int_{4\pi} \psi(\mathbf{x}, \boldsymbol{\Omega}') d\boldsymbol{\Omega}' + \frac{1}{4\pi}S_0(\mathbf{x}), \quad (5)$$

describes the angular flux distribution, $\psi(\mathbf{x}, \boldsymbol{\Omega})$, as a function of position, \mathbf{x} , and direction of travel, $\boldsymbol{\Omega}$. For the present work, we assume the cross sections are only dependent upon the spatial position. The scalar flux,

$$\phi(\mathbf{x}) = \int_{4\pi} \psi(\mathbf{x}, \boldsymbol{\Omega}') d\boldsymbol{\Omega}', \quad (6)$$

describes the density of particles traveling in each direction at every point \mathbf{x} . Hereafter, we have dropped the energy and time variables from the arguments for brevity (recall they are constant).

1.2.1 Direction of Travel Discretization

We approximate the continuum of directions that particles can travel by assuming they only travel in discrete ordinate (S_N) directions. Figure 2 shows an example of a set of discrete ordinates. Specifically, this octant of the S_6 level-symmetric quadrature demonstrates that $\boldsymbol{\Omega}$ is discretized into discrete directions $\boldsymbol{\Omega}_m$ and can be described as a function of μ , η , and ξ , the three coordinate axes shown in Figure 2.

We utilize the discrete ordinate weights to approximate the integral in Equation 6

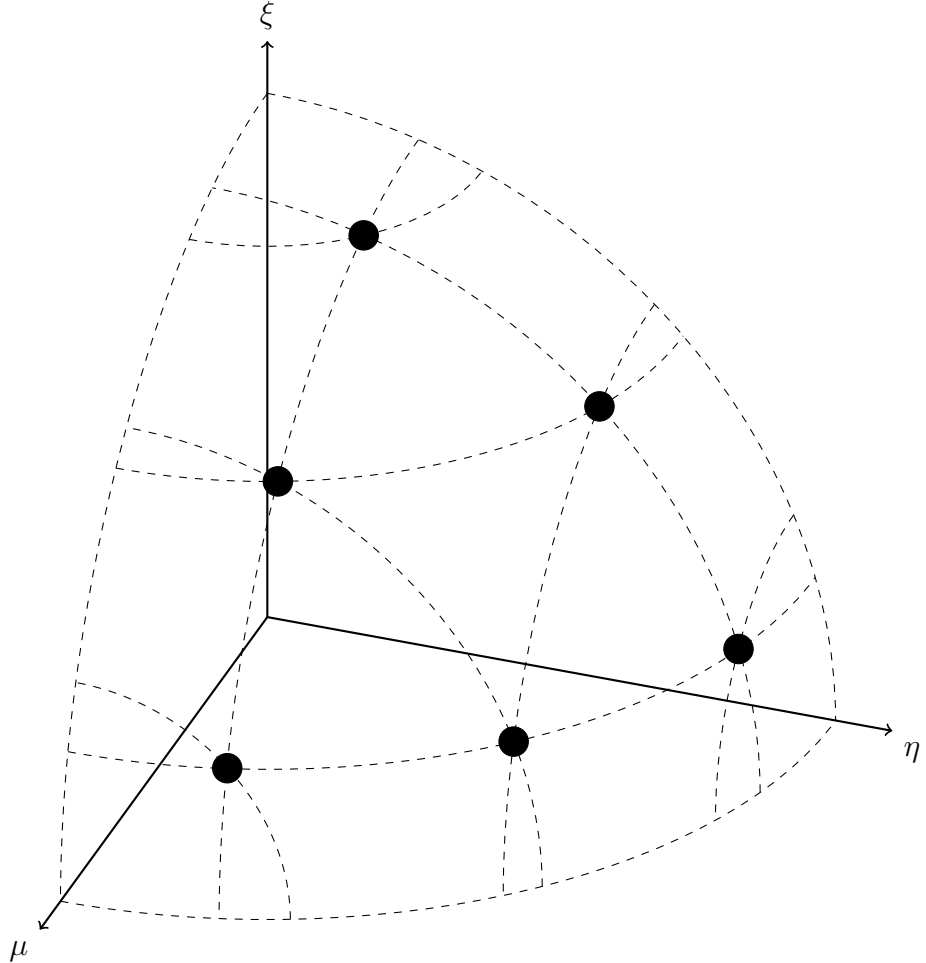


Figure 2: The positive octant for S_6 level-symmetric angular quadrature.

by

$$\phi \approx \sum_m^M w_m \psi_m, \quad (7)$$

where $M = N(N + 2)$. This approximation is utilized in these numerical methods outlined below. The set of angular quadrature data includes the μ_m , η_m , ξ_m , and w_m values for each discrete ordinate direction m for $m = 1, \dots, M$, and we define $\psi_m \equiv \psi(\mathbf{x}, \Omega_m)$. It is possible to generate these data sets [11] but we employ pre-generated data sets from ARDRA,⁵ a S_N radiation transport code being developed

⁵<https://wci.llnl.gov/simulation/computer-codes>

at LLNL.

1.2.2 Spatial Discretization

There are countless methods of spatial discretization that appear in the transport community. Among the most common are characteristic methods [12], finite difference methods [1], finite volume methods, and finite element methods (FEM) [1].

Typically, the problem domain is divided into a larger number of smaller domains. The equations are then numerically solved on each of these smaller regions where the solution is likely to be less varying when compared to the entire problem. The FEM was introduced to the transport community in the 1970's. The utility of this method was that it was more accurate than finite differencing methods [13]. Since then, radiation transport research using the FEM has proliferated. In particular, the discontinuous FEM (DFEM) has been favored for its accuracy in the thick diffusion limit [14] (discussed in Section 1.4). Thus, this research uses the DFEM where the solution is approximated to have a functional form within each mesh element. More discussion of various discretization methods can be found in Lewis and Miller [1].

Additionally, these radiation transport problems are solved in ~~each of~~ Cartesian, cylindrical, and spherical coordinates in one-, two-, and three-dimensions. The present research is concerned with X - Y and R - Z geometries — two-dimensional Cartesian and cylindrical geometries, respectively.

1.2.3 High-Order Finite Elements

The FEM spatial discretization for the radiation transport equation has been continually investigated since the 1970s [13, 15]. Although FEMs require more computer memory than finite-difference methods for the same spatial mesh, low-order (LO) methods, such as the linear discontinuous FEM (LD), have been used because of

their increased accuracy [14] and continue to be used and researched [16, 17, 18]. Studying and implementing more accurate methods becomes increasingly important as computational hardware performance increases. Computers can process and communicate quicker, and larger memory can store more variables. LO FEMs have been used and shown to be accurate in production codes like Attila [19], a three-dimensional transport code. Attila later adapted Trilinear DFEM (TLD), the three-dimensional analog to bilinear DFEM (BLD) [20]. Other methods have been studied as well, such as the piece-wise linear DFEM (PWLD) [21].

Higher order DFEMs (polynomial orders $p \geq 2$) have become more popular as modern computer performance improves. Several authors [22, 23, 24, 25] saw increased accuracy for up to 4th-order finite elements over lower-order methods with the same mesh refinement. Woods et al. [26] saw increased accuracy for up to 8th-order finite elements. These results further motivate the need for additional investigation of these HO methods.

Negative solutions can arise from oscillations within the HO FEM when the solution is near zero [27, 26]. These negative solutions are non-physical and must be corrected. Several authors have addressed negative scalar fluxes [17, 18, 28, 29, 30] with corrective methods generally falling into two categories: *ad hoc* modification after calculating a solution, and modification of the equations beforehand to yield positive results. In this dissertation, we characterize the behavior of the HO methods on meshes with curved surfaces, so we retain the negative fluxes as results of this methodology. With favorable results supporting continued analysis, we will leave the relevant investigation of negative flux corrections to future work.

1.2.4 Meshes

There are a wide variety of meshes used with triangular and quadrilateral (and their three-dimensional equivalents) being the most common. Modeling curved boundaries with quadrilateral spatial meshes can be difficult without significant mesh refinement. Triangular meshes may be used in these cases and are often seen in literature [13, 23, 24, 31]. Additionally, unstructured meshes are popular for modeling complex spatial geometries. For example, in three-dimensions, Attila can discretize the spatial domain using unstructured tetrahedral meshes [19].

Recently, meshes with curved surfaces have been investigated using finite elements for radiation transport. Liu and Larsen [32] used meshes with circular arcs to model a fuel pin geometry exactly. They performed their calculations using an average normal direction for the zone surface and swept through the mesh with surface averages fluxes equal to the zone average fluxes. Schunert et al. [33] used 1st-order FEM but with 2nd-order polynomial mesh surfaces instead of circular arcs for their fuel lattice geometry. They demonstrated an increase in accuracy using the higher-order mesh without an increase in computational time. Woods [27] and Woods et al. [26] demonstrated the use of up to 8th-order meshes. The motivation behind using meshes with curved surfaces is to model curved boundaries within a problem without requiring additional mesh refinement. Woods et al. [26] performed a spatial convergence study using meshes with curved surfaces and saw convergence rates of $(p + 1)$ that is consistent with predictions and results from Lasaint and Raviart [15] and Wang and Ragusa [23].

Other fields have investigated the use of meshes with curved surfaces. Cheng [34] demonstrated that straight-edged meshes, compared to curved meshes, restricted the accuracy of the solution of the compressible Euler equations, pointing to the necessity of curved meshes for higher-order accuracy. Dobrev et al. [7] saw increased

accuracy using such meshes for Lagrangian hydrodynamics. They mapped the reference element to the physical element using the basis functions that resulted in curved surfaces for HO finite elements. Subsequently, Dobrev et al. [35] demonstrated the use of curved meshes in axisymmetric geometries and noted that it modeled some features of the flow more accurately, among other improvements.

1.2.5 R-Z Geometry

The radiation transport equation has been solved in *R-Z* (i.e., two-dimensional cylindrical) geometry for many years. One particular difficulty with cylindrical coordinates is that an angular derivative is present within the streaming term. This results in the description of the *direction-of-travel* being dependent upon the spatial position. Despite a particle traveling in a straight line, the coordinate system describing that direction changes with position.

The streaming operator in three-dimensional cylindrical geometry is [1]

$$\boldsymbol{\Omega} \cdot \nabla \psi = \frac{\mu}{r} \frac{\partial}{\partial r}(r\psi) + \frac{\eta}{r} \frac{\partial \psi}{\partial \zeta} + \xi \frac{\partial \psi}{\partial z} - \frac{1}{r} \frac{\partial}{\partial \omega}(\eta\psi), \quad (8)$$

where $\boldsymbol{\Omega}$ is the direction of travel unit vector, ψ is the angular flux, and

$$\mu \equiv \boldsymbol{\Omega} \cdot \hat{e}_\mu = \sqrt{1 - \xi^2} \cos \omega = \sin(\theta) \cos(\omega), \quad (9)$$

$$\eta \equiv \boldsymbol{\Omega} \cdot \hat{e}_\eta = \sqrt{1 - \xi^2} \sin \omega = \sin(\theta) \sin(\omega), \quad (10)$$

$$\xi \equiv \boldsymbol{\Omega} \cdot \hat{e}_\xi = \cos(\theta). \quad (11)$$

The variables μ , η , ξ , ω , θ , and ζ are shown in the cylindrical coordinate system in Figure 3. Since the \hat{e}_μ -axis is always in the r -direction, the coordinate system describing $\boldsymbol{\Omega}$ depends upon the spatial position.

In *R-Z* geometry, we assume there is no solution variation in the azimuthal direc-

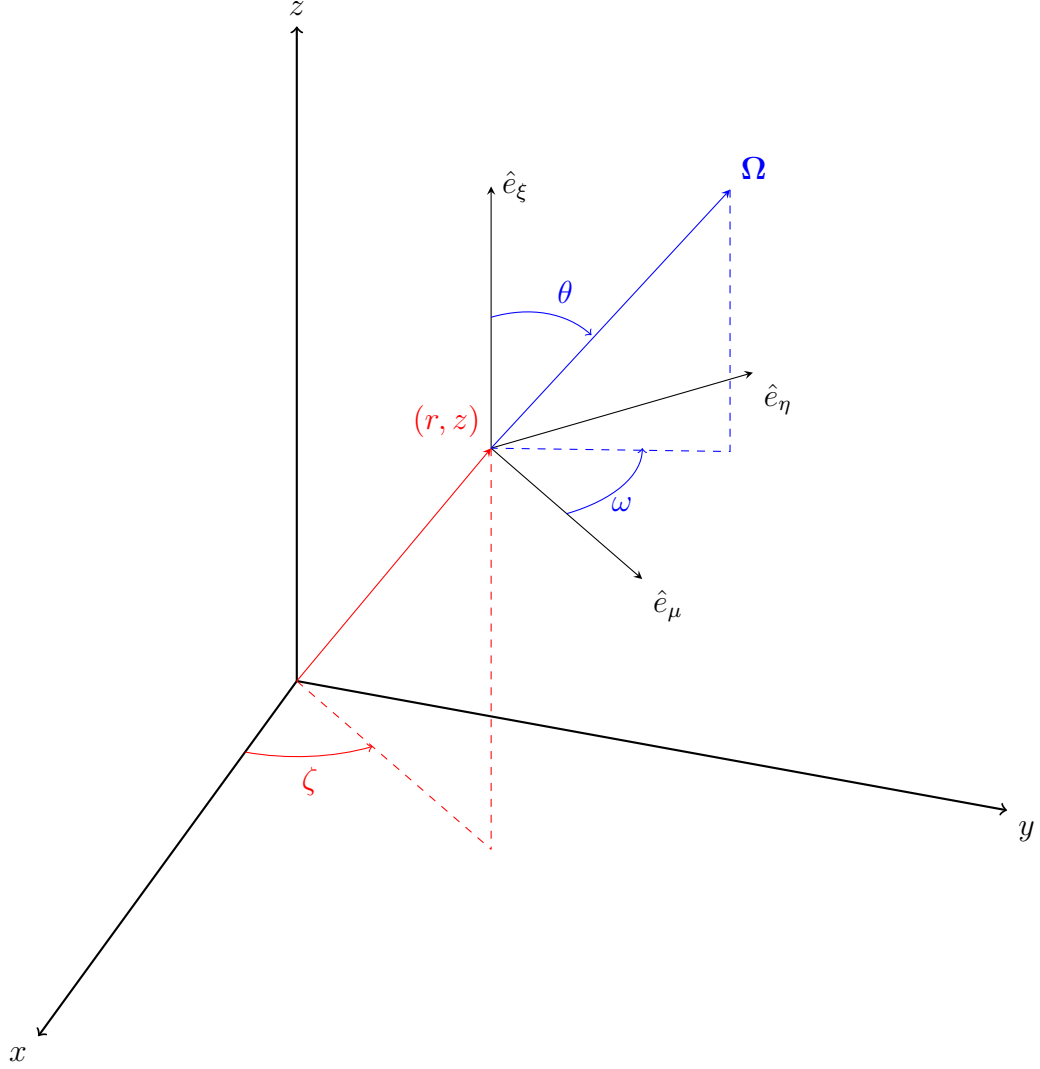


Figure 3: Cylindrical space-angle coordinate system showing the position (r, z) and direction of travel Ω .

tion, i.e.

$$\frac{\partial \psi}{\partial \zeta} \equiv 0, \quad (12)$$

which simplifies the streaming term to

$$\boldsymbol{\Omega} \cdot \nabla \psi = \frac{\mu}{r} \frac{\partial}{\partial r} (r\psi) + \xi \frac{\partial \psi}{\partial z} - \frac{1}{r} \frac{\partial}{\partial \omega} (\eta \psi), \quad (13)$$

where the third term is the angular derivative term.

The common method of handling the spatial discretization (developed by Morel and Montry [36] and described in detail in Section 2.4) is to discretize the direction of travel using level-symmetric angular quadrature, implement an approximation for the angular derivative, and sweep through the angular quadrature directions propagating angular flux information through the directions of travel. This method for handling the angular derivative has been implemented in other research that was focused on spatial discretizations. Following is a brief overview of that work.

Bailey et al. [21] derived the PWLD transport equation for *R-Z* geometry on arbitrary polygonal meshes and showed that their method is accurate in the diffusion limit. Bailey [37] performed an asymptotic diffusion limit analysis for PWLD in *R-Z* geometry on an arbitrary polygonal mesh and found the leading order angular flux is isotropic. The PWLD scheme also displayed $O(h^2)$ convergence rates in several test problems, as expected.

Morel et al. [31] performed an asymptotic diffusion limit analysis for the LLD method in *R-Z* geometry on a triangular mesh. The LLD equations satisfy a lumped linear continuous (LLC) diffusion discretization to leading order on the mesh interior. They also numerically demonstrate a $O(h^2)$ spatial convergence in the thick diffusion limit.

Efforts to maintain positivity on non-orthogonal meshes in *R-Z* geometry have been successful. Morel et al. [38] derived a lumped BLD scheme for quadrilaterals that “is conservative, preserves the constant solution, preserves the thick diffusion limit, behaves well with unresolved boundary layers, and gives second-order accuracy in both the transport and thick diffusion-limit regimes.”

At this time, only Woods and Palmer [39] have applied the HO DFEM in *R-Z* geometry on meshes with curved surfaces. That work is presented in this dissertation in support of the present research objectives.

1.3 Spherical Symmetry in *R-Z* Geometry

As previously mentioned, radiation-hydrodynamics is a multiphysics problem comprised of a thermal radiation problem coupled with a hydrodynamics problem. In cases with an axis of symmetry, a three-dimensional problem can be reduced to one or two spatial dimensions. For instance, a hohlraum could be modeled in *R-Z* geometry where a physical (or assumed) symmetry exists along the z -axis. This dimension reduction may save on computational memory. Some ICF applications employ a spherical target inside of a hohlraum. It is important to preserve the spherical symmetry of the target while using *R-Z* geometry. Since the hydrodynamics equations are being solved in *R-Z* geometry, the radiation transport equations must also be solved in *R-Z* geometry. Moreover, the transport equation must preserve spherical symmetry using the *R-Z* geometry spatial discretization.

There has been relatively little research in preserving spherical symmetry with the radiation transport equation in *R-Z* geometry. As previously mentioned, in hydrodynamics, Dobrev et al. [35] demonstrated this spherical symmetry preservation. In radiation diffusion, Brunner et al. [40] demonstrated conditional spherical symmetry preservation. To date, we are only aware of one published article discussing the ability of the *R-Z* transport equation to preserve 1-D spherical symmetry. Chaland and Samba [41] qualitatively demonstrated spherical symmetry preservation in a void with an initial condition of scalar flux in the center of the “sphere”. They demonstrated that ray-effects are created from the S_N transport equations in a void, whereas their alternative angular discretization qualitatively preserves the 1-D spherical symmetry. We follow the direction of Brunner et al. [40] by determining the spherical symmetry preservation by using the method of manufactured solutions (MMS) [42] with a manufactured solution in spherical geometry.

1.4 Diffusion Limit

In high energy density physics (HEDP) problems, a particle can have a very small mean free path (mfp) compared to the size of a spatial zone. The mfp is the inverse of the total cross section $\Lambda = \sigma_t^{-1}$. Therefore, when the total macroscopic cross section, σ_t , becomes very large, a span of length can be described as being many mfp's long. These problems are called “optically thick”. We require the transport equation (Equation 5) to resolve solutions in the optically thick regime. We can assess the behavior of Equation 5 as the problem becomes increasingly optically thick by performing an asymptotic analysis. Specifically, a small factor ε can be used to scale the physical processes of Equation 5:

$$\boldsymbol{\Omega} \cdot \nabla \psi + \frac{\sigma_t}{\varepsilon} \psi = \frac{1}{4\pi} \left(\frac{\sigma_t}{\varepsilon} - \varepsilon \sigma_a \right) \int_{4\pi} \psi d\Omega' + \varepsilon S_0, \quad (14)$$

where arguments have been dropped for brevity. Then, as $\varepsilon \rightarrow 0$, the mean free path $\Lambda = \varepsilon/\sigma_t \rightarrow 0$. In this limit, the problem is said to be optically thick and diffusive. It can be shown [43, 44] that this scaled analytic transport equation limits to the analytic radiation diffusion equation to $O(\varepsilon^2)$. The diffusion equation provides accurate solutions to optically thick and diffusive problems in the problem interior. Determining that the analytic transport equation limits to the analytic diffusion equation is physically meaningful. Optically thick and diffusive problems that may be typically solved with the radiation diffusion equation may also be solved using the radiation transport equation.

The diffusion equation has substantially fewer degrees of freedom for the same spatial discretization making it much quicker to solve numerically. This benefit is accompanied by some drawbacks. The diffusion equation ~~cannot resolve~~ optically thin problems ~~nor solutions~~ near highly absorbing regions, voids, ~~nor~~ strong material discontinuities [3]. However, the transport equation can resolve solutions in all of

these regimes, including the diffusive regions. Therefore, this dissertation employs the transport equation to solve problems that are optically thick and diffusive.

Although the analytic transport equation limits to the analytic diffusion equation in the ~~diffusion~~ limit, it is important that the discretized transport equation limits to a meaningful discretized diffusion equation. The diffusion limit analysis has been applied to spatially discretized transport problems. The LD and lumped LD (LLD) methods were shown to have the diffusion limit in one-dimension by Larsen and Morel [14] and Larsen [45], respectively, which is one of the reasons for their continued popularity in literature. In multiple dimensions, the LD method generally fails in the diffusion limit [46], but the LLD [31, 47], BLD [18], and fully lumped BLD (FLBLD) [48] methods possess the diffusion limit. Lumping the BLD equations in curvilinear geometry ~~has been demonstrated to possess~~ the diffusion limit as well [49, 38]. Attila has been demonstrated to solve problems in the diffusion limit using TLD, despite having the potential for negative fluxes [20].

The PWLD has also been popular for its performance in the diffusion limit. Stone and Adams [50] concluded the PWLD should behave as well as BLD ~~but on unstructured meshes~~. Bailey et al. [21, 37] corroborated this and extended the PWLD method to RZ geometry and concluded this method has the diffusion limit. Bailey et al. [51] then introduced piece-wise BLD (PWBLD) that allows for more curvature in a solution and has properties favorable to having the diffusion limit, although they do not perform the asymptotic analysis to be conclusive.

Palmer and Adams [49] and Palmer [52] solved the *R-Z S_N* equations (discussed in Section 1.2.5) using BLD, mass lumped BLD (MLBLD), surface lumped BLD (SLBLD), FLBLD, and simple corner balance (SCB) methods but found that only the FLBLD and SCB methods are accurate in the thick diffusion limit, as predicted by their asymptotic diffusion limit analysis. They determined that the support points

must be sufficiently “local” to achieve a reasonable discretization of the diffusion equation.

Guermond and Kanschat [53] performed an analytical diffusion limit analysis for arbitrary-order spatially discretized transport equations that are exactly integrated in angle. Haut [54] followed this work to demonstrate that the arbitrary-order spatially discretized transport equation also has the diffusion limit using the discrete ordinates method to discretize in angle. Woods et al. [26] numerically demonstrate that two-dimensional Cartesian HO finite elements trend toward the diffusion limit ~~despite not being conclusive about possessing the diffusion limit~~. Their study was performed without a source iteration acceleration technique so they were unable to perform calculations for optically thick media. Their work was performed on a quadrilateral mesh with curved surfaces.

1.5 Source Iteration Acceleration

Radiation transport is integral to applications such as inertial confinement fusion and astrophysics. These problems often have materials that can be exceptionally optically thick (material regions are many mean-free-path lengths across) and diffusive (highly scattering). A transport solver should be capable of performing accurate and efficient calculations on such problems. The source iteration (SI) method [1] is commonly employed to solve the transport equation. The algorithm

$$\boldsymbol{\Omega} \cdot \nabla \psi_m^{(\ell+1/2)} + \sigma_t \psi_m^{(\ell+1/2)} = \frac{1}{4\pi} \sigma_s \phi^{(\ell)} + S_0 \quad (15a)$$

$$\phi^{(\ell+1/2)} = \sum_m w_m \psi_m^{(\ell+1/2)} \quad (15b)$$

$$\phi^{(\ell+1)} = \phi^{(\ell+1/2)} \quad (15c)$$

describes the calculation of the angular flux using the lagged scalar flux followed by an update to the scalar flux using all of the angular fluxes. All spatial locations are coupled within each angle, and all angles are coupled at each spatial location. This coupling lends itself to a two-stage iterative method. One iteration of Equations 15 is shown within the boxed region of Figure 1. Specifically, Equation 15a falls within “Radiation transport solve” where all spatial locations are coupled within each angle. Equations 15b and 15c are within “Update scalar flux”, where all angles are coupled at each spatial position. This iterative process is continued until the scalar flux, ϕ , converges to within some defined tolerance.

The SI algorithm can converge arbitrarily slowly in optically thick and diffusive problems [55] resulting in impractical computational times. One alternative method to avoid these slowly converging problems is to solve the problem using the radiation diffusion equation instead of the transport equation. The diffusion equation can resolve solutions in optically thick and diffusive media and does not require source iteration. However, the diffusion equation cannot resolve solutions in highly absorbing media, optically thin media, nor media with strong material discontinuities including vacuum boundaries [3]. We retain the ability to obtain accurate solutions in a wide variety of media, including those that the diffusion equation cannot resolve, by solving the transport equation despite the potential drawback of slowly converging SI.

In order to preserve the transport solution on optically thick and diffusive problems, we must reduce the SI computational time in one of two ways. We may refine the mesh until the optical thickness of a typical mesh cell is on the order of a mean-free-path to effectively solve an optically thin problem in each mesh zone. However, this option may not be computationally efficient because it might introduce a large number of degrees of freedom to the problem, thereby increasing the solution time. Alternatively, acceleration techniques may be applied to the SI to compensate for

slow convergence.

Several SI acceleration schemes have been developed. The Wareing-Larsen-Adams (WLA) method [56], accelerates the source iterations but its effectiveness was found to degrade as cells become optically thick [57]. Another alternative, the modified four-step (M4S) [58], is effective in 1-D but is only conditionally stable in 2-D for unstructured meshes. Diffusion synthetic acceleration (DSA) is a very common method. Using DSA, Larsen [55] and Larsen and McCoy [59] showed that one-dimensional LD is unconditionally accelerated. Wareing et al. [56] and Adams and Martin [60] extended unconditionally accelerating DSA to two-dimensions. It is well known that the DSA algorithm can lose its effectiveness in multidimensional problems with strong material discontinuities. However, this degradation can be eliminated by preconditioning a Krylov iterative method with DSA [61]. In the present work, we focus on the DSA discretization method and its efficiency on homogeneous problems, and therefore avoid the need for a preconditioned Krylov solver.

The general DSA algorithm is

$$\boldsymbol{\Omega} \cdot \nabla \psi_m^{(\ell+1/2)} + \sigma_t \psi_m^{(\ell+1/2)} = \frac{1}{4\pi} (\sigma_s \phi^{(\ell)} + S_0) \quad (15a)$$

$$\phi^{(\ell+1/2)} = \sum_m w_m \psi_m^{(\ell+1/2)} \quad (15b)$$

$$-\nabla \cdot D \nabla \varphi^{(\ell+1/2)} + \sigma_a \varphi^{(\ell+1/2)} = \sigma_s (\phi^{(\ell+1/2)} - \phi^{(\ell)}) \quad (16a)$$

$$\phi^{(\ell+1)} = \phi^{(\ell+1/2)} + \varphi^{(\ell+1/2)} \quad (16b)$$

where $\phi^{(\ell+1/2)}$ is the radiation transport scalar flux solution at iteration $(\ell+1/2)$ prior to the DSA solve. Specifically, we solve for Equation 15a for each of the angular fluxes, $\psi_m^{(\ell+1/2)}$ at a half-step. Then, we perform a weighted summation of the angular fluxes to obtain the scalar flux at the half step, $\phi^{(\ell+1/2)}$. For comparison, the unaccelerated

source iteration method can then be performed by Equation 15c. The DSA algorithm then solves the DSA equation (Equation 16a), a diffusion equation with a modified source. Finally, the summation of the solution to the DSA equation and the scalar flux at the half step becomes the scalar flux solution at the end of the iteration.

The discretization scheme of the Equation 16a is very important and can determine whether a DSA method is stable or not. Fully consistent DSA schemes are unconditionally convergent and use the zeroeth and first moments of the discretized transport equation resulting in the mixed-form of the discretized diffusion equation [57]. Recently, Wang and Ragusa [22] developed the modified interior penalty (MIP) form for the DSA equations. Considered a partially consistent scheme, their derivation only utilizes the zeroeth moment of the discretized transport equation and results in a second-order diffusion equation. The MIP DSA method was developed from the interior penalty (IP) form of a discretized diffusion equation and was originally applied to HO DFEM S_N transport on triangular meshes. The IP method is not stable for optically thick media so it was combined with a spatial discretization they derived — diffusion conforming form (DCF) — that is stable in the optically thick regime. The MIP DSA equations switch between the IP and DCF methods and was demonstrated to be an effective SI acceleration scheme for HO DFEM methods. Wang and Ragusa's Fourier analysis demonstrated the effectiveness of this DSA scheme and corroborated it with numerical results. It has since been used with PWLD on arbitrary polygonal meshes [62] and later with BLD [63]. Woods et al. [2] implemented the MIP DSA equations and investigated the performance on meshes with curved surfaces; demonstrating that the method remains unconditionally stable.

The MIP DSA equations were derived with homogeneous Dirichlet boundary conditions according to Kanschat [64]. It has been acknowledged that homogeneous Dirichlet boundary conditions may degrade performance [25]. Other DSA implemen-

tations utilize Robin (also referred to as Marshak, zero incident current, mixed, or vacuum) boundary conditions [57, 60]. This allows for a nonzero DSA solution on the problem boundaries, thereby allowing a nonzero update to the transport scalar flux solution. In this dissertation, we present an extension of the work done by Woods et al. [2] that demonstrates a rapidly-convergent iterative solver for the transport equation spatially discretized with the HO DFEM, which employs the MIP DSA equations with homogeneous Robin boundary conditions.

1.6 Research Objectives

The research objectives of this dissertation are to:

- derive, implement, and characterize the transport equation in X - Y geometry using HO DFEM on meshes with curved surfaces,
- derive, implement, and characterize the transport equation in R - Z geometry using HO DFEM on meshes with curved surfaces, and
- derive, implement, and characterize the modified interior penalty (MIP) diffusion synthetic acceleration (DSA) method using Robin boundary conditions.

1.7 Outline

The remainder of this dissertation is organized as follows. In Section 2, we discuss the HO DFEM, meshes with curved surfaces, and the solution methods. In Section 3, we show the results as a result of implementing these methods. Finally, we make some concluding remarks in Section 4.

2 Methods

In this section we describe the high-order (HO) basis functions that we employ in this research (Section 2.1), the HO mesh transformation required (Section 2.2), and the solution method that we employ to solve the system of equations (Section 2.3). This spatial discretization falls within the “Spatial discretization” step of Figure 1.

2.1 High-Order Finite Elements Spatial Discretization

We discretize the spatial domain, \mathcal{D} , by first applying a spatial mesh to subdivide the problem spatial domain into non-overlapping mesh zones, \mathcal{D}_k , where we will solve Equation 5 on each zone. After applying the S_N approximation to Equation 5 (see Section 1.2.1), we multiply each term by a test function, v_{ki} for $i = 1, \dots, L_k$, where mesh zone k has $L_k = (p + 1)^b$ test functions for finite element order p in d spatial dimensions. We integrate the resulting equation over the volume of the mesh zone. After applying Equation 6, the weak form for mesh zone \mathcal{D}_k is obtained for direction Ω_m :

$$(\boldsymbol{\Omega}_m \cdot \nabla \psi_m, v_{ki})_{\mathcal{D}_k} + (\sigma_t \psi_m, v_{ki})_{\mathcal{D}_k} = \frac{1}{4\pi} (\sigma_s \phi, v_{ki})_{\mathcal{D}_k} + \frac{1}{4\pi} (S_0, v_{ki})_{\mathcal{D}_k}, \quad (17)$$

where we have dropped the arguments for brevity, and we define $\psi_m \equiv \psi(\mathbf{x}, \boldsymbol{\Omega}_m)$. We utilize the inner product notation,

$$(a(x, y), b(x, y))_{\mathcal{D}_k} \equiv \int_{\mathcal{D}_k} a(x, y) b(x, y) dx dy. \quad (18)$$

in this dissertation.

We integrate the streaming term in Equation 17 by parts,

$$\begin{aligned} -(\boldsymbol{\Omega}_m \cdot \nabla v_{ki}, \psi_m)_{\mathcal{D}_k} + \sum_{\partial\mathcal{D}_k} (\boldsymbol{\Omega}_m \cdot \hat{n} \psi_m, v_{ki})_{\partial\mathcal{D}_k} + (\sigma_t \psi_m, v_{ki})_{\mathcal{D}_k} \\ = \frac{1}{4\pi} (\sigma_s \phi, v_{ki})_{\mathcal{D}_k} + \frac{1}{4\pi} (S_0, v_{ki})_{\mathcal{D}_k}, \quad (19) \end{aligned}$$

where we sum over all surfaces for each zone. $\partial\mathcal{D}_k$ denotes the surfaces of \mathcal{D}_k , and $\hat{n} \equiv \hat{n}(\mathbf{x})$ is the outward unit normal vector at position \mathbf{x} on $\partial\mathcal{D}_k$.

We separate the surface integral term into interior surface $\partial\mathcal{D}_k^i$ and boundary surface $\partial\mathcal{D}_k^b$ terms,

$$\begin{aligned} -(\boldsymbol{\Omega}_m \cdot \nabla v_{ki}, \psi_m)_{\mathcal{D}_k} + (\sigma_t \psi_m, v_{ki})_{\mathcal{D}_k} \\ + \sum_{\partial\mathcal{D}_k^i} (\boldsymbol{\Omega}_m \cdot \hat{n} \psi_m^\uparrow, v_{ki})_{\partial\mathcal{D}_k^i} + \sum_{\partial\mathcal{D}_k^b} (\boldsymbol{\Omega}_m \cdot \hat{n} \psi_m^\uparrow, v_{ki})_{\partial\mathcal{D}_k^b} \\ = \frac{1}{4\pi} (\sigma_s \phi, v_{ki})_{\mathcal{D}_k} + \frac{1}{4\pi} (S_0, v_{ki})_{\mathcal{D}_k}. \quad (20) \end{aligned}$$

We have applied the upwind approximation in both surface terms. In general, a surface may not be purely upwind (or downwind). Curvature of a mesh zone may cause $\boldsymbol{\Omega}_m \cdot \hat{n}(\mathbf{x})$ to switch between negative (upwind) and positive (downwind) for various $\mathbf{x} \in \partial\mathcal{D}_k^i$. These re-entrant faces are not unique to high-order mesh zones — they may also occur in three-dimensional 1st-order hexahedral zones. We split the surface integral into two terms to account for the surface variation of the normal vector:

$$\sum_{\partial\mathcal{D}_k^i} (\boldsymbol{\Omega}_m \cdot \hat{n} \psi_m^\uparrow, v_{ki})_{\partial\mathcal{D}_k^i} = \sum_{\partial\mathcal{D}_k^i} (\boldsymbol{\Omega}_m \cdot \hat{n} \mathcal{I}_m^+, v_{ki})_{\partial\mathcal{D}_k^i} + \sum_{\partial\mathcal{D}_k^i} (\boldsymbol{\Omega}_m \cdot \hat{n} \mathcal{I}_m^-, v_{ki})_{\partial\mathcal{D}_k^i}, \quad (21)$$

These upwinding surface integrals are numerically integrated by the following defini-

tions:

$$(\boldsymbol{\Omega}_m \cdot \hat{n}(\mathbf{x}) \mathcal{I}_m^+(\mathbf{x}), v_{ki}(\mathbf{x}))_{\partial\mathcal{D}_k^i} \approx \sum_q^Q w_q \boldsymbol{\Omega}_m \cdot \hat{n}(\mathbf{x}_q) v_{ki}(\mathbf{x}_q) P^+(\mathbf{x}_q, \boldsymbol{\Omega}_m), \text{ and} \quad (22)$$

$$(\boldsymbol{\Omega}_m \cdot \hat{n}(\mathbf{x}) \mathcal{I}_m^-(\mathbf{x}), v_{ki}(\mathbf{x}))_{\partial\mathcal{D}_k^i} \approx \sum_q^Q w_q \boldsymbol{\Omega}_m \cdot \hat{n}(\mathbf{x}_q) v_{ki}(\mathbf{x}_q) P^-(\mathbf{x}_q, \boldsymbol{\Omega}_m) \quad (23)$$

where

$$P^+(\mathbf{x}_q, \boldsymbol{\Omega}_m) = \begin{cases} \psi_m^+, & \text{if } \boldsymbol{\Omega}_m \cdot \hat{n}(\mathbf{x}_q) < 0 \\ 0, & \text{if } \boldsymbol{\Omega}_m \cdot \hat{n}(\mathbf{x}_q) > 0 \end{cases}, \quad (24)$$

$$P^-(\mathbf{x}_q, \boldsymbol{\Omega}_m) = \begin{cases} 0, & \text{if } \boldsymbol{\Omega}_m \cdot \hat{n}(\mathbf{x}_q) < 0 \\ \psi_m^-, & \text{if } \boldsymbol{\Omega}_m \cdot \hat{n}(\mathbf{x}_q) > 0 \end{cases}, \quad (25)$$

and ψ^- is just inside cell k and ψ^+ is just outside (i.e. in the neighboring cell that shares surface $\partial\mathcal{D}_k^i$). At each spatial quadrature point \mathbf{x}_q on surface $\partial\mathcal{D}_k^i$, the direction of $\boldsymbol{\Omega}_m \cdot \hat{n}(\mathbf{x}_q)$ determines if that location is incident or outgoing. The upwind value is used if it exists or the value is set to zero. Figure 4 illustrates a surface that has both incident and outgoing angular fluxes. The blue portion represents an incident

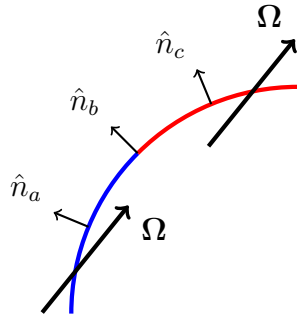


Figure 4: Example of an incident and outgoing surface.

flux because $\boldsymbol{\Omega} \cdot \hat{n}_a < 0$. The P^+ numerical integration is performed along the entire

surface but only the integration points on the blue portion are nonzero. The red portion represents an outgoing flux because $\boldsymbol{\Omega} \cdot \hat{n}_c > 0$. The P^- numerical integration is performed along the entire surface but only the integration points on the red portion are nonzero. The default integration order is $\mathcal{Q} = 2p + d \cdot g - 1$ along the surface $\partial\mathcal{D}_k^i$, where d is the dimension of the spatial domain (this research uses $d = 2$) and g is the order of the mesh zone.

Substituting Equation 21 into Equation 20, we have

$$\begin{aligned} & -(\boldsymbol{\Omega}_m \cdot \nabla v_{ki}, \psi_m)_{\mathcal{D}_k} + (\sigma_t \psi_m, v_{ki})_{\mathcal{D}_k} + \sum_{\partial\mathcal{D}_k^b} (\boldsymbol{\Omega}_m \cdot \hat{n} \mathcal{I}_m^-, v_{ki})_{\partial\mathcal{D}_k^b} \\ & + \sum_{\partial\mathcal{D}_k^i} (\boldsymbol{\Omega}_m \cdot \hat{n} \mathcal{I}_m^+, v_{ki})_{\partial\mathcal{D}_k^i} + \sum_{\partial\mathcal{D}_k^i} (\boldsymbol{\Omega}_m \cdot \hat{n} \mathcal{I}_m^-, v_{ki})_{\partial\mathcal{D}_k^i} \\ & = \frac{1}{4\pi} (\sigma_s \phi, v_{ki})_{\mathcal{D}_k} + \frac{1}{4\pi} (S_0, v_{ki})_{\mathcal{D}_k} + \sum_{\partial\mathcal{D}_k^b} (|\boldsymbol{\Omega}_m \cdot \hat{n}| \mathcal{I}_m^b, v_{ki})_{\partial\mathcal{D}_k^b}. \end{aligned} \quad (26)$$

Here we computed the boundary surface terms using the same approach as for interior surfaces, with a known boundary condition $\mathcal{I}_m^+ \equiv \mathcal{I}_m^b$ as the upwind value. If we performed a transport sweep (spatial sweep) through the mesh, the known (previously computed) upwind values ψ_m^+ would be used in the \mathcal{I}_m^+ term and subtracted to the right-hand-side. Since we generate a matrix that contains all spatial degrees of freedom, we leave this term in the bilinear form. These upstream values are dependent upon the degrees of freedom in each neighboring mesh zone. Thus, our global matrix contains off-diagonal sub-matrices that contain these couplings between mesh zones.

We assume the unknown angular and scalar fluxes in each mesh zone can be expanded in terms of basis functions $\varphi(\mathbf{r})$,

$$\psi(\mathbf{x}, \boldsymbol{\Omega}_m) \approx \sum_{j=1}^{L_k} \psi_{kj}(\boldsymbol{\Omega}_m) \varphi_{kj}(\mathbf{x}), \quad \mathbf{x} \in \mathcal{D}_k, \quad (27)$$

$$\phi(\mathbf{x}) \approx \sum_{j=1}^{L_k} \phi_{kj} \varphi_{kj}(\mathbf{x}), \quad \mathbf{x} \in \mathcal{D}_k \quad (28)$$

for basis functions $j = 1, \dots, L_k$, for L_k basis functions in mesh zone k . We use the standard Galerkin finite element method, in which the basis functions are equal to the test (weight) functions [65].

We employ Lagrange basis functions — the function equals unity at the integration point they “live” on and zero at all of the others. In two-dimensions, the general form of the first-order polynomial basis function is

$$b(x, y) = axy + bx + cy + d, \quad (29)$$

and the second-order basis function,

$$b(x, y) = ax^2y^2 + bx^2y + cx^2 + dxy^2 + exy + fx + gy^2 + hy + j, \quad (30)$$

where the sets $\{a, b, c, d\}$ and $\{a, b, c, d, e, f, g, h, j\}$ are the sets of coefficients that define the unique basis function for each integration point, respectively. This same methodology applies to higher-order basis functions. The location of the integration points is important. For example, we may place these evenly across the reference element or at Gauss-Legendre quadrature locations. On the unit square $[0, 1] \times [0, 1]$, the Gauss-Legendre integration points are located at the cross product of the nodes on $[0, 1]$. Listed for linear, quadratic, and cubic finite elements in Table 1, the Gauss-Legendre integration point abscissas [66] were transformed from the traditional $[-1, 1]$ to the reference element length $[0, 1]$.

Once the finite element order and the set of integration points is determined, the linear system can be arranged to determine the coefficients. For example, to determine the first-order basis function that “lives” at integration point (x_1, y_1) (and is equal to unity at that integration point and is zero at the remaining three), we

Table 1: Gaussian quadrature locations.

FE order	Points on $[-1, 1]$	Points on $[0, 1]$
1	$\pm \frac{1}{\sqrt{3}}$	$\frac{1}{3 + \sqrt{3}}$ $1 - \frac{1}{3 + \sqrt{3}}$
2	0 $\pm \sqrt{\frac{3}{5}}$	$\frac{1}{5 + \sqrt{15}}$ 0.5 $1 - \frac{1}{5 + \sqrt{15}}$
3	$\pm \sqrt{\frac{3}{7} - \frac{2}{7}\sqrt{\frac{6}{5}}}$ $\pm \sqrt{\frac{3}{7} + \frac{2}{7}\sqrt{\frac{6}{5}}}$	$\frac{10 + \sqrt{30}}{35 + \sqrt{35(15 - 2\sqrt{30})}}$ $\frac{10 - \sqrt{30}}{35 + \sqrt{35(15 - 2\sqrt{30})}}$ $1 - \frac{10 + \sqrt{30}}{35 + \sqrt{35(15 - 2\sqrt{30})}}$ $1 - \frac{10 - \sqrt{30}}{35 + \sqrt{35(15 - 2\sqrt{30})}}$

assemble the system of equations

$$\begin{bmatrix} x_1 y_1 & x_1 & y_1 & 1 \\ x_2 y_2 & x_2 & y_2 & 1 \\ x_3 y_3 & x_3 & y_3 & 1 \\ x_4 y_4 & x_4 & y_4 & 1 \end{bmatrix} \begin{bmatrix} a \\ b \\ c \\ d \end{bmatrix} = \begin{bmatrix} 1 \\ 0 \\ 0 \\ 0 \end{bmatrix}. \quad (31)$$

The 1 inside the solution vector on the right-hand-side determines which basis function coefficients will be obtained. For example, the right-hand-side vector $[0, 0, 1, 0]^T$ will return the basis function coefficients for the third integration point at (x_3, y_3) .

2.2 Meshes with Curved Surfaces

The basis functions are spatially dependent. Therefore, they are unique to each physical mesh zone due to the shape and location of each zone. We avoid having to perform calculations with arbitrarily large set of basis functions by utilizing the reference element and transforming the reference element into the physical element. We employ the same reference element for each mesh zone, where the basis functions are identical regardless of the physical element shape and position. After performing the DFEM integrations, we transform the solution from the reference element to the physical element. Each mesh zone will have a unique transformation but an identical set of basis functions to obtain the solution on the reference element. In general, the basis functions are allowed to be unique to each element, but we use the same set of basis functions across all elements for simplicity.

We can perform arbitrary-order mapping, preserving arbitrary-order curved mesh elements. To demonstrate, we provide an example bi-quadratic mapping. Figure 5 shows the bi-quadratic mapping from the reference element to a physical element and has the following functional form

$$\begin{bmatrix} x(\lambda, \kappa) \\ y(\lambda, \kappa) \end{bmatrix} = \sum_{i=1}^{J_k} \sum_{j=1}^{J_k} \begin{bmatrix} x_{ij} \\ y_{ij} \end{bmatrix} N_i(\lambda) N_j(\kappa) \quad (32)$$

where

$$N_l(\chi) = \begin{cases} (2\chi - 1)(\chi - 1), & l = 1 \\ 4\chi(1 - \chi), & l = 2 \\ \chi(2\chi - 1), & l = 3 \end{cases} \quad (33)$$

are the quadratic basis functions that have support points at typical vertices shown in the left image of Figure 5. The (x_{ij}, y_{ij}) coordinates are the locations of the vertices

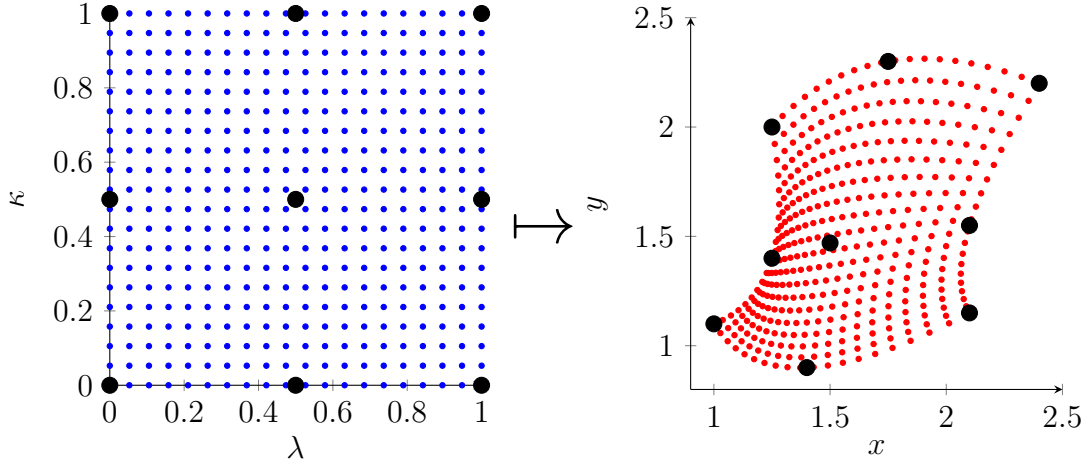


Figure 5: Example of mapping the reference element to a physical element.

in the physical element and are generally known. Equations 32 and 33 determine the (x, y) coordinates for each (λ, κ) vertex in the reference element. For example, the physical element vertex $(x_{12}, y_{12}) = (1.25, 1.4)$ is the location on the physical zone that is mapped from $(\lambda, \kappa) = (0, 0.5)$ on the reference element. That is,

$$x(0, 0.5) = 1.25, \text{ and} \quad (34)$$

$$y(0, 0.5) = 1.4. \quad (35)$$

The determinant of the Jacobian of the transformation,

$$\det [J(\lambda, \kappa)] = \begin{vmatrix} \frac{\partial x(\lambda, \kappa)}{\partial \lambda} & \frac{\partial y(\lambda, \kappa)}{\partial \lambda} \\ \frac{\partial x(\lambda, \kappa)}{\partial \kappa} & \frac{\partial y(\lambda, \kappa)}{\partial \kappa} \end{vmatrix}, \quad (36)$$

is used to perform the mapping from the physical space to λ - κ space. We perform the coordinate transformation from the reference element using the determinant of the Jacobian of the mapping and evaluate numerically. For example, applied to

Equation 18, this mapping is

$$\int_{\mathcal{D}_k} a(x, y) b(x, y) dx dy = \int_0^1 d\kappa \int_0^1 d\lambda a(\lambda, \kappa) b(\lambda, \kappa) \det(J(\lambda, \kappa)) \quad (37a)$$

$$\approx \sum_{i,j}^{\mathcal{Q}} w_i w_j a(\lambda_i, \kappa_j) b(\lambda_i, \kappa_j) \det(J(\lambda_i, \kappa_j)), \quad (37b)$$

where λ_i and κ_j are Gauss-Legendre integration points with associated quadrature weights w_i and w_j , and \mathcal{Q} is large enough to exactly integrate the polynomials. The default integration order we used is $\mathcal{Q} = 2p + dg - 1$, where p is the finite element order, d is the number of spatial dimensions, and g is the order of the mesh.

2.3 Solution Method

This section falls within the “Radiation transport solve” and “Update scalar flux” steps of Figure 1. We employ the Modular Finite Elements Library (MFEM)⁶ to perform integrations to assemble the system of equations for each element. These elements are then assembled into a global matrix that acts on each spatial degree of freedom simultaneously.

The meshes described in Section 2.2 add complexities to the numerical methods used to solve the transport equation. It is common to solve for a single mesh zone using incident angular flux information and propagate that angular flux from mesh zone to mesh zone, sweeping through the grid [67, 68]. However, if any particular mesh zone has both incident and outgoing angular fluxes to another mesh zone, they depend upon each other in a cyclic manner. “Breaking the cycle” is some fashion is necessary to perform the numerical computation. Instead of sweeping through the grid, we utilize MFEM to assemble each local element system of equations into a global system of equations, where the inter-element dependencies appear as off-

⁶mfem.org

diagonal block matrices. This global system of equations solves for all spatial degrees of freedom within all mesh zones for the entire problem. This is computationally intensive, but it bypasses the need to consider any cycles that may occur. The goal of this work is to evaluate the methodology, not solution efficiency.

After generating the system of equations, we use UMFPack, a direct solver that performs a LU decomposition [69, 70] to solve for all of the spatial degrees of freedom for direction Ω_m . This satisfies the “End of m loop” criterion of Figure 1. We solve the global system of equations for the scalar flux, ϕ , using either the source iteration method (SI) (Equations 15 and “Update scalar flux” of Figure 1) or the DSA SI (Equations 15a, 15b, and 16, and both “DSA solve” and “Update scalar flux” within Figure 1). The iterative process continues until the convergence criterion

$$\|\phi^{(\ell+1)} - \phi^{(\ell)}\|_\infty < \varepsilon_{\text{conv}} (1 - \rho_{\text{sr}}) \|\phi^{\ell+1}\|_\infty, \quad (38)$$

is met, where $\varepsilon_{\text{conv}}$ is some small tolerance, ρ_{sr} is the estimated spectral radius,

$$\rho_{\text{sr}} \approx \frac{\|\phi^{(\ell+1)} - \phi^{(\ell)}\|_\infty}{\|\phi^{(\ell)} - \phi^{(\ell-1)}\|_\infty}, \quad (39)$$

as described by Adams and Larsen [58], and where

$$\|\mathbf{y}\|_\infty = \max_i(y_i). \quad (40)$$

This satisfies the “Scalar flux converged” criterion of Figure 1. The spectral radius is the measure of the convergence rate during the source iteration. This convergence criterion protects against false convergence. That is, for slowly converging solutions, two sequential scalar fluxes may be sufficiently similar, appearing to be converged. The spectral radius is used in the convergence criterion to signal the slow convergence and prevent the false indication that the scalar flux has converged. We initiated all of the iterative solves with an initial scalar flux at each integration point randomly varying between -1000 and $+1000$.

2.4 R-Z Geometry

This section falls within the “Spatial discretization” step of Figure 1. Solving the transport equation in different coordinate systems may provide simpler ways of modeling a particular geometry or symmetry. In this section, we derive the *R-Z* transport equation to be solved. Section 1.2.5 contains the introduction to the streaming operator in *R-Z* geometry. Some of that work is reproduced here for completeness.

The streaming operator in *R-Z* geometry is [1]

$$\boldsymbol{\Omega} \cdot \nabla \psi = \frac{\mu}{r} \frac{\partial}{\partial r} (r\psi) + \xi \frac{\partial \psi}{\partial z} - \frac{1}{r} \frac{\partial}{\partial \omega} (\eta\psi), \quad (13)$$

where $\boldsymbol{\Omega}$ is the direction of travel unit vector, ψ is the angular flux, and

$$\mu \equiv \boldsymbol{\Omega} \cdot \hat{e}_\mu = \sqrt{1 - \xi^2} \cos \omega = \sin(\theta) \cos(\omega), \quad (9)$$

$$\eta \equiv \boldsymbol{\Omega} \cdot \hat{e}_\eta = \sqrt{1 - \xi^2} \sin \omega = \sin(\theta) \sin(\omega), \quad (10)$$

$$\xi \equiv \boldsymbol{\Omega} \cdot \hat{e}_\xi = \cos(\theta). \quad (11)$$

The variables μ , η , ξ , ω , and θ are shown in the cylindrical coordinate system in Figure 3. The key point is that the coordinate system describing $\boldsymbol{\Omega}$ depends upon the spatial position. The steady-state, mono-energetic transport equation in *R-Z* geometry is then

$$\begin{aligned} \frac{\mu}{r} \frac{\partial}{\partial r} r\psi(r, z, \boldsymbol{\Omega}) + \xi \frac{\partial}{\partial z} \psi(r, z, \boldsymbol{\Omega}) - \frac{1}{r} \frac{\partial}{\partial \omega} \eta\psi(r, z, \boldsymbol{\Omega}) + \sigma_t(r, z) \psi(r, z, \boldsymbol{\Omega}) \\ = \frac{1}{4\pi} \sigma_s(r, z) \phi(r, z) + S_0(r, z, \boldsymbol{\Omega}). \end{aligned} \quad (41)$$

We divide the angular-spatial discretizations into two sections. In Section 2.4.1, we discretize the *R-Z* transport equation using the discrete ordinates method. In Section 2.4.2, we perform the discretization of the spatial domain using HO DFEM.

2.4.1 Angular Discretization

This section falls within the “Angular discretization” step of Figure 1. Discretizing Equation 41 with a level-symmetric angular quadrature results in

$$\begin{aligned} \frac{\mu_{n,m}}{r} \frac{\partial}{\partial r} r \psi_{n,m}(r, z) + \xi_n \frac{\partial}{\partial z} \psi_{n,m}(r, z) - \frac{1}{r} \frac{\partial}{\partial \omega} \eta_{n,m} \psi_{n,m}(r, z) + \sigma_t(r, z) \psi_{n,m}(r, z) \\ = \frac{1}{4\pi} \int_{4\pi} \sigma_s(r, z) \phi(r, z, \Omega') d\Omega' + S_0(r, z, \Omega) \quad (42) \end{aligned}$$

for direction $\Omega_{n,m}$, where index n describes a level of quadrature with constant ξ and the m index denotes the quadrature point on that level. The (n, m) indexing is shown in Figure 6.

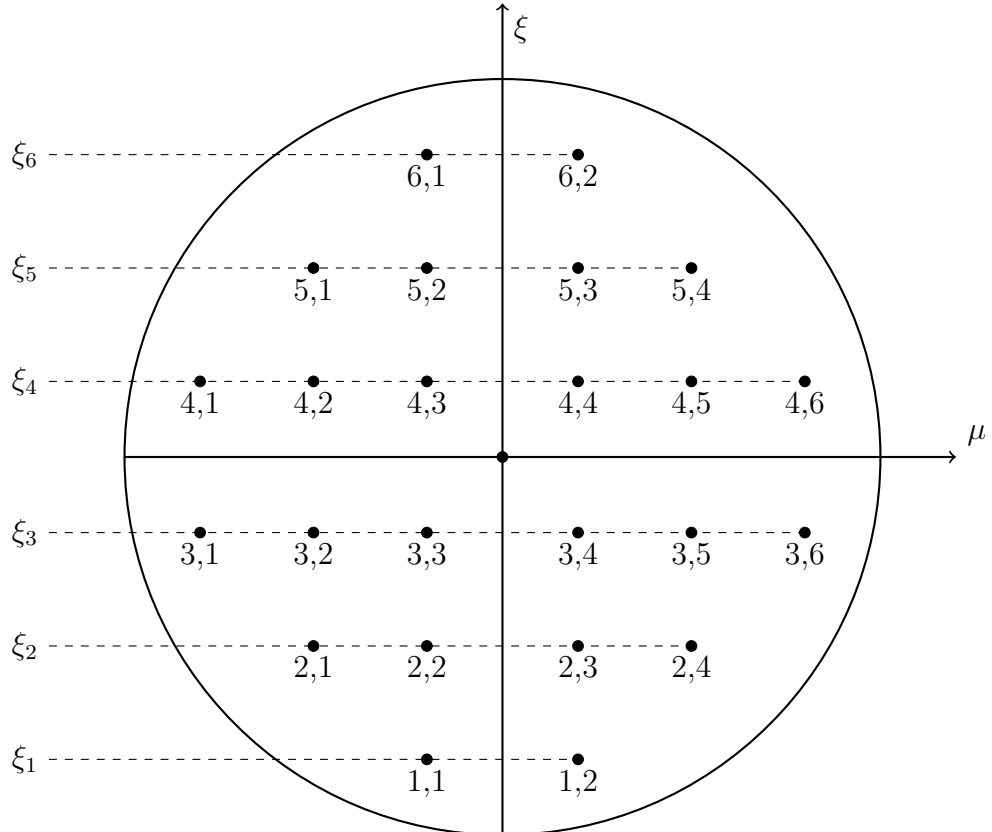


Figure 6: Angular discretization showing (ξ, μ) pairs; adapted from [1]

One of the major challenges is handling the angular derivative term. Lewis and Miller [1] describes an approximation for the partial derivative of the angular flux with respect to ω :

$$-\frac{1}{r} \frac{\partial}{\partial \omega} \eta_{m,n} \psi_{n,m}(r, z) = \frac{\alpha_{m+1/2}^n \psi_{n,m+1/2}(r, z) - \alpha_{m-1/2}^n \psi_{n,m-1/2}(r, z)}{rw_{n,m}} \quad (43)$$

where $\alpha_{m+1/2}^n$ and $\alpha_{m-1/2}^n$ are angular differencing coefficients, $\psi_{n,m+1/2}$ and $\psi_{n,m-1/2}$ are the angular fluxes in the $(\xi_n, \mu_{n,m+1/2})$ - and $(\xi_n, \mu_{n,m-1/2})$ -directions, respectively, and $w_{n,m}$ is the angular quadrature weight. We substitute this into Equation 42,

$$\begin{aligned} & \frac{\mu_{n,m}}{r} \frac{\partial}{\partial r} r \psi_{n,m}(r, z) + \xi_n \frac{\partial}{\partial z} \psi_{n,m}(r, z) \\ & + \frac{\alpha_{m+1/2}^n \psi_{n,m+1/2}(r, z) - \alpha_{m-1/2}^n \psi_{n,m-1/2}(r, z)}{rw_{n,m}} + \sigma_t(r, z) \psi_{n,m}(r, z) \\ & = \frac{1}{4\pi} \int_{4\pi} \sigma_s(r, z) \psi(r, z, \Omega') d\Omega' + \frac{1}{4\pi} S_0(r, z) \end{aligned} \quad (44)$$

Here, we pause to notice that there are similarities and differences between a Cartesian discretization. The absorption term, axial derivative term, and right-hand-side are the same in both coordinate systems. The differences arise in the radial and angular derivative terms.

Requiring Equation 44 to satisfy the uniform infinite medium solution results in the condition,

$$\alpha_{m+1/2}^n = \alpha_{m-1/2}^n - \mu_{n,m} w_{n,m} \quad (45)$$

If $\alpha_{1/2}^n$ is known, then the remaining coefficients are uniquely determined. To find $\alpha_{1/2}^n$, we require that the angular flux of Equation 44 also satisfy the conservation equation (Equation 41). Given a quadrature set with an even number of $\mu_{n,m}$ values, setting $\alpha_{1/2}^n = 0$ results in $\alpha_{M_n+1/2}^n = 0$ per Equation 45 and the conservation equation is satisfied.

A relationship between $\psi_{n,m}$, $\psi_{n,m+1/2}$, and $\psi_{n,m-1/2}$ must be established. A

weighted diamond difference scheme has been established by Morel and Montry [36],

$$\psi_{n,m}(r, z) = \tau_{n,m} \psi_{n,m+1/2} + (1 - \tau_{n,m}) \psi_{n,m-1/2}, \quad (46)$$

where $\tau_{n,m}$ linearly interpolates $\mu_{n,m}$:

$$\tau_{n,m} = \frac{\mu_{n,m} - \mu_{n,m-1/2}}{\mu_{n,m+1/2} - \mu_{n,m-1/2}}, \quad (47)$$

with

$$\mu_{n,m+1/2} = \sqrt{1 - \xi_n^2} \cos(\varphi_{n,m+1/2}), \quad (48)$$

$$\varphi_{n,m+1/2} = \varphi_{n,m-1/2} + \pi \frac{w_{n,m}}{w_n}, \text{ and} \quad (49)$$

$$w_n = \sum_{m=1}^{M_n} w_{n,m}, \quad (50)$$

where M_n is the number of discrete ordinate directions along ξ_n .

We multiply Equation 44 through by r and perform a product rule on the r -derivative term,

$$\begin{aligned} & \mu_{n,m} \left[\psi_{n,m}(r, z) + r \frac{\partial}{\partial r} \psi_{n,m}(r, z) \right] + r \xi_n \frac{\partial}{\partial z} \psi_{n,m}(r, z) \\ & + \frac{\alpha_{m+1/2}^n \psi_{m+1/2,n}(r, z) - \alpha_{m-1/2}^n \psi_{m-1/2,n}(r, z)}{w_{n,m}} + r \sigma_t(r, z) \psi_{n,m}(r, z) \\ & = \frac{r}{4\pi} \int_{4\pi} \sigma_s(r, z) \psi(r, z, \Omega') d\Omega' + \frac{r}{4\pi} S_0(r, z). \end{aligned} \quad (51)$$

We solve Equation 46 for $\psi_{n,m+1/2}$, perform a substitution, and move the known quantities to the right-hand-side,

$$\begin{aligned} & \mu_{n,m} r \frac{\partial}{\partial r} \psi_{n,m}(r, z) + r \xi_n \frac{\partial}{\partial z} \psi_{n,m}(r, z) + \mu_{n,m} \psi_{n,m}(r, z) \\ & + \frac{\alpha_{m+1/2}^n}{\tau_{n,m} w_{n,m}} \psi_{n,m}(r, z) + r \sigma_t(r, z) \psi_{n,m}(r, z) \\ & = \frac{r}{4\pi} \int_{4\pi} \sigma_s(r, z) \psi(r, z, \Omega') d\Omega' + \frac{r}{4\pi} S_0(r, z) \\ & + \left(\frac{1 - \tau_{n,m}}{\tau_{n,m}} \frac{\alpha_{m+1/2}^n}{w_{n,m}} + \frac{\alpha_{m-1/2}^n}{w_{n,m}} \right) \psi_{n,m-1/2}(r, z). \end{aligned} \quad (52)$$

Given a level-symmetric quadrature set, all of the $\alpha_{n,m\pm 1/2}^n$ and $\tau_{n,m}$ values can be computed. We solve the starting direction equation to obtain $\psi_{n,1/2}$. That is, we solve the X - Y system for directions $\Omega_{n,1/2}$,

$$\Omega_{n,1/2} \cdot \nabla \psi_{n,1/2} + \sigma_t \psi_{n,1/2} = \frac{1}{4\pi} \sigma_s \phi + \frac{1}{4\pi} S_0 \quad (53)$$

2.4.1.1 Reflecting Boundary at $r = 0$

The angular flux at $r = 0$ is a reflecting boundary — there is rotational symmetry around the z -axis. This arises naturally in the analytic transport equation. Beginning with Equation 41, we multiply through by r , perform a product rule on the r -derivative term and set $r = 0$. On the z -axis, the transport equation becomes

$$\mu \psi - \frac{\partial}{\partial \omega} (\eta \psi) = 0. \quad (54)$$

Then, performing a product rule on the angular derivative term results in,

$$\mu \psi - \psi \frac{\partial \eta}{\partial \omega} - \eta \frac{\partial \psi}{\partial \omega} = 0. \quad (55)$$

Since

$$\frac{\partial \eta}{\partial \omega} \equiv \mu, \quad (56)$$

we can simplify this to

$$\eta \frac{\partial \psi}{\partial \omega} = \eta \frac{\partial \psi}{\partial \mu} \frac{\partial \mu}{\partial \omega} = \eta^2 \frac{\partial \psi}{\partial \mu} = 0. \quad (57)$$

$$(58)$$

Finally, we write

$$\frac{\partial \psi}{\partial \omega} = 0, \quad (59)$$

and

$$\frac{\partial \psi}{\partial \mu} = 0. \quad (60)$$

That is, the angular flux does not depend on ω (nor μ) along the z -axis. Analytically, the transport equation has a naturally occurring reflecting boundary at $r = 0$. This condition is also satisfied by the Morel and Montry discretization scheme. Beginning with Equation 44, we multiply through by r , perform a product rule on the r -derivative term, and set $r = 0$, resulting in

$$\mu_{n,m} \psi_{n,m} + \frac{\alpha_{m+1/2}^n \psi_{n,m+1/2} - \alpha_{m-1/2}^n \psi_{n,m-1/2}}{w_{n,m}} = 0. \quad (61)$$

We utilize the weighted diamond differencing relationship (Equation 46) to eliminate $\psi_{n,m+1/2}$ and rearrange:

$$(\mu_{n,m} w_{n,m} \tau_{n,m} + \alpha_{m+1/2}^n) \psi_{n,m} = [(1 - \tau_{n,m}) \alpha_{m+1/2}^n + \alpha_{m-1/2}^n \tau_{n,m}] \psi_{n,m-1/2}. \quad (62)$$

We also utilize Equation 45 and rearrange:

$$(\mu_{n,m} w_{n,m} \tau_{n,m} + \alpha_{m+1/2}^n) \psi_{n,m} = (\alpha_{m+1/2}^n + \mu_{n,m} w_{n,m} \tau_{n,m}) \psi_{n,m-1/2}. \quad (63)$$

Finally, this simplifies to

$$\psi_{n,m} = \psi_{n,m-1/2}, \quad (64)$$

which satisfies Equation 60.

2.4.2 Spatial Discretization

Here, we discretize the spatial domain using the discontinuous finite element method (DFEM). The methodology is similar to the Cartesian geometry (i.e., Section 2.1). First, we subdivide a problem domain using a spatial mesh. Then, we multiply Equation 42 by a test function and integrate over the volume of mesh zone \mathcal{D}_k ,

dropping the arguments for brevity,

$$\begin{aligned}
& \left(r \boldsymbol{\Omega}_{n,m} \cdot \left[\frac{\partial}{\partial r} \psi_{n,m} + \frac{\partial}{\partial z} \psi_{n,m} \right], v_i \right)_{\mathcal{D}_k} + (\mu_{n,m} \psi_{n,m}, v_i)_{\mathcal{D}_k} \\
& + (r \sigma_t \psi_{n,m}, v_i)_{\mathcal{D}_k} + \left(\frac{\alpha_{m+1/2}^n}{\tau_{n,m} w_{n,m}} \psi_{n,m}, v_i \right)_{\mathcal{D}_k} \\
& = \left(\frac{1}{4\pi} r \sigma_s \phi, v_i \right)_{\mathcal{D}_k} + \left(\frac{1}{4\pi} r S_0, v_i \right)_{\mathcal{D}_k} \\
& + \left(\left[\frac{\alpha_{m+1/2}^n (1 - \tau_{n,m})}{w_{n,m} \tau_{n,m}} + \frac{\alpha_{m-1/2}^n}{w_{n,m}} \right] \psi_{n,m-1/2}, v_i \right)_{\mathcal{D}_k} \quad (65)
\end{aligned}$$

where Equation 6 and the inner product notation of Equation 18 have been used. We perform an integration by parts on the streaming term,

$$\begin{aligned}
& \sum_{\partial\mathcal{D}_k} (\boldsymbol{\Omega}_{n,m} \cdot \hat{n} r \psi_{n,m}^\dagger, v_i)_{\partial\mathcal{D}_k} - \left(r \psi_{n,m}, \boldsymbol{\Omega}_{n,m} \cdot \left[\frac{\partial}{\partial r} v_i + \frac{\partial}{\partial z} v_i \right] \right)_{\mathcal{D}_k} + (\mu_{n,m} \psi_{n,m}, v_i)_{\mathcal{D}_k} \\
& + (r \sigma_t \psi_{n,m}, v_i)_{\mathcal{D}_k} + \left(\frac{\alpha_{m+1/2}^n}{\tau_{n,m} w_{n,m}} \psi_{n,m}, v_i \right)_{\mathcal{D}_k} \\
& = \left(\frac{1}{4\pi} r \sigma_s \phi, v_i \right)_{\mathcal{D}_k} + \left(\frac{1}{4\pi} r S_0, v_i \right)_{\mathcal{D}_k} \\
& + \left(\left[\frac{\alpha_{m+1/2}^n (1 - \tau_{n,m})}{w_{n,m} \tau_{n,m}} + \frac{\alpha_{m-1/2}^n}{w_{n,m}} \right] \psi_{n,m-1/2}, v_i \right)_{\mathcal{D}_k} \quad (66)
\end{aligned}$$

to obtain the angular and spatially discretized *R-Z* transport equation, where $\partial\mathcal{D}_k$ is each of the surfaces on zone \mathcal{D}_k .

We perform numerical integrations to incorporate the mesh transformation from the reference element to the physical element by employing the determinant of the Jacobian defined by Equation 36. The general volume integrations are performed as described by Equations 37.

The numerical integration of the surface term is more complicated. The sign of $\boldsymbol{\Omega}_{n,m} \cdot \hat{n}(r, z)$ is evaluated at each spatial quadrature point along some surface $\partial\mathcal{D}_k$. Therefore, on a non-planar surface, the sign may switch between positive and negative denoting an outgoing or incident angular flux at the location of the quadrature point

(see Figure 4 and surrounding text). Since we perform a Gaussian integration along each surface, we are approximating a continuous function that has a discontinuous first-derivative with a polynomial shape.

We apply the upwind approximation to the surface term

$$\begin{aligned}
& \sum_{\partial\mathcal{D}_k} (r\boldsymbol{\Omega}_{n,m} \cdot \hat{n}\psi_{n,m}^\uparrow, v_{ki})_{\partial\mathcal{D}_k} - (r\psi_{n,m}, \boldsymbol{\Omega}_{n,m} \cdot \nabla v_i)_{\mathcal{D}_k} + (\mu_{n,m}\psi_{n,m}, v_i)_{\mathcal{D}_k} \\
& \quad + \left(\frac{\alpha_{m+1/2}^n}{\tau_{n,m}w_{n,m}}\psi_{n,m}, v_i \right)_{\mathcal{D}_k} + (r\sigma_t\psi_{n,m}, v_i)_{\mathcal{D}_k} \\
& = \left(\frac{r}{4\pi} \int_{4\pi} \sigma_s \psi d\Omega', v_i \right)_{\mathcal{D}_k} + \left(\frac{r}{4\pi} S_0, v_i \right)_{\mathcal{D}_k} \\
& \quad + \left(\left(\frac{1-\tau_{n,m}}{\tau_{n,m}} \frac{\alpha_{m+1/2}^n}{w_{n,m}} + \frac{\alpha_{m-1/2}^n}{w_{n,m}} \right) \psi_{n,m-1/2}, v_i \right)_{\mathcal{D}_k}, \quad (67)
\end{aligned}$$

where

$$\begin{aligned}
& \sum_{\partial\mathcal{D}_k} (r \boldsymbol{\Omega}_{n,m} \cdot \hat{n}(r, z) \psi_{n,m}^\uparrow, v_{ki})_{\partial\mathcal{D}_k} \\
& = \sum_{\partial\mathcal{D}_k^i} (r \boldsymbol{\Omega}_{n,m} \cdot \hat{n}(r, z) \psi_{n,m}^\uparrow, v_{ki})_{\partial\mathcal{D}_k^i} + \sum_{\partial\mathcal{D}_k^b} (r \boldsymbol{\Omega}_{n,m} \cdot \hat{n}(r, z) \psi_{n,m}^\uparrow, v_{ki})_{\partial\mathcal{D}_k^b}. \quad (68)
\end{aligned}$$

That is, we perform the upwinding approximation on the interior and the boundary surfaces, i.e. $\partial\mathcal{D}_k^i$ and $\partial\mathcal{D}_k^b$, respectively. These upwinding surface integrals are numerically integrated by the following definitions:

$$\begin{aligned}
& \sum_{\partial\mathcal{D}_k^i} (r \boldsymbol{\Omega}_{n,m} \cdot \hat{n}(r, z) \psi_{n,m}^\uparrow, v_{ki})_{\partial\mathcal{D}_k^i} \\
& = \sum_{\partial\mathcal{D}_k^i} (r \boldsymbol{\Omega}_{n,m} \cdot \hat{n}(r, z) \mathcal{I}_{n,m}^+, v_{ki})_{\partial\mathcal{D}_k^i} + \sum_{\partial\mathcal{D}_k^i} (r \boldsymbol{\Omega}_{n,m} \cdot \hat{n}(r, z) \mathcal{I}_{n,m}^-, v_{ki})_{\partial\mathcal{D}_k^i}, \quad (69)
\end{aligned}$$

where we define

$$(r \cdot \Omega_{n,m} \cdot \hat{n}(r, z) \mathcal{I}_{n,m}^+, v_{ki})_{\partial\mathcal{D}_k^i} \quad (70)$$

$$\approx \sum_q^Q w_q r \cdot \Omega_{n,m} \cdot \hat{n}(r_q, z_q) v_{ki} P^+(r_q, z_q, \Omega_{n,m}) \quad (71)$$

$$\approx \sum_q^Q w_q r_q \cdot \Omega_{n,m} \cdot \hat{n}(\lambda_q, \kappa_q) v_{ki} P^+(\lambda_q, \kappa_q, \Omega_{n,m}) \det(J(\lambda_q, \kappa_q)), \quad (72)$$

and

$$(r \cdot \Omega_{n,m} \cdot \hat{n}(r, z) \mathcal{I}_{n,m}^-, v_{ki})_{\partial\mathcal{D}_k^i} \quad (73)$$

$$\approx \sum_q^Q w_q r \cdot \Omega_{n,m} \cdot \hat{n}(r_q, z_q) v_{ki} P^-(r_q, z_q, \Omega_{n,m}) \quad (74)$$

$$\approx \sum_q^Q w_q r_q \cdot \Omega_{n,m} \cdot \hat{n}(\lambda_q, \kappa_q) v_{ki} P^-(\lambda_q, \kappa_q, \Omega_{n,m}) \det(J(\lambda_q, \kappa_q)), \quad (75)$$

where P^+ and P^- are defined,

$$P^+(r_q, z_q, \Omega_{n,m}) = \begin{cases} \psi_{n,m}^+, & \text{if } \Omega_{n,m} \cdot \hat{n}(r_q, z_q) < 0 \\ 0, & \text{if } \Omega_{n,m} \cdot \hat{n}(r_q, z_q) > 0 \end{cases}, \quad (76)$$

and

$$P^-(r_q, z_q, \Omega_{n,m}) = \begin{cases} 0, & \text{if } \Omega_{n,m} \cdot \hat{n}(r_q, z_q) < 0 \\ \psi_{n,m}^-, & \text{if } \Omega_{n,m} \cdot \hat{n}(r_q, z_q) > 0 \end{cases}, \quad (77)$$

where $\psi_{n,m}^-$ is just inside cell k and $\psi_{n,m}^+$ is just outside (i.e. in the neighboring cell that shares surface $\partial\mathcal{D}_k^i$). Therefore, at each spatial quadrature point (r_q, z_q) on surface $\partial\mathcal{D}_k^i$, the direction of $\Omega_{n,m} \cdot \hat{n}(r_q, z_q)$ determines if that location is incident or outgoing. The upwind value is used if it exists or the value is set to zero.

2.5 Modified Interior Penalty DSA

This section falls within the “DSA solve” step of Figure 1. The discretization of the DSA equation (Equation 16a) is of particular importance. Presently, we discretize this equation in X - Y geometry only. The finite element discretized form of the MIP DSA equations is

$$b_{\text{MIP,D}}(\varphi, v) = l_{\text{MIP}}(v) \quad (78)$$

where,

$$\begin{aligned} b_{\text{MIP,D}}(\varphi, v) &= (\sigma_a \varphi, v)_{\mathcal{D}_k} + (D \nabla \varphi, \nabla v)_{\mathcal{D}_k} \\ &+ (\kappa_e [\![\varphi]\!], [\![v]\!])_{\partial \mathcal{D}_k^i} + ([\![\varphi]\!], \{\{D \partial_n v\}\})_{\partial \mathcal{D}_k^i} + (\{\{D \partial_n \varphi\}\}, [\![v]\!])_{\partial \mathcal{D}_k^i} \\ &+ (\kappa_e \varphi, v)_{\partial \mathcal{D}_k^b} - \frac{1}{2} (\varphi, D \partial_n v)_{\partial \mathcal{D}_k^b} - \frac{1}{2} (D \partial_n \varphi, v)_{\partial \mathcal{D}_k^b}, \end{aligned} \quad (79a)$$

and the linear form is

$$l_{\text{MIP}}(v) = (Q_0, v)_{\mathcal{D}_k} \quad (79b)$$

where

$$[\![\varphi]\!] = \varphi^+ - \varphi^-, \quad (80)$$

$$\{\{\varphi\}\} = (\varphi^+ + \varphi^-)/2, \text{ and} \quad (81)$$

$$Q_0 = \sigma_s (\phi^{(l+1/2)} - \phi^{(l)}). \quad (82)$$

The discretization of the diffusion term in the DSA equation requires an integration by parts. The resultant surface term is then divided into mesh interior surfaces denoted by $\partial \mathcal{D}_k^i$ and domain boundary surfaces, $\partial \mathcal{D}_k^b$. The second and third lines of Equation 79a are the mesh interior and problem domain surface terms, respectively. These are weakly enforced homogeneous Dirichlet conditions, as denoted by $b_{\text{MIP,D}}$.

The penalty terms in the bilinear form (Equation 79a) is

$$\kappa_e = \max \left(\kappa_e^{IP}, \frac{1}{4} \right), \quad (83)$$

where the IP stabilization parameter is

$$\kappa_e^{IP} = \begin{cases} \frac{f(p^+)}{2} \frac{D^+}{h_\perp^+} + \frac{f(p^-)}{2} \frac{D^-}{h_\perp^-}, & \text{on interior surfaces, i.e., } \partial\mathcal{D}_k^i \\ f(p) \frac{D}{h_\perp}, & \text{on boundary surfaces, i.e., } \partial\mathcal{D}_k^b \end{cases}, \quad (84)$$

and where

$$f(p) = Cp(p+1). \quad (85)$$

The value h_\perp^\pm is the perpendicular cell size on either side of the cell surface, p is the finite element order, C is a user defined constant that is investigated in this research. The IP method is not stable for optically thick mesh zones so it was combined with the diffusion conforming form (DCF), a spatially discretized diffusion equation derived from the spatially discretized S_N equations that is not stable for intermediate or low optical thicknesses. The MIP equations employ Equation 83 that performs as a “switch” between the IP method for optically thin regions and the DCF method for optically thick regions. The IP and DCF employ penalty coefficients κ_e^{IP} and $1/4$, respectively. The IP penalty coefficient is described in Equation 84. The DCF coefficient $1/4$ results from a derivation from the discretized transport equation to the discretized DSA equation. We refer the interested reader to Equation 33 of Wang and Ragusa [22]. Equations 84 and 85 determine when the switch occurs and are largely dependent upon problem constraints.

We consider the effects of several parameters to the spectral radius (Equation 39). Previous literature has reported on some of the sensitivities that impact the spectral radius of DSA schemes: mesh zone aspect ratios [60, 62], angular quadrature [60, 62], finite element order [2, 22], and scattering ratios [2, 22, 56]. Presently, we focus on

the sensitivity of the spectral radius to the finite element order and the constant C , for varying cell thicknesses.

2.6 MIP DSA with Robin Boundary Conditions

Kanschat [64] shows that Equation 79a employs Nitsche's method for "a fully conforming method of treating Dirichlet boundary values." The boundary terms $(\partial\mathcal{D}_k^b)$ in this form are homogeneous Dirichlet boundary conditions. The DSA correction for the scalar flux at the problem boundaries is fixed to zero, so the scalar flux is only updated by the transport solution. That is, the DSA correction only accelerates the interior solution. Consequently, the scalar fluxes on the problem boundary are only subjected to the transport equation solution source iterations.

Instead, a DSA update equation should incorporate Robin boundary conditions (zero incident partial current) on the boundaries,

$$\mathbf{J}_- = 0 = \frac{1}{4}\phi + \frac{1}{2}D\boldsymbol{\nabla}\phi \cdot \hat{n}, \quad (86)$$

$$-\frac{1}{2}\phi = D\boldsymbol{\nabla}\phi \cdot \hat{n}, \quad (87)$$

thereby allowing a correction of the boundary scalar fluxes. This boundary condition requires modification of Equation 79a. We begin by integrating the diffusion term by parts and separating the surface term into the mesh interior and problem domain boundaries:

$$-(\boldsymbol{\nabla} \cdot D\boldsymbol{\nabla}\varphi, v)_{\mathcal{D}_k} = (D\boldsymbol{\nabla}\varphi, \boldsymbol{\nabla}v)_{\mathcal{D}_k} - (D\boldsymbol{\nabla}\varphi \cdot \hat{n}, v)_{\partial\mathcal{D}_k^i} - (D\boldsymbol{\nabla}\varphi \cdot \hat{n}, v)_{\partial\mathcal{D}_k^b}. \quad (88)$$

We substitute the analytic vacuum boundary condition,

$$0 = \frac{1}{4}\varphi + \frac{1}{2}D\partial_n\varphi, \quad (89)$$

into the problem boundary term,

$$-(D\boldsymbol{\nabla}\varphi \cdot \hat{n}, v)_{\partial\mathcal{D}_k^b} = \frac{1}{2}(\varphi, v)_{\partial\mathcal{D}_k^b}. \quad (90)$$

The vacuum boundary condition MIP DSA equation becomes,

$$\begin{aligned} b_{\text{MIP,R}}(\varphi, v) &= (\sigma_a \varphi, v)_{\mathcal{D}_k} + (D\boldsymbol{\nabla}\varphi, \boldsymbol{\nabla}v)_{\partial\mathcal{D}_k} \\ &\quad + (\kappa_e [\![\varphi]\!], [\![v]\!])_{\partial\mathcal{D}_k^i} + ([\![\varphi]\!], \{D\partial_n v\})_{\partial\mathcal{D}_k^i} + (\{D\partial_n \varphi\}, [\![v]\!])_{\partial\mathcal{D}_k^i} \\ &\quad + \frac{1}{2}(\varphi, v)_{\partial\mathcal{D}_k^b}, \end{aligned} \quad (91)$$

and the linear form remains Equation 79b. The only difference between Equations 79a and 91 are the problem boundary terms. We then solve

$$b_{\text{MIP,R}}(\varphi, v) = l_{\text{MIP}}(v) \quad (92)$$

We consider the effects of several parameters to the spectral radius (Equation 39).

We focus on the sensitivity of the spectral radius to the finite element order and the constant C , for varying cell thicknesses.

3 Results

This section presents all of the results that were performed utilizing the methods described in Section 2. In Section 3.1, we discuss results from the implementation of the X - Y geometry spatial discretization described in Section 2.1. In Section 3.2, we show results from the implementation of the R - Z geometry angular and spatial discretizations discussed in Section 2.4. In Section 3.3, we show results from the implementation of the modified interior penalty (MIP) diffusion synthetic acceleration (DSA) discussed in Section 2.5.

3.1 X - Y Geometry

In this section, we present additional results in X - Y geometry to supplement the work done in Woods [27]. The spatial discretization in this section is discussed in Section 2.1. We solve a uniform infinite medium problem in Section 3.1.1. We perform a spatial convergence study in Section 3.1.2. In Section 3.1.3, we exercise the methodology on an optically thick and diffusive problem. Finally, we show results that investigate the integration scheme for the surface integrals in Section 3.1.4.

3.1.1 Uniform Infinite Medium

We solved a uniform infinite medium problem on a high-order mesh that has sufficient curvature to have incident and outgoing angular fluxes on some mesh surfaces for the same angular direction Ω . This solution was obtained using 4th-order finite elements and S_{12} level-symmetric angular quadrature. The homogeneous material has $\sigma_t = 1$, $\sigma_a = 0.7$, $S_0 = 0.7$, and has analytic solution $\phi = 1$. The mesh is overlaid on top of the solution in Figure 7. Despite performing numerical integrations of a discontinuous function along some of the surfaces, we still obtain the exact solution for this problem.

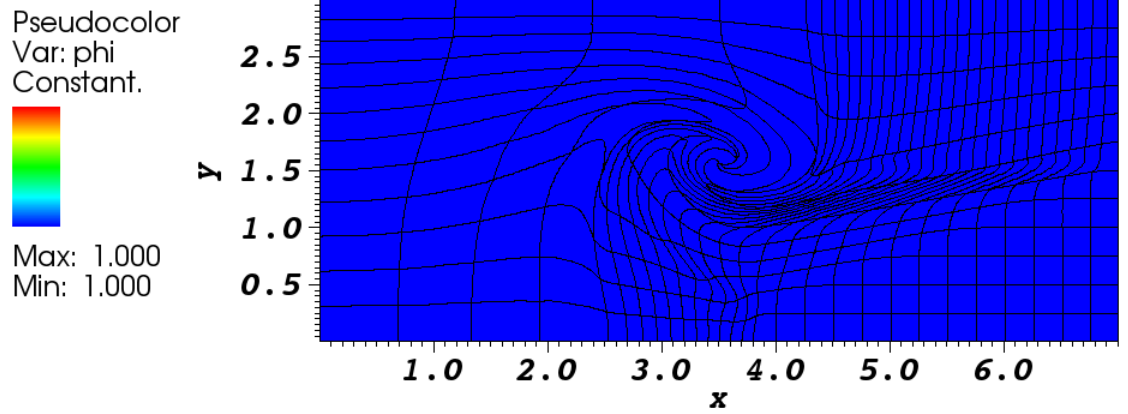


Figure 7: Uniform infinite medium scalar flux solution.

3.1.2 Spatial convergence on a highly curved mesh

We use the manufactured solution

$$\psi_{\text{MMS}}(x, y, \mu, \eta) = (1 - \mu^2)(1 - \eta^2) \sin(\alpha\pi x) \cos(\beta\pi y) \quad (93)$$

on a *highly* curved mesh with $\alpha = 1$ and $\beta = 1/2$. We obtain the analytical source S_0 that gives the exact manufactured solution by inserting Equation 93 into the X - Y transport equation:

$$\begin{aligned} & \Omega \cdot \nabla [(1 - \mu^2)(1 - \eta^2) \sin(\alpha\pi x) \cos(\beta\pi y)] \\ & + \sigma_t [(1 - \mu^2)(1 - \eta^2) \sin(\alpha\pi x) \cos(\beta\pi y)] \\ & = \frac{1}{4\pi} \sigma_s \phi_{\text{MMS}} + \frac{1}{4\pi} S_0, \end{aligned} \quad (94)$$

where

$$\phi_{\text{MMS}} = \int_{4\pi} \psi_{\text{MMS}} d\Omega, \quad (95)$$

$$= \frac{8\pi}{5} \sin(\alpha\pi x) \cos(\beta\pi y). \quad (96)$$

Given,

$$\begin{aligned} \Omega \cdot \nabla & [(1 - \mu^2)(1 - \eta^2) \sin(\alpha\pi x) \cos(\beta\pi y)] \\ & = (1 - \mu^2) (1 - \eta^2) [\mu \alpha \pi \cos(\alpha\pi x) \cos(\beta\pi y) - \eta \beta \pi \sin(\alpha\pi x) \sin(\beta\pi y)] \quad (97) \end{aligned}$$

we obtain the analytical source for the manufactured solution

$$\begin{aligned} S_0 = 4\pi & \left[(1 - \mu^2) (1 - \eta^2) (\mu \alpha \pi \cos(\alpha\pi x) \cos(\beta\pi y) \right. \\ & - \eta \beta \pi \sin(\alpha\pi x) \sin(\beta\pi y) + \sigma_t \sin(\alpha\pi x) \cos(\beta\pi y)) \\ & \left. - \frac{8\pi}{5} \sigma_s \sin(\alpha\pi x) \cos(\beta\pi y) \right]. \quad (98) \end{aligned}$$

Reproduced from Woods et al. [71], the solution using $p = 4$ and S_{12} level-symmetric angular quadrature is shown in Figure 8 with the coarsest mesh overlaid. Figure 9 shows the errors from a spatial convergence study with select reference lines.

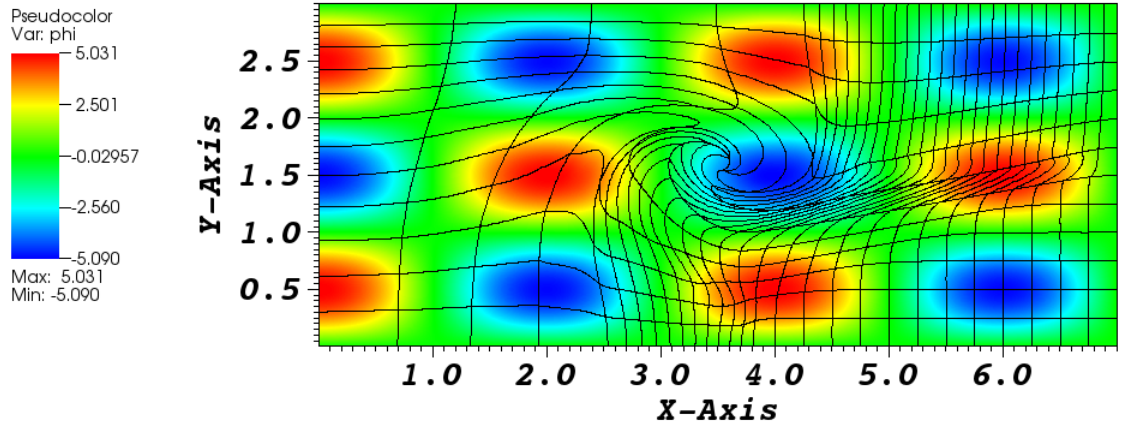


Figure 8: MMS solution on a *highly* curved mesh.

For coarser meshes, we observe degraded convergence rates as low as $O(p + 1/2)$. As the mesh is refined, the convergence rates reach $O(p + 1)$. This is possibly the effect of the finite element and mesh zone not resolving the solution enough to be in the

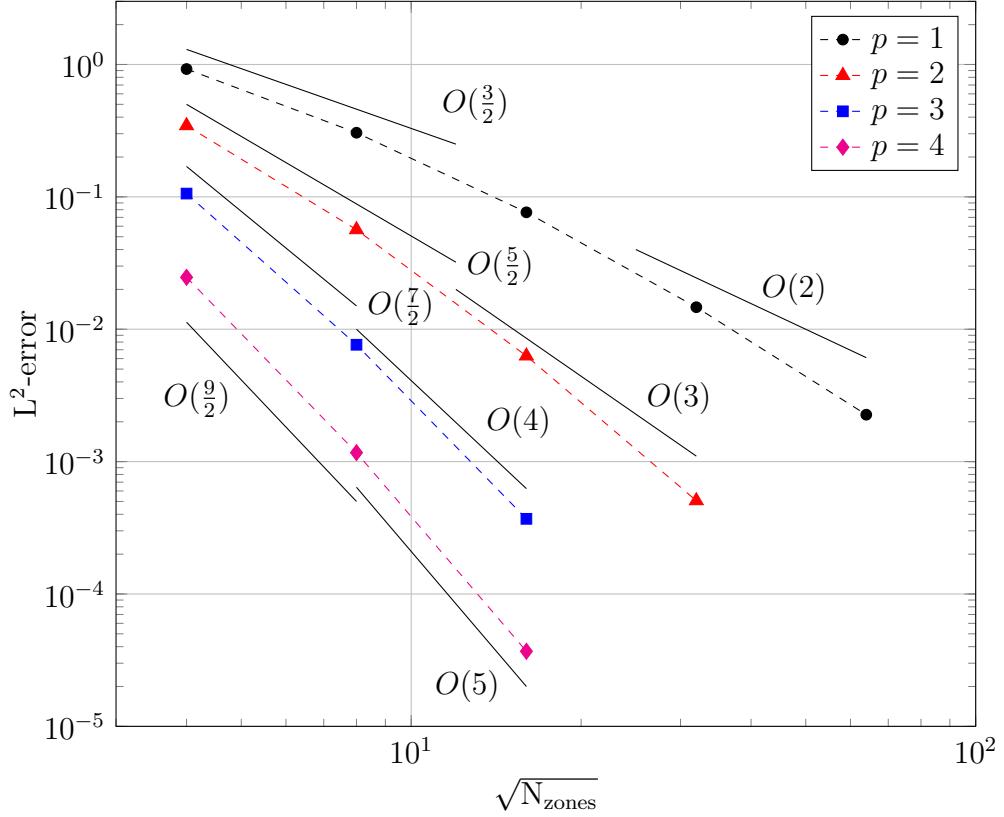


Figure 9: Errors between the manufactured and DFEM solutions. Reference lines depict order of spatial convergence $O(n) \equiv O\left((N_{\text{zones}})^{n/2}\right)$.

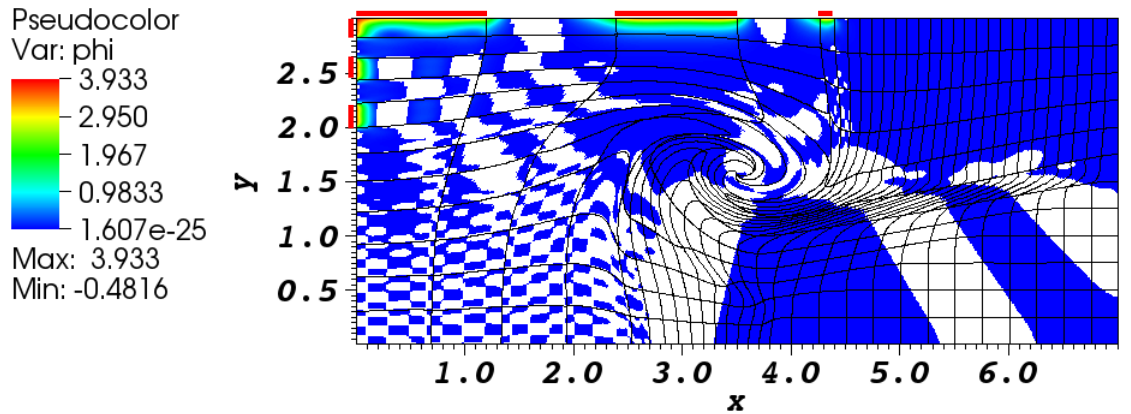
asymptotic region. Figure 9 reveals that the spatial convergence rates appear to be consistently dependent upon the finite element order.

In this work, we numerically compute all integrals with Gaussian quadrature, which does not accurately integrate functions with discontinuous derivatives. In practice, this mesh would likely be refined and the coarse mesh effects that we observe would be inconsequential.

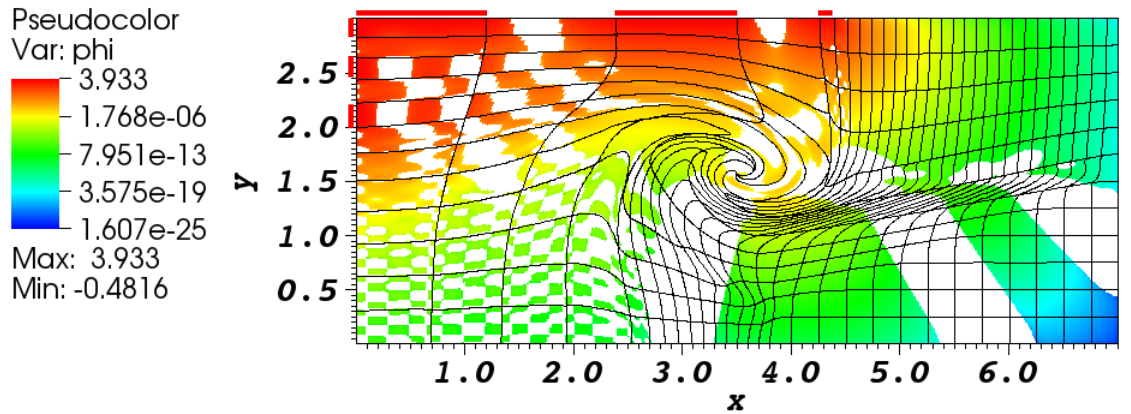
3.1.3 Alternating Incident angular flux Boundary Conditions

This numerical test problem highlights some deficiencies in the DFEM method in the optically thick diffusion limit. The material is homogeneous with no volumetric

source, $\sigma_t = 250$, and $\sigma_s = 0.999\sigma_t$. There are vacuum boundary conditions on all sides except zones with incident boundaries of strength $\psi_{\text{inc}} = 1/\pi$. We use 4th-order finite elements, S_{12} level-symmetric angular quadrature, and the mesh has 4th-order surfaces. Reproduced from Woods et al. [71], the solution is shown in Figure 10 with the incident boundaries marked with red bars.



(a) Scalar flux; red bars denote incident boundary locations.



(b) Log of the scalar flux; red bars denote incident boundary locations.

Figure 10: Scalar flux solution for Test Problem 3.

This problem reveals oscillations in the solution that dip below zero. These nega-

tive scalar fluxes have been removed and are depicted by white space. These oscillations are boundary layers generated from the discontinuous boundary conditions that propagated into the problem interior. The left-most zones are very optically thick and exhibit oscillations from the boundary layer being propagated into that space. The most refined mesh zones are in the upper right are substantially thinner and are far enough away from the discontinuous boundary conditions to not exhibit oscillations. The central highly curved zones are optically thick and exhibit oscillations within those zones. From this region, we observe large regions of negative solutions that get propagated radially outward.

Palmer and Adams [49] and Palmer [52] solved a similar discontinuous boundary problem and observed these oscillations in the boundary layers. They also demonstrated that these oscillations can be damped or eliminated by lumping the various matrices to make the solution more local. Lumping may prove to be increasingly important to prevent the propagation of these oscillations into the highly curved central region. Other methods are currently being investigated to eliminate negative solutions [72]. In practice this mesh would likely be refined and reduce the large negative bands that emanate from the central region.

3.1.4 Sensitivities on a highly curved mesh

In this section, we first investigate changing the integration order \mathcal{Q} of the surface integrals. This problem utilizes the MMS with the same manufactured solution in Equation 93 with $\alpha = 1$ and $\beta = 1/2$. The material is defined by $\sigma_t = 3$, $\sigma_s = 0.9\sigma_t$, and $\sigma_a = \sigma_t - \sigma_s$. We solve for each of $p = \{1, 2, 3, 4\}$ on the mesh shown in Figure 11, where it is easy to identify surfaces that will have both outgoing ($\boldsymbol{\Omega}_m \cdot \hat{n}(\mathbf{x}) > 0$) and incoming ($\boldsymbol{\Omega}_m \cdot \hat{n}(\mathbf{x}) < 0$) angular fluxes. We solve using S_{12} level-symmetric angular quadrature. Reproduced from Woods et al. [71], Figure 12 shows the relative errors

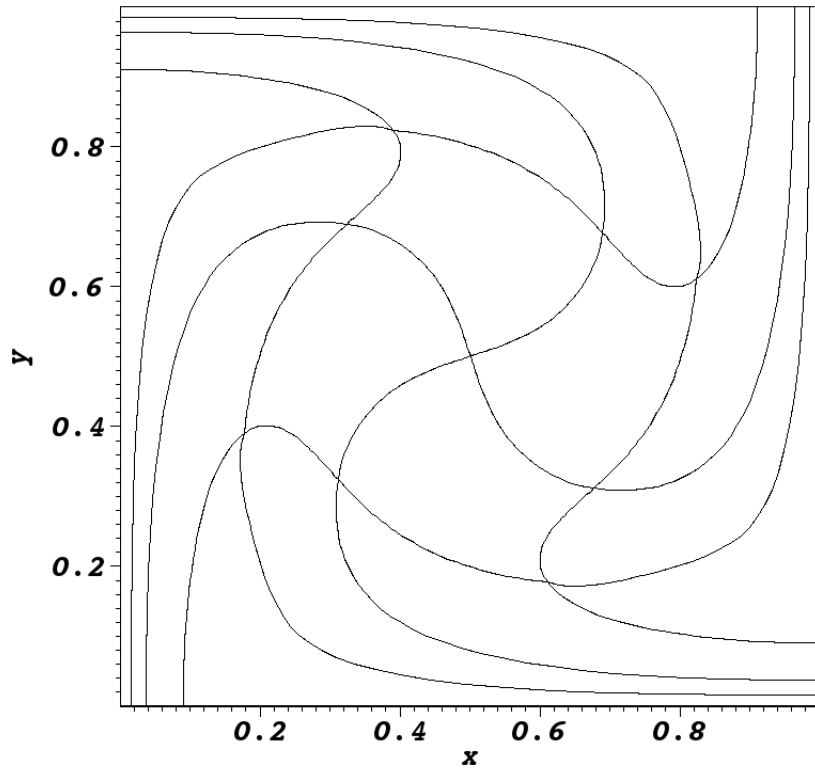


Figure 11: 4th-order mesh with surfaces that are both incident and outgoing.

for various finite element orders given the quadrature rule for the surface terms. The

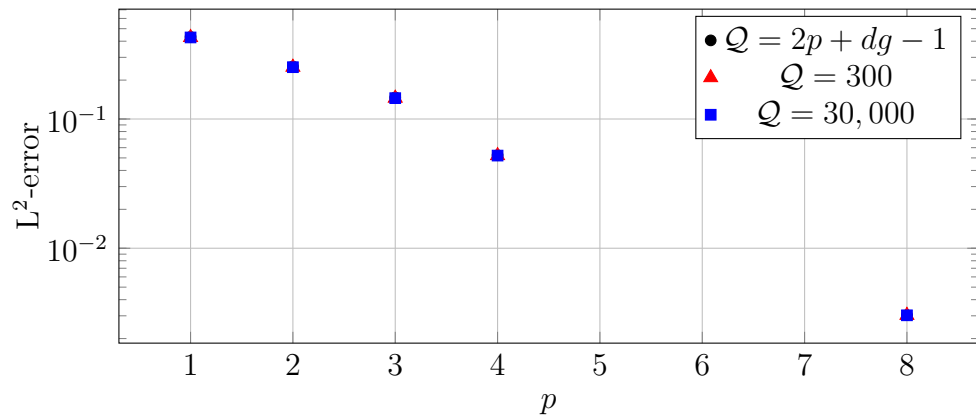


Figure 12: Error for various surface numerical integration order schemes, where p is the finite element order, g is the mesh order, and $d = 2$ is the spatial dimension of the problem.

value $\mathcal{Q} = 2p + dg - 1$ is the default scheme for both the volumetric and the surface integrals, where p is the finite element order, g is the mesh order, and d is the spatial dimension of the problem ($d = 2$ in this research). Since the errors were all calculated on the same mesh, the quadrature rule is only dependent upon the finite element order p . In Figure 12, we observe that for each finite element order, the integration order only varies the errors of the solutions by a slight amount. The spatial error is the dominating error in these calculations. Therefore, we have used the default integration order for the majority of this work.

We continue this section by investigating changing the S_N order using the same problem just described. Figure 13 shows the relative errors for various finite element orders given the S_N order. We use the default integration scheme $\mathcal{Q} = 2p + dg - 1$

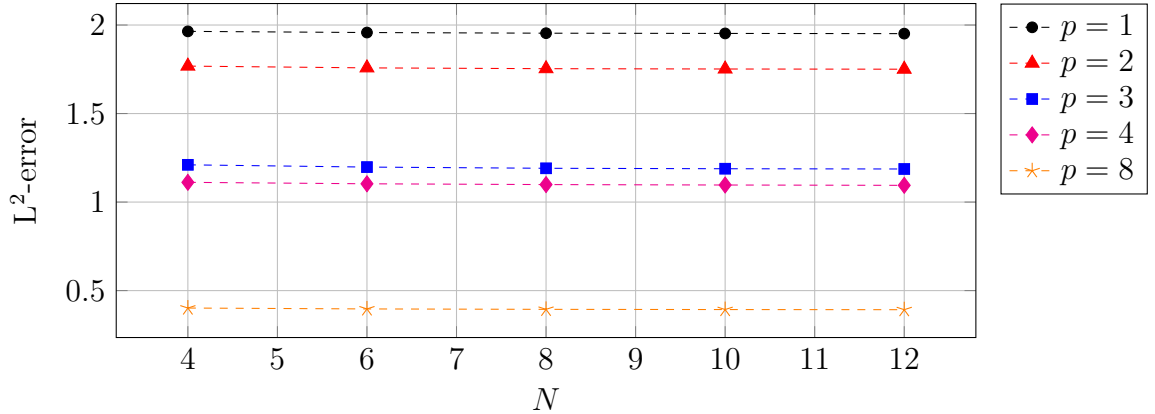


Figure 13: Error for various S_N orders.

for the volume and surfaces. We observe that there are negligible changes in error by increasing the angular quadrature order.

3.2 R-Z Geometry

In this section, we perform studies of the methodology presented above. Section 3.2.1 considers a uniform infinite medium problem. In Section 3.2.2, we use a manufactured solution with an angular dependence. In Section 3.2.3, we consider a spatial convergence study to demonstrate $O(p + 1)$ spatial convergence rates on a smooth solution. In Section 3.2.4, we demonstrate the preservation of 1-D spherical symmetry using *R-Z* geometry. In Section 3.2.5, we stress the methodology with an optically thick and diffusive problem. Finally, in Section 3.2.6, we stress the methodology with a strongly heterogeneous problem.

3.2.1 Uniform Infinite Medium

We first solved a uniform infinite medium problem in *R-Z* geometry with $\sigma_t = 1.0$, $\sigma_s = 0.3$, and $S_0 = 0.7$ for 1st-order FEM on a 2nd-order mesh using S_4 level-symmetric angular quadrature. The solution, shown in Figure 14, demonstrates we get the exact flat solution of $\phi = \S_0/\sigma_a = 1.0$. This solution shows that we have particle conservation. We determined it was necessary to integrate the linear form numerical integrations to the same order as the bilinear form integrals in order to preserve particle conservation.

3.2.2 Angular Dependence Study

In this section, we use the method of manufactured solutions (MMS) to perform a spatial convergence study in *R-Z* geometry. We obtain spatial convergence rates that describe the reduction of the error as a function of spatial mesh refinement. We consider two manufactured solutions. First, a smooth manufactured solution just as a function of space. Then, a smooth manufactured solution as a function of space

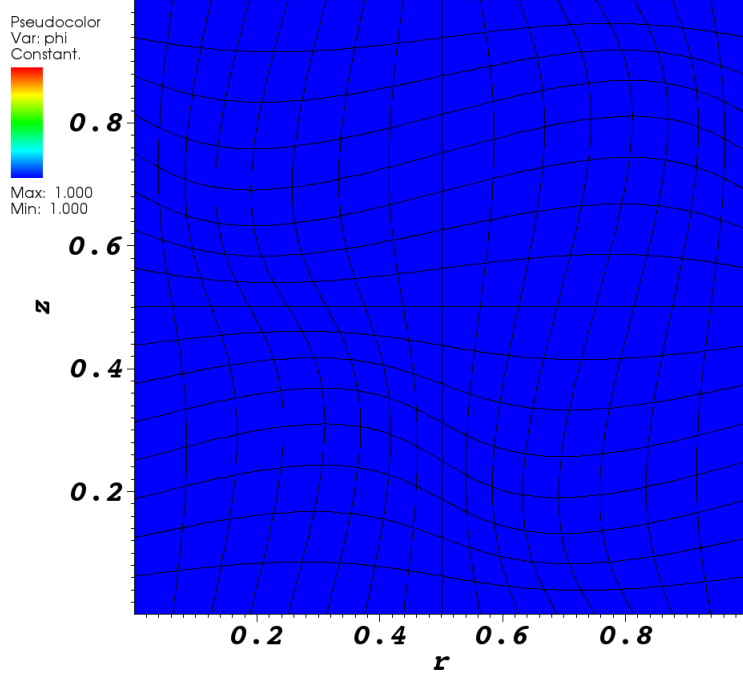


Figure 14: Uniform infinite medium solution.

and angle.

First, we defined a smooth manufactured solution as a function of space,

$$\psi_{\text{MMS}} = \sin\left(\frac{\pi}{2}r\right) \cos(\pi z). \quad (99)$$

We obtain the analytical source S_0 that gives the exact manufactured solution by inserting Equation 99 into the R - Z transport equation:

$$\begin{aligned} & \mu \frac{\partial}{\partial r} \left[\sin\left(\frac{\pi}{2}r\right) \cos(\pi z) \right] + \frac{\mu}{r} \left[\sin\left(\frac{\pi}{2}r\right) \cos(\pi z) \right] + \xi \frac{\partial}{\partial z} \left[\sin\left(\frac{\pi}{2}r\right) \cos(\pi z) \right] \\ & - \frac{\mu}{r} \left[\sin\left(\frac{\pi}{2}r\right) \cos(\pi z) \right] - \frac{\eta}{r} \frac{\partial}{\partial \omega} \left[\sin\left(\frac{\pi}{2}r\right) \cos(\pi z) \right] + \sigma_t \left[\sin\left(\frac{\pi}{2}r\right) \cos(\pi z) \right] \\ & = \sigma_s \sin\left(\frac{\pi}{2}r\right) \cos(\pi z) + \frac{1}{2\pi} S_0, \end{aligned} \quad (100)$$

where

$$\phi_{\text{MMS}} = \int_{2\pi} \psi_{\text{MMS}} d\Omega \quad (101)$$

$$= 2\pi \sin\left(\frac{\pi}{2}r\right) \cos(\pi z). \quad (102)$$

Given,

$$\frac{\partial}{\partial r} \left[\sin\left(\frac{\pi}{2}r\right) \cos(\pi z) \right] = \frac{\pi}{2} \cos\left(\frac{\pi}{2}r\right) \cos(\pi z), \quad (103)$$

$$\frac{\partial}{\partial z} \left[\sin\left(\frac{\pi}{2}r\right) \cos(\pi z) \right] = -\pi \sin\left(\frac{\pi}{2}r\right) \sin(\pi z), \quad (104)$$

and

$$\frac{\partial \psi_{\text{MMS}}}{\partial \omega} = 0, \quad (105)$$

we obtain the analytical source for the manufactured solution

$$S_0 = 2\pi \left[\frac{\mu\pi}{2} \cos\left(\frac{\pi}{2}r\right) \cos(\pi z) - \xi\pi \sin\left(\frac{\pi}{2}r\right) \sin(\pi z) + \sigma_t \sin\left(\frac{\pi}{2}r\right) \cos(\pi z) - \sigma_s \sin\left(\frac{\pi}{2}r\right) \cos(\pi z) \right]. \quad (106)$$

Shown in Figure 15, the L^2 -error between the DFEM scalar flux and the angular integrated manufactured solution was 4.59×10^{-5} .

Next, we added an angular dependence to the manufactured solution,

$$\psi_{\text{MMS}} = (1 - \mu^2)(1 - \xi^2) \sin\left(\frac{\pi}{2}r\right) \cos(\pi z). \quad (107)$$

We obtain the analytical source S_0 that gives the exact manufactured solution by

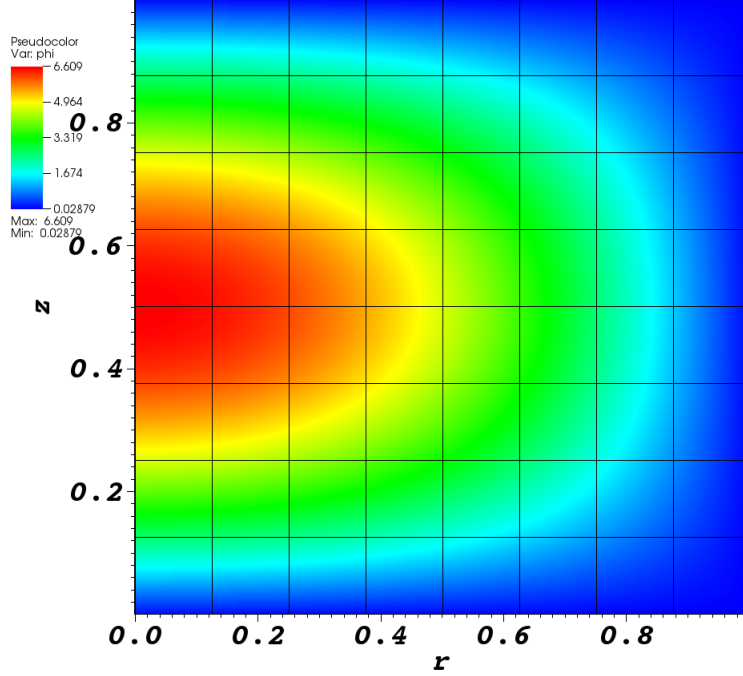


Figure 15: MMS solution for Equation 99.

inserting Equation 99 into the R - Z transport equation:

$$\begin{aligned}
 & \mu \frac{\partial}{\partial r} \left[(1 - \mu^2)(1 - \xi^2) \sin \left(\frac{\pi}{2} r \right) \cos(\pi z) \right] + \frac{\mu}{r} \left[(1 - \mu^2)(1 - \xi^2) \sin \left(\frac{\pi}{2} r \right) \cos(\pi z) \right] \\
 & + \xi \frac{\partial}{\partial z} \left[(1 - \mu^2)(1 - \xi^2) \sin \left(\frac{\pi}{2} r \right) \cos(\pi z) \right] - \frac{\mu}{r} \left[(1 - \mu^2)(1 - \xi^2) \sin \left(\frac{\pi}{2} r \right) \cos(\pi z) \right] \\
 & - \frac{\eta}{r} \frac{\partial}{\partial \omega} \left[(1 - \mu^2)(1 - \xi^2) \sin \left(\frac{\pi}{2} r \right) \cos(\pi z) \right] + \sigma_t \left[(1 - \mu^2)(1 - \xi^2) \sin \left(\frac{\pi}{2} r \right) \cos(\pi z) \right] \\
 & = \frac{4\pi}{5} \sigma_s \sin \left(\frac{\pi}{2} r \right) \cos(\pi z) + \frac{1}{2\pi} S_0, \quad (108)
 \end{aligned}$$

where

$$\phi_{\text{MMS}} = \int_{2\pi} \psi_{\text{MMS}} d\Omega \quad (109)$$

$$= \frac{4\pi}{5} \sin \left(\frac{\pi}{2} r \right) \cos(\pi z). \quad (110)$$

Given,

$$\begin{aligned} \frac{\partial}{\partial r} \left[(1 - \mu^2)(1 - \xi^2) \sin \left(\frac{\pi}{2} r \right) \cos(\pi z) \right] \\ = \frac{\pi}{2} (1 - \mu^2)(1 - \xi^2) \cos \left(\frac{\pi}{2} r \right) \cos(\pi z), \quad (111) \end{aligned}$$

$$\begin{aligned} \frac{\partial}{\partial z} \left[(1 - \mu^2)(1 - \xi^2) \sin \left(\frac{\pi}{2} r \right) \cos(\pi z) \right] \\ = -\pi (1 - \mu^2)(1 - \xi^2) \sin \left(\frac{\pi}{2} r \right) \sin(\pi z), \text{ and} \quad (112) \end{aligned}$$

$$\begin{aligned} \frac{\partial}{\partial \omega} \left[(1 - \mu^2)(1 - \xi^2) \sin \left(\frac{\pi}{2} r \right) \cos(\pi z) \right] \\ = \frac{\partial}{\partial \omega} \left[1 - (1 - \xi^2) \cos^2(\omega) \right] (1 - \xi^2) \sin \left(\frac{\pi}{2} r \right) \cos(\pi z), \quad (113) \end{aligned}$$

$$= [2 (1 - \xi^2) \mu \eta] (1 - \xi^2) \sin \left(\frac{\pi}{2} r \right) \cos(\pi z), \quad (114)$$

we obtain the analytical source for the manufactured solution

$$\begin{aligned} S_0 = 2\pi \left[\frac{\mu\pi}{2} (1 - \mu^2)(1 - \xi^2) \cos \left(\frac{\pi}{2} r \right) \cos(\pi z) \right. \\ - \pi \xi (1 - \mu^2)(1 - \xi^2) \sin \left(\frac{\pi}{2} r \right) \sin(\pi z) \\ + [2 (1 - \xi^2) \mu \eta] (1 - \xi^2) \sin \left(\frac{\pi}{2} r \right) \cos(\pi z) \\ \left. + \sigma_t (1 - \mu^2)(1 - \xi^2) \sin \left(\frac{\pi}{2} r \right) \cos(\pi z) - \frac{4\pi}{5} \sigma_s \sin \left(\frac{\pi}{2} r \right) \cos(\pi z) \right]. \quad (115) \end{aligned}$$

We solve this with 2nd-order FEM, orthogonal quadrilateral mesh, $\sigma_t = 1.0$, $\sigma_s = 0.3$, $S_0 = 0.7$, S_4 level-symmetric angular quadrature. The solution is shown in Figure 16 and the L²-error between the DFEM scalar flux and the angular integrated manufactured solution was 0.132. Since there was an increase in the error, it is clear that there is a dependence of the spatial error upon the angular discretization.

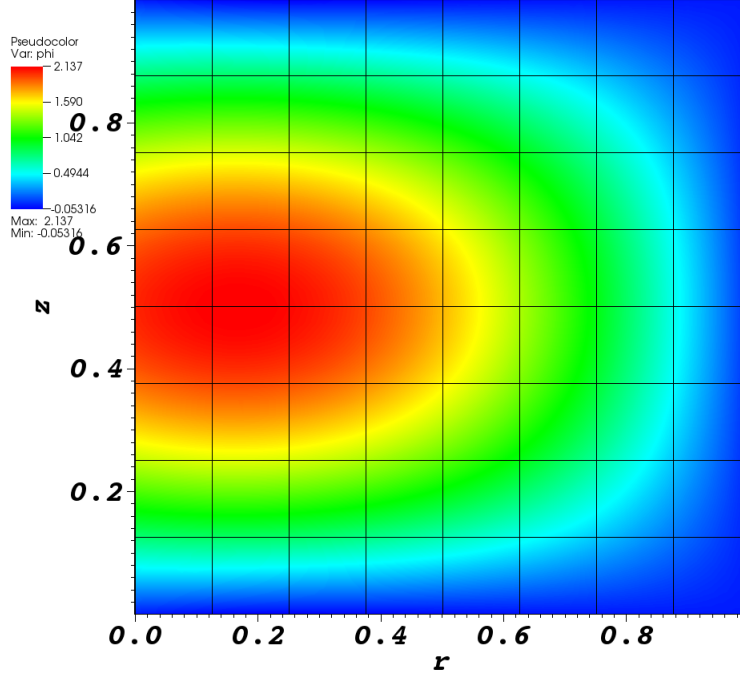


Figure 16: MMS solution for Equation 107.

3.2.3 Spatial Convergence Studies

We perform two spatial convergence studies here, both in R - Z geometry. First, we use a smooth manufactured solution to demonstrate optimal convergence rates to compare with the literature in Section 3.2.3.1. Then, in Section 3.2.3.2, we solve a MMS problem that is only a function of space but contains discontinuities in the first-derivative to demonstrate a regularity constrained convergence rate.

3.2.3.1 Smooth Manufactured Solution

Bailey et al. [21] performed this first spatial convergence study and showed 2nd-order convergence using piece-wise linear DFEM (PWLD) and bilinear DFEM (BLD) using

the manufactured solution

$$\psi_{\text{MMS}}(r, z) = (\sin(\pi r) + 1 - r) \sin(\pi z). \quad (116)$$

We obtain the analytical source S_0 that gives the exact manufactured solution by inserting Equation 116 into the R - Z transport equation

$$\begin{aligned} & \mu \frac{\partial}{\partial r} [(\sin(\pi r) + 1 - r) \sin(\pi z)] + \frac{\mu}{r} [(\sin(\pi r) + 1 - r) \sin(\pi z)] \\ & + \xi \frac{\partial}{\partial z} [(\sin(\pi r) + 1 - r) \sin(\pi z)] - \frac{\mu}{r} [(\sin(\pi r) + 1 - r) \sin(\pi z)] \\ & - \frac{\eta}{r} \frac{\partial}{\partial \omega} [(\sin(\pi r) + 1 - r) \sin(\pi z)] + \sigma_t [(\sin(\pi r) + 1 - r) \sin(\pi z)] \\ & = \sigma_s (\sin(\pi r) + 1 - r) \sin(\pi z) + \frac{1}{2\pi} S_0, \end{aligned} \quad (117)$$

where

$$\phi_{\text{MMS}} = \int_{2\pi} \psi_{\text{MMS}} d\Omega \quad (118)$$

$$= 2\pi (\sin(\pi r) + 1 - r) \sin(\pi z). \quad (119)$$

Given,

$$\frac{\partial}{\partial r} [(\sin(\pi r) + 1 - r) \sin(\pi z)] = \pi \cos(\pi r) \sin(\pi z), \quad (120)$$

$$\frac{\partial}{\partial z} [(\sin(\pi r) + 1 - r) \sin(\pi z)] = \pi (\sin(\pi r) + 1 - r) \cos(\pi z), \quad (121)$$

and

$$\frac{\partial \psi_{\text{MMS}}}{\partial \omega} = 0, \quad (122)$$

we obtain the analytical source for the manufactured solution

$$\begin{aligned} S_0 = 2\pi & [\mu \pi \cos(\pi r) \sin(\pi z) + \xi \pi (\sin(\pi r) + 1 - r) \cos(\pi z) \\ & + (\sigma_t - \sigma_s) (\sin(\pi r) + 1 - r) \sin(\pi z)]. \end{aligned} \quad (123)$$

We solve this using $\sigma_t = 3 \text{ cm}^{-1}$ and $\sigma_s = 0.9999\sigma_t$. We solved this same prob-

lem using $p = \{1, 2, 4, 6, 8\}$ on an orthogonal and 2nd-order curved mesh using S_8 level-symmetric angular quadrature. We set the incident angular flux to ψ_{MMS} of Equation 116. Figure 17 shows the $p = 2$ solution on a 2nd-order mesh.

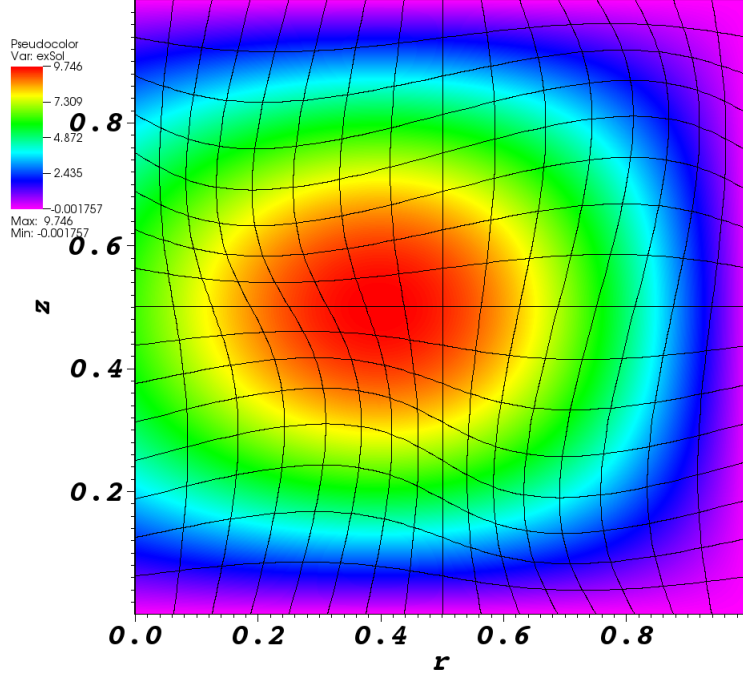


Figure 17: MMS solution to Equation 116.

The spatial convergence study performed by Bailey et al. [21] demonstrated 2nd-order converge for their 1st-order methods. Figures 18a and 18b demonstrate $O(p+1)$ convergence on an orthogonal mesh and 2nd-order mesh, respectively. Reference lines calculated by a least squares fit are also provided for comparison. These results have been reproduced from Woods and Palmer [39].

Increasing the number of unknowns reduces the error in all cases. For a given finite element order, refining the mesh reduces the error. For a given mesh refinement, the

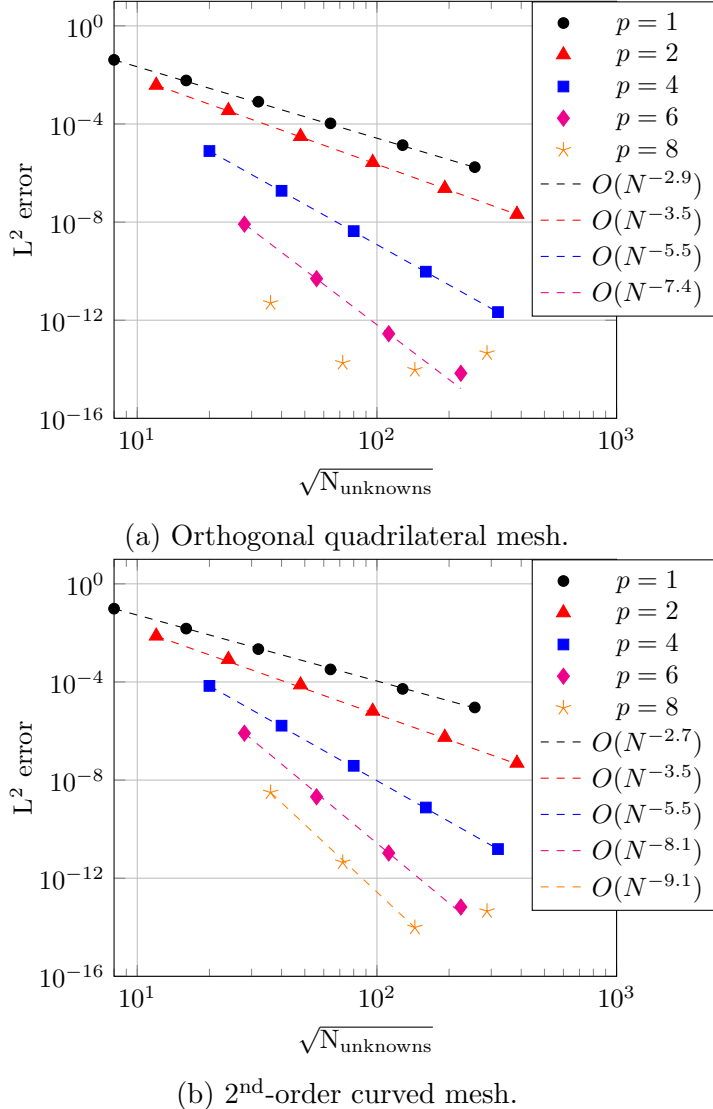


Figure 18: L^2 -norm of the errors from the manufactured solution and reference lines computed from a least squares fit, where $N_{\text{unknowns}} = N_{\text{cells}}(p + 1)^2$.

error is smaller for higher-order finite elements. In general, the error values on the curved mesh are larger than corresponding error values on the orthogonal mesh.

3.2.3.2 Reduced Regularity Manufactured Solution

We subsequently looked at the manufactured solution

$$\psi_{\text{MMS}} = \begin{cases} 1.0 + 4.0r, & 0 \leq r < 0.33 \\ 3.31 - 3.0r, & 0.33 \leq r < 0.66, \\ 2.32 - 1.5r, & r \leq 1.0 \end{cases} \quad (124)$$

that is continuous in $\psi(r, z)$, but discontinuous in $\partial_r \psi$. The solution, shown in Figure 19, was solved using 1st- and 2nd-order finite elements (i.e., $p = 1$ and $p = 2$, respectively), S_{12} level-symmetric angular quadrature, on a 2nd-order mesh. We re-

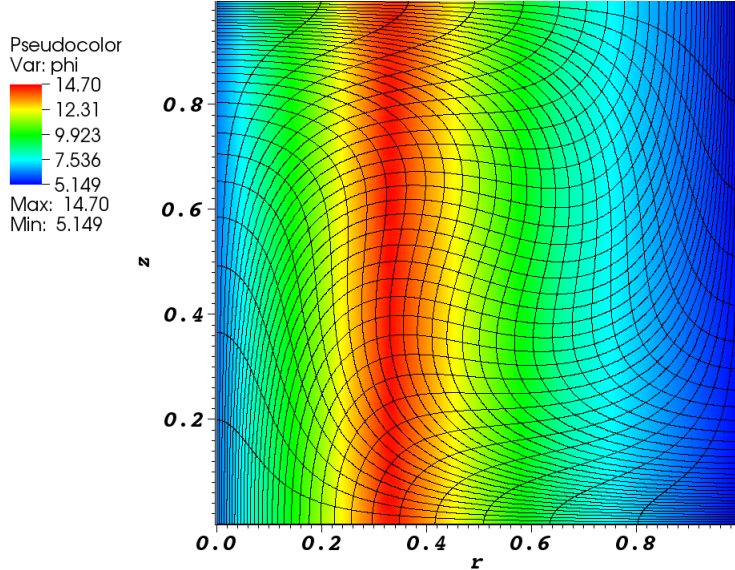


Figure 19: DGFEM scalar flux solution to Equation 124.

fined the mesh sequentially and plotted the errors as a function of the square root of the number of unknowns in the spatial domain in Figure 20. We observe there is a degradation in the spatial convergence rate compared to the smooth (infinitely differentiable) manufactured solution. The analysis by Asadzadeh [73] predicts the

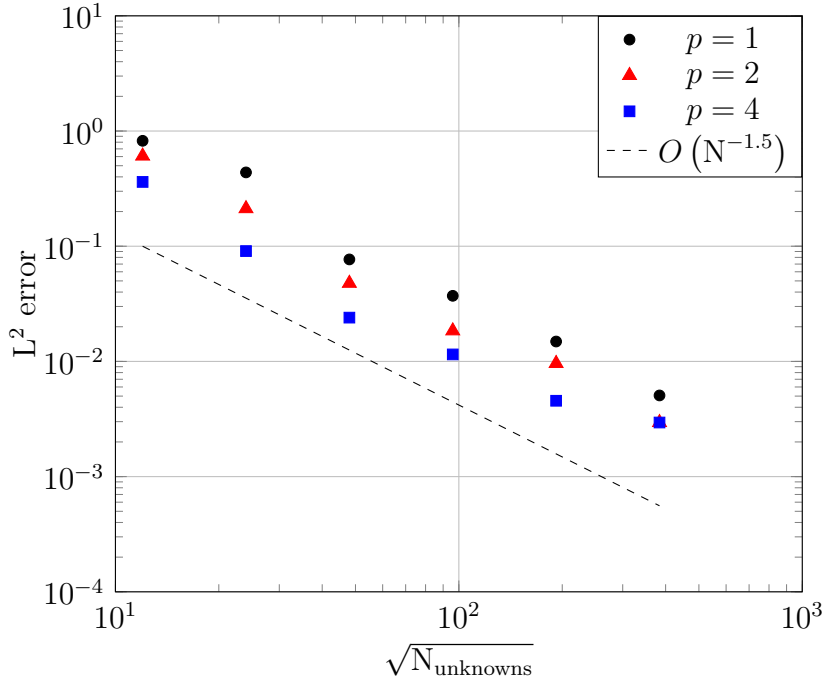


Figure 20: L^2 -norm of the errors from the manufactured solution and reference line, where $N_{\text{unknowns}} = N_{\text{cells}}(p + 1)^2$.

spatial convergence rate to be as low as $O(1/2)$ or $O(3/2)$ for solutions that have less regularity (i.e., fewer continuous derivatives). We observe the $O(3/2)$ spatial convergence rate for this problem with discontinuous derivatives.

We solved this problem again on an orthogonal mesh with the discontinuities aligned with the mesh surfaces. This restores the spatial convergence rates to the $O(p + 1)$ as with a smooth solution. This trivial result is not shown.

3.2.4 Spherical Symmetry Preservation

Numerically solving the radiation transport equation in R - Z geometry for a spherically shaped problem using spherical geometry is a very reasonable idea. However, it is also necessary to solve a spherical problem using cylindrical geometry. One particular application of the transport equation is coupling it to the hydrodynamics equations to solve radiation-hydrodynamics problems. Numerical modeling hydrody-

namics problems in cylindrical geometry is common [35] so we too must demonstrate the ability to model spherical problems using cylindrical geometry. We want *R-Z* geometry to solve and preserve 1-dimensional spherical solutions. We use MMS to solve a 1-D spherical problem using the *R-Z* geometry spatial discretization.

We evaluate the relative asymmetry by calculating the averages of all nodes at each $\rho = \sqrt{r^2 + z^2}$ value and

$$\phi_{\text{asym}}(\rho, \theta) = \frac{\phi_{\text{code}}(\rho, \theta) - \phi_{\text{avg}}(\rho)}{\phi_{\text{avg}}(\rho)}, \quad (125)$$

where

$$\phi_{\text{avg}}(\rho) = \frac{1}{N_{\text{nodes}}(\rho)} \sum_{i=1}^{N_{\text{nodes}}(\rho)} \phi(\rho, \theta_i) \quad (126)$$

is the average scalar flux at all nodes at the same spherical radius ρ .

The three traditional coordinate systems are Cartesian, cylindrical, and spherical. It is straight forward to describe a spatial position using any one of them. However, challenges arise when spatially discretizing. Specifically, angular derivatives arise inside the streaming term in cylindrical and spherical geometries. Cylindrical geometry may be used in lieu of spherical coordinates to describe a spherical problem and is performed this way in some hydrodynamics calculations [35]. In this section, we demonstrate the use of *R-Z* geometry to preserve a 1-D spherical solution.

Previously, two papers demonstrated spherical modeling of the radiation field using *R-Z* geometry. Brunner et al. [40] performed this analysis for the diffusion equation with an incident boundary condition on the outside of the moderately scattering homogeneous sphere with zero source. Their results were mixed whether each discretization method preserved accuracy of their analytical solution and preserved the axisymmetry. Chanland and Sama [41] performed an analysis with the time-dependent transport equation with an initial source at the center of a void. They concluded that the S_N method produces ray-effects in the void and their unique

angular discretization qualitatively preserved axisymmetry. While there are applications for considering radiation propagation through a voided region, this current work focuses on material problems.

We use the method of manufactured solutions (MMS) with the manufactured solution

$$\psi_{\text{MMS}}(r, z) = \rho = \sqrt{r^2 + z^2}. \quad (127)$$

This solution is linear in the 1-D spherical coordinate ρ . We obtain the analytical source S_0 that gives the exact manufactured solution by inserting Equation 127 into the R - Z transport equation

$$\mu \frac{\partial \rho}{\partial r} + \frac{\mu}{r} \rho + \xi \frac{\partial \rho}{\partial z} - \frac{\mu}{r} \rho - \frac{\eta}{r} \frac{\partial \rho}{\partial \omega} + \sigma_t \rho = \sigma_s \rho + \frac{1}{2\pi} S_0, \quad (128)$$

$$\mu \frac{\partial \rho}{\partial r} + \xi \frac{\partial \rho}{\partial z} - \frac{\eta}{r} \frac{\partial \rho}{\partial \omega} + \sigma_t \rho = \sigma_s \rho + \frac{1}{2\pi} S_0 \quad (129)$$

where

$$\phi_{\text{MMS}} = \int_{2\pi} \psi_{\text{MMS}} d\Omega \quad (130)$$

$$= 2\pi\rho. \quad (131)$$

Given,

$$\frac{\partial \rho}{\partial r} = \frac{r}{\sqrt{r^2 + z^2}}, \quad (132)$$

$$\frac{\partial \rho}{\partial z} = \frac{z}{\sqrt{r^2 + z^2}}, \quad (133)$$

and

$$\frac{\partial \rho}{\partial \omega} = 0, \quad (134)$$

we obtain the analytical source for the manufactured solution

$$S_0 = 2\pi \left(\frac{\mu r}{\sqrt{r^2 + z^2}} + \frac{\xi z}{\sqrt{r^2 + z^2}} - \sigma_s \sqrt{r^2 + z^2} \right). \quad (135)$$

There are numerous discretizations that may impact the solution to this MMS problem, including: angular discretization order, finite element order, spatial mesh refinement, and mesh curvature. We perform numerical tests to investigate the impact of each of these discretizations have on preserving spherical symmetry. Additionally, we perform several cross-correlation tests for a few of these. We solve this MMS problem on a LO mesh and a HO (2^{nd} -order) mesh in Sections 3.2.4.1 and 3.2.4.2, respectively. Within these sections, we solve this MMS problem using S_N level symmetric angular quadrature with $N = \{4, 6, 8, 10, 12\}$, for finite element orders $p = \{1, 2, 4\}$, and various levels of mesh refinement. These discretization approximations (mesh and mesh order, S_N order, and finite element order) contribute to the asymmetry of the solution. We study each one individually to characterize the effects of each on the asymmetry. The problem has physical parameters $\sigma_t = 5.0$ and $\sigma_a = 2.0$. We summarize all of these results and make some concluding remarks in Section 3.2.4.3.

An example scalar flux solution is shown in Figure 21. The solution appears smooth in all spherical radial directions.

3.2.4.1 Low-Order Mesh

In this section, we observe the sensitivity of the scalar flux spherical asymmetry to changing the discrete ordinates order, finite element order, and spatial refinement on a low-order mesh. Specifically, a low-order mesh is one that has linear surfaces. The vertices of the low-order meshes used in this section are located in concentric rings of equal $\rho = \sqrt{r^2 + z^2}$. The results in this section are organized as follows: comparing the discrete ordinates order for each of $p = \{1, 2, 4, 8\}$, comparing each of $p = \{1, 2, 4, 8\}$ for S_8 level symmetric angular quadrature, and mesh refinement studies for each of $p = \{1, 4\}$.

Figure 22 shows the ϕ_{asym} values calculated using Equation 125 for 1st-order fi-

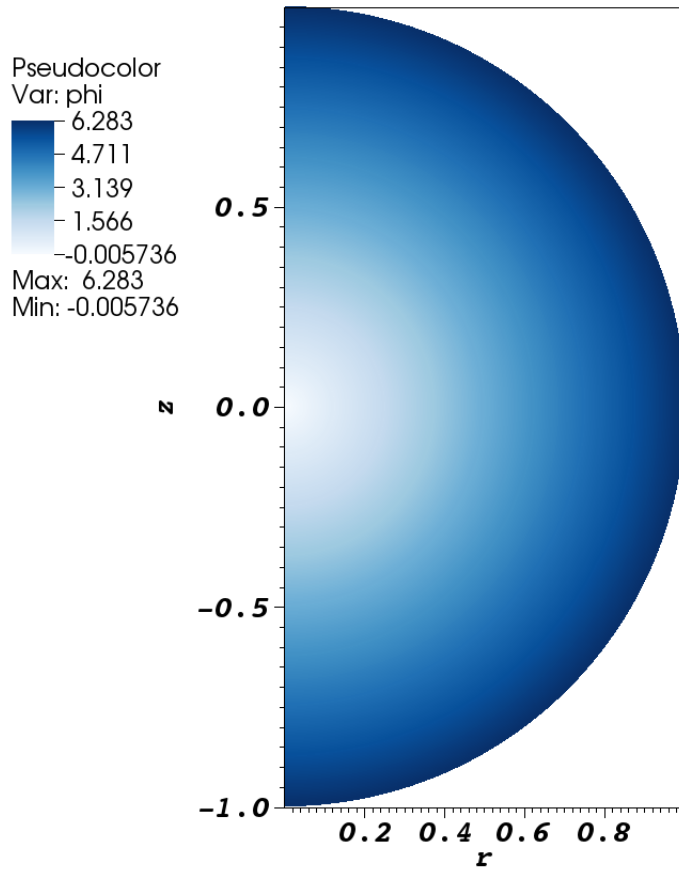


Figure 21: Example scalar flux solution using 1st-order finite elements, S_8 level-symmetric angular quadrature, 2nd-order mesh, and refined mesh with 8128 mesh zones.

nite elements on a 1st-order mesh with 120 zones for several angular quadrature discretizations. The asymmetry is plotted on a log scale. The scale colors assist in demonstrating the qualitative locations of the asymmetries. The yellow region is the least symmetric, red regions have increased symmetry, and blue regions have the most symmetry. The ϕ_{asym} solution is plotted using the same finite element shape functions as the scalar flux. There is no perceptible gain in symmetry by increasing the angular discretization order. We confirm this by plotting the asymmetry values

as a function of the spherical radius (i.e., $\rho = \sqrt{r^2 + z^2}$) in Figure 23. The spherical radial asymmetry solutions are indistinguishable between discrete ordinate orders. The location of the largest asymmetries are near the polar axis (i.e., $r = 0$). We observe groupings along the top profile of this figure. These asymmetry values occur along the z -axis where the remaining nodal solutions in the problem interior have smaller asymmetries. Moreover, Figure 24 demonstrates there is no gain in accuracy by increasing the S_N order.

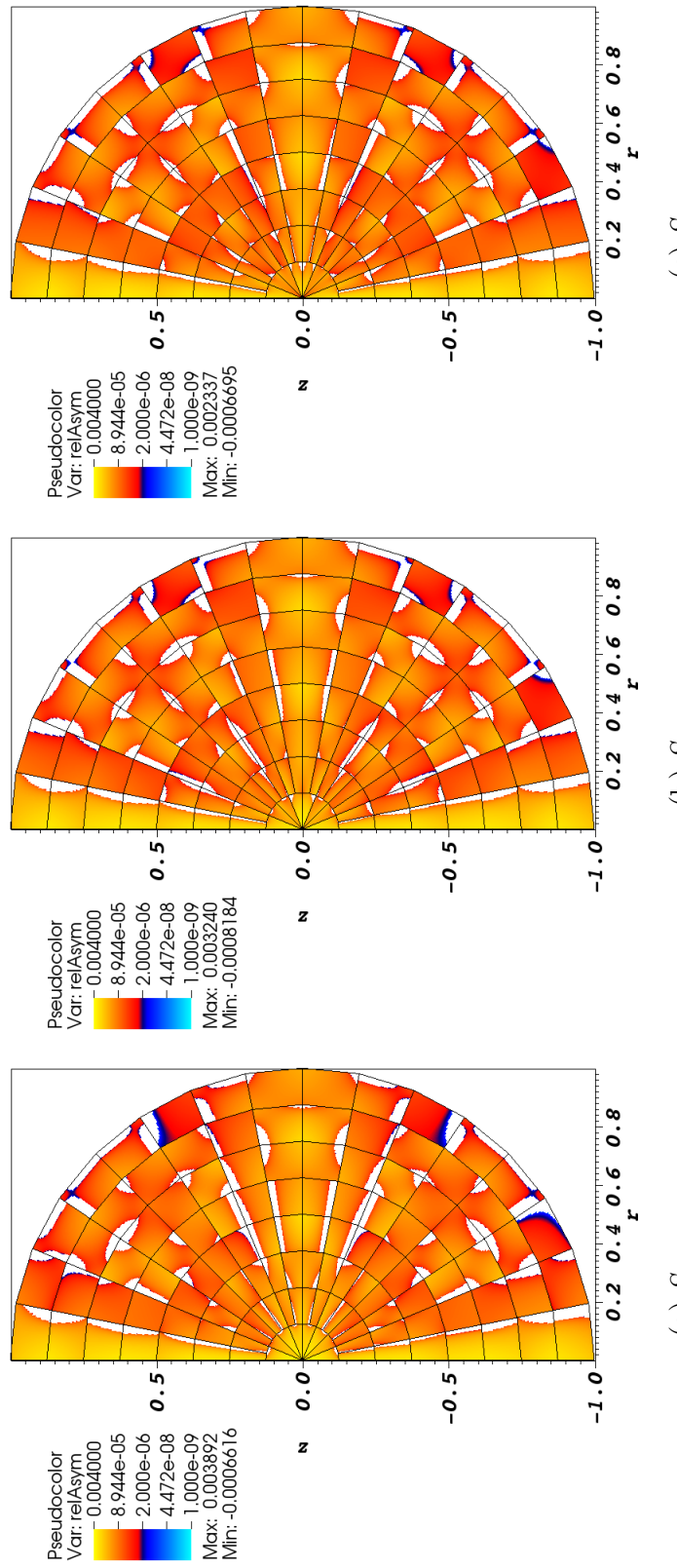


Figure 22: Relative asymmetry for 1st-order finite elements on a 1st-order mesh for given order of level-symmetric angular quadrature.

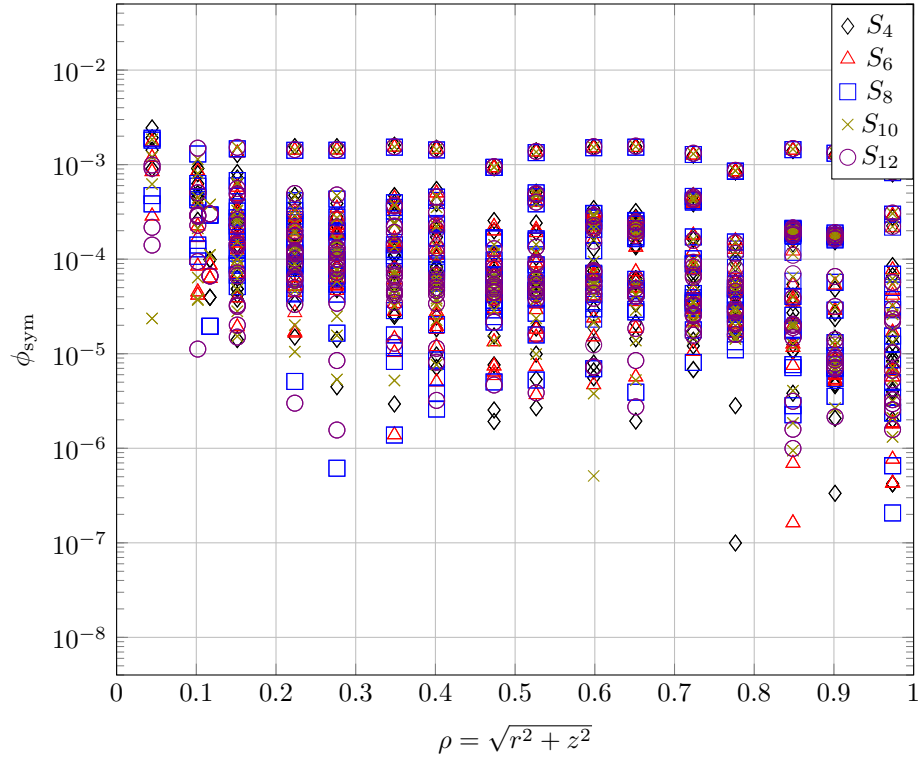


Figure 23: Measure of the asymmetry for each finite element node for the given level-symmetric angular quadrature order for 1st-order DFEM and 1st-order mesh with 120 zones (see Figure 22).

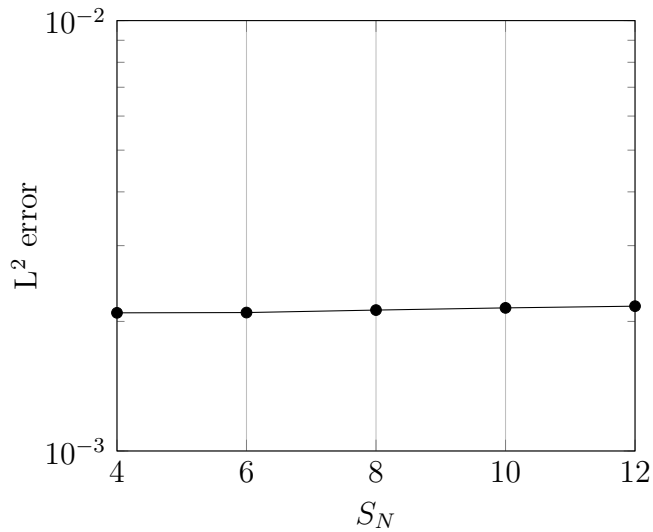


Figure 24: Accuracy of solutions for given angular quadrature using $p = 1$ on a 1st-order mesh with 120 zones.

Figure 25 shows the ϕ_{asym} values calculated using Equation 125 for 2nd-order finite elements on a 1st-order mesh with 120 zones for several angular quadrature discretizations. The asymmetry is plotted on a log scale. The scale colors assist in demonstrating the qualitative locations of the asymmetries. The yellow region is the least symmetric, red regions have increased symmetry, and blue regions have the most symmetry. The ϕ_{asym} solution is plotted using the same finite element shape functions as the scalar flux. There is a little perceptible gain in symmetry (indicated by more blue area) on the periphery by increasing the angular discretization order. However, plotting the asymmetry values as a function of the spherical radius (i.e., $\rho = \sqrt{r^2 + z^2}$) in Figure 26 shows that there may not actually be any symmetry gains — the spherical radial asymmetry solutions are indistinguishable between discrete ordinate orders. The asymmetries are predominantly located near the origin (i.e., $\rho = \sqrt{r^2 + z^2} = 0$). Moreover, Figure 27 demonstrates there is no gain in accuracy by increasing the S_N order.

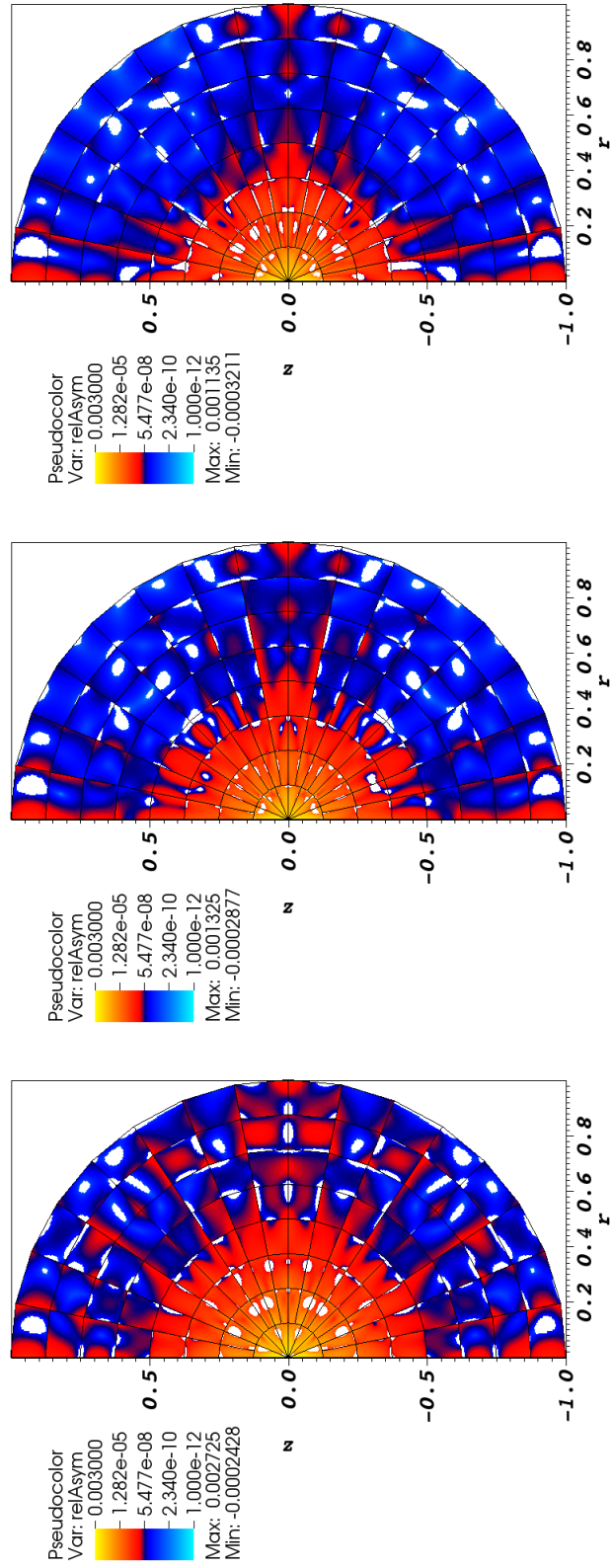


Figure 25: Relative asymmetry for 2nd-order finite elements on a 1st-order mesh for given order of level-symmetric angular quadrature.

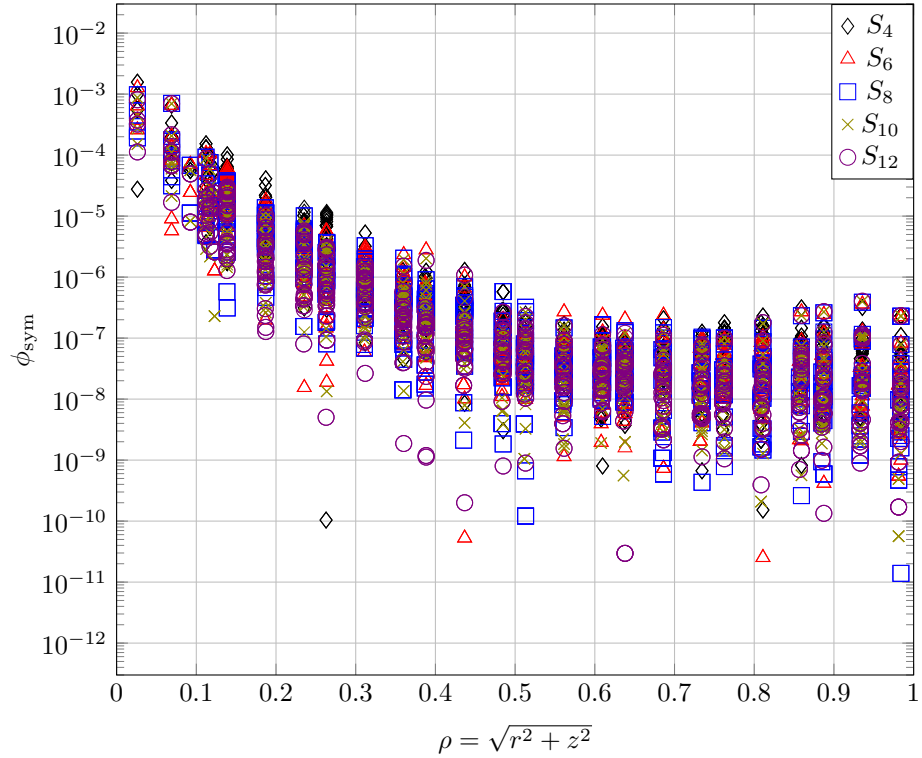


Figure 26: Measure of the asymmetry for each finite element node for the given level-symmetric angular quadrature order for 2nd-order DFEM and 1st-order mesh with 120 zones (see Figure 25).

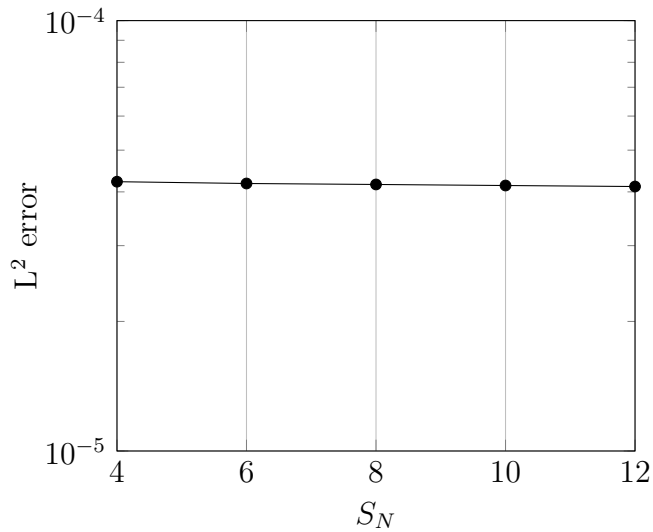


Figure 27: Accuracy of solutions for given angular quadrature using $p = 2$ on a 1st-order mesh with 120 zones.

Figure 28 shows the ϕ_{asym} values calculated using Equation 125 for 4th-order finite elements on a 1st-order mesh with 120 zones for several angular quadrature discretizations. The asymmetry is plotted on a log scale. The scale colors assist in demonstrating the qualitative locations of the asymmetries. The yellow region is the least symmetric, red regions have increased symmetry, and blue regions have the most symmetry. The ϕ_{asym} solution is plotted using the same finite element shape functions as the scalar flux. There is no perceptible gain in symmetry by increasing the angular discretization order. This is confirmed by plotting the asymmetry values as a function of the spherical radius (i.e., $\rho = \sqrt{r^2 + z^2}$) in Figure 29. Unlike Figure 25, the asymmetry of the scalar flux appears to be a function of the spherical radius, ρ . Moreover, Figure 30 demonstrates there is no gain in accuracy by increasing the S_N order.

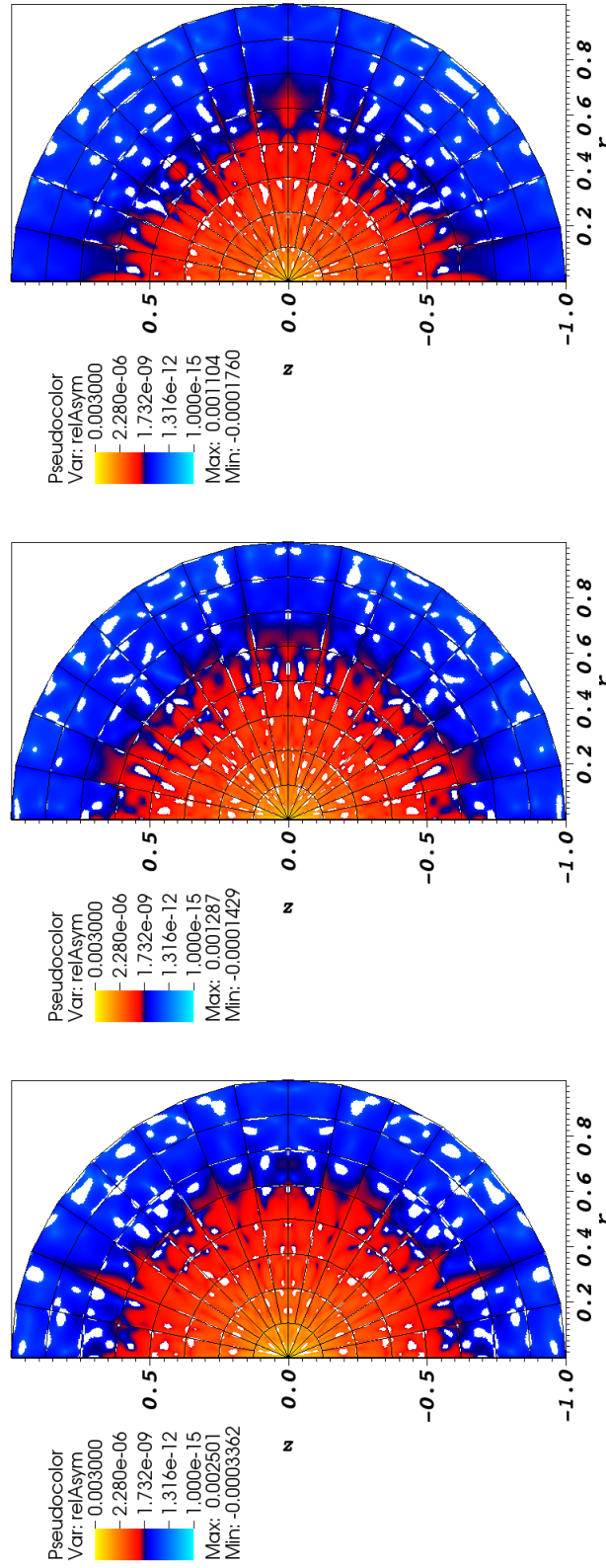


Figure 28: Relative asymmetry for 4st-order finite elements on a 1st-order mesh for given order of level-symmetric angular quadrature.

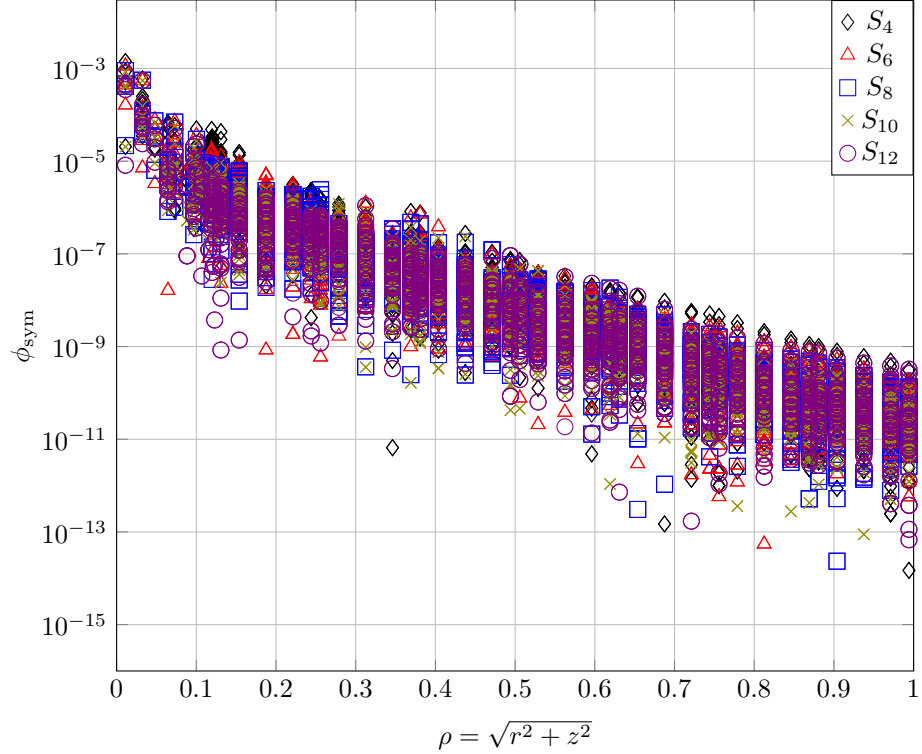


Figure 29: Measure of the asymmetry for each finite element node for the given level-symmetric angular quadrature order for 4th-order DFEM and 1st-order mesh with 120 zones (see Figure 28).

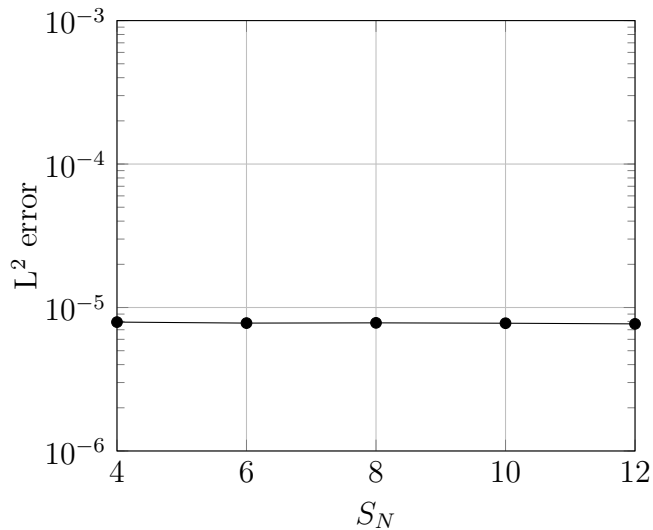


Figure 30: Accuracy of solutions for given angular quadrature using $p = 4$ on a 1st-order mesh with 120 zones.

Figure 31 shows the ϕ_{asym} values calculated using Equation 125 for 8th-order finite elements on a 1st-order mesh with 120 zones for several angular quadrature discretizations. The asymmetry is plotted on a log scale. The scale colors assist in demonstrating the qualitative locations of the asymmetries. The yellow region is the least symmetric, red regions have increased symmetry, and blue regions have the most symmetry. The ϕ_{asym} solution is plotted using the same finite element shape functions as the scalar flux. There is no perceptible gain in symmetry by increasing the angular discretization order. However, Figure 32 shows there is a slight increase in symmetry from S_4 for $\rho \geq 0.7$. Similar to Figure 28, the asymmetry of the scalar flux appears to be a function of the spherical radius, ρ . Moreover, Figure 33 demonstrates there is an increase in accuracy by increasing the finite element order.

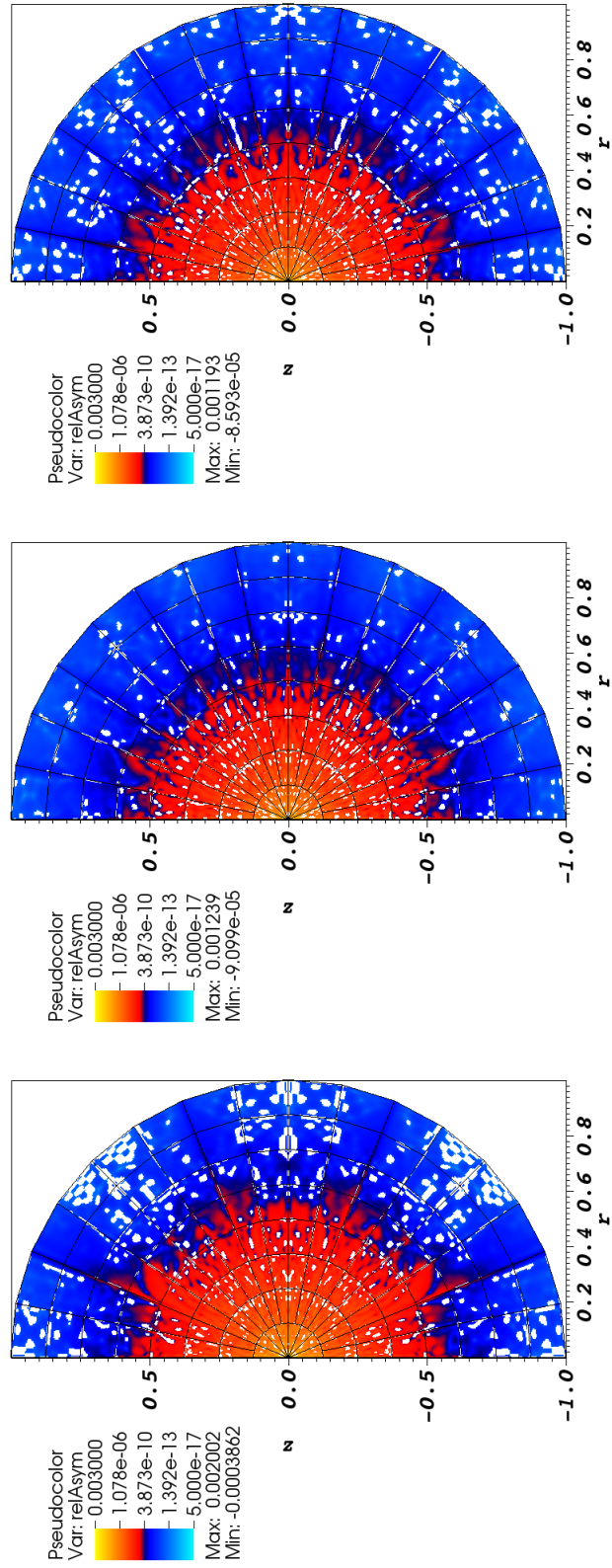


Figure 31: Relative asymmetry for 8st-order finite elements on a 1st-order mesh for given order of level-symmetric angular quadrature.

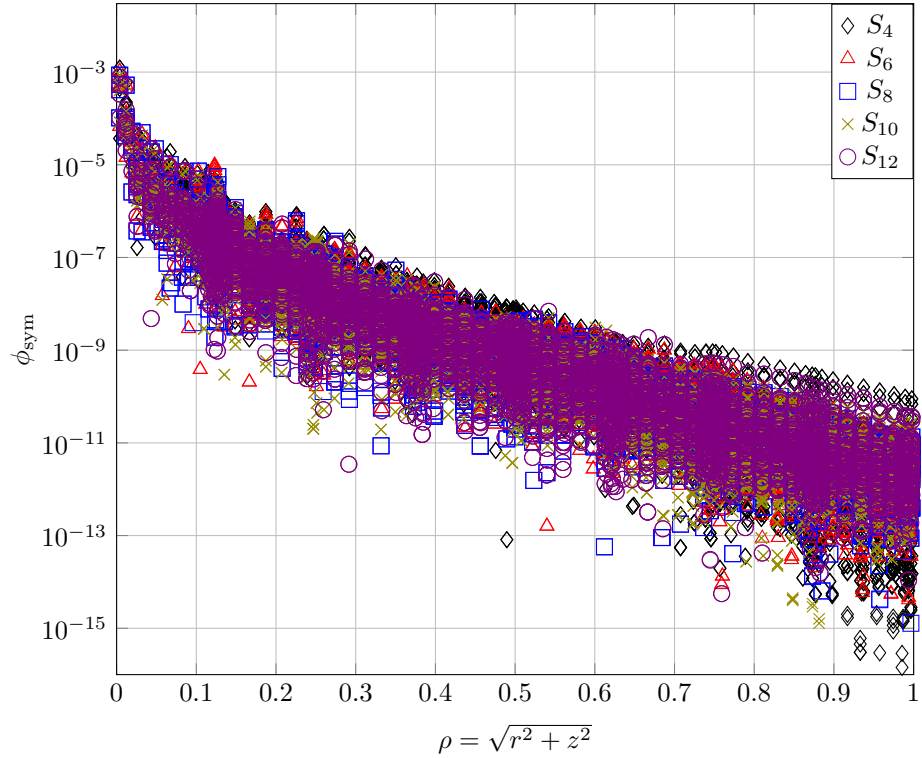


Figure 32: Measure of the asymmetry for each finite element node for the given level-symmetric angular quadrature order for 8th-order DFEM and 1st-order mesh with 120 zones (see Figure 31).

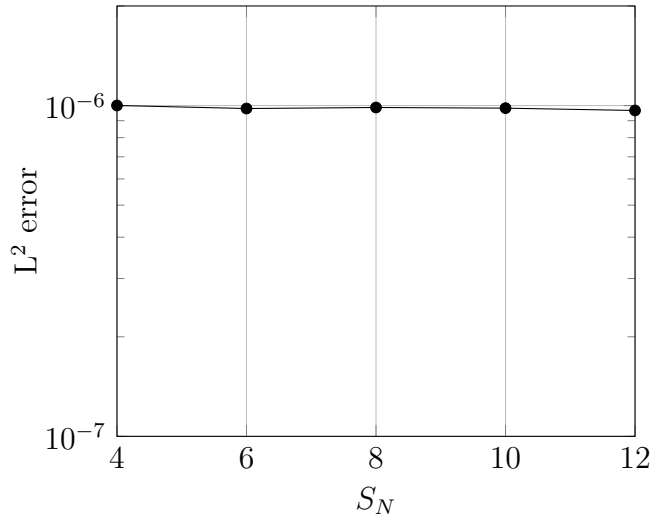


Figure 33: Accuracy of solutions for given angular quadrature using $p = 8$ on a 1st-order mesh with 120 zones.

Figure 34 shows the ϕ_{asym} values calculated using Equation 125 for $p = \{1, 2, 4\}$ finite elements on a 2nd-order mesh with 120 zones with S_8 level-symmetric angular quadrature repeated from Figures 22, 25, and 28 and plotted on the same scale. Increasing the finite element order provides significant gains in symmetry shown by the reduction in yellow regions and increase in blue regions. We corroborate these results by plotting the asymmetry values as a function of the spherical radius (i.e., $\rho = \sqrt{r^2 + z^2}$) in Figure 35. It is evident that increasing the finite element order provides gains in spherical symmetry. Moreover, Figure 36 demonstrates there is an increase in accuracy by increasing the finite element order except for 8th-order finite elements.

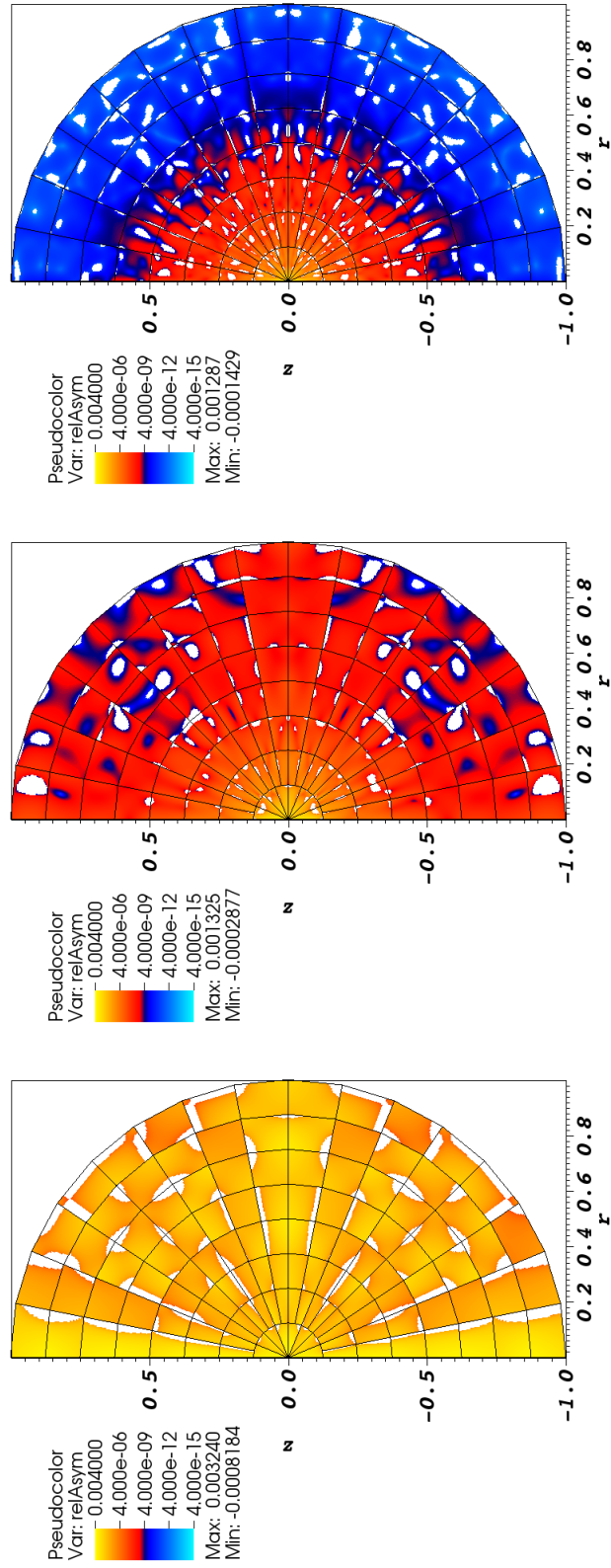


Figure 34: Relative asymmetry for $p = \{1, 2, 4\}$ finite elements on a 1st-order mesh with 120 zones for S_8 level-symmetric angular quadrature.

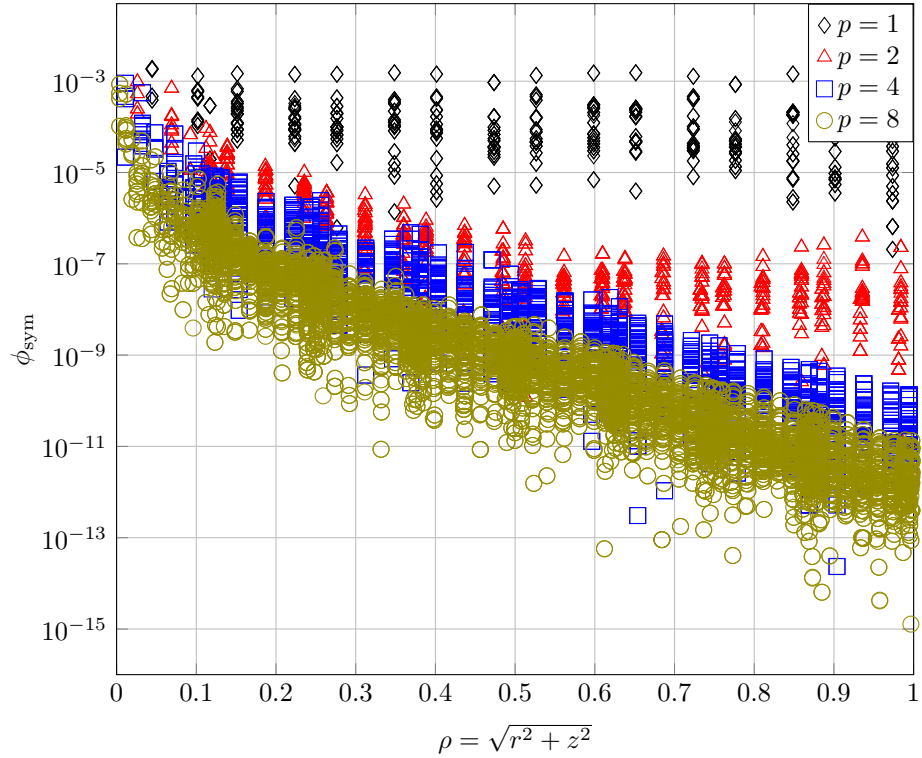


Figure 35: Measure of the asymmetry for each finite element node for the given finite element order using S_8 level-symmetric angular quadrature on a 1st-order mesh with 120 zones (see Figure 34).

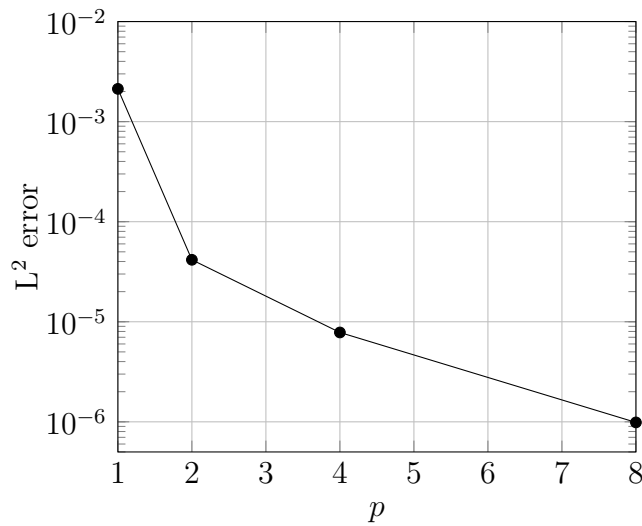


Figure 36: Accuracy of solutions for given finite element order using S_8 level-symmetric angular quadrature on a 1st-order mesh with 120 zones.

We also investigated the symmetry preservation by performing sequential mesh refinements for $p = 1$ with S_8 level-symmetric angular quadrature. Figures 37 and 38 show the first several mesh refinement steps. The asymmetry is plotted on a log scale. The scale colors assist in demonstrating the qualitative locations of the asymmetries. The yellow region is the least symmetric, red regions have increased symmetry, and blue regions have the most symmetry. The ϕ_{asym} solution is plotted using the same finite element shape functions as the scalar flux. There is some gain (a few orders of magnitude) in symmetry by refining the 1st-order mesh. We observe large regions of ϕ_{asym} changing from yellow to red through the mesh refinement. Plotting the symmetry values as a function of the spherical radius (i.e., $\rho = \sqrt{r^2 + z^2}$) in Figure 39 shows that there is some symmetry gain by refining the mesh. The largest asymmetry magnitude of the scalar flux is near the polar axis (i.e. $r = 0$) as previously seen in Figure 22. Moreover, Figure 40 demonstrates there is an increase in accuracy by refining the spatial mesh.

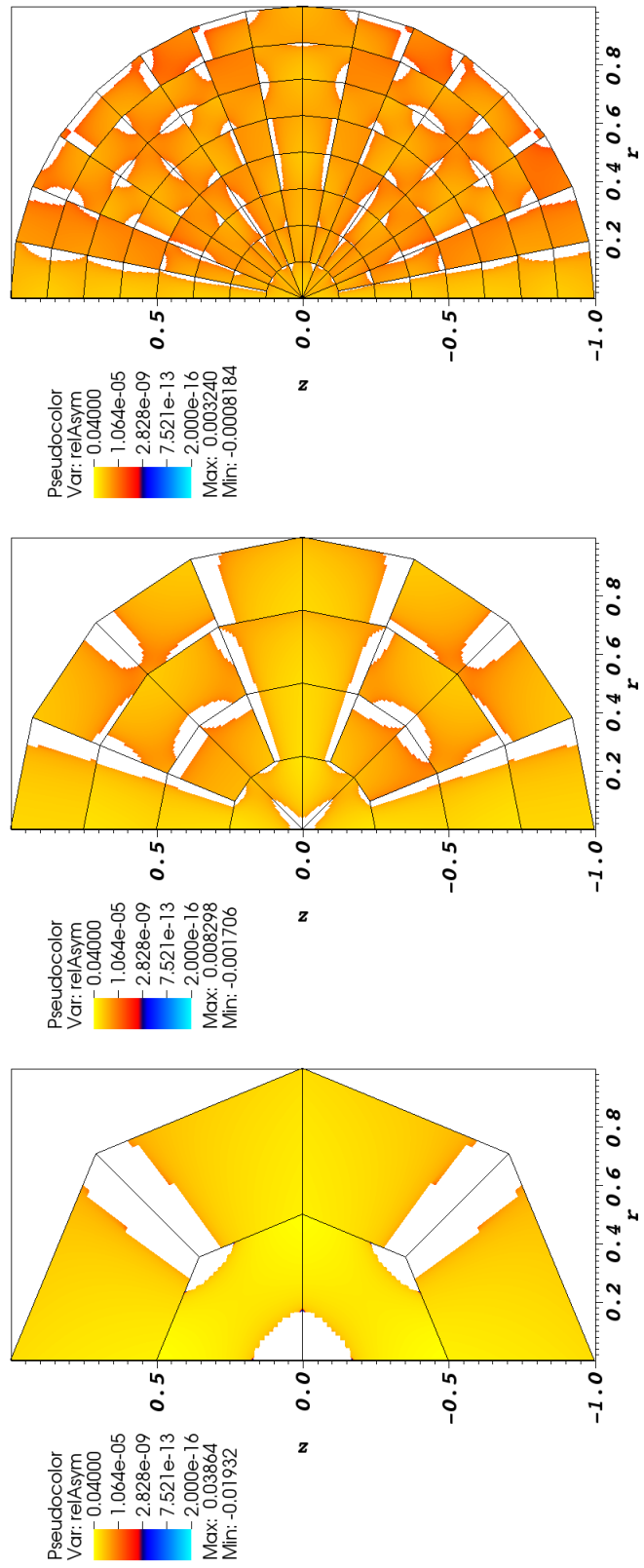


Figure 37: Relative asymmetry for $p = 1$ finite elements on a 1st-order mesh for S_8 level-symmetric angular quadrature for $N_{\text{zones}} = \{6, 28, 120\}$.

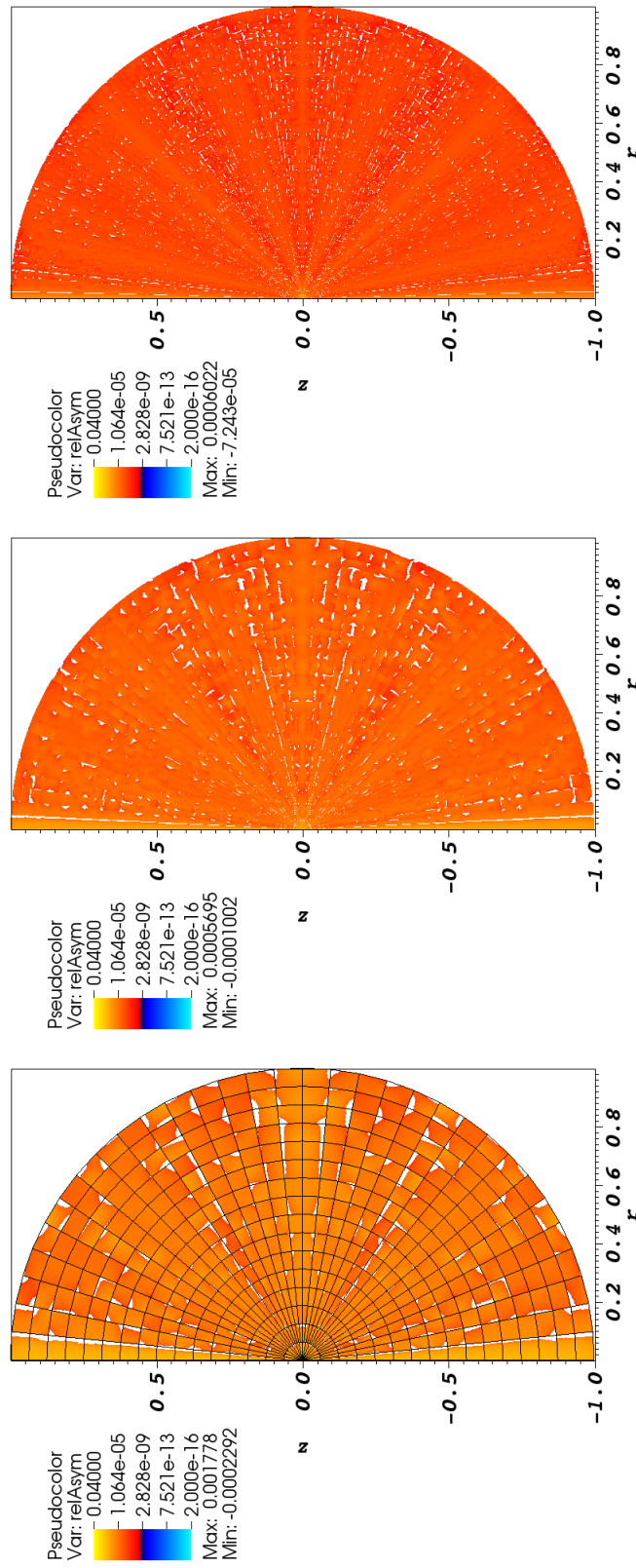


Figure 38: Relative asymmetry for $p = 1$ finite elements on a 1st-order mesh for S_8 level-symmetric angular quadrature for $N_{\text{zones}} = \{496, 2016, 8128\}$; mesh overlay may be removed for clarity.

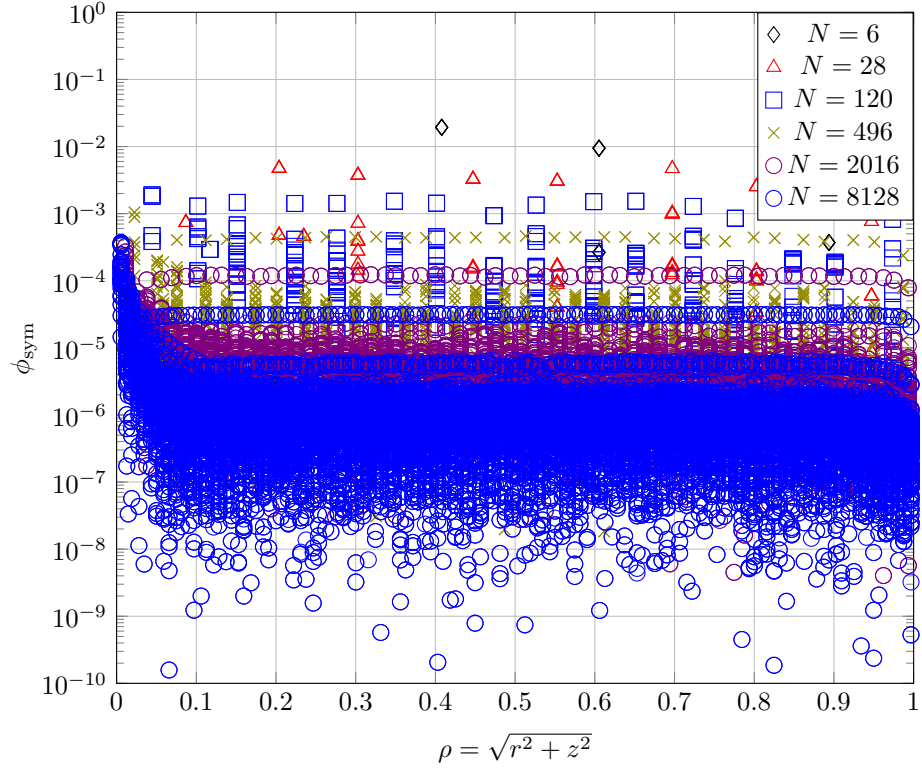


Figure 39: Measure of the asymmetry for each finite element node for 1th-order finite elements using S_8 level-symmetric angular quadrature on a 1st-order mesh with various number of zones (see Figures 37-38).

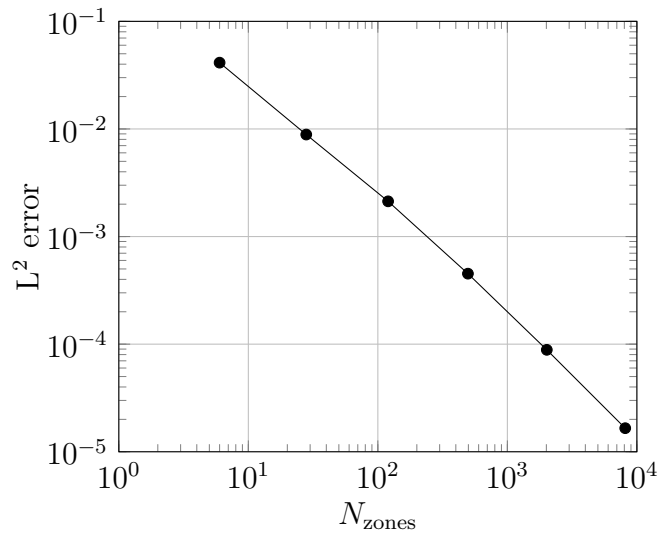


Figure 40: Accuracy of solutions for given mesh refinement for $p = 1$ using S_8 level-symmetric angular quadrature on a 1st-order mesh.

We also investigated the symmetry preservation by performing sequential mesh refinements for $p = 4$ with S_8 level-symmetric angular quadrature. Figures 41 and 42 show the first several mesh refinement steps. The asymmetry is plotted on a log scale. The scale colors assist in demonstrating the qualitative locations of the asymmetries. The yellow region is the least symmetric, red regions have increased symmetry, and blue regions have the most symmetry. The ϕ_{asym} solution is plotted using the same finite element shape functions as the scalar flux. There is tremendous gain (many orders of magnitude) in symmetry by refining the 1st-order mesh. We observe large regions of ϕ_{asym} changing from yellow to red to blue throughout the mesh refinement. Plotting the symmetry values as a function of the spherical radius (i.e., $\rho = \sqrt{r^2 + z^2}$) in Figure 43 confirms the substantial symmetry gain by refining the mesh. The largest asymmetry magnitude of the scalar flux remains near the origin (i.e. $\rho = \sqrt{r^2 + z^2} = 0$) as previously seen, but also remains prevalent in the discrete ordinates directions as though there were ray effects. Moreover, Figure 44 demonstrates there is an increase in accuracy by refining the spatial mesh.

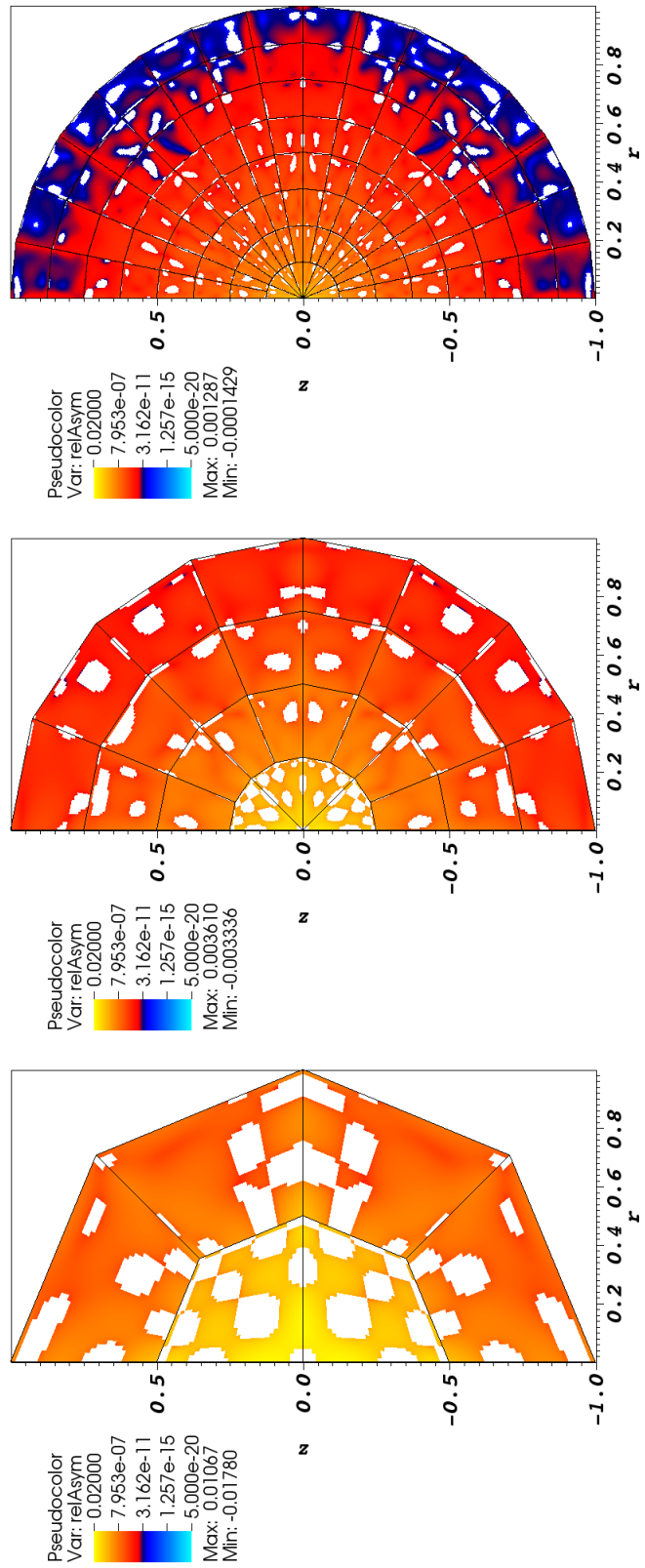
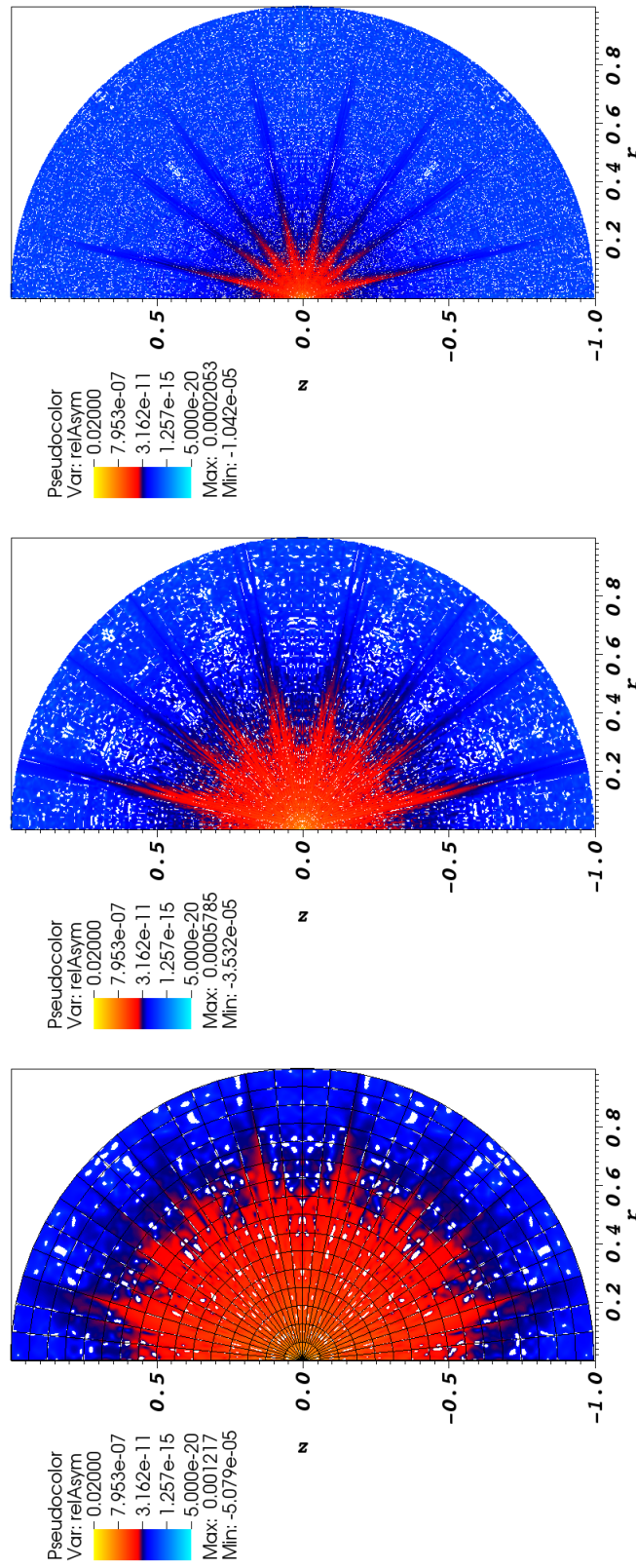


Figure 41: Relative asymmetry for $p = 4$ finite elements on a 1st-order mesh for S_8 level-symmetric angular quadrature for $N_{\text{zones}} = \{6, 28, 120\}$.



(a) $N_{\text{zones}} = 496$.
 (b) $N_{\text{zones}} = 2016$.
 (c) $N_{\text{zones}} = 8128$.

Figure 42: Relative asymmetry for $p = 4$ finite elements on a 1st-order mesh for S_8 level-symmetric angular quadrature for $N_{\text{zones}} = \{496, 2016, 8128\}$; mesh overlay may be removed for clarity.

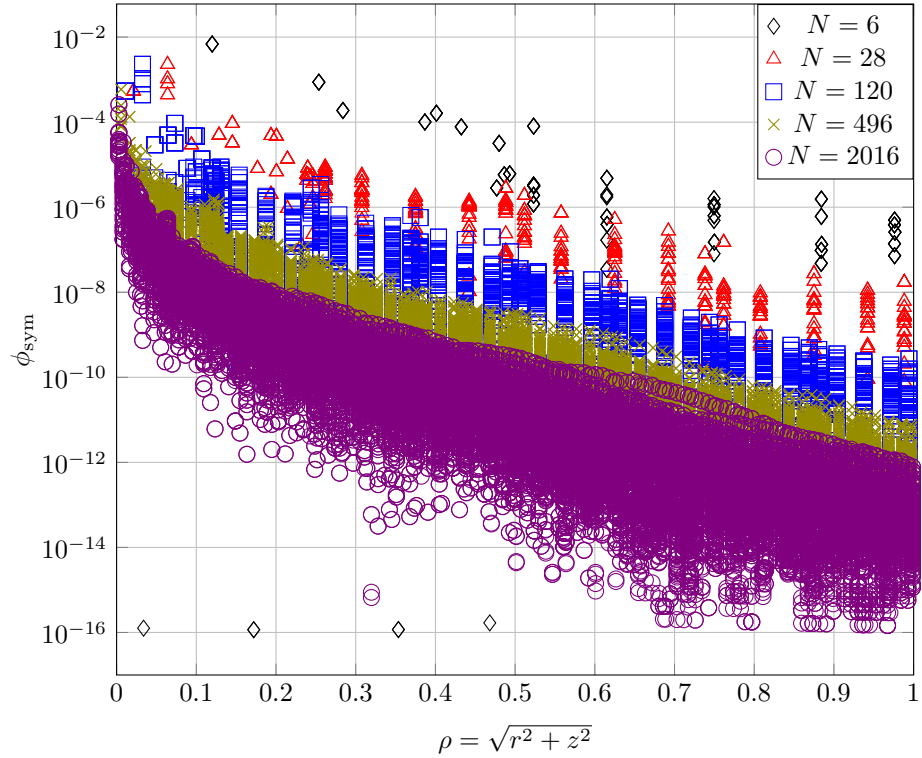


Figure 43: Measure of the asymmetry for each finite element node for 4th-order finite elements using S_8 level-symmetric angular quadrature on a 1st-order mesh with various number of zones (see Figures 41-42).

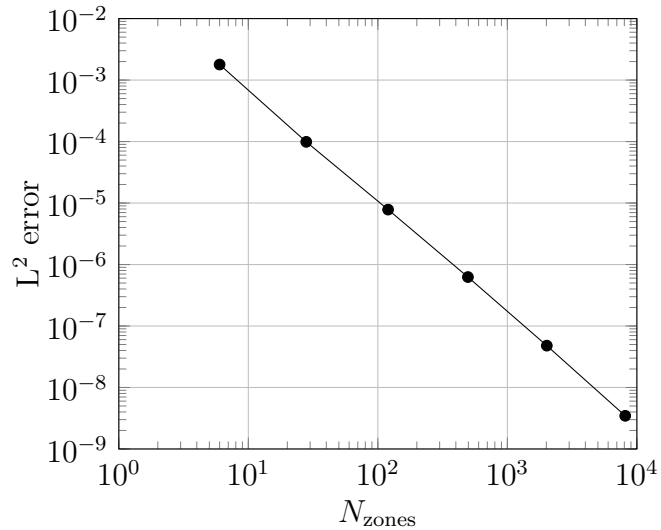


Figure 44: Accuracy of solutions for given mesh refinement for $p = 4$ using S_8 level-symmetric angular quadrature on a 1st-order mesh.

3.2.4.2 High-Order Mesh

Now, we perform the same asymmetry analysis using a high-order mesh. In this section, we observe the sensitivity of the scalar flux spherical asymmetry to changing the discrete ordinates order, finite element order, and spatial refinement on a high-order mesh. A high-order mesh is one that has curved polynomial surfaces. Specifically, we use 2nd-order meshes here. The vertices of the 2nd-order meshes used in this section are located in concentric rings of equal $\rho = \sqrt{r^2 + z^2}$, including the midpoint vertices. The results in this section are organized as follows: comparing the discrete ordinates order for each of $p = \{1, 2, 4\}$, comparing each of $p = \{1, 2, 4\}$ for S_8 level symmetric angular quadrature, mesh refinement studies for each of $p = \{1, 4\}$, and comparing the discrete ordinates refinement on the most refined spatial mesh.

Figure 45 shows the ϕ_{asym} values calculated using Equation 125 for 1st-order finite elements on a 2nd-order mesh with 120 zones for several angular quadrature discretizations. The asymmetry is plotted on a log scale. The scale colors assist in demonstrating the qualitative locations of the asymmetries. The yellow region is the least symmetric, red regions have increased symmetry, and blue regions have the most symmetry. The ϕ_{asym} solution is plotted using the same finite element shape functions as the scalar flux. There is no perceptible gain in symmetry by increasing the angular discretization order. We confirm this by plotting the asymmetry values as a function of the spherical radius (i.e., $\rho = \sqrt{r^2 + z^2}$) in Figure 46. The spherical radial asymmetry solutions are indistinguishable between discrete ordinate orders. Moreover, Figure 47 demonstrates there is no increase in accuracy by increasing the S_N order.

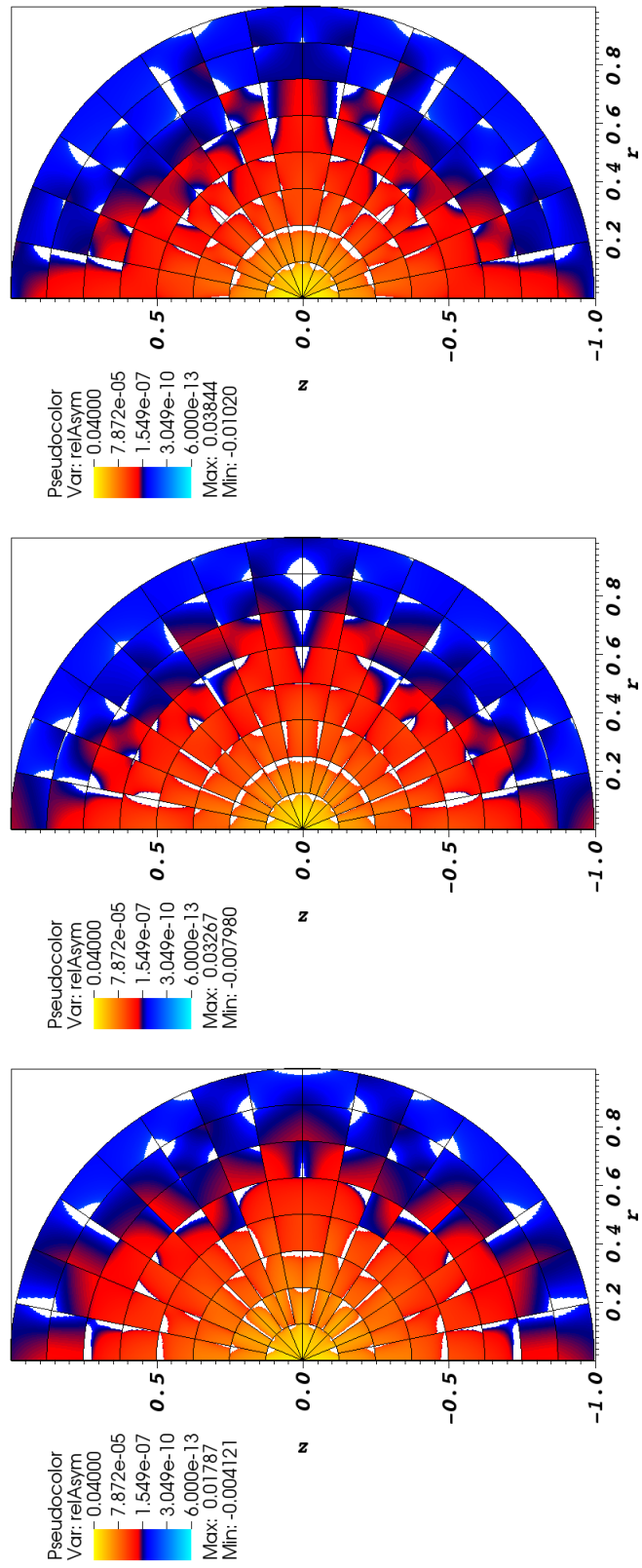


Figure 45: Relative asymmetry for 1st-order finite elements on a 2nd-order mesh for given order of level-symmetric angular quadrature.

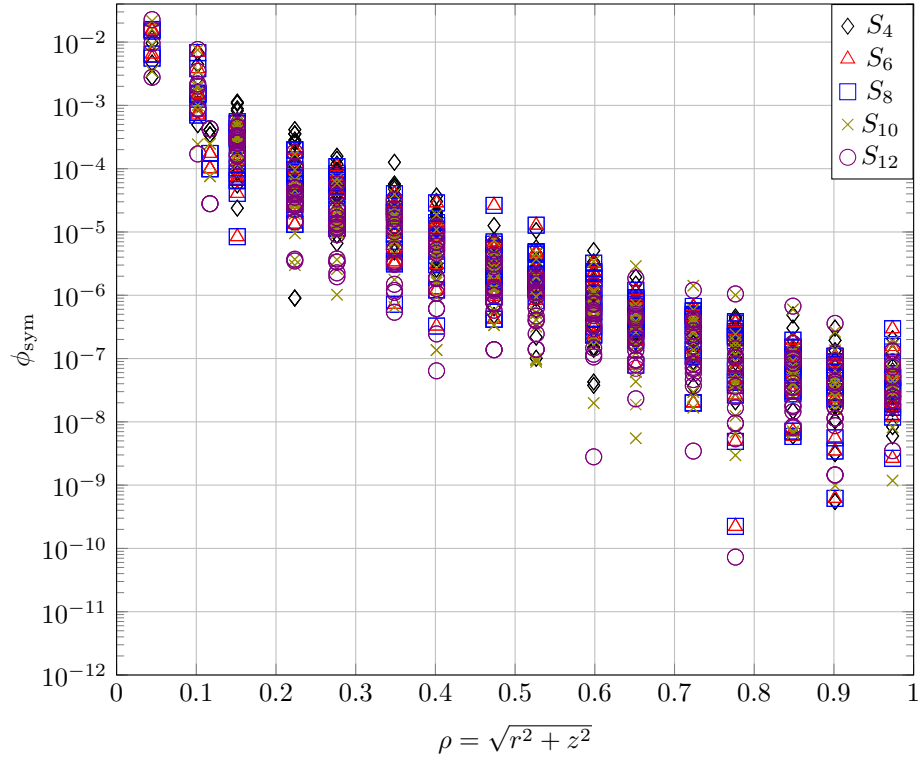


Figure 46: Measure of the asymmetry for each finite element node for the given level-symmetric angular quadrature order for 1st-order DFEM and 2nd-order mesh with 120 zones (see Figure 45).

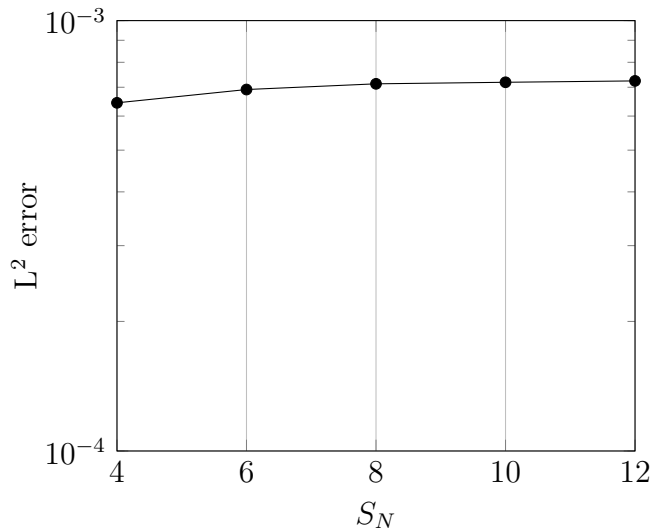


Figure 47: Accuracy of solutions for given angular quadrature using $p = 1$ on a 2nd-order mesh with 120 zones.

Figure 48 shows the ϕ_{asym} values calculated using Equation 125 for 2nd-order finite elements on a 2nd-order mesh with 120 zones for several angular quadrature discretizations. The asymmetry is plotted on a log scale. The scale colors assist in demonstrating the qualitative locations of the asymmetries. The yellow region is the least symmetric, red regions have increased symmetry, and blue regions have the most symmetry. The ϕ_{asym} solution is plotted using the same finite element shape functions as the scalar flux. There is very little perceptible gain in symmetry near the equator (i.e., $z = 0$) by increasing the angular discretization order. However, plotting the asymmetry values as a function of the spherical radius (i.e., $\rho = \sqrt{r^2 + z^2}$) in Figure 49 shows that there may not actually be any symmetry gains — the spherical radial asymmetry solutions are indistinguishable between discrete ordinate orders. The asymmetries are predominantly located near the polar axis (i.e., $r = 0$). Moreover, Figure 50 demonstrates there is no increase in accuracy by increasing the S_N order.

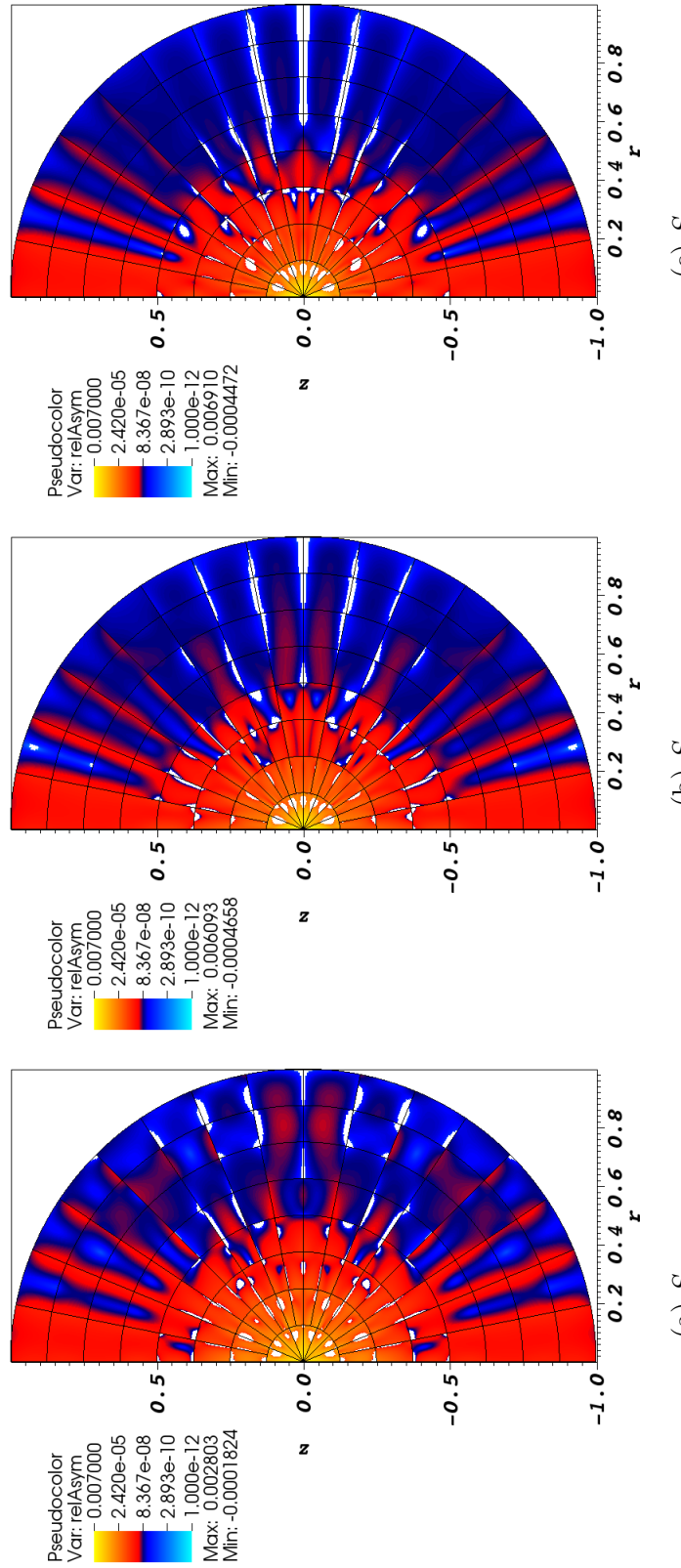


Figure 48: Relative asymmetry for 2nd-order finite elements on a 2nd-order mesh for given order of level-symmetric angular quadrature.

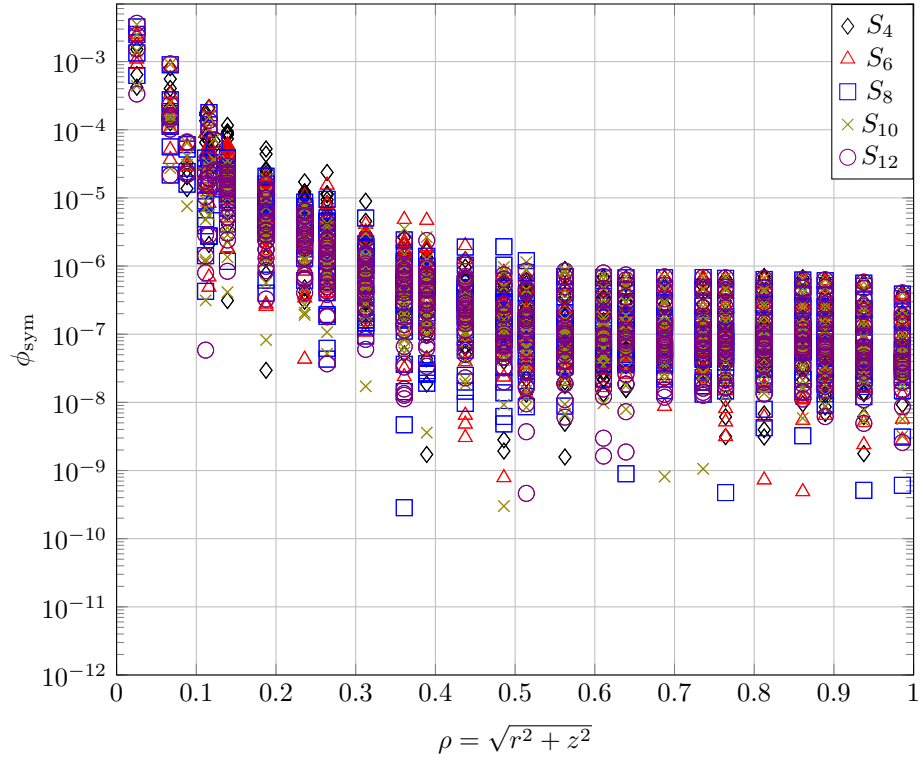


Figure 49: Measure of the asymmetry for each finite element node for the given level-symmetric angular quadrature order for 2nd-order DFEM and 2nd-order mesh with 120 zones (see Figure 48).

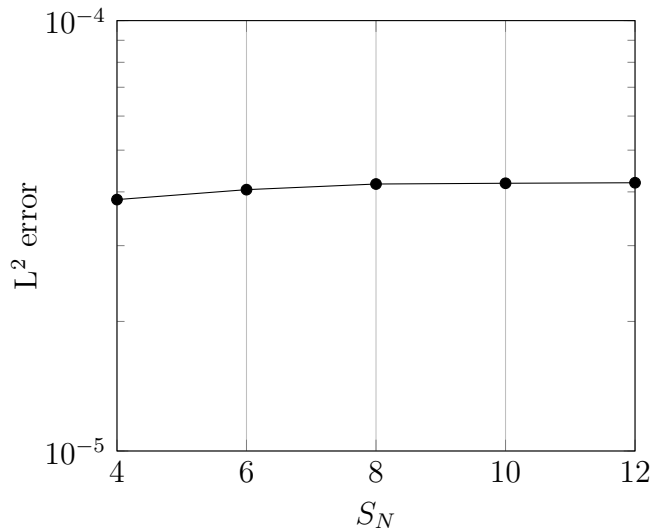


Figure 50: Accuracy of solutions for given angular quadrature using $p = 2$ on a 2nd-order mesh with 120 zones.

Figure 51 shows the ϕ_{asym} values calculated using Equation 125 for 4th-order finite elements on a 2nd-order mesh with 120 zones for several angular quadrature discretizations. The asymmetry is plotted on a log scale. The scale colors assist in demonstrating the qualitative locations of the asymmetries. The yellow region is the least symmetric, red regions have increased symmetry, and blue regions have the most symmetry. The ϕ_{asym} solution is plotted using the same finite element shape functions as the scalar flux. There is no perceptible gain in symmetry by increasing the angular discretization order. However, plotting the asymmetry values as a function of the spherical radius (i.e., $\rho = \sqrt{r^2 + z^2}$) in Figure 52 shows that there may be a symmetry gain from S_4 to higher angular discretization orders for $\rho \geq 0.7$. Unlike Figure 48, the asymmetry of the scalar flux appears to be a function of the spherical radius, ρ . Moreover, Figure 53 demonstrates there is no increase in accuracy by increasing the S_N order.

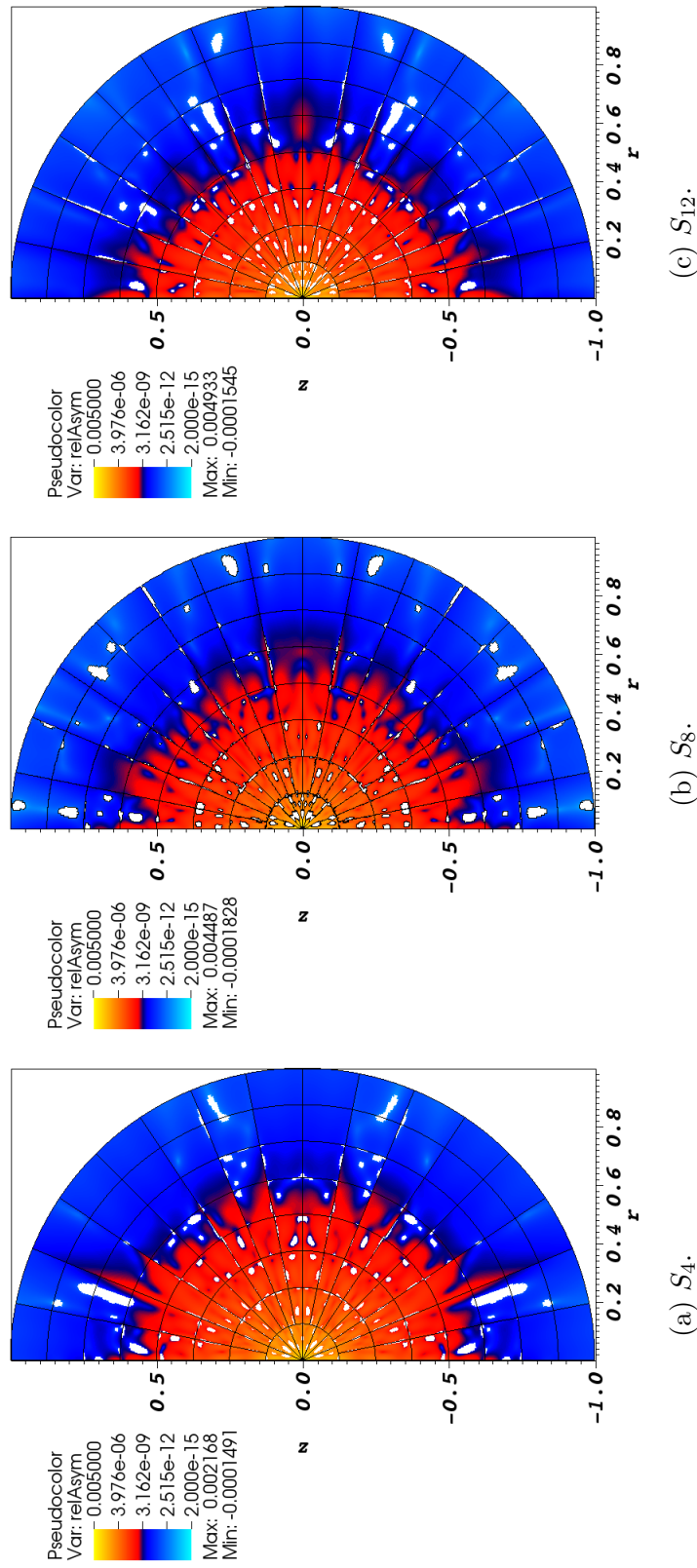


Figure 51: Relative asymmetry for 4th-order finite elements on a 2nd-order mesh for given order of level-symmetric angular quadrature.

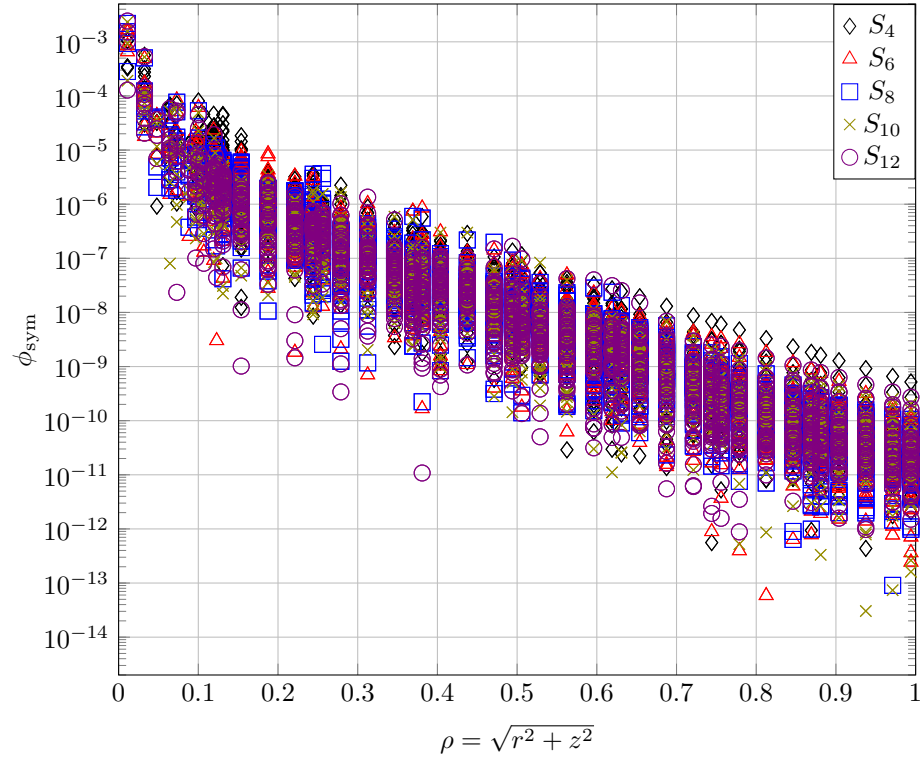


Figure 52: Measure of the asymmetry for each finite element node for the given level-symmetric angular quadrature order for 4th-order DFEM and 2nd-order mesh with 120 zones (see Figure 51).

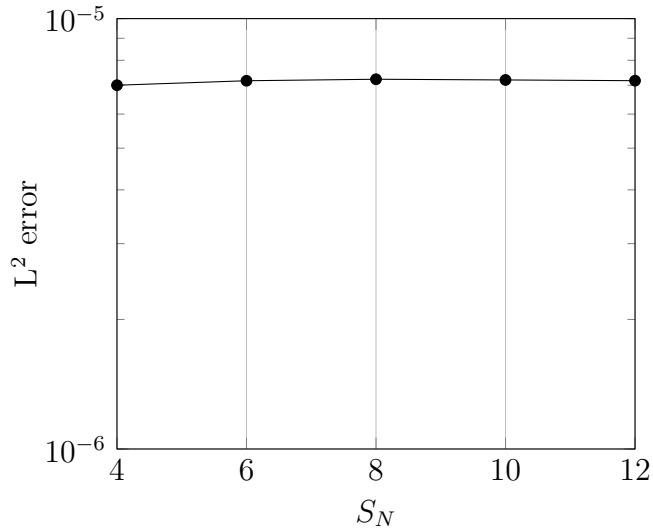


Figure 53: Accuracy of solutions for given angular quadrature using $p = 4$ on a 2nd-order mesh with 120 zones.

Figure 54 shows the ϕ_{asym} values calculated using Equation 125 for $p = \{1, 2, 4\}$ finite elements on a 2nd-order mesh with 120 zones with S_8 level-symmetric angular quadrature repeated from Figures 45, 48, 51 and plotted on the same scale. Increasing the finite element order from $p = 1$ to $p = 2$ increases the symmetry near the origin slightly, indicated by a reduction in yellow. However, increasing the finite element order to $p = 4$ provides significant gains in symmetry shown by the relatively larger blue region for $\rho = \sqrt{r^2 + z^2} \geq 0.5$. We corroborate these results by plotting the asymmetry values as a function of the spherical radius (i.e., $\rho = \sqrt{r^2 + z^2}$) in Figure 55. It is evident that increasing the finite element order provides gains in spherical symmetry. Moreover, Figure 56 demonstrates there is an increase in accuracy by increasing the finite element order.

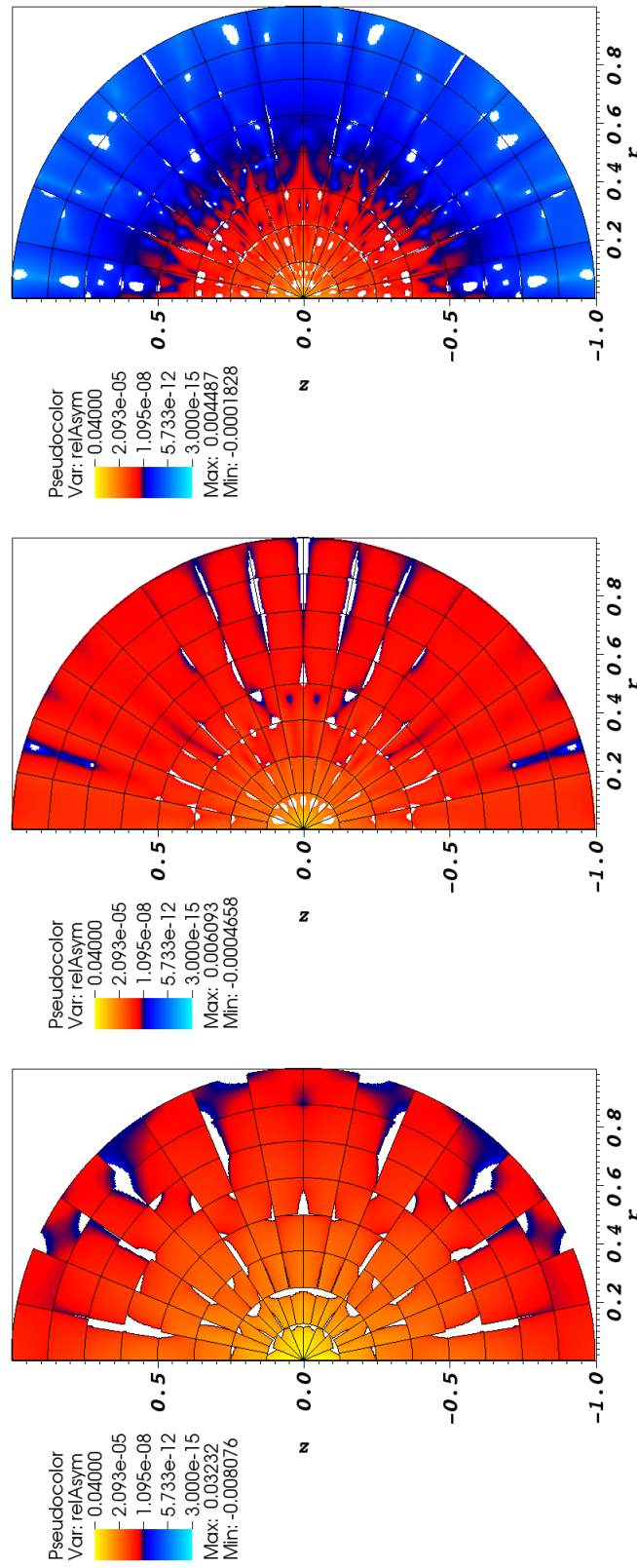


Figure 54: Relative asymmetry for $p = \{1, 2, 4\}$ finite elements on a 2nd-order mesh for S_8 level-symmetric angular quadrature.

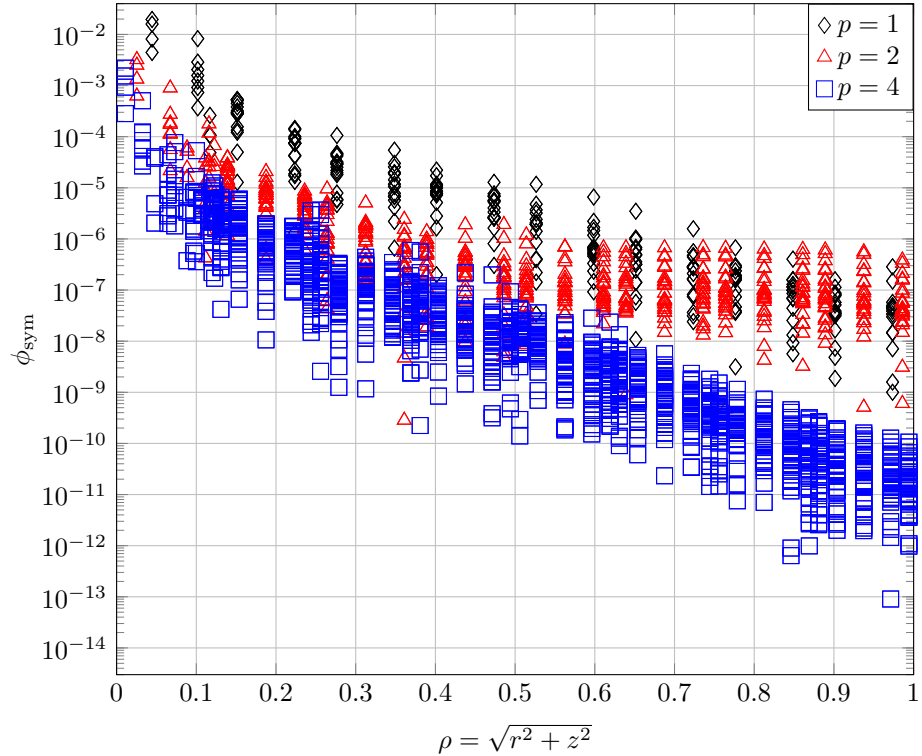


Figure 55: Measure of the asymmetry for each finite element node for the given finite element order using S_8 level-symmetric angular quadrature on a 2nd-order mesh with 120 zones (see Figure 54).

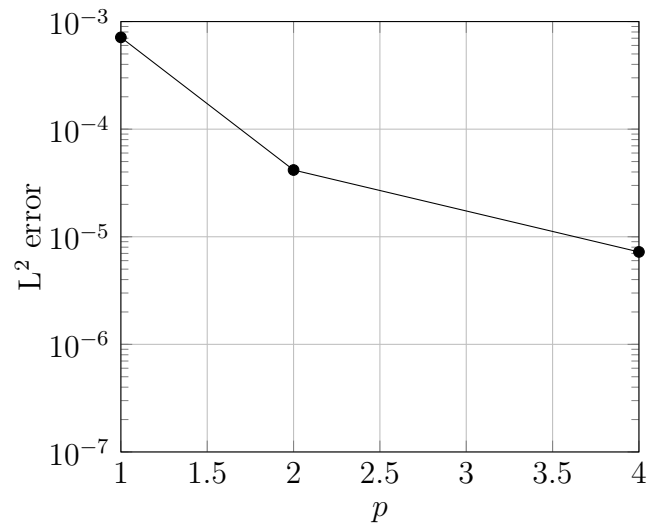


Figure 56: Accuracy of solutions for given angular quadrature using S_8 level-symmetric angular quadrature on a 2nd-order mesh with 120 zones.

We investigated the symmetry preservation by performing sequential mesh refinements for $p = 1$ with S_8 level-symmetric angular quadrature. Figures 57 and 58 show the first several mesh refinement steps. The asymmetry is plotted on a log scale. The scale colors assist in demonstrating the qualitative locations of the asymmetries. The yellow region is the least symmetric, red regions have increased symmetry, and blue regions have the most symmetry. The ϕ_{asym} solution is plotted using the same finite element shape functions as the scalar flux. As on the 1st-order mesh, there is tremendous gain (many orders of magnitude) in symmetry by refining the 2nd-order mesh. We observe large regions of ϕ_{asym} changing from yellow to red to blue throughout the mesh refinement. Plotting the symmetry values as a function of the spherical radius (i.e., $\rho = \sqrt{r^2 + z^2}$) in Figure 59 confirms the substantial symmetry gain by refining the mesh. The largest asymmetry magnitude of the scalar flux remains near the origin (i.e. $\rho = \sqrt{r^2 + z^2} = 0$) as previously seen, but also remains prevalent in the discrete ordinates directions as though there were ray effects. Moreover, Figure 60 demonstrates there is an increase in accuracy by refining the spatial mesh.

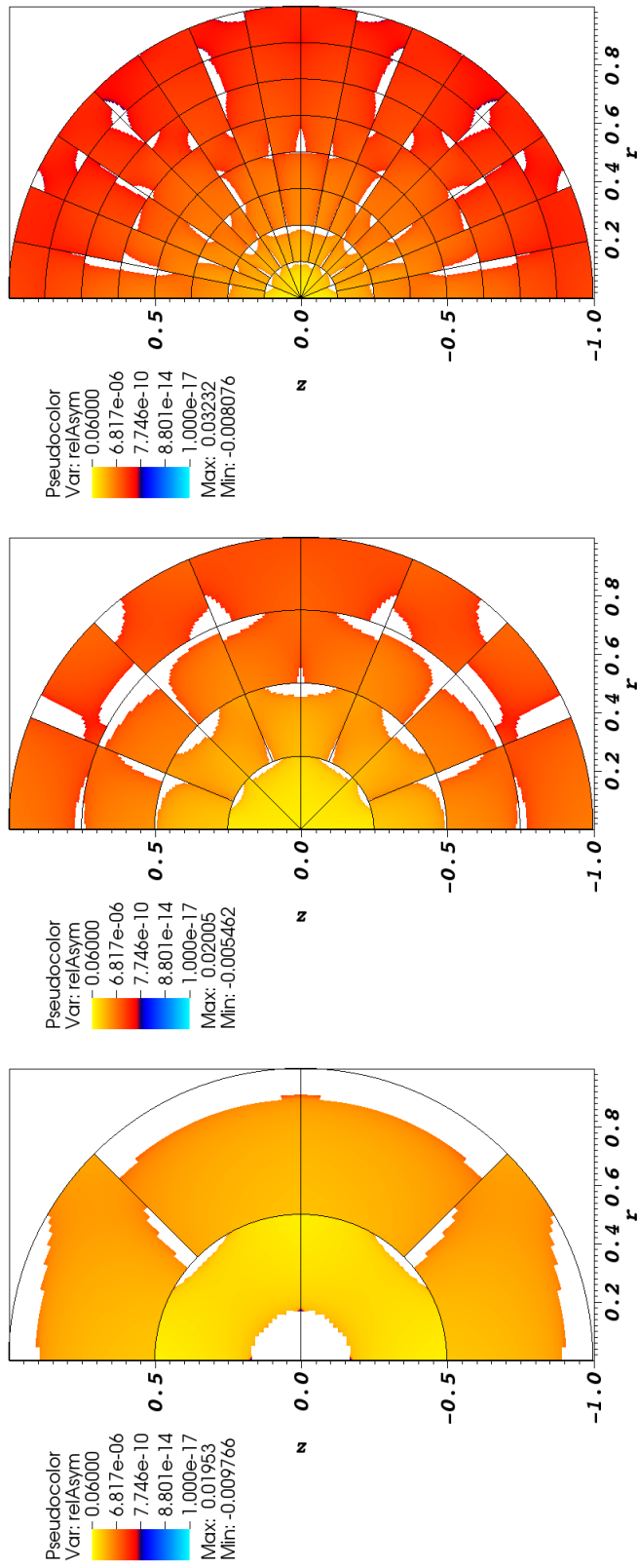


Figure 57: Relative asymmetry for $p = 1$ finite elements on a 2nd-order mesh for S_8 level-symmetric angular quadrature.

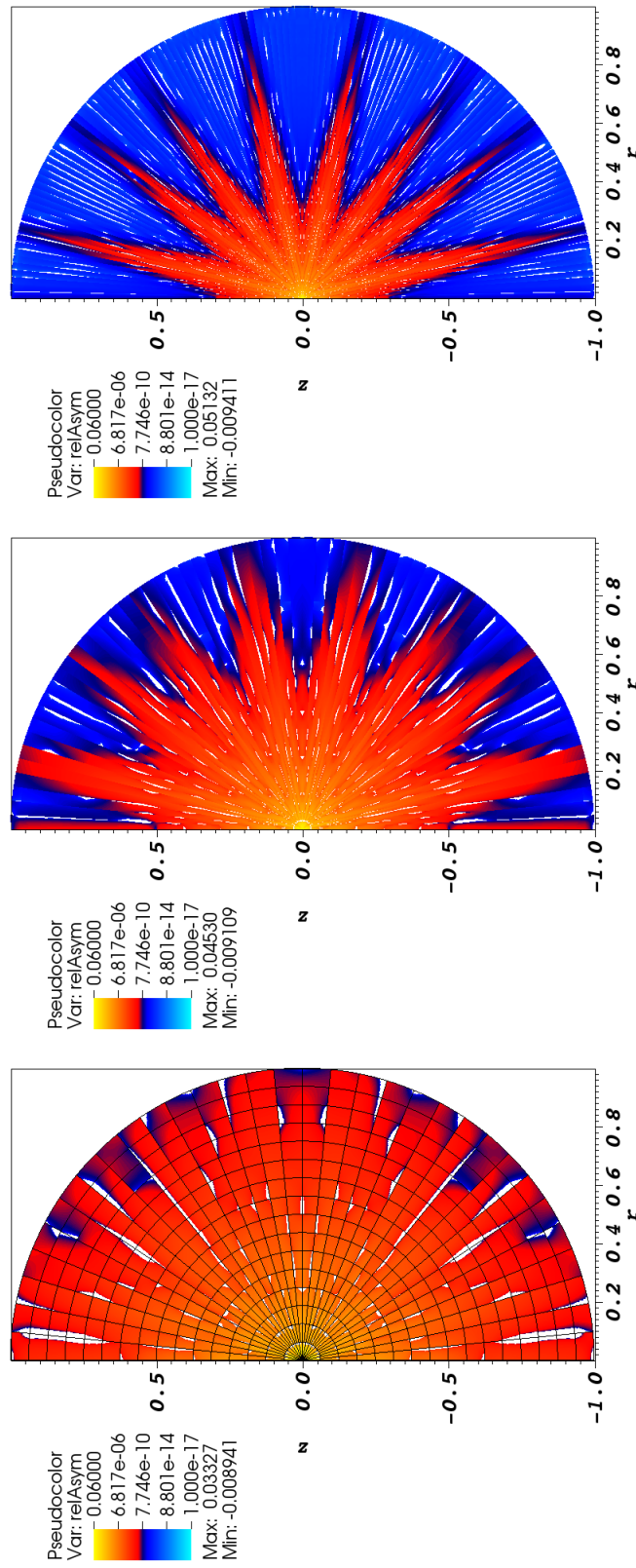


Figure 58: Relative asymmetry for $p = 1$ finite elements on a 2nd-order mesh for S_8 level-symmetric angular quadrature; mesh overlay may be removed for clarity.

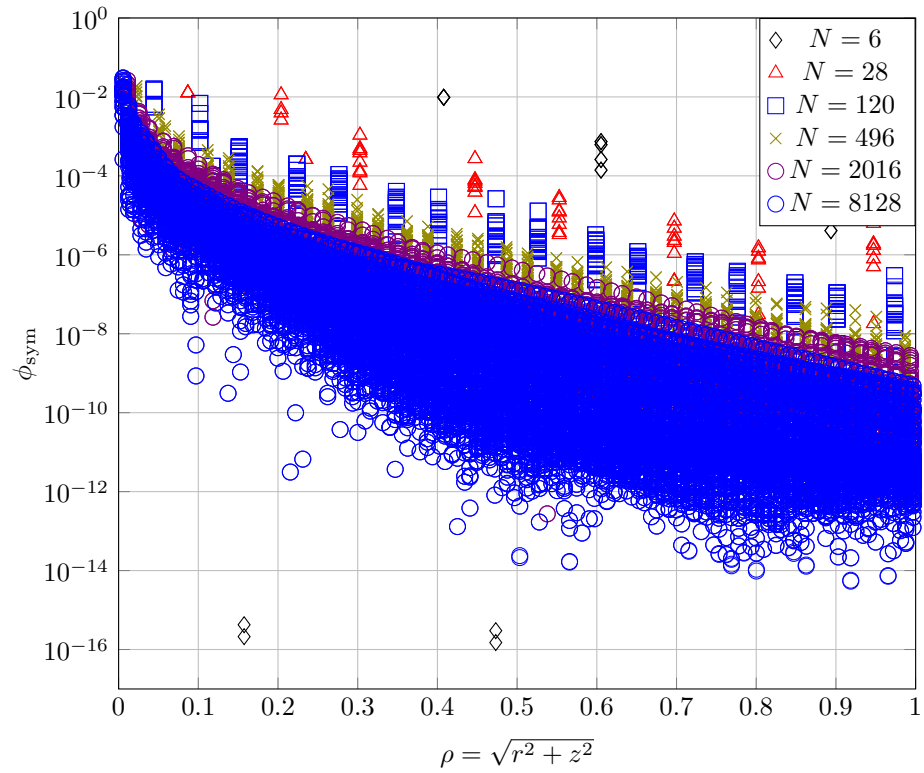


Figure 59: Measure of the asymmetry for each finite element node for 1st-order finite elements using S_8 level-symmetric angular quadrature on a 2nd-order mesh with various number of zones (see Figures 57-58).

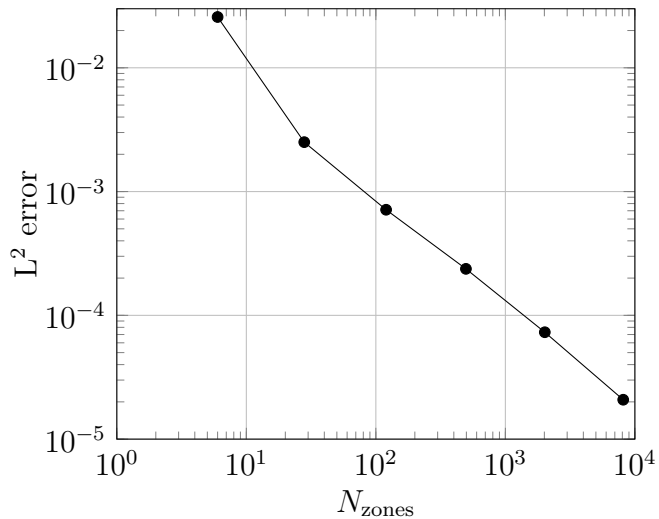


Figure 60: Accuracy of solutions for mesh refinement study using $p = 1$, S_8 level-symmetric angular quadrature, on a 2nd-order mesh.

We also investigated the symmetry preservation by performing sequential mesh refinements for $p = 1$ with S_8 level-symmetric angular quadrature. Figures 61 and 62 show the first several mesh refinement steps. The asymmetry is plotted on a log scale. The scale colors assist in demonstrating the qualitative locations of the asymmetries. The yellow region is the least symmetric, red regions have increased symmetry, and blue regions have the most symmetry. The ϕ_{asym} solution is plotted using the same finite element shape functions as the scalar flux. As on the 1st-order mesh, there is tremendous gain (many orders of magnitude) in symmetry by refining the 2nd-order mesh. We observe large regions of ϕ_{asym} changing from yellow to red to blue throughout the mesh refinement. Plotting the symmetry values as a function of the spherical radius (i.e., $\rho = \sqrt{r^2 + z^2}$) in Figure 63 confirms the substantial symmetry gain by refining the mesh. The largest asymmetry magnitude of the scalar flux remains near the origin (i.e. $\rho = \sqrt{r^2 + z^2} = 0$) as previously seen, but also remains prevalent in the discrete ordinates directions as though there were ray effects. Moreover, Figure 64 demonstrates there is an increase in accuracy by refining the spatial mesh.

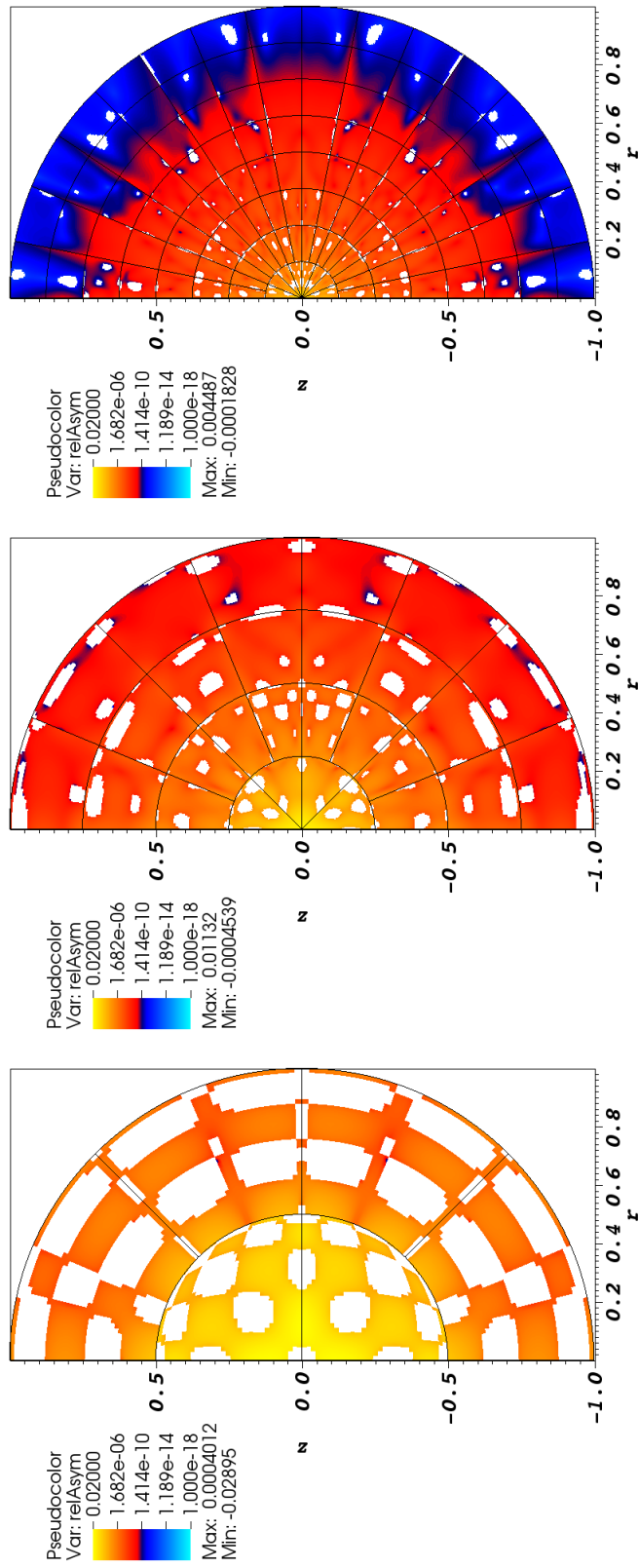


Figure 61: Relative asymmetry for $p = 4$ finite elements on a 2nd-order mesh for S_8 level-symmetric angular quadrature.

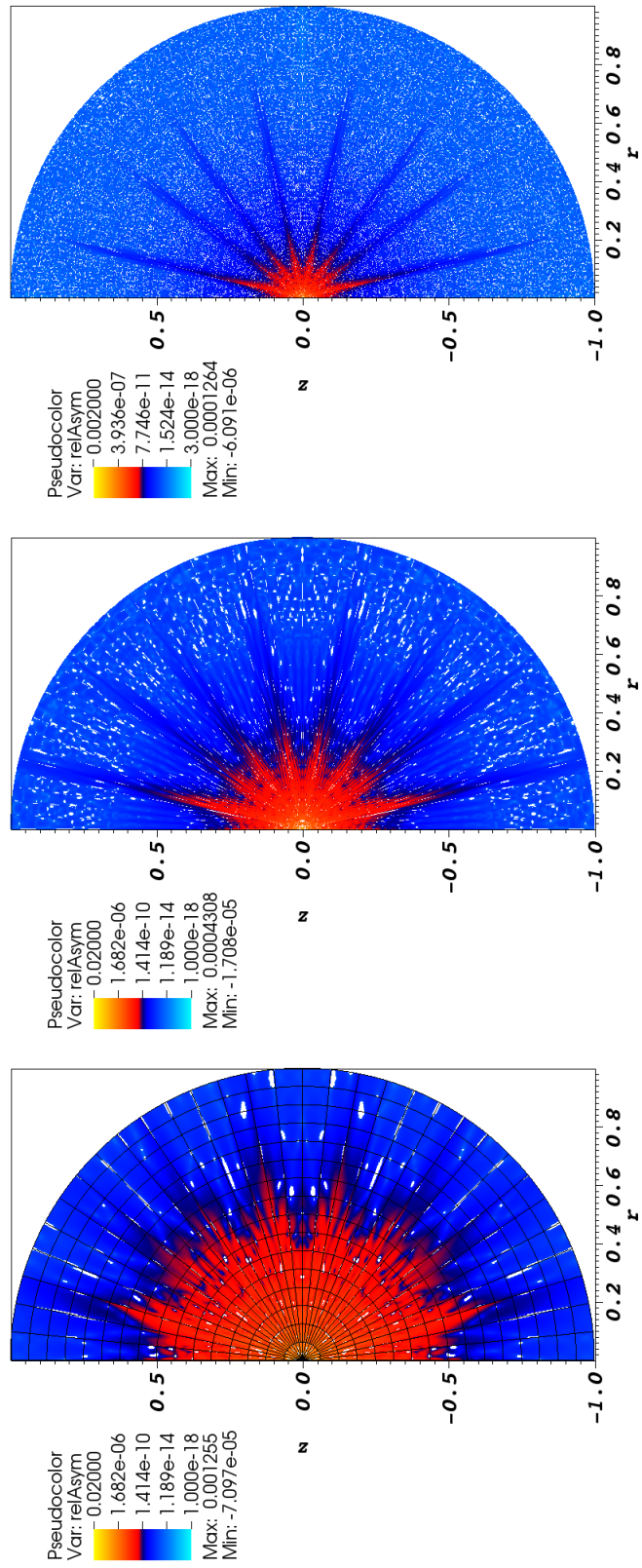


Figure 62: Relative asymmetry for $p = 4$ finite elements on a 2nd-order mesh for S_8 level-symmetric angular quadrature; mesh overlay may be removed for clarity.

(a) $N_{\text{zones}} = 496$.

(b) $N_{\text{zones}} = 2016$.

(c) $N_{\text{zones}} = 8128$.

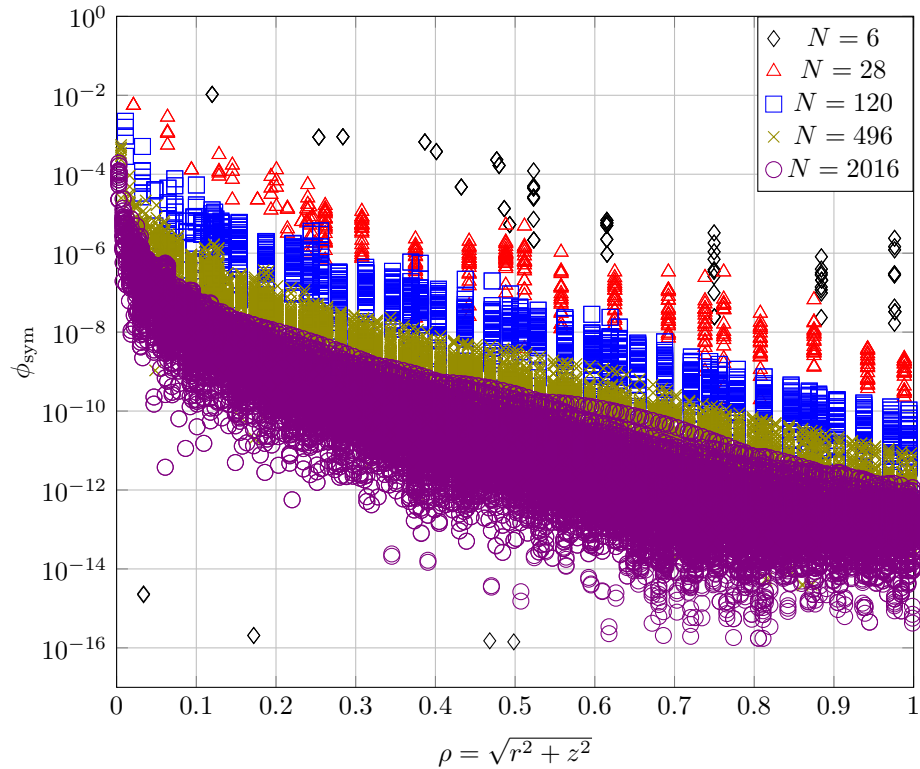


Figure 63: Measure of the asymmetry for each finite element node for 4th-order DFEM, S_8 level-symmetric angular quadrature, and 2nd-order mesh with various number of zones (see Figures 61 - 62).

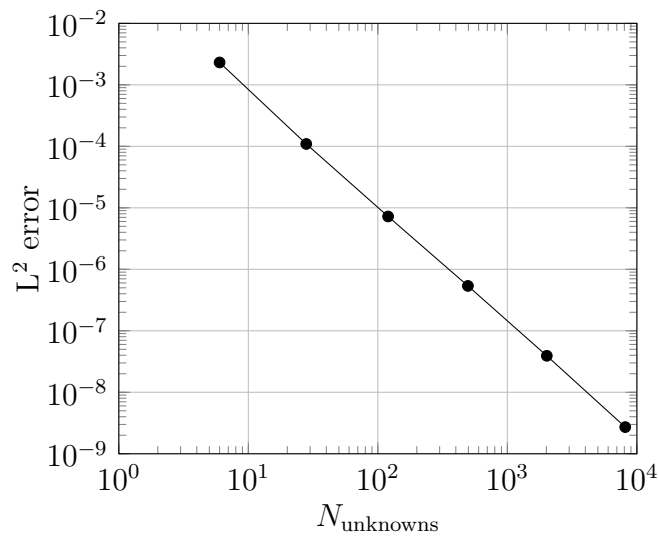


Figure 64: Accuracy of solutions for mesh refinement study using $p = 4$, S_8 level-symmetric angular quadrature, on a 2nd-order mesh.

In the most refined case of Figures 58 and 62, we observe some ray effects. These effects are dependent on the discrete ordinates discretization order. Here, we investigate the symmetry preservation by performing sequential discrete ordinates refinements for $p = 1$ on a 2nd-order mesh with 8128 zones. Figure 65 show the first several mesh refinement steps. The asymmetry is plotted on a log scale. The scale colors assist in demonstrating the qualitative locations of the asymmetries. The yellow region is the least symmetric, red regions have increased symmetry, and blue regions have the most symmetry. The ϕ_{asym} solution is plotted using the same finite element shape functions as the scalar flux. The ray effects are dependent upon the discrete ordinates discretization order. Despite the appearance of a reduction in overall symmetry, plotting the symmetry values as a function of the spherical radius (i.e., $\rho = \sqrt{r^2 + z^2}$) in Figure 63 demonstrates that the overall asymmetry is not very dependent upon the discrete ordinates discretization. The locations of these ray effects may introduce asymmetries themselves when coupling to other physics.

We also plot the asymmetry values as a function of the spherical radius (i.e., $\rho = \sqrt{r^2 + z^2}$). Figure 66 shows the ϕ_{asym} values calculated using Equation 125 for 1st-order finite elements on a 2nd-order mesh with 8128 zones for several angular quadrature discretizations. Moreover, Figure 67 demonstrates there is no increase in accuracy by increasing the S_N order.

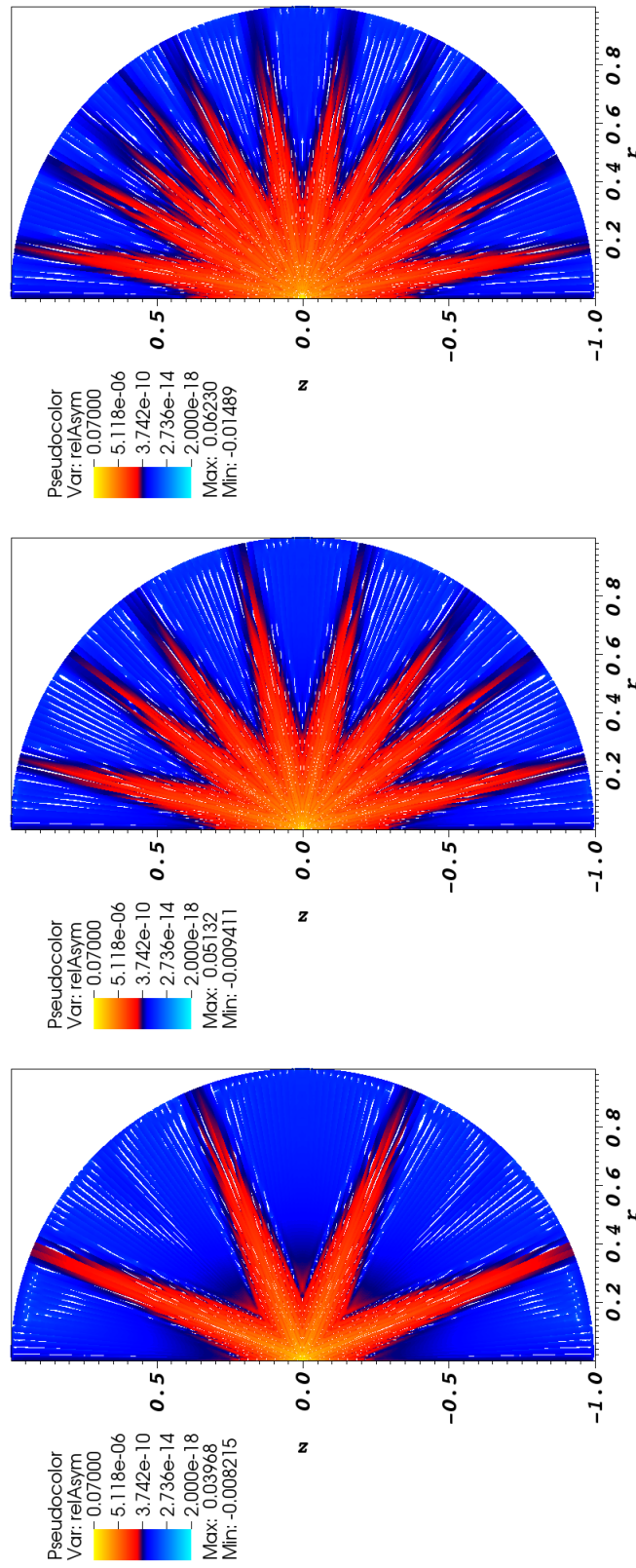


Figure 65: Relative asymmetry for $p = 1$ finite elements on a 2nd-order mesh with 8128 zones; mesh overlay may be removed for clarity.

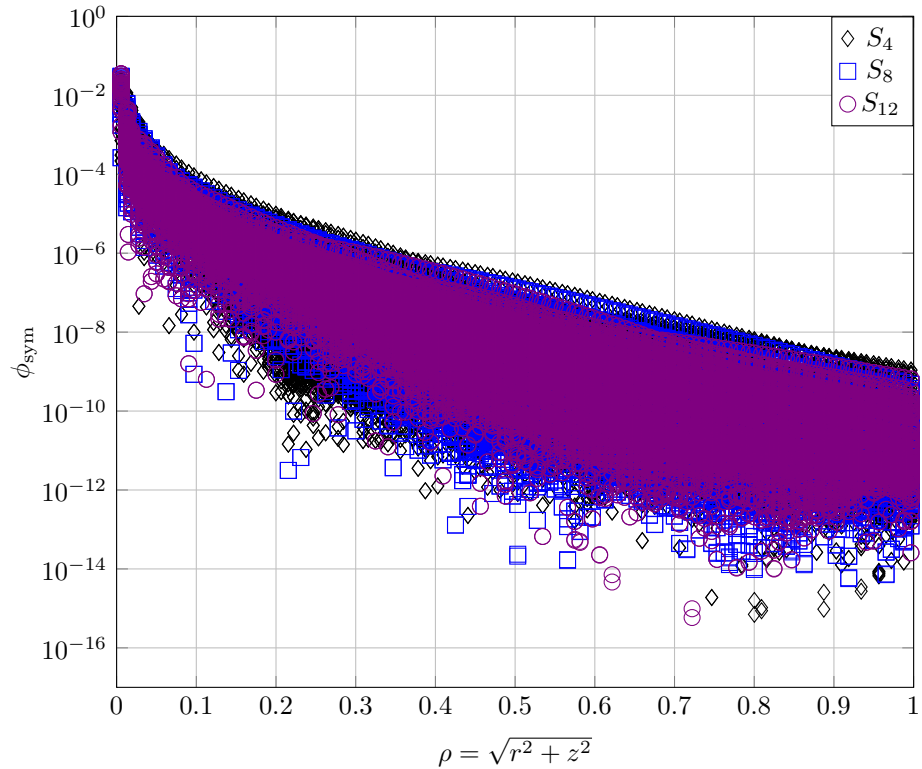


Figure 66: Measure of the asymmetry for each finite element node for the given level-symmetric angular quadrature order for 1st-order DFEM and 2nd-order mesh with 8128 zones.

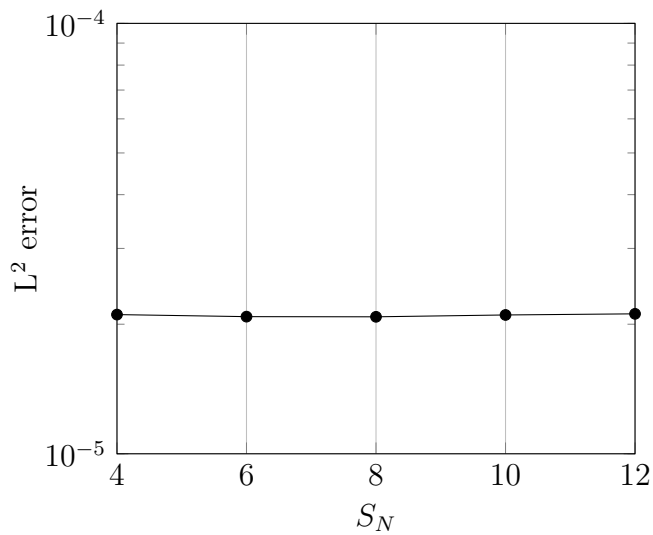
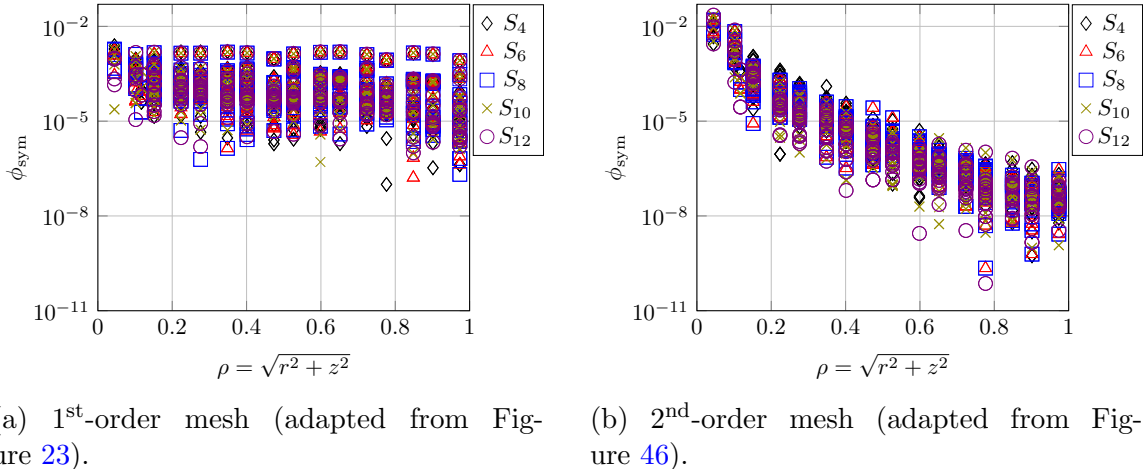


Figure 67: Accuracy of solutions for given angular quadrature using $p = 4$ on a 2nd-order mesh with 8128 zones.

3.2.4.3 Axisymmetry Summary and Discussion

For completeness, we compare some of the nodal asymmetry plots for ease of comparing the 2nd-order mesh to the 1st-order mesh on the same scales.

Figure 68 compares the 1st-order finite element solutions on both 1st- and 2nd-order meshes. While we have observed that the S_N order does not provide any additional

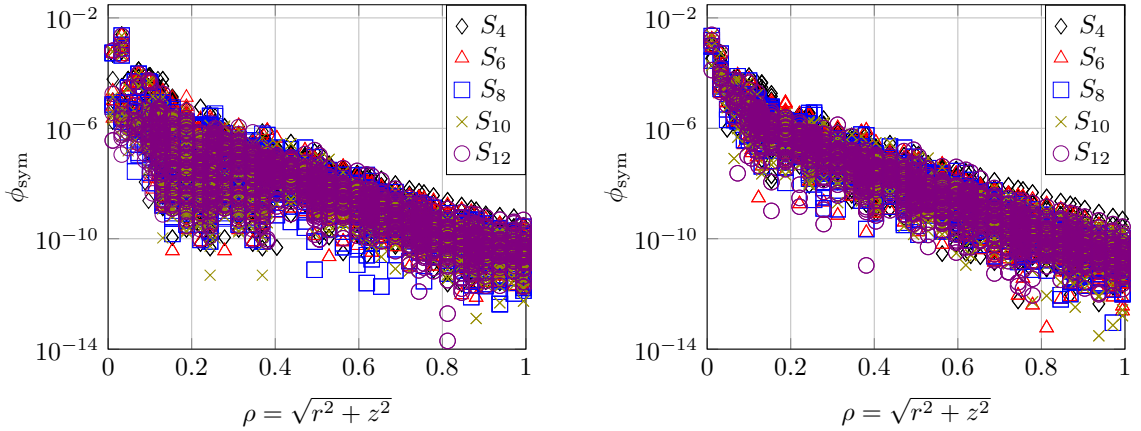


(a) 1st-order mesh (adapted from Figure 23). (b) 2nd-order mesh (adapted from Figure 46).

Figure 68: Measure of the asymmetry for each finite element node for the given level-symmetric angular quadrature order for 1st-order DFEM on the given mesh with 120 zones.

accuracy or spherical symmetry, increasing the mesh order for 1st-order finite elements does increase the spherical symmetry with increasing ρ . However, Figure 69 demonstrates that the mesh curvature does not benefit the spherical symmetry with HO (4th-order) finite elements. Finally, Figure 70 illustrates that refining the mesh does increase the symmetry preservation for 4th-order finite elements but adding curvature to the mesh zones does not.

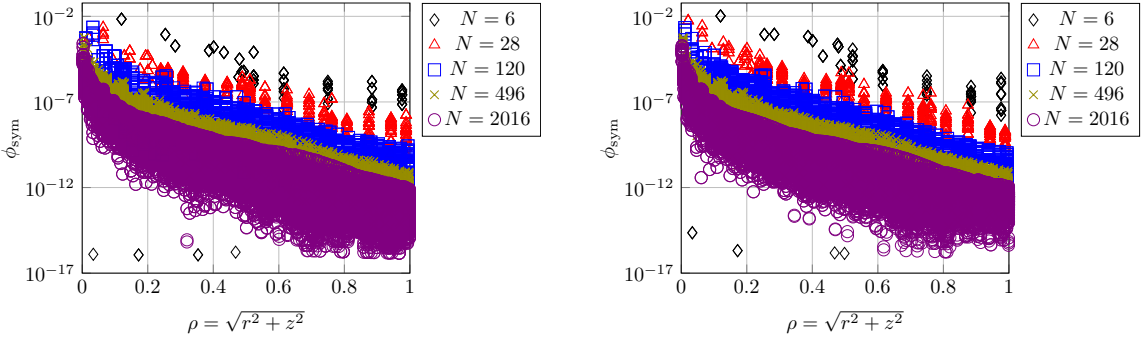
Table 2 summarizes these findings of whether or not each discretization property reduces the asymmetry or not.



(a) 1st-order mesh (adapted from Figure 29).

(b) 2nd-order mesh (adapted from Figure 52).

Figure 69: Measure of the asymmetry for each finite element node for the given level-symmetric angular quadrature order for 4th-order DFEM on the given mesh with 120 zones.



(a) 1st-order mesh (adapted from Figure 43).

(b) 2nd-order mesh (adapted from Figure 63).

Figure 70: Measure of the asymmetry for each finite element node for 4th-order DFEM, S_8 level-symmetric angular quadrature, on the given mesh with various number of zones.

Although the manufactured solution (Eq. 127) is seemingly simple, a steep gradient appears in the MMS source term near $(r, z) = (0, 0)$. We look at each term of the transport equation using the manufactured solution in Figure 71. The gradient operated on the manufactured solution generates a very steep gradient near the origin. This contributes to the shape of the source term — $S_0/(2\pi)$ is complicated near

Table 2: Summary of discretizations and determination of whether they reduce the asymmetry.

Property	Reduce Asymmetry?
S_N order	no
Finite element order	yes
mesh refinement	yes
mesh curvature	conditional

the origin. In practice, this source is an analytic driver for the radiation field in the problem. The source term is approximated by the finite element shape function using the analytic values for the nodes. So although the source is exact at the node points, the shape function does not capture the analytic shape of the source term necessary to achieve the axisymmetry we desire.

In the future, we will examine this effect of the approximation on the analytical source term by one of two ways. We could utilize the same manufactured solution (Equation 127) in a spatial region that does not have as strong of a gradient (i.e., away from the origin). Or, we may have to consider alternative manufactured solutions that avoid the gradient at the origin. It would be ideal to have a manufactured solution that operates well in a region of interest but employing $\rho = \sqrt{r^2 + z^2}$ will always result in some form of $(r^2 + z^2)^{(-1/2)}$ in the streaming term.

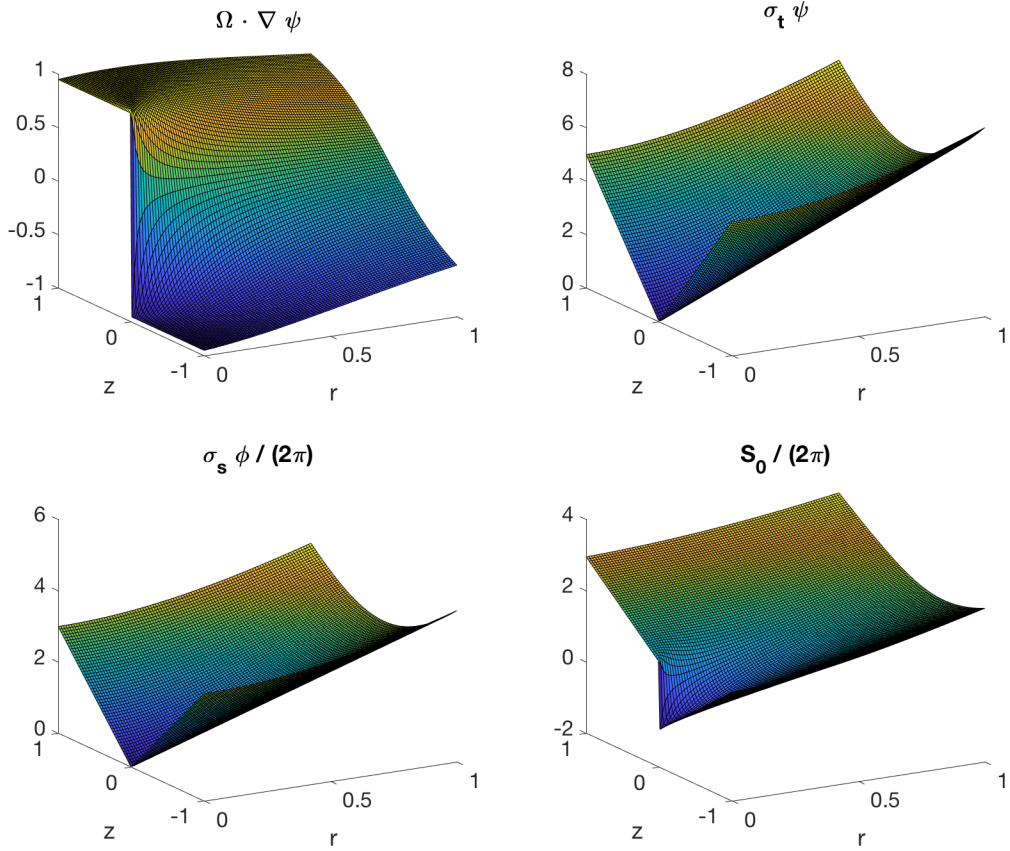


Figure 71: Analytic representation of each term of the transport equation using the manufactured solution, Equation 127, for $(\mu, \xi) \approx (0.218, 0.951)$. The complicated shapes of the streaming and source terms are typical of the other Ω directions.

3.2.5 Strong Scatter with Alternating Boundaries Test

We previously tested a higher-order X - Y transport methodology on an optically thick and highly scattering problem [26]. Here, we perform the same calculation in R - Z geometry as originally introduced by Palmer and Adams [49] and Palmer [52]. The medium is homogeneous, highly scattering ($c = 0.999$), has cross sections $\sigma_t = 1000 \text{ cm}^{-1}$, $\sigma_s = 999 \text{ cm}^{-1}$, and has no external source. The incident angular flux boundary conditions of strength $\psi_{inc} = 1/(2\pi) \text{ cm}^{-1} \text{ s}^{-1} \text{ ster}^{-1}$ on alternating locations denoted in Figure 72 by gray bars. This incident angular flux strength is

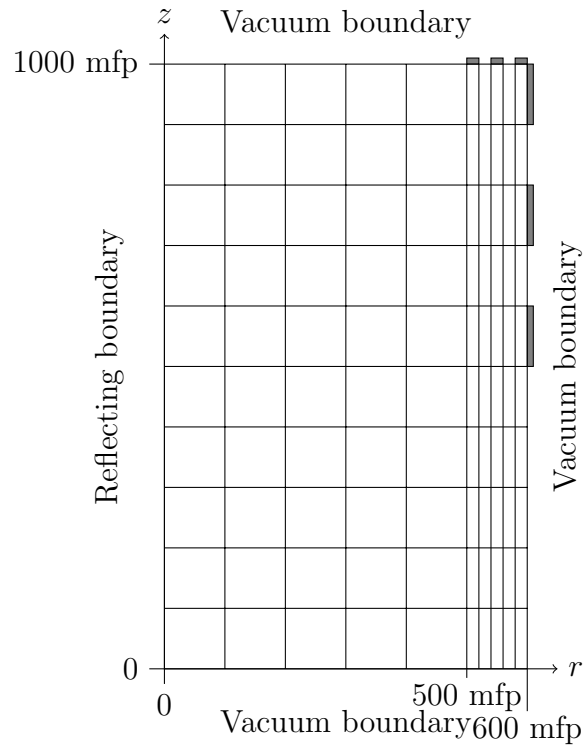


Figure 72: Strong scatter with discontinuous BCs with MIP DSA problem geometry; gray boundaries indicate incident boundary locations.

an estimated value obtained from other research solving this problem [49, 52]. For comparison to previous research using BLD, we solve this problem using $p = 1$ Gauss-Legendre DGFEM with S_4 level-symmetric angular quadrature. The solution is shown in Figure 73. While the previous research was investigating lumping techniques to reduce the negative solutions, this work seeks to characterize the behavior of higher-order solutions in R - Z geometry. We observe oscillations in the solution that result in some negative scalar fluxes. The solution changes several orders of magnitude. Compared to other research [52], we observe similar oscillations in the boundary layers, however the solution also presents oscillations in the problem interior. This may be due to the use of different basis functions or a result of not discretizing the conservation equation (Eq. 41).

We also solve with S_8 level-symmetric angular quadrature using 4th-order finite

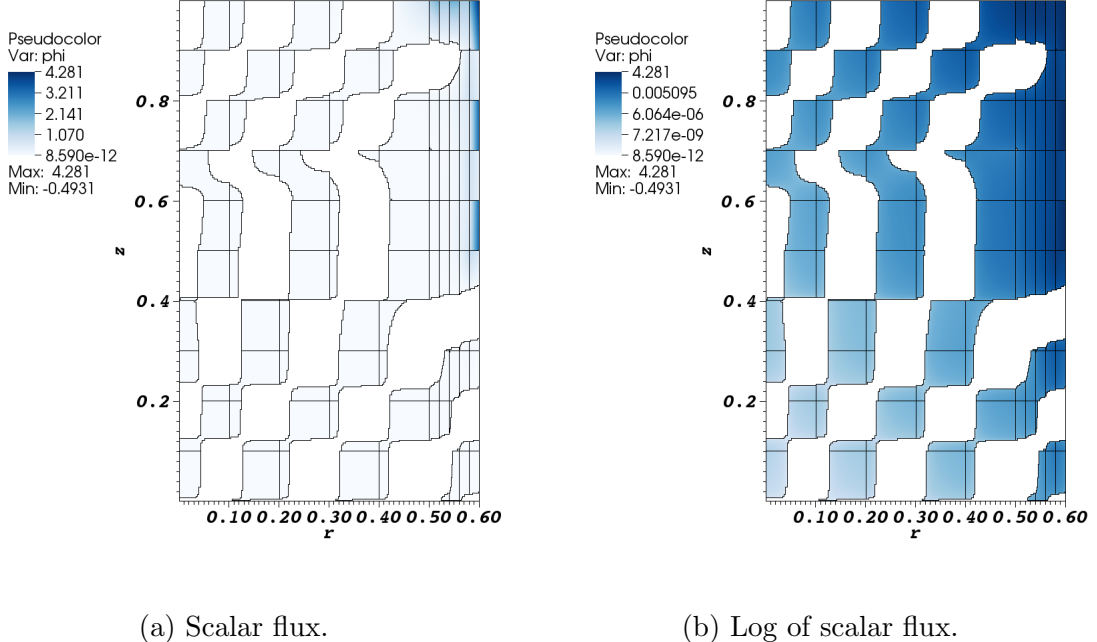


Figure 73: Solution to strong scatter with discontinuous boundary conditions with $p = 1$ finite elements and S_4 level-symmetric angular quadrature. White regions indicate negative scalar fluxes.

elements. This solution is shown in Figure 74. We observe oscillations in the scalar flux that results in negative solutions. These are predominantly in the boundary layer regions near the upper right and lower left. The solution changes about 20 orders of magnitude.

Comparing Figures 73 and 74, we observe that the areas of negative solution in the problem interior is suppressed with the use of higher-order finite elements. We also observe that the higher-order FEM modeled a steeper gradient in the solution. The HO solution drove an additional 8 orders of magnitude further than the LO solution. While refining the mesh may help the LO method to model the steep gradient, the HO method was able to do so.

We also solve this problem on a 2nd-order curved mesh. We distort the original mesh by translating the vertices and reconnecting them with 2nd-order polynomials.

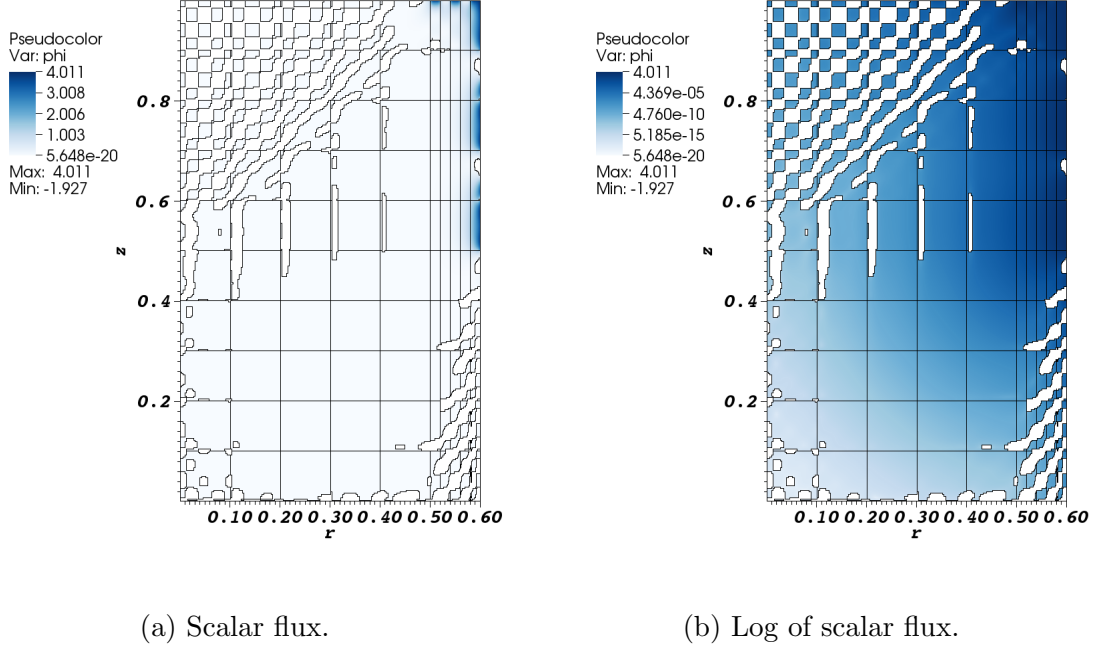


Figure 74: Solution to strong scatter with discontinuous boundary conditions with $p = 4$ finite elements and S_8 level-symmetric angular quadrature. White regions indicate negative scalar fluxes.

We solved using 4th-order finite elements and S_{12} level-symmetric angular quadrature. This solution is shown in Figure 75. We observe similar behavior as Figure 74, indicating that the curved surfaces may not introduce additional errors. Specifically, there are boundary layers that penetrate into the problem interior in the upper-left and bottom-right regions, as well as the slight negativities in the interior near $z = 0.5$. From the mesh distortion, some of the zones become larger, resulting in the appearance of larger areas of negative solutions. The reverse is true for zones that became smaller.

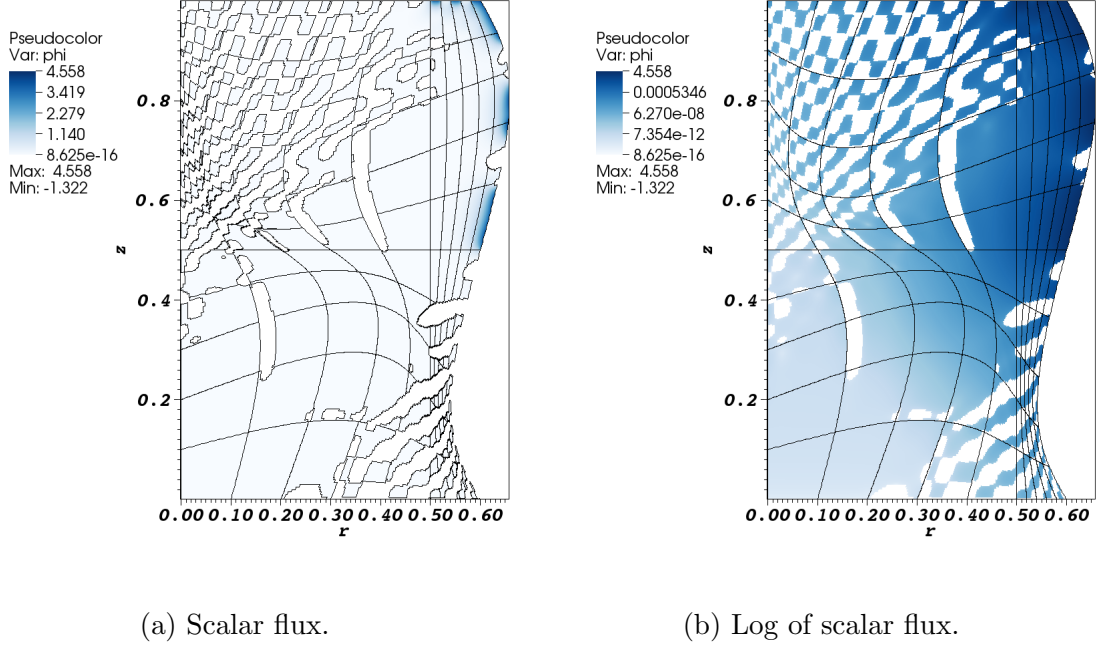


Figure 75: Solution to strong scatter with discontinuous boundary conditions with $p = 4$ finite elements and S_{12} level-symmetric angular quadrature on a 2nd-order mesh. White regions indicate negative scalar fluxes.

3.2.6 Material Discontinuity Stress Test

We adapted this problem from Palmer [52] and solved it in X - Y without DSA in Woods et al. [26]. Presently, we solve this in R - Z geometry. There are five different material regions described in Table 3 and Figure 76.

Table 3: Material discontinuity stress test with MIP DSA material properties.

Material Region	$\sigma_t \text{ cm}^{-1}$	$\sigma_s \text{ cm}^{-1}$	$S_0 \text{ cm}^{-2} \text{ s}^{-1}$
Source	1.0	1.0	1.0
Very thin absorber	0.0001	0.0	0.0
Thick absorber	10.0	0.0	0.0
Very thick absorber	100.0	0.0	0.0
Very thick scatterer	1000.0	1000.0	0.0

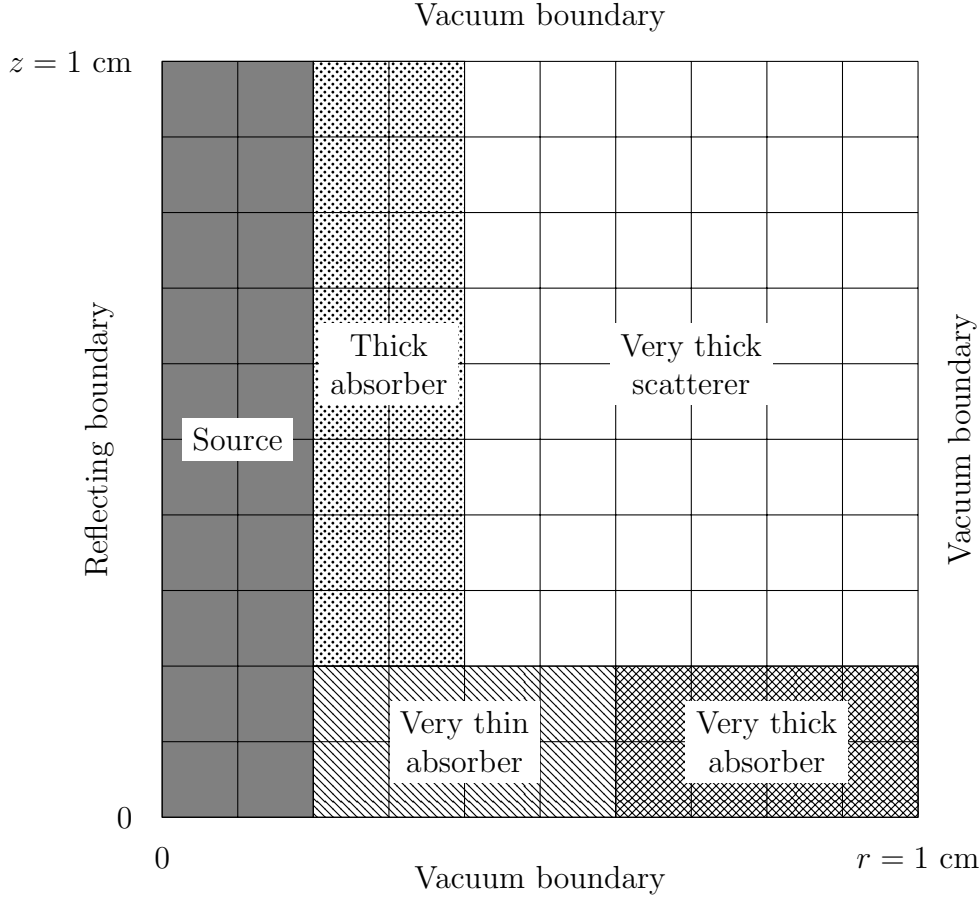


Figure 76: Material discontinuity stress test with MIP DSA problem geometry; materials defined in Table 3.

This problem has cross sections that range several orders of magnitude, resulting in strong material discontinuities. We also introduce anisotropic incident angular fluxes into the scattering region by preferentially attenuating angular fluxes that are not perpendicular to the thick absorber. We expect some degradation in the DSA in problems with strong material discontinuities [25]. We also expect boundary layers to form from the anisotropic incident angular fluxes [48]. We solve this using 2nd-order finite elements, S_4 level-symmetric angular quadrature, and unaccelerated SI. The scalar flux solution is shown in Figure 77a and the log of the scalar flux is shown in

Figure 77b. The white regions are negative fluxes that were removed. We observe a relatively smooth solution throughout most of the problem. There are oscillations (and negativities) in the “Very thick absorber” region where the problem is very optically thick. There are very slight numerical artifacts inside the scattering region near the boundary of the “Very thin absorber” region.

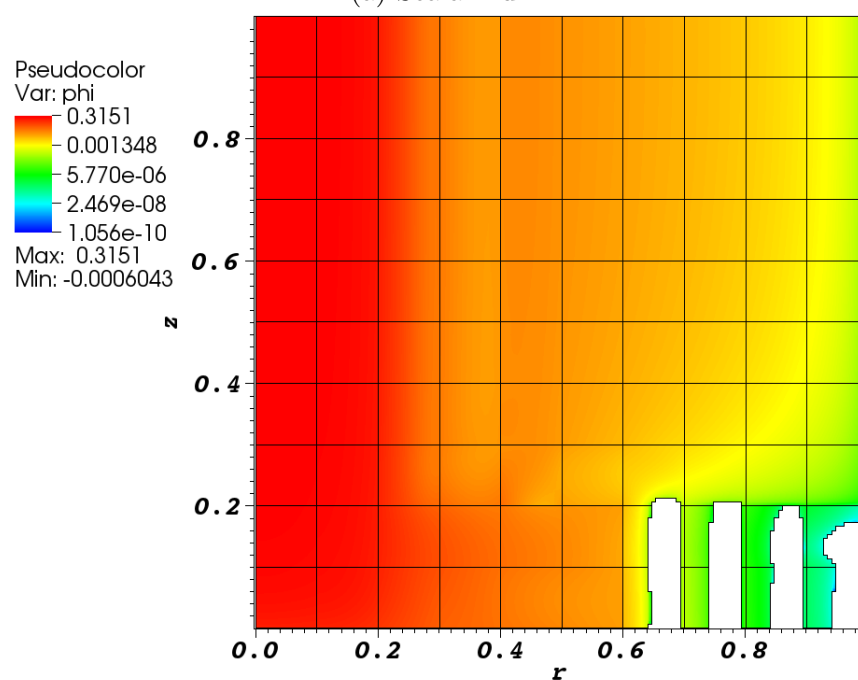
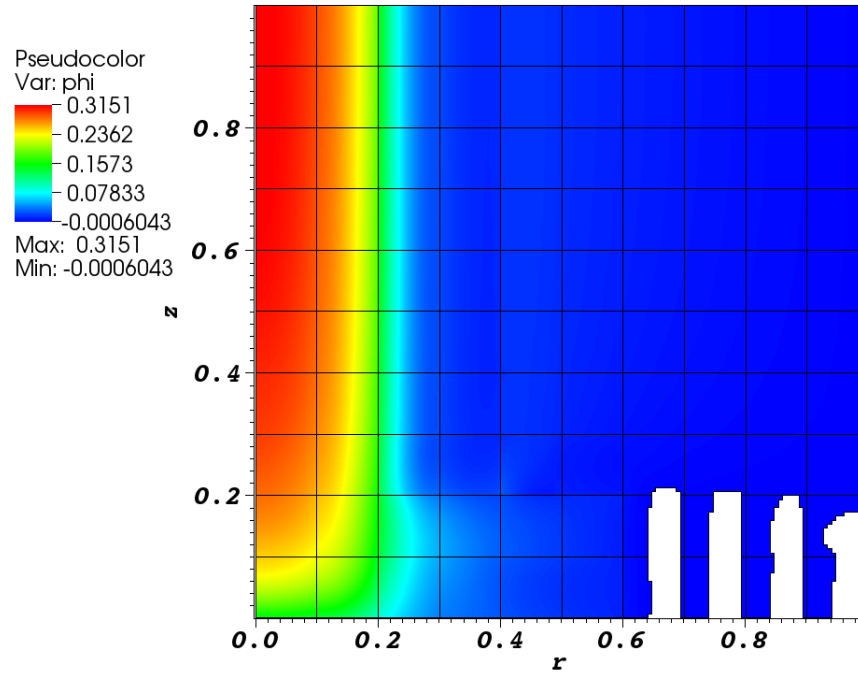


Figure 77: Solution to multi-material stress test. White regions indicate negative scalar fluxes.

3.3 Modified Interior Penalty Diffusion Synthetic Acceleration

In this section, we perform studies of the methodology presented above. This section is divided into two parts: in Section 3.3.1, we discuss results using the MIP DSA equations with homogeneous Dirichlet boundary conditions, and, in Section 3.3.2, we discuss results using the MIP DSA equations with homogeneous Robin boundary conditions. With each of these sections, we perform sensitivity analyses of the spectral radius.

3.3.1 MIP DSA with Homogeneous Dirichlet Boundary Conditions

This section shows the results from the MIP DSA method with homogeneous Dirichlet boundary conditions implementation from Section 2.5. We study the sensitivity of the spectral radius to the constant C in Section 3.3.1.1 and to the scattering ratio c in Section 3.3.1.2.

3.3.1.1 Spectral Radius Sensitivity to Constant C

Previous researchers used values for C arbitrarily. Wang and Ragusa [22] used $C = 2$ and Turcksin and Ragusa [62] used $C = 4$. Here, we perform a study to assess the sensitivity of the spectral radius to changes in the constant C (see Equation 85) for various cell thicknesses and finite element orders.

These test problems are the same as the ones used by Wang and Ragusa [22] so that we can compare our results against theirs. These problems have homogeneous materials with vacuum boundaries, have a scattering ratio $c = 0.9999$, and an isotropic volumetric source $S_0 = 1 \text{ cm}^{-3} \text{ s}^{-1}$. The mesh is a 10 cm by 10 cm quadrilateral grid uniformly divided into 100 zones, and we use S_8 level symmetric angular quadrature.

The total cross section σ_t is chosen at run-time for the appropriate optical thickness. For cell thicknesses less than 1 mfp, σ_t is set to 1 cm^{-1} and the mesh is incrementally refined to make each zone less optically thick. Each data point on the following plots represents the spectral radius of an individual solution to a homogeneous problem with a particular σ_t .

Figure 78 shows the spectral radii of various finite element orders on an orthogonal mesh for $C = 2$. Each data point represents the spectral radius for a unique problem

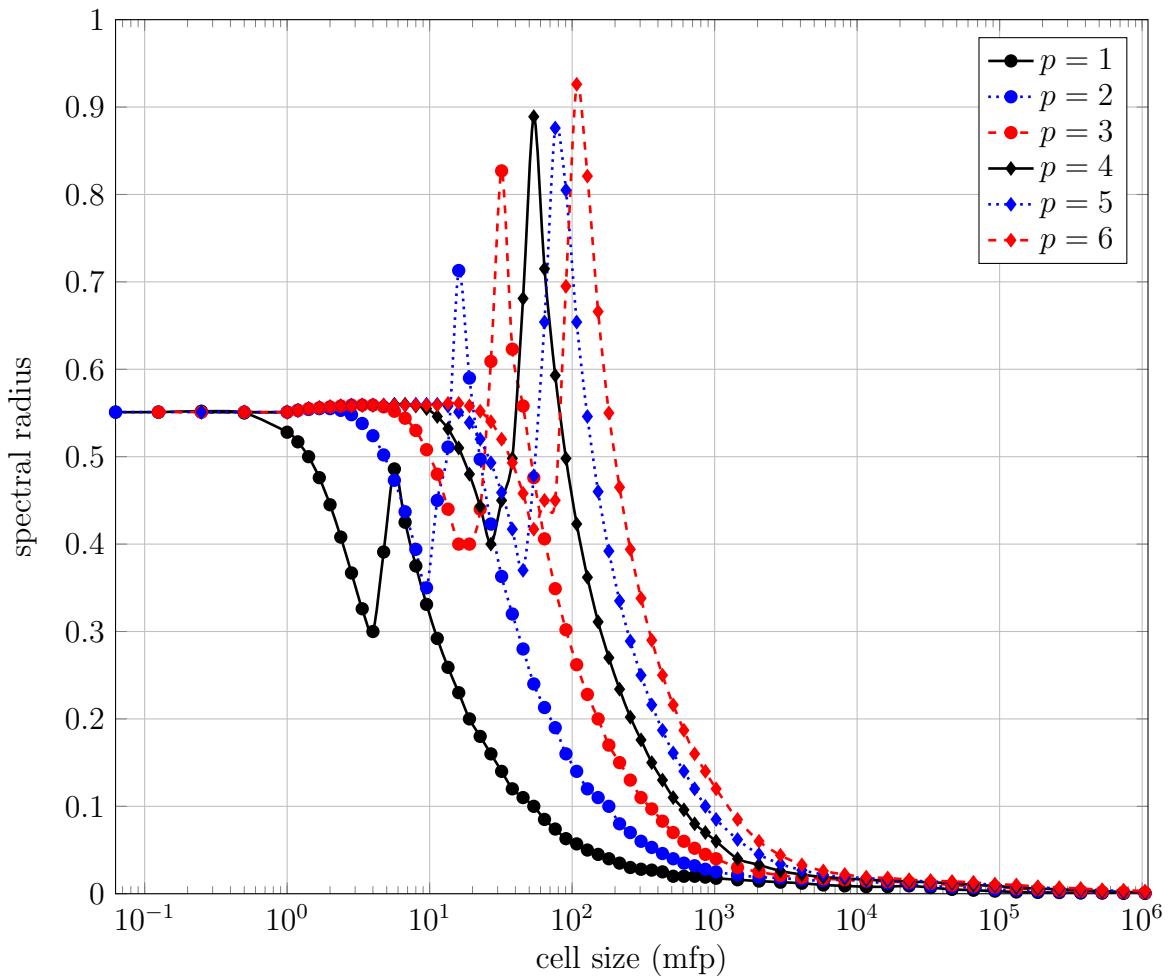


Figure 78: Spectral radius data for varying p with $C = 2$ on an orthogonal mesh with homogeneous Dirichlet boundary conditions in the DSA solve; plot reproduced from Woods et al. [2].

with constant material properties. We observe peaks approaching $\rho = 0.9$, where the method performs the “switch”. The IP method works well in the optically thin region (smaller cell sizes) and the DCF method works well in the intermediate and optically thick regions (larger cell sizes). There is little sensitivity of finite element order in the very optically thin and optically thick regions. However, the intermediate optical thickness range has a strong dependence on the choice of the finite element order. In this range, the spectral radius is generally smaller for lower finite element orders.

This result for $p = 1$ is the same as results for $p = 1$ from Wang and Ragusa [22]. However, the higher-order solutions begin to diverge from [22], likely as a result of using a different mesh. This work uses a quadrilateral mesh rather than a triangular mesh, as Wang and Ragusa [22] used. The effect of using a triangular mesh is that h_{\perp}^{\pm} is smaller, increasing κ_e^{IP} in Equation 84. This impact is similar to increasing the value of the constant C . Higher-order finite elements for larger choices of C do behave like the higher-order results of Wang and Ragusa [22].

Figure 79 shows the spectral radius of various finite element orders on an orthogonal mesh for $C = 4$. We observe that the peaks from Figure 78 are significantly diminished. The value of C moved the “switch” toward the optically thick region, thereby not requiring the DCF method to operate in the optically thin regime. The larger value of C also impacts the IP method spectral radius, resulting in a slight rise (of nearly 0.1 for higher finite element orders) before the switch to the DCF method. Again, there is little sensitivity of finite element order in the very optically thin and optically thick regions. Still, the intermediate optical thickness range has a strong dependence on the choice of the finite element order. In this range, the spectral radius is generally smaller for lower finite element orders.

These results are very similar to those reported by Wang and Ragusa [22]. This work uses a quadrilateral mesh rather than a triangular mesh, as Wang and Ra-

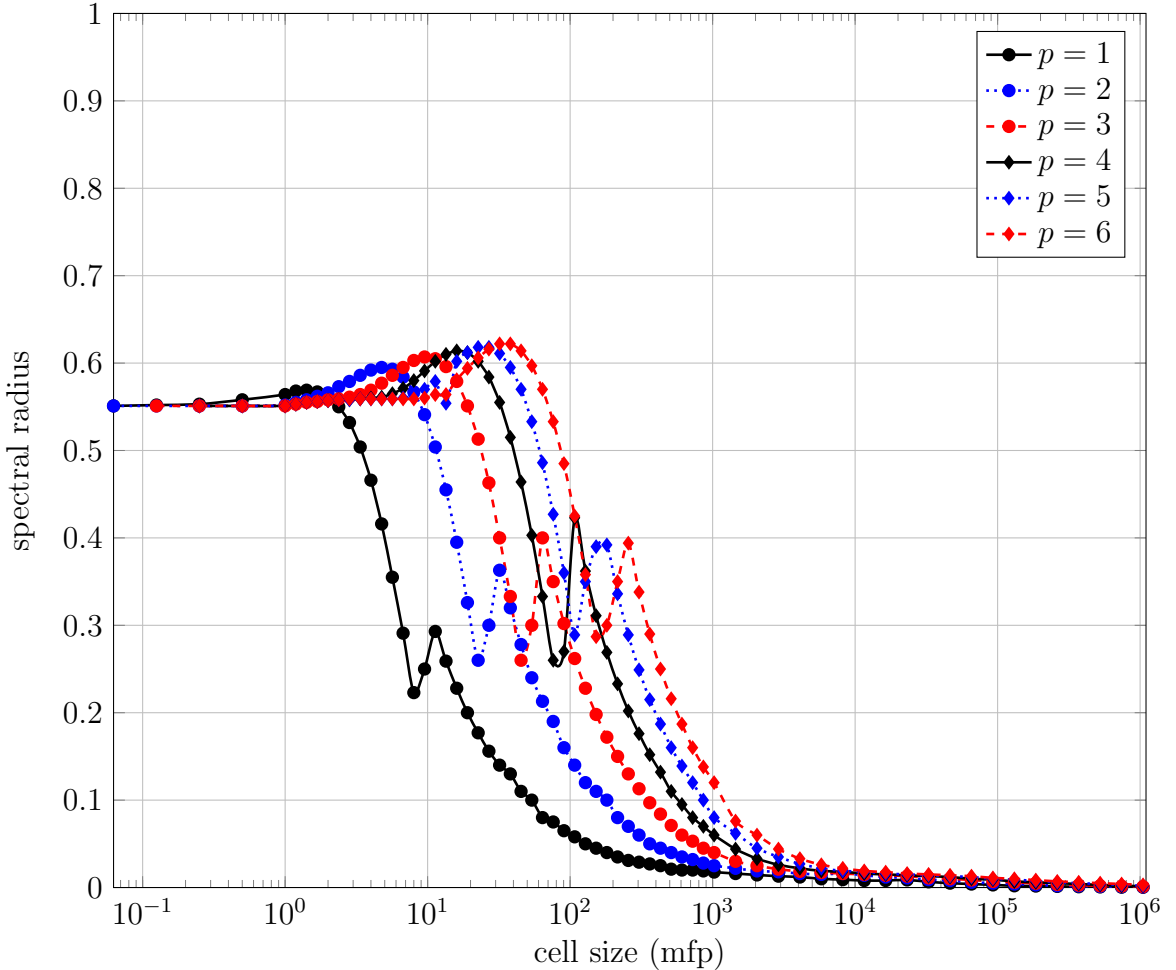


Figure 79: Spectral radius data for varying p with $C = 4$ on an orthogonal mesh with homogeneous Dirichlet boundary conditions in the DSA solve; plot reproduced from Woods et al. [2].

gusa [22] used. The effect of using a triangular mesh is that h_{\perp}^{\pm} is smaller, increasing κ_e^{IP} in Equation 84. This impact is similar to increasing the value of the constant C . Higher-order finite elements for larger choices of C do behave like the higher-order results of Wang and Ragusa [22].

Figure 80 shows the spectral radius of various finite element orders on an orthogonal mesh for $C = 6$. We observe that the peaks from Figure 78 remain significantly diminished like with $C = 4$. The value of C moved the “switch” further toward the

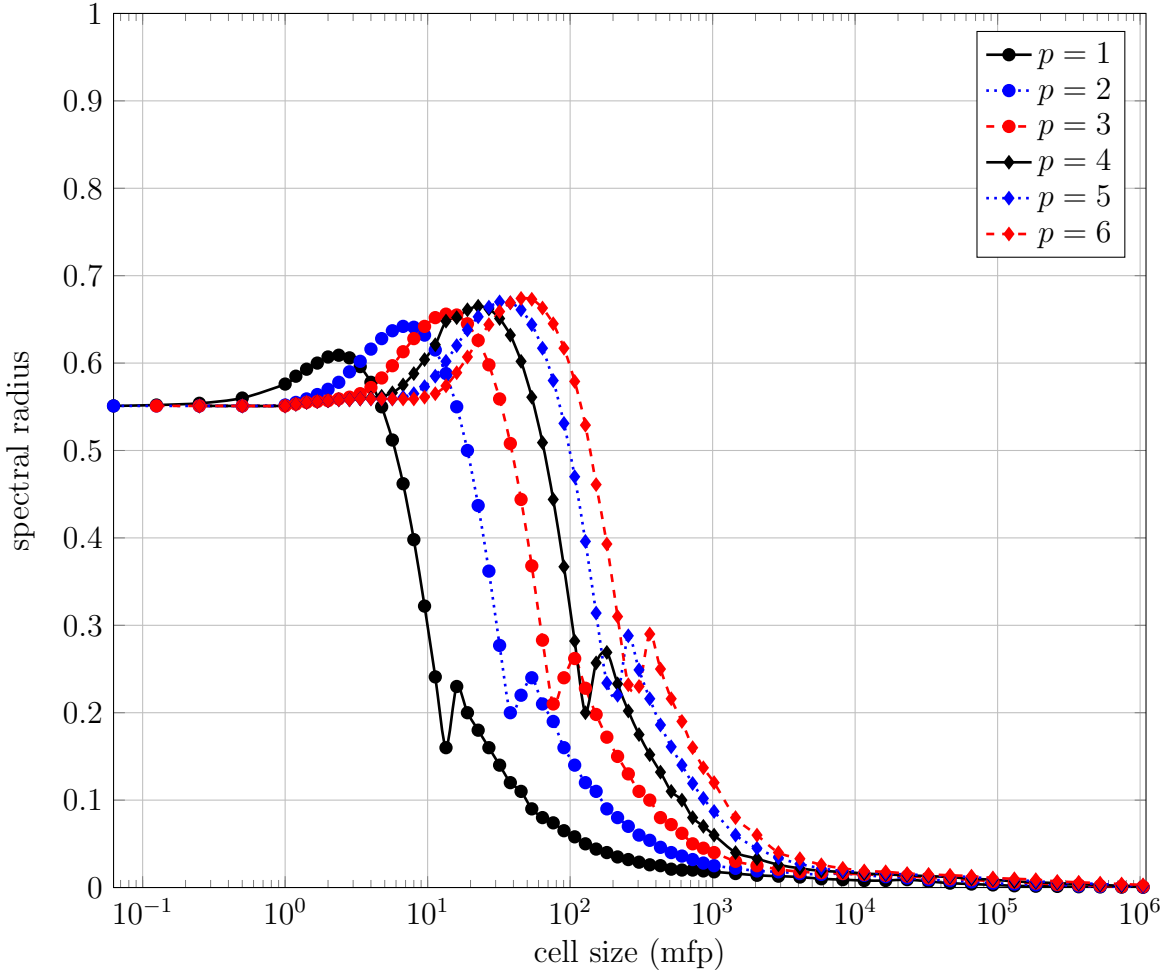


Figure 80: Spectral radius data for varying p with $C = 6$ on an orthogonal mesh with homogeneous Dirichlet boundary conditions in the DSA solve; plot reproduced from Woods et al. [2].

optically thick region, thereby requiring the DCF method to operate even less in the optically thin regime. The larger value of C impacts the IP method spectral radius again, resulting in a slight rise of over 0.1 (for higher finite element orders) before the switch to the DCF method. Again, there is little sensitivity of finite element order in the very optically thin and optically thick regions. Still, the intermediate optical thickness range has a strong dependence on the choice of the finite element order. In this range, the spectral radius is generally smaller for lower finite element orders.

These results are very similar to those reported by Wang and Ragusa [22]. This work uses a quadrilateral mesh rather than a triangular mesh, as Wang and Ragusa [22] used. The effect of using a triangular mesh is that h_{\perp}^{\pm} is smaller, increasing κ_e^{IP} in Equation 84. This impact is similar to increasing the value of the constant C . Higher-order finite elements for larger choices of C do behave like the higher-order results of Wang and Ragusa [22].

In all cases $C = \{2, 4, 6\}$, the spectral radius was less than one, indicating these methods are unconditionally converging. We observed that larger values of C reduce the spectral radius in the intermediate range by mitigating the observable peaks. However, the larger C values increased the spectral radius toward the optically thin region by introducing a “hump”. Assuming that the optical thickness, diffusion coefficient D^{\pm} , the mesh size h^{\pm} , and finite element order p^{\pm} are all problem dependent, only the value of C remains user defined. Knowing the problem specifications *a priori* may inform a particular choice of C .

3.3.1.2 Sensitivity of the Spectral Radius to the Scattering Ratio c

The problems here have the same cross sections and source as Section 3.3.1.1 but 1 cm by 1 cm grid uniformly divided into 100 zones. (An orthogonal grid would have 0.1 cm by 0.1 cm zoning.) Figure 81 shows the spectral radii for varying the scattering ratios using 4th-order finite elements and $C = 4$ on an orthogonal mesh. Figure 82 shows the same results on a 3rd-order mesh. Increasing the scattering ratio increased the spectral radius, approaching an apparent limit. Adding curvature to the mesh surfaces also increased the spectral radius. Although the spectral radius is higher, the jump when the “switch” occurs is not as significant on the 3rd-order mesh as it is with the orthogonal grid.

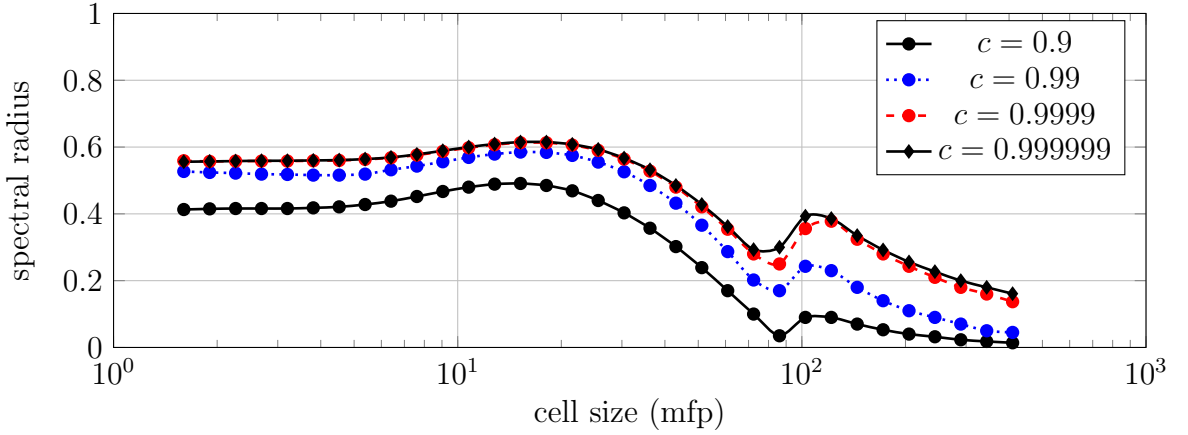


Figure 81: Spectral radius data for various scattering ratios c using 4th-order finite elements, constant $C = 4$, and orthogonal mesh.

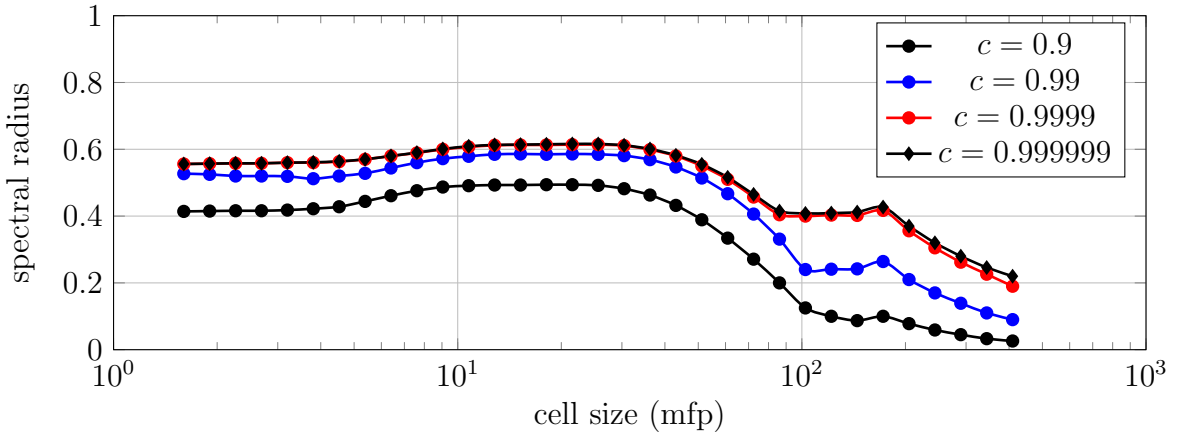


Figure 82: Spectral radius data for various scattering ratios c using 4th-order finite elements, constant $C = 4$, and 3rd-order mesh.

3.3.1.3 Infinite Medium MIP DSA Results

It is possible that the previous finite domain problems did not excite all of the error modes. Here, we test a uniform grid with periodic boundaries on all four sides of the problem. We performed some of the same calculations as in the previous subsection. Figures 83 - 85 show the results for $C = 2$, $C = 4$, and $C = 6$, respectively.

We see the spectral radii in all plots has similar behavior as in the finite domain plots. However, the magnitudes are lower in general and the peaks are almost nonex-

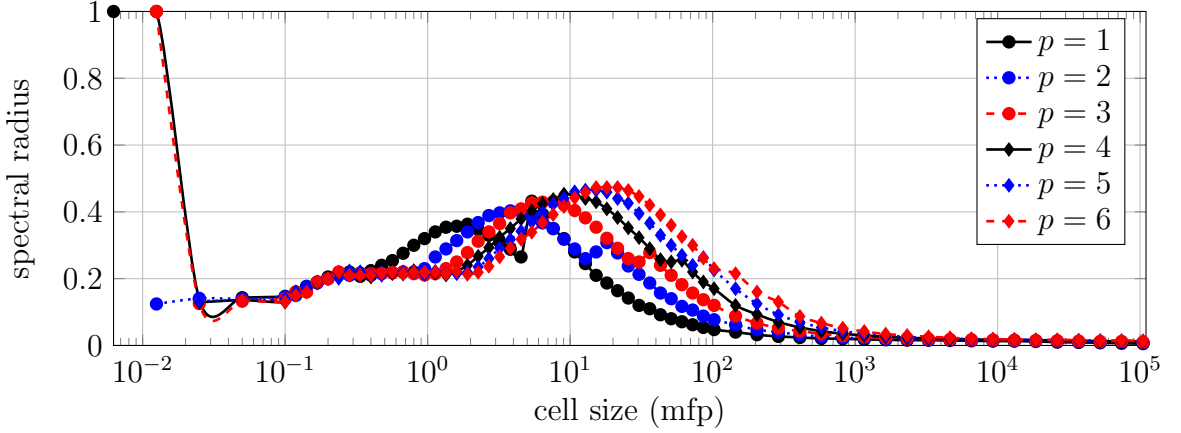


Figure 83: Spectral radius data for varying p with $C = 2$ on a periodic orthogonal mesh.

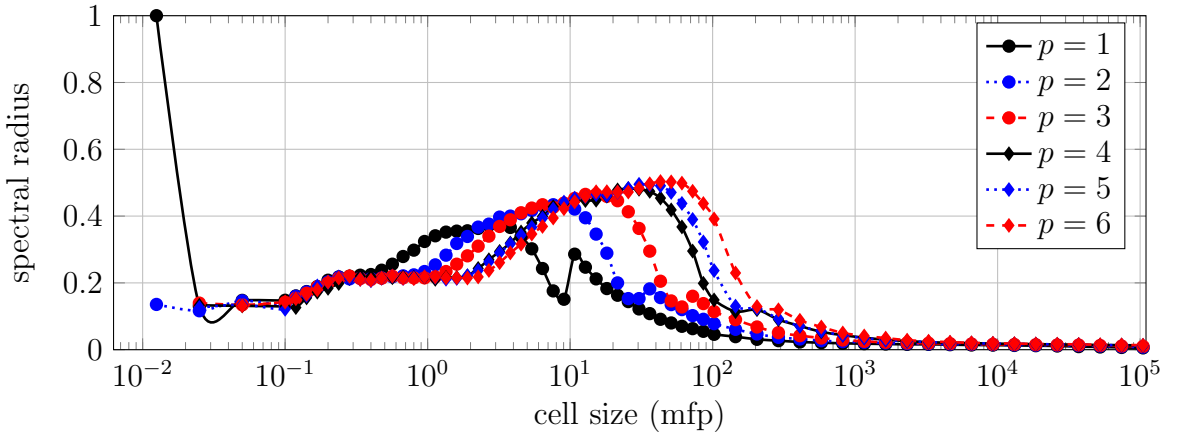


Figure 84: Spectral radius data for varying p with $C = 4$ on a periodic orthogonal mesh.

istent at the “switch”. Notably, $p = 1$ has the largest peak. The Fourier analysis performed by Wang and Ragusa [22] spans 10^{-3} to 10^3 mfps with smooth behavior at either of the ends. Numerically, we observe the smooth behavior for thicker cells but the optically thin cells do not behave as well. In some instances, the spectral radius is erratic and does not converge. These erratic spectral radii are given the value of 1 in Figures 83 - 85. Without DSA, these thin problems converge very quickly. The observed instability occurs outside the range of the results published by Wang and

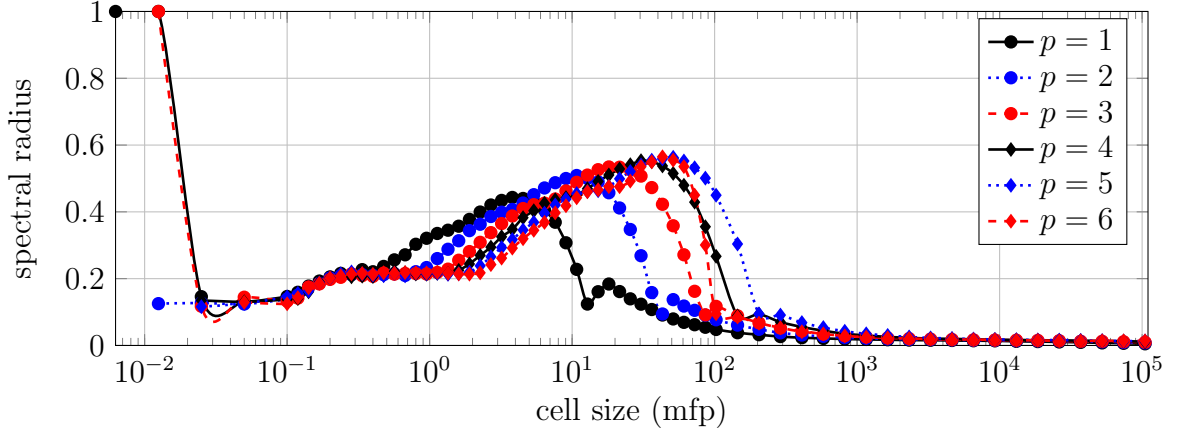


Figure 85: Spectral radius data for varying p with $C = 6$ on a periodic orthogonal mesh.

Ragusa. We speculate on possible explanations for these instabilities: the MIP DSA equations are only partially consistent and could benefit from being wrapped in a Krylov solver [61], or the DSA equation is under-performing due to inaccuracies from trying to solve in the optically thin regime.

3.3.2 MIP DSA with Homogeneous Robin Boundary Conditions

This section shows the results from the MIP DSA method with homogeneous Robin boundary conditions implementation from Section 2.6. We first check the accuracy of the Robin boundary condition implementation in Section 3.3.2.1. We study the sensitivity of the spectral radius to the constant C in Section 3.3.2.2.

3.3.2.1 Accuracy

An analytic one-dimensional diffusion equation solution with zero incident current boundary conditions was used to benchmark the solution to the diffusion equation using the proposed Robin boundary condition methods. The original MIP DSA method (Equation 79a) was also solved for comparison. The analytic solution to the 1-D dif-

fusion equation with homogeneous Robin boundary conditions is

$$\phi(x) = c_1 e^{x/L} + c_2 e^{-x/L} + \frac{S_0}{\sigma_a}, \quad (136a)$$

$$c_1 = \frac{1}{4} \frac{S_0}{\sigma_a} \left[\left(\frac{1}{4} + \frac{1}{2} \frac{D}{L} \right) e^{1/L} - \left(\frac{1}{4} - \frac{1}{2} \frac{D}{L} \right) \right] \cdot \left[\left(\frac{1}{4} - \frac{1}{2} \frac{D}{L} \right)^2 - \left(\frac{1}{4} + \frac{1}{2} \frac{D}{L} \right)^2 e^{2/L} \right]^{-1}, \quad (136b)$$

$$c_2 = \left[-c_1 \left(\frac{1}{4} + \frac{1}{2} \frac{D}{L} \right) e^{1/L} - \frac{1}{4} \frac{S_0}{\sigma_a} \right] e^{1/L} \left(\frac{1}{4} - \frac{1}{2} \frac{D}{L} \right)^{-1}, \quad (136c)$$

where $L^2 = D/\sigma_a$.

Table 9 shows the errors between the DGFEM solution and the analytic diffusion equation for various cell sizes. For all cell sizes, the Robin boundary condition

Table 4: L_2 norm of the errors between the diffusion equation using the given boundary condition method and the reference solution (1-D analytic solution) using 3rd-order elements, $C = 4$, on an orthogonal mesh with 2304 zones.

ε	Robin BC	Dirichlet BC
10	4.05×10^{-11}	0.722
1	2.03×10^{-10}	0.363
0.1	3.39×10^{-10}	0.0607
0.01	3.63×10^{-10}	0.00650
1×10^{-3}	3.66×10^{-10}	6.55×10^{-4}
1×10^{-4}	3.66×10^{-10}	6.56×10^{-5}
1×10^{-5}	3.67×10^{-10}	6.54×10^{-6}
1×10^{-6}	4.08×10^{-10}	3.91×10^{-7}

method achieves errors on the order of 10^{-10} or better. This helps confirm the correct implementation of the vacuum boundary conditions on the DSA equation. We also

notice that as $\varepsilon \rightarrow 0$, we have $D = \varepsilon/(3\sigma_t) \rightarrow 0$, and

$$\left[(\kappa_e \varphi, v)_{\partial D^b} - \frac{1}{2} (\varphi, D\partial_n v)_{\partial D^b} - \frac{1}{2} (D\partial_n \varphi, v)_{\partial D^b} \right] \rightarrow (\kappa_e \varphi, v)_{\partial D^b}. \quad (137)$$

Further, we have $\kappa_e^{IP} \rightarrow 0$ and thus, $\kappa_e \rightarrow 1/4$ by Equation 83. So, as the material becomes increasingly optically thick, the homogeneous Dirichlet boundary condition converges to

$$\frac{1}{4} (\varphi, v)_{\partial D^b}, \quad (138)$$

the homogeneous Robin boundary condition implementation.

3.3.2.2 Sensitivity Study of the Spectral Radius

Figure 86 shows the spectral radius of various finite element orders on an orthogonal mesh for $C = 2$ using the homogeneous Robin boundary condition. We observe that the peaks from Figure 78 no longer appear. Thus, it is challenging to determine when the “switch” between the IP and DCF methods occurs. Contrasting the homogeneous Dirichlet boundary condition method, there is very little sensitivity of finite element order in the intermediate optical thickness region. However, we observe slight dependencies of the spectral radius to the finite element order in the optically thin and optically thick regions. Also, contrasting the Dirichlet boundary conditions, the spectral radii in the optically thick region are substantially higher with the Robin boundary conditions.

Figure 87 shows the spectral radius of various finite element orders on an orthogonal mesh for $C = 4$ using the homogeneous Robin boundary condition. Again, we observe that the peaks from Figure 78 no longer appear. Contrasting the homogeneous Dirichlet boundary condition method, there is very little sensitivity of finite element order in the intermediate optical thickness region. However, we observe slight dependencies of the spectral radius to the finite element order in the optically thin

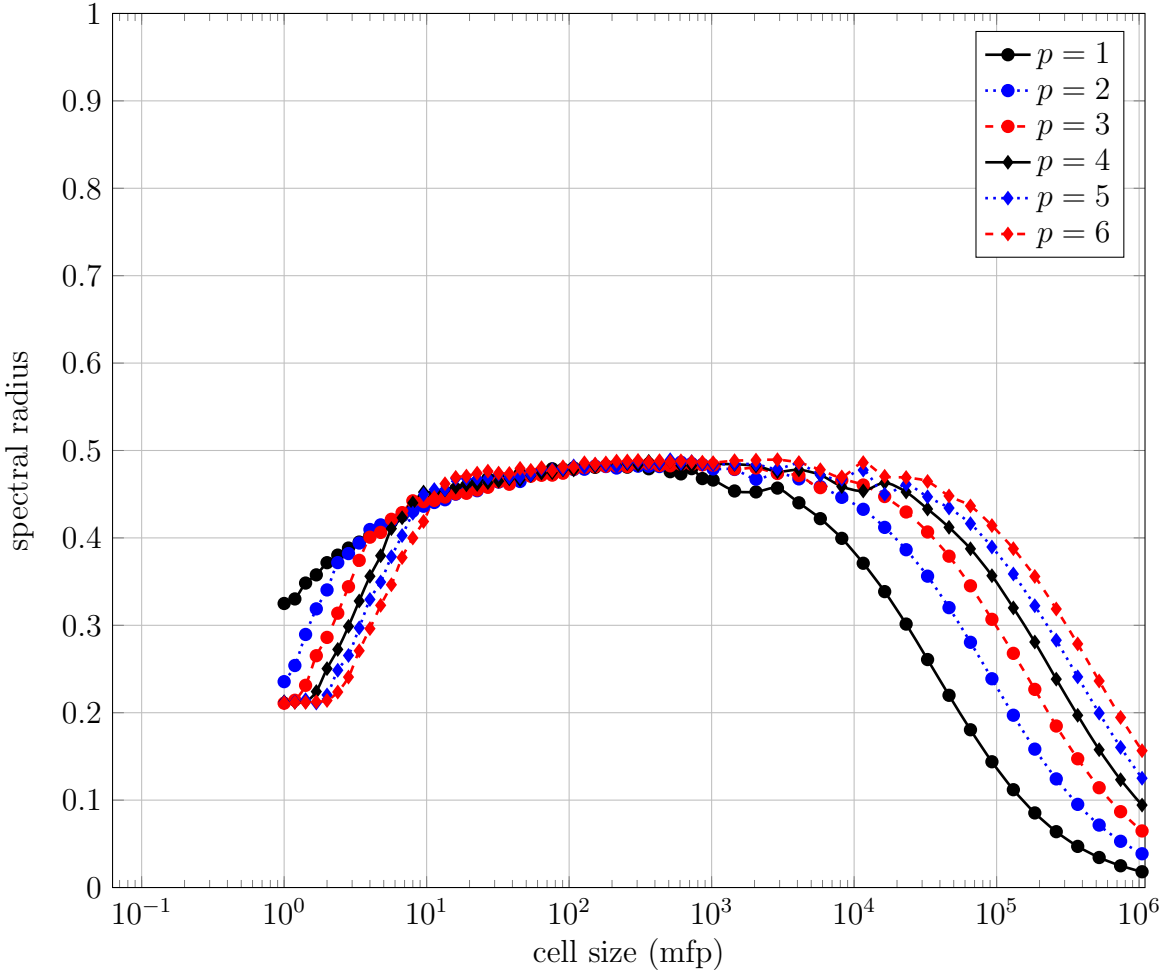


Figure 86: Spectral radius data for varying p with $C = 2$ on an orthogonal mesh using the vacuum boundary MIP DSA method.

and optically thick regions. Also, contrasting the Dirichlet boundary conditions, the spectral radii in the optically thick region are substantially higher with the Robin boundary conditions. The results in Figure 87 are remarkably similar to Figure 86, indicating that the spectral radius is less sensitive to the interior surface terms than the problem boundary conditions.

Figure 88 shows the spectral radius of various finite element orders on an orthogonal mesh for $C = 6$ using the homogeneous Robin boundary condition. Again, we observe that the peaks from Figure 78 no longer appear. However, similar to

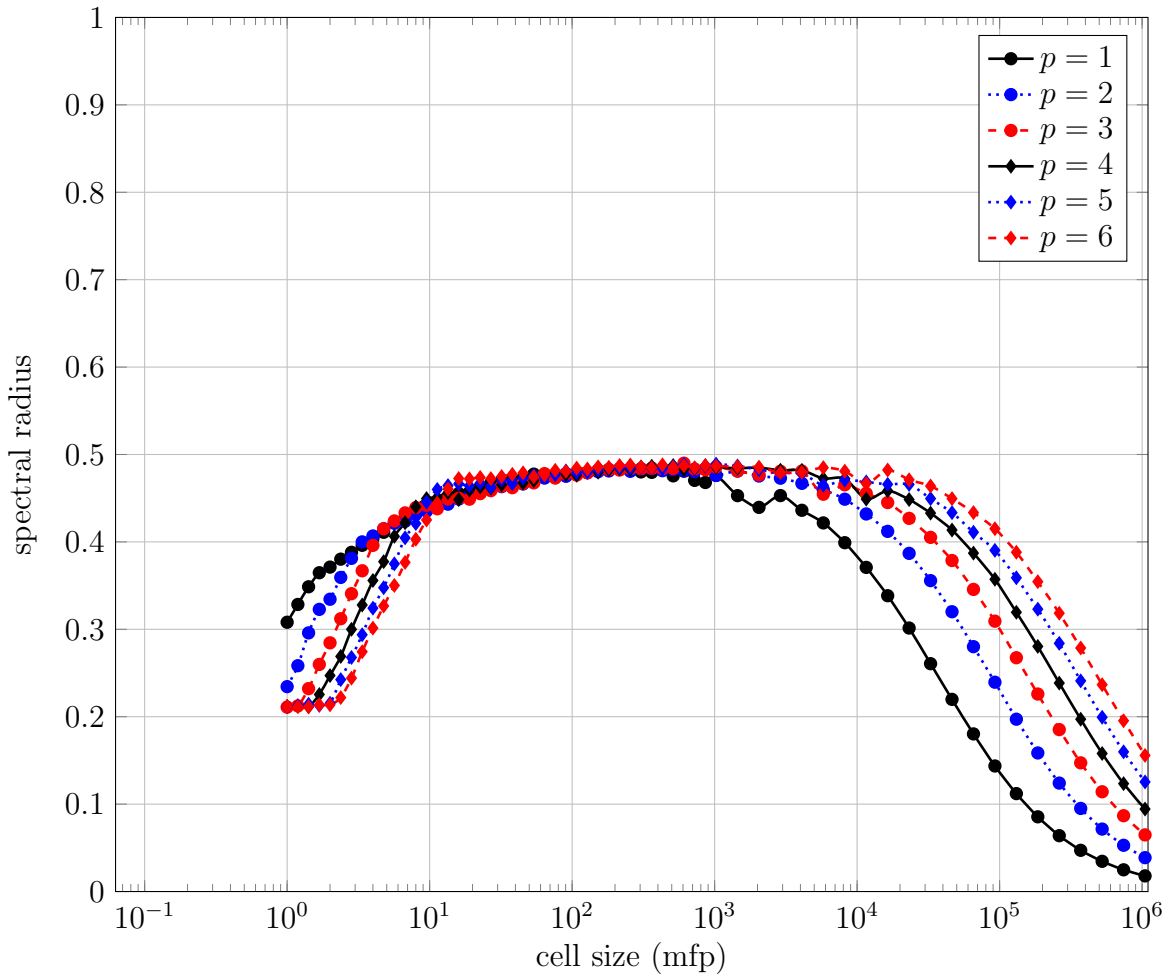


Figure 87: Spectral radius data for varying p with $C = 4$ on an orthogonal mesh using the zero incident current DSA method.

Figure 80, there is a rise in the spectral radius (a “hump”) in nearly the same cell size range. The remainder of the spectral radii profiles are very similar to those of Figures 86 and 87. Since there is no spectral radius improvement in any other cell regimes, this choice for C is undesirable. Again, we observe the spectral radii in the optically thick region are substantially higher with the Robin boundary conditions than with using homogeneous Dirichlet boundary conditions.

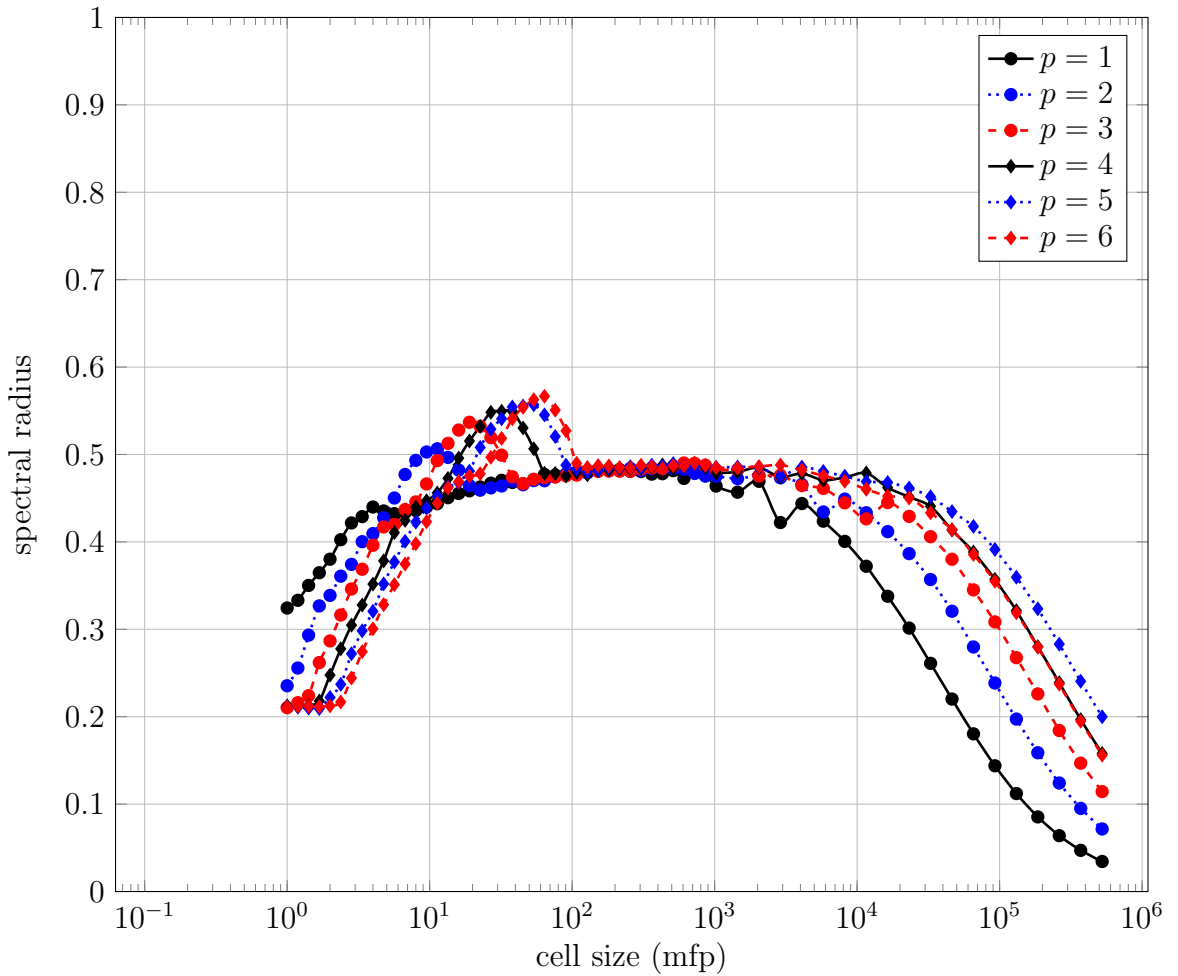


Figure 88: Spectral radius data for varying p with $C = 6$ on an orthogonal mesh using the zero incident current DSA method.

4 Conclusions

In this dissertation, we investigated the effects of surfaces that have incident and outgoing angular fluxes for the same discrete ordinates direction in X - Y geometry. We derived and implemented an R - Z geometry spatial discretization for the high-order (HO) discontinuous finite element method (DFEM). Additionally, we derived and implemented the Robin boundary condition for the modified interior penalty (MIP) diffusion synthetic acceleration (DSA) equations. We discuss the conclusions

for each of the objectives independently in Sections 4.1, 4.2 and 4.3. We note the future work in Section 4.4.

4.1 X-Y Geometry Conclusions

We furthered the research conducted by Woods [27] by investigating the effects of performing numerical integrations on surfaces that have curved surfaces. Specifically, surfaces that are both incident and outgoing for the same discrete ordinates direction. We observed a slight degradation in the spatial convergence rates until the mesh was refined. This effect may be partly due to the spatial discretizations not being resolved ~~enough~~ to be in the asymptotic regime.

We solved an optically thick and diffusive problem with alternating incident boundaries that resulted in oscillations in the boundary layers. On the *highly* curved mesh, these boundary oscillations were propagated far into the problem interior. It becomes increasingly important to employ methods that reduce or eliminate the negative solutions on these meshes.

4.2 R-Z Geometry Conclusions

We discretized the transport equation in *R-Z* geometry and ~~performed~~ several test problems to qualitatively and quantitatively assess the behavior of the high-order finite element spatial discretization method. Instead of ~~performing~~ the spatial discretization on the conservation form of the transport equation, we performed a product rule and ~~pulled a radius variable out of the r -derivative term~~. This ~~allowed us to easily extend~~ a *X-Y* geometry implementation in MFEM to *R-Z* geometry. We discretized the direction of travel using level-symmetric angular quadrature and used the method of Morel and Montry to sweep across each angular quadrature level to

solve for the angular flux at each discrete ordinate. The source iteration method was employed, where we calculated the scalar flux from a weighted sum of the angular fluxes, used that scalar flux in the scattering source, and iterated on the scalar flux until it converges.

The uniform infinite medium problem revealed the need to perform the bilinear and linear form numerical integrations to the same order. We extended the analysis to a spatial convergence study using the method of manufactured solutions. The chosen manufactured solution is smooth everywhere and resulted in the expected $O(p + 1)$ spatial convergence rates, which was expected from other research. Subsequently, we demonstrated that a non-smooth manufactured solution degrades the spatial convergence rate to $O(3/2)$, which does not depend on the finite element order p .

Finally, we performed a study on preserving 1-D spherical symmetry. An ideal method will be able to preserve 1-D spherical symmetry using a R - Z geometry discretization. We solved using the method of manufactured solutions and determined a measure of symmetry. We varied the finite element order, angular quadrature order, spatial refinement level, and mesh order. For a 1st-order mesh, we determined that the angular quadrature order has very little impact on the relative symmetry of the solution. However, the finite element order and mesh refinement had significant impacts on the symmetry preservation. Specifically, increasing the finite element order or refining the mesh increased the solution symmetry.

For a 2nd-order mesh, we determined that the angular quadrature order has very little impact on the relative symmetry of the solution. As with the 1st-order mesh, increasing the finite element order or refining the mesh increased the solution symmetry. At a sufficient mesh refinement, the relative symmetry produces distinct “rays”. The number of these rays increases with the angular quadrature order. However, these rays were drastically damped by increasing the finite element order. However,

Comparing these 2nd-order mesh results to the 1st-order mesh, the only case where the higher-order mesh provided any additional symmetry benefit was for the 1st-order finite element. This is contrary to results seen by Brunner et al. [40]. This may be a result of the other discretization errors dominating the mesh discretization error. From the discussion above, the spatial error may be the dominant error and masking the errors from the other discretizations.

4.3 MIP DSA Conclusions

We characterized the spectral radius for several combinations of the constant C and the finite element order p for variable cell sizes. While we see SI acceleration in all cases, there is not a set of parameters that promote smaller spectral radii in all regimes, but problem constraints may motivate the parameter choice. Each variable, C and p , increased the spectral radius to some degree.

The original discretization with homogeneous Dirichlet boundary conditions was unconditionally convergent in all optical thicknesses for all choices of the constant C . We observed that the spectral radius is moderately dependent upon the scattering ratio, and only slightly dependent upon the curvature of the mesh. Assuming that the materials, mesh, mesh size, and finite element order are problem dependent, the user defined choice of C may be important for efficiently accelerating the SI.

The Robin boundary condition method tremendously reduced the impact of the constant C . This method is also unconditionally stable in all optical thicknesses for all choices of the constant C . We observed a degradation in the convergence rate in optically thick media. We leave that investigation to future work. This Robin boundary condition MIP DSA methodology shows these particular benefits over the homogeneous Dirichlet boundary condition method, and warrants continued investigation.

4.4 Future Work

Negative scalar fluxes, observed in some of the test problems above, are non-physical and must be addressed. Other research has utilized lumping techniques on several of the matrices that constitute the bilinear form (see Section 1.2.3). Alternatively, negative flux fix-up methods could be employed to correct the negativities after solving for the scalar flux. This results in a non-linear system of equations that may be acceptable in more complicated multiphysics applications that are already non-linear.

The results presented above studied the effects of the numerical integration order for the surface integrals. However, integrating a surface that has a discontinuous first-derivative with a polynomial approximation may not be the most effective method and other integration schemes should be considered. It may be possible that the spatial error may be small enough to reveal errors due to the integration method. It would be prudent to employ an efficient and effective method of reducing the surface integration error if it were to become dominant.

Future work could implement the numerical solution to the conservative form of the radiation transport equation in R - Z geometry. Although it is analytically conservative, it is possible that the present discretization scheme is not conservative. The general finite element library would need to be modified to implement the derivative with respect to r of $rb_j(\mathbf{x})$.

Future work should also include a Fourier analysis of the implemented vacuum boundary condition MIP DSA method. Also, a wider range of problems including heterogeneous media should be considered. To avoid a substantial degradation in effectiveness, this requires the technique of preconditioning a Krylov method with the DSA operator [61]. Wang and Ragusa [22] observed this degradation of effectiveness but MIP DSA has yet to be used as a preconditioner to a Krylov method.

The **results** from the Robin boundary condition MIP DSA method were much smoother than with the homogeneous Dirichlet boundary conditions. This made it difficult to determine where the “switch” occurred between the IP and DCF methods. An examination of each method individually through the entire range of cell sizes is prudent.

To efficiently solve for larger problems (i.e., more degrees of freedom), it is essential to investigate methods for solving the system of equations. Currently we simultaneously solve for every degree of freedom in the problem. This limits the overall number of unknowns that we can accommodate because they all get stored in memory. However, if we solved individual mesh cells and systematically “swept through the mesh” (solve the sparse system of equations for each quadrature direction, in parallel or sequentially), we eliminate this limitation. This research will require allowing for cycles in the mesh, which will require careful handling.

References

- [1] E. E. Lewis and W. F. Miller, Jr. *Computational Methods of Neutron Transport*. American Nuclear Society, 1993.
- [2] Douglas N. Woods and Todd S. Palmer. Diffusion synthetic acceleration for high order S_N transport on meshes with curved surfaces. *Transactions of the American Nuclear Society*, (116):639–642, 2017.
- [3] James J. Duderstadt and Louis J. Hamilton. *Nuclear Reactor Analysis*. Wiley-Interscience, 1976.
- [4] Peter A. Sandwall, Yuntao Feng, Michael Platt, Michael Lamba, and Sudha Mahalingam. Evolution of brachytherapy treatment planning to deterministic radiation transport for calculation of cardiac dose. *Medical Dosimetry*, 43(2):150–158, 2018.
- [5] John Castor. *Radiation Hydrodynamics*. Cambridge, 2007.
- [6] R. Paul Drake. High-energy-density physics. *Physics Today*, 63(3):8–9, June 2010.
- [7] Veselin A. Dobrev, Tzanio V. Kolev, and Robert N. Rieben. High-order curvilinear finite element methods for Lagrangian hydrodynamics. *SIAM Journal of Scientific Computing*, 34(5):B606 – B641, 2012.
- [8] V. A. Dobrev, T. E. Ellis, Tz. V. Kolev, and R. N. Rieben. Curvilinear finite elements for lagrangian hydrodynamics. *International Journal for Numerical Methods in Fluids*, 2010.
- [9] MFEM: Modular finite element methods. mfem.org, 2015.
- [10] K. D. Lathrop and B. G. Carlson. Discrete ordinates angular quadrature of the neutron transport equation. Technical report, Los Alamos Scientific Laboratory of the University of California, 1965.
- [11] Peter J. Spence. The generation of arbitrary order, non-classical, Gauss-type quadrature for transport applications. *Journal of Computational Physics*, 296:25–27, 2015.
- [12] Marvin L. Adams, Todd A. Wareing, and Wallace F. Walters. Characteristic methods in thick diffusive problems. *Nuclear Science and Engineering*, 130:18–46, 1998.

- [13] W. H. Reed and T. R. Hill. Triangular mesh methods for the neutron transport equation. Technical Report LA-UR-73-479, Los Alamos National Laboratory, 1973.
- [14] Edward W. Larsen and J. E. Morel. Asymptotic solutions of numerical transport problems in optically thick, diffusive regimes II. *Journal of Computational Physics*, 83:212–236, 1989.
- [15] P. Lasaint and P. A. Raviart. On a finite element method for solving the neutron transport equation. In Carl de Boor, editor, *Mathematical Aspects of Finite Elements in Partial Differential Equations*, pages 89–123. Academic Press, 1974.
- [16] Edward W. Larsen and Warren F. Miller, Jr. Convergence rates of spatial difference equations for the discrete-ordinates neutron transport equations in slab geometry. *Nuclear Science and Engineering*, 1980.
- [17] Steven Hamilton, Michele Benzi, and Jim Warsa. Negative flux fixups in discontinuous finite element S_N transport. *International Conference on Mathematics, Computational Methods & Reactor Physics*, May 2009.
- [18] Marvin L. Adams. Discontinuous finite element transport solutions in thick diffusive problems. *Nuclear Science and Engineering*, 137(3):298–333, 2001.
- [19] Todd A. Wareing, John M. McGhee, and Jim E. Morel. ATTILA: A three-dimensional, unstructured tetrahedral mesh discrete ordinates transport code. *Transactions of the American Nuclear Society*, 75:146–147, 1996.
- [20] J. M. McGhee and T.A. Wareing. *Attila Version 2: User's Manual*. Los Alamos National Laboratory, 2000.
- [21] Teresa S. Bailey, Marvin L. Adams, Jae H. Chang, and James S. Warsa. A piecewise linear discontinuous finite element spatial discretization of the transport equation in 2D cylindrical geometry. *International Conference on Mathematics, Computational Methods & Reactor Physics*, 2009.
- [22] Yaqi Wang and Jean C. Ragusa. Diffusion synthetic acceleration for high-order discontinuous finite element S_N transport schemes and application to locally refined unstructured meshes. *Nuclear Science and Engineering*, 166:145–166, 2010.
- [23] Yaqi Wang and Jean C. Ragusa. A high-order discontinuous Galerkin method for the S_N transport equations on 2D unstructured triangular meshes. *Annals of Nuclear Energy*, 36:931–939, 2009.
- [24] Yaqi Wang and Jean C. Ragusa. On the convergence of DGFEM applied to the discrete ordinates transport equation for structured and unstructured triangular meshes. *Nuclear Science and Engineering*, 163:56–72, 2009.

- [25] Yaqi Wang. *Adaptive Mesh Refinement Solution Techniques for the Multigroup S_N Transport Equation Using a Higher-Order Discontinuous Finite Element Method*. PhD thesis, Texas A&M University, 2009.
- [26] Douglas N. Woods, Thomas A. Brunner, and Todd S. Palmer. High order finite elements S_N transport in X-Y geometry on meshes with curved surfaces. *Transactions of the American Nuclear Society*, 114:377 – 380, June 2016.
- [27] Douglas N. Woods. High order finite elements S_N transport in X-Y geometry on meshes with curved surfaces in the thick diffusion limit. Master's thesis, Oregon State University, February 2016.
- [28] Peter G. Maginot, Jim E. Morel, and Jean C. Ragusa. A non-negative moment-preserving spatial discretization scheme for the linearized Boltzmann transport equation in 1-D and 2-D Cartesian geometries. *Journal of Computational Physics*, 231:6801–6826, 2012.
- [29] Peter G. Maginot, Jean C. Ragusa, and Jim E. Morel. Lumping techniques for DFEM S_N transport in slab geometry. *Nuclear Science and Engineering*, 2015.
- [30] Thomas A. Brunner. Preserving positivity of solutions to the diffusion equation for higher-order finite elements in under resolved regions. In *ANS M&C - Joint International Conference on Mathematics and Computation (M&C), Supercomputing in Nuclear Applications (SNA) and the Monte Carlo (MC) Method*, April 2015.
- [31] Jim E. Morel, Alejandro Gonzales-Aller, and James S. Warsa. A lumped linear-discontinuous spatial discretization scheme for triangular-mesh S_N calculations in r-z geometry. *Nuclear Science and Engineering*, 155:168–178, 2007.
- [32] *Discrete Ordinates Methods with Curved Spatial Grids : an Alternative Method to MOC*, September 2015.
- [33] Sebastian Schunert, Yaqi Wang, Vincent Laboure, Javier Ortensi, and Mark DeHart. Approximate transport sweeps for DFEM on higher order meshes with spatially varying cross sections. *Transactions of the American Nuclear Society*, 117:701–705, 2017.
- [34] Juan Cheng and Chi-Wang Shu. A third order conservative Lagrangian type scheme on curvilinear meshes for the compressible Euler equations. *Communications in Computational Physics*, 4(5):1008–1024, 2008.
- [35] Veselin A. Dobrev, Truman E. Ellis, Tzanio V. Kolev, and Robert N. Rieben. High-order curvilinear finite elements for axisymmetric Lagrangian hydrodynamics. *Computers & Fluids*, 2012.

- [36] J. E. Morel and G. R. Montry. Analysis and elimination of the discrete-ordinates flux dip. *Transport Theory and Statistical Physics*, 13(5):615–633, 1984.
- [37] Teresa Bailey. *A Piecewise Linear Discontinuous Finite Element Method Applied to the RZ and XYZ Transport Equations*. PhD thesis, Texas A&M University, 2008.
- [38] J. E. Morel and J. S. Warsa. A lumped bilinear-discontinuous S_N spatial discretization for R-Z quadrilateral meshes. *Transactions of the American Nuclear Society*, 95:873, 2006.
- [39] Douglas N. Woods and Todd S. Palmer. R-Z geometry discrete ordinates radiation transport using higher-order finite element spatial discretizations on meshes with curved surfaces. *Journal of Computational and Theoretical Transport*, In Review.
- [40] Thomas A. Brunner, Tzanio V. Kolev, and Teresa S. Bailey. Preserving spherical symmetry in axisymmetric coordinates for diffusion problems. *International Conference on Mathematics and Computational Methods Applied to Nuclear Science and Engineering*, 2013.
- [41] F. Chaland and G. Samba. Discrete ordinates method for the transport equation preserving one-dimensional spherical symmetry in two-dimensional cylindrical geometry. *Nuclear Science and Engineering*, 182:417–434, 2016.
- [42] C. Lingus. Analytical test case's for neutron and radiation transport codes. In *Second Conference on Transport Theory*, pages 655–659, Los Alamos, New Mexico, January 1971. United States Atomic Energy Commission - Division of Technical Information.
- [43] Edward W. Larsen, J. E. Morel, and Warren F. Miller, Jr. Asymptotic solutions of numerical transport problems in optically thick, diffusive regimes. *Journal of Computational Physics*, 69:283–324, 1987.
- [44] F. Malvagi and G. C. Pomraning. Initial and boundary conditions for diffusive linear transport problems. *Journal of Mathematical Physics*, 32(3):805–820, 1991.
- [45] Edward W. Larsen. The asymptotic diffusion limit of discretized transport problems. *Nuclear Science and Engineering*, 112:336–346, 1992.
- [46] Christoph Börgers, Edward W. Larsen, and Marvin L. Adams. The asymptotic diffusion limit of a linear discontinuous discretization of a two-dimensional linear transport equation. *Journal of Computational Physics*, 98(2):285–300, 1992.
- [47] Jim E. Morel and James S. Warsa. An S_N spatial discretization scheme for tetrahedral meshes. *Nuclear Science and Engineering*, 151:157–166, 2005.

- [48] Marvin L. Adams. Discontinuous finite-element transport solutions in the thick diffusion limit in Cartesian geometry. *The American Nuclear Society International Topical Meeting*, 1991.
- [49] Todd S. Palmer and Marvin L. Adams. Curvilinear geometry transport discretization in the "thick" diffusion limit. *Proceedings of the International Conference Math. Methods & Supercomputing in Nuc. Appl.*, 1993.
- [50] Hiromi G. Stone and Marvin L. Adams. A piecewise linear finite element basis with application to particle transport. *Nuclear Mathematical and Computational Sciences: A Century in Review, A Century Anew*, 2003.
- [51] T. S. Bailey, J. H. Chang, J. S. Warsa, and M. L. Adams. A piecewise bi-linear discontinuous finite element spatial discretization of the S_N transport equation. *International Conference on Mathematics and Computational Methods Applied to Nuclear Science and Engineering*, 2011.
- [52] Todd S. Palmer. *Curvilinear Geometry Transport Discretization in Thick Diffusive Regions*. PhD thesis, University of Michigan, 1993.
- [53] Jean-Luc Guermond and Guido Kanschat. Asymptotic analysis of upwind discontinuous Galerkin approximation of the radiative transport equation in the diffusion limit. *SIAM Journal of Numerical Analysis*, 48(1):53–78, 2010.
- [54] Terry Haut and Vladimir Tomov. Personal communication, 2018.
- [55] Edward W. Larsen. Unconditionally stable diffusion-synthetic acceleration methods for the slab geometry discrete ordinates equations. part I: Theory. *Nuclear Science and Engineering*, 82(1):47–63, 1982.
- [56] Todd A. Wareing, Edward W. Larsen, and Marvin L. Adams. Diffusion accelerated discontinuous finite element schemes for the S_N equations in slab and X,Y geometries. 1991.
- [57] James S. Warsa, Todd A. Wareing, and Jim E. Morel. Fully consistent diffusion synthetic acceleration of linear discontinuous S_N transport discretizations on unstructured tetrahedral meshes. *Nuclear Science and Engineering*, 141:236–251, 2002.
- [58] Marvin L. Adams and Edward W. Larsen. Fast iterative methods for discrete-ordinates particle transport calculations. *Progress in Nuclear Energy*, 40(1):3–159, 2002.
- [59] Donald R. McCoy and Edward W. Larsen. Unconditionally stable diffusion-synthetic acceleration methods for the slab geometry discrete ordinates equations. part II: Numerical results. *Nuclear Science and Engineering*, 82(1):64–70, 1982.

- [60] Marvin L. Adams and William R. Martin. Diffusion synthetic acceleration of discontinuous finite element transport iterations. *Nuclear Science and Engineering*, 111:145–167, 1992.
- [61] James S. Warsa, Todd A. Wareing, and Jim E. Morel. Krylov iterative methods and the degraded effectiveness of diffusion synthetic acceleration for multidimensional S_N calculations in problems with material discontinuities. *Nuclear Science and Engineering*, 147(3):218–248, 2004.
- [62] Bruno Turcksin and Jean C. Ragusa. Discontinuous diffusion synthetic acceleration for S_N transport on 2D arbitrary polygonal meshes. *Journal of Computational Physics*, 274:356–369, 2014.
- [63] Bruno Turcksin and Jean C. Ragusa. A diffusion synthetic acceleration scheme for rectangular geometries based on bilinear discontinuous finite elements. In *International Conference on Mathematics and Computational Methods, Applied to Nuclear Science and Engineering*. Sun Valley, Idaho, 2013.
- [64] Guido Kanschat. *Discontinuous Galerkin Methods for Viscous Incompressible Flow*. Deutscher Universitäts-Verlag, 2007.
- [65] S. S. Antman, J. E. Marsden, and L. Sirovich, editors. *Theory and Practice of Finite Elements*, volume 159. Springer-Verlag, 2004.
- [66] Milton Abramowitz and Irene A. Stegun. *Handbook of Mathematical Functions with Formulas, Graphs, and Mathematical Tables*. Applied mathematics series (Washington, D.C.) ; 55. U.S. Dept. of Commerce : U.S. G.P.O., Washington, D.C., 10th print., with corrections. edition, 1972.
- [67] Shawn D. Pautz. An algorithm for parallel S_n sweeps on unstructured meshes. *Nuclear Science and Engineering*, 140:111–136, 2002.
- [68] Todd A. Wareing, John M. McGhee, Jim E. Morel, and Shawn D. Pautz. Discontinuous finite element S_N methods on three-dimensional unstructured grids. *Nuclear Science and Engineering*, 138:256–268, 2001.
- [69] Timothy A. Davis. *Direct Methods for Sparse Linear Systems*. Society for Industrial and Applied Mathematics, 2006.
- [70] Timothy A. Davis. Algorithm 832: Umfpack v4.3 — an unsymmetric-pattern multifrontal method. *ACM Transactions on Mathematical Software*, 30(2):196–199, June 2004.
- [71] Douglas N. Woods, Thomas A. Brunner, and Todd S. Palmer. High order finite element S_N radiation transport on meshes with curved surfaces. *Nuclear Science and Engineering*, In Review.

- [72] Peter G. Maginot, Jean C. Ragusa, and Jim E. Morel. Nonnegative methods for bilinear discontinuous differencing of the S_N equations on quadrilaterals. *Nuclear Science and Engineering*, 185:53–69, 2017.
- [73] Mohammad Asadzadeh. Analysis of a fully discrete scheme for neutron transport in two-dimensional geometry. *SIAM Journal of Numerical Analysis*, 23(3):543–561, 1986.
- [74] Hank Childs, Eric Brugger, Brad Whitlock, Jeremy Meredith, Sean Ahern, David Pugmire, Kathleen Biagas, Mark Miller, Cyrus Harrison, Gunther H. Weber, Hari Krishnan, Thomas Fogal, Allen Sanderson, Christoph Garth, E. Wes Bethel, David Camp, Oliver Rübel, Marc Durant, Jean M. Favre, and Paulr Navrátil. Visit: An end-user tool for visualizing and analyzing very large data. In *High Performance Visualization—Enabling Extreme-Scale Scientific Insight*, pages 357–372. Oct 2012.

A Implementation in MFEM

The open source finite element library Modular Finite Elements Method (MFEM)⁷ [9] was used to create the system of linear equations to be solved by a linear algebra solver. The user chooses various parameters to create the system of equations and passes them into MFEM as arguments (i.e. the order of finite elements, the mesh, the number of times to refine the mesh, the order of the mesh, any mesh transformations, the linear algebra solver method, the source iteration convergence criteria, the maximum number of source iterations to perform, the initial guess for the scalar flux, and, in diffusion limit problems, the scaling factor to be applied).

MFEM creates the matrices and a linear solver computes the angular flux. This research utilizes the serial version of MFEM (as opposed to the parallel version where the spatial domain is solved in parallel) and the direct solver UMFPack⁸ [69, 70] to solve the equations using a *LU* decomposition. It is common for transport solvers to solve the local system of equations for an individual spatial cell and sweep through the problem domain, propagating information from one cell to the next. Instead, we use MFEM to create the system of equations for the entire problem domain and solve for all of the unknowns in all cells simultaneously. This is more computationally intensive because all of the degrees of freedom in the entire problem domain must be solved for simultaneously. However, mesh zone complications, such as cycles, may be present in the mesh. We avoid having to “break the cycles” by solving for the entire problem simultaneously.

The following two sections describe the operators used in MFEM to accomplish this research. Specifically, Section A.1 describes the operators used to solve the

⁷mfem.org

⁸<http://faculty.cse.tamu.edu/davis/suitesparse.html>

transport equation. Section A.2 describes the operators used to solve the MIP DSA equations.

A.1 Transport Operators

Shown in Table 5 are the functions within MFEM that integrate and assemble the various operators of the transport equation in X - Y geometry. These are all available by default in the MFEM distribution. The functions are displayed along with the general form of their equation and their translation to the applicable component of the transport equation. The last two entries of Table 5 are the interior boundaries using the upstream values (no. 5) and the problem boundary (no. 6). Several of the MFEM equations have coefficients, α and β , that are required input.

The normal vector \hat{n} in MFEM is outward of the upwind mesh surface so a negative was applied to the normal vector to convert it to be the outward normal of the surface of cell k like it has been previously defined in this dissertation.

In order to perform the spatial integrations with a factor of r we needed to modify the existing MFEM integrators. In general, this required multiplying the integrand by the physical r location. Since we performed an integration by parts on the streaming operator to remove the r from the r -derivative term, this greatly simplified our modification of these terms. Future research may require multiplying the basis function by r prior to calculating the derivative at the integration point in order to preserve the conservation form of the R - Z transport equation. The operators for the R - Z transport equation and their MFEM implementations are shown in Table 6.

MFEM has default settings for determining the degree of numerical integration to integrate each of the integrals of Tables 5 and 6. These default integration orders are shown in Table 7. It was discovered that integrating all of the terms consistently was important for numerical conservation. For simplicity, each of the integration orders

were set to the largest of the default integration orders. Table 7 shows that the integration order is the same for all of the integrators except DomainLFIntegrator, which is the largest integration order only if $p = 0$ (piece-wise constant). While the results presented in this dissertation do not consider the circumstance of piece-wise constant finite elements, this integration order was included in the code for future use.

MFEM is equipped to visualize data using various tools requiring additional user input. The images presented in this dissertation were produced with VisIt, an open source visualization analysis tool [74].

A.2 MIP DSA Operators

There are some specific function calls to MFEM for the diffusion equation that are listed in Table 8. Items 3 and 4 have a σ_D value that controls the DG method to be used, where $\sigma_D = -1$ is for the symmetric interior penalty method. Item 6 is for the Robin boundary condition described by Equation 87.

no.	Discretized Equation	MFEM Equation	MFEM Integrator Function
1	$(\boldsymbol{\Omega} \cdot \nabla \psi_j, v_i)_{\mathcal{D}_k}$	$(\alpha \boldsymbol{\Omega} \cdot \nabla \psi, v)_{\mathcal{D}_k}$	ConvectionIntegrator($\boldsymbol{\Omega}, \alpha$)
2	$(\sigma_t \psi_j, v_i)_{\mathcal{D}_k}$	$(\sigma_t \psi, v)_{\mathcal{D}_k}$	MassIntegrator(σ_t)
3	$(\sigma_s \phi, v_i)_{\mathcal{D}_k}$	$(\varphi, v)_{\mathcal{D}_k}$	DomainLFIIntegrator(φ)
4	$(S_0, v_i)_{\mathcal{D}_k}$	$(S_0, v)_{\mathcal{D}_k}$	DomainLFIIntegrator(S_0)
5	$(\boldsymbol{\Omega} \cdot \hat{n} \psi_j, v_i)_{\partial \mathcal{D}_k^e}$	$\alpha (\boldsymbol{\Omega} \cdot \hat{n} \psi, v)_{\partial \mathcal{D}_k^e}$ + $\beta (\boldsymbol{\Omega} \cdot \hat{n} \psi, v)_{\partial \mathcal{D}_k^e}$	DGTraceIntegrator($\boldsymbol{\Omega}, \alpha, \beta$) (applied to interior surfaces)
6	$(\boldsymbol{\Omega} \cdot \hat{n} \psi_j, v_i)_{\partial \mathcal{D}_k^b}$	$\alpha (\boldsymbol{\Omega} \cdot \hat{n} \psi, v)_{\partial \mathcal{D}_k^b}$ + $\beta (\boldsymbol{\Omega} \cdot \hat{n} \psi, v)_{\partial \mathcal{D}_k^b}$	DGTraceIntegrator($\boldsymbol{\Omega}, \alpha, \beta$) (applied to boundary surfaces)
7	$(\boldsymbol{\Omega} \cdot \hat{n} \psi_{inc}, v_i)_{\partial \mathcal{D}_k}$	$\frac{\alpha}{2} (\psi_{inc} \boldsymbol{\Omega} \cdot \hat{n}, v)_{\partial \mathcal{D}_k}$ - $\beta (\psi_{inc} \boldsymbol{\Omega} \cdot \hat{n} , v)_{\partial \mathcal{D}_k}$	BoundaryFlowIntegrator($\psi_{inc}, \boldsymbol{\Omega}, \alpha, \beta$)

Table 5: MFEM transport operator function calls where the arguments have been dropped.

no.	Discretized Equation	MFEM Equation	MFEM Integrator Function
1	$(r \mu_{n,m} \cdot \partial_r \psi_{n,m,j}, v_i)_{\mathcal{D}_k}$ $(r \xi_m \cdot \partial_z \psi_{n,m,j}, v_i)_{\mathcal{D}_k}$	$(r \alpha \Omega \cdot \nabla \psi, v)_{\mathcal{D}_k}$	RZConvectionIntegrator(Ω, α)
2	$(r \mu_{n,m} \cdot \hat{n} \psi_{n,m,j}, v_i)_{\mathcal{D}_k^e}$ $(r \xi_m \cdot \hat{n} \psi_{n,m,j}, v_i)_{\mathcal{D}_k^e}$	$\alpha(r \Omega \cdot \hat{n} \psi, v)_{\partial \mathcal{D}_k^e}$ $+ \beta(r \Omega \cdot \hat{n} \psi, v)_{\partial \mathcal{D}_k^e}$	RZDGTraceIntegrator(Ω, α, β)
3	$(r \mu_{n,m} \cdot \hat{n} \psi_{n,m,j}, v_i)_{\mathcal{D}_k^b}$ $(r \xi_m \cdot \hat{n} \psi_{n,m,j}, v_i)_{\mathcal{D}_k^b}$	$\alpha(r \Omega \cdot \hat{n} \psi, v)_{\partial \mathcal{D}_k^b}$ $+ \beta(r \Omega \cdot \hat{n} \psi, v)_{\partial \mathcal{D}_k^b}$	RZDGTraceIntegrator(Ω, α, β)
4	$(\mu_{n,m} \psi_j, v_i)_{\mathcal{D}_k}$	$(\mu_{n,m} \psi, v)_{\mathcal{D}_k}$	MassIntegrator($\mu_{n,m}$)
5	$\left(\frac{\alpha_{m+1/2} n}{\tau_{n,m} w_{n,m}} \psi_j, v_i \right)_{\mathcal{D}_k}$	$\left(\frac{\alpha_{m+1/2} n}{\tau_{n,m} w_{n,m}} \psi, v \right)_{\mathcal{D}_k}$	MassIntegrator($\frac{\alpha_{m+1/2} n}{\tau_{n,m} w_{n,m}}$)
6	$(r \sigma_t \psi_j, v_i)_{\mathcal{D}_k}$	$(r \sigma_t \psi, v)_{\mathcal{D}_k}$	RZMassIntegrator(σ_t)
7	$\frac{1}{4\pi} (r \sigma_s \phi, v_i)_{\mathcal{D}_k}$	$(r \varphi, v)_{\mathcal{D}_k}$	RZDomainLFIntegrator($\frac{1}{4\pi} \sigma_s \phi$)
8	$\frac{1}{4\pi} (r S_0, v_i)_{\mathcal{D}_k}$	$(r S_0, v)_{\mathcal{D}_k}$	RZDomainLFIntegrator($\frac{S_0}{4\pi}$)
9	$(r \Omega \cdot \hat{n} \psi_{inc}, v_i)_{\partial \mathcal{D}_k}$	$\frac{\alpha}{2} (r \psi_{inc} \Omega \cdot \hat{n}, v)_{\partial \mathcal{D}_k}$ $- \beta(r \psi_{inc} \Omega \cdot \hat{n} , v)_{\partial \mathcal{D}_k}$	RZBoundaryFlowIntegrator($\psi_{inc}, \Omega, \alpha, \beta$)

Table 6: MFEM R - Z transport operator function calls where the arguments have been dropped.

Table 7: MFEM default integration orders for transport operators. The notation for the finite element order is p , mesh order is g , and problem spatial dimension is d .

MFEM Integrator	Default Integration Order
DGTraceIntegrator	$g \cdot d + 2 \cdot p - 1$
ConvectionIntegrator	$g \cdot d + 2 \cdot p - 1$
MassIntegrator	$g \cdot d + 2 \cdot p - 1$
DomainLFIntegrator	$2 \cdot g$
BoundaryFlowIntegrator	$g \cdot d + 2 \cdot p - 1$

no.	FEM Equations	MFEM Equation	User Input
1	$(\sigma_a \phi, v)_{\mathcal{D}}$	$(\sigma_a \phi, v)_{\mathcal{D}}$	MassIntegrator(σ_a)
2	$(D \nabla \phi, \nabla v)_{\mathcal{D}}$	$(D \nabla \phi, \nabla v)_{\mathcal{D}}$	DiffusionIntegrator(D)
3	$(\{\{ D \partial_n \phi \}, [v] \})_{\partial \mathcal{D}^e}$ + $([\phi], \{\{ D \partial_n v \}\})_{\partial \mathcal{D}^e}$ + $(\kappa_e [\phi], [v])_{\partial \mathcal{D}^e}$	$(\{\{ D \nabla \phi \cdot \hat{n} \}, [v] \})_{\partial \mathcal{D}^e}$ + $\sigma_D ([\phi], \{\{ D \nabla v \cdot \hat{n} \}\})_{\partial \mathcal{D}^e}$ + $\kappa \left(\left\{ \left\{ \frac{D}{h_{\perp}} \right\} [\phi], [v] \right\} \right)_{\partial \mathcal{D}^e}$	DGDiffusionIntegrator(D, σ_D, κ)
4	$(\{\{ D \partial_n \phi \}, [v] \})_{\partial \mathcal{D}^b}$ - $\frac{1}{2} ([\phi], \{\{ D \partial_n v \}\})_{\partial \mathcal{D}^b}$ - $\frac{1}{2} (\kappa_e [\phi], [v])_{\partial \mathcal{D}^b}$	$(\{\{ D \nabla \phi \cdot \hat{n} \}, [v] \})_{\partial \mathcal{D}^b}$ + $\sigma_D ([\phi], \{\{ D \nabla v \cdot \hat{n} \}\})_{\partial \mathcal{D}^b}$ + $\kappa \left(\left\{ \left\{ \frac{D}{h_{\perp}} \right\} [\phi], [v] \right\} \right)_{\partial \mathcal{D}^b}$	DGDiffusionIntegrator(D, σ_D, κ)
5	$(\sigma_s [\phi^{(\ell+1/2)} - \phi^{(\ell)}], v)_{\mathcal{D}}$	$(Q_0, v)_{\mathcal{D}}$	DomainLFIntegrator(Q_0)
6	$\left(\frac{1}{2} \phi, v \right)_{\partial \mathcal{D}^b}$	$\left(\frac{1}{2} \phi, v \right)_{\partial \mathcal{D}^b}$	BoundaryMassIntegrator($\frac{1}{2}$)

Table 8: MFEM diffusion equation function calls.

B Alternative Implementations for DSA with Robin Boundary Conditions

We considered two other implementations for the Robin boundary conditions. Method 1 substitutes Equation 87 into Equation 79a:

$$\begin{aligned} b_{MIP,1}(\varphi, v) = & (\sigma_a \varphi, v)_{\mathcal{D}_k} + (D \nabla \varphi, \nabla v)_{\mathcal{D}_k} \\ & + (\kappa_e [\![\varphi]\!], [\![v]\!])_{\partial \mathcal{D}_k^i} + ([\![\varphi]\!], \{D \partial_n v\})_{\partial \mathcal{D}_k^i} + (\{D \partial_n \varphi\}, [\![v]\!])_{\partial \mathcal{D}_k^i} \\ & + (\kappa_e \varphi, v)_{\partial \mathcal{D}_k^b} - \frac{1}{2} (\varphi, D \partial_n v)_{\partial \mathcal{D}_k^b} + \frac{1}{4} (\varphi, v)_{\partial \mathcal{D}_k^b} \end{aligned} \quad (139)$$

Method 2 is very similar to Method 1 with one term removed:

$$\begin{aligned} b_{MIP,2}(\varphi, v) = & (\sigma_a \varphi, v)_{\mathcal{D}_k} + (D \nabla \varphi, \nabla v)_{\mathcal{D}_k} \\ & + (\kappa_e [\![\varphi]\!], [\![v]\!])_{\partial \mathcal{D}_k^i} + ([\![\varphi]\!], \{D \partial_n v\})_{\partial \mathcal{D}_k^i} + (\{D \partial_n \varphi\}, [\![v]\!])_{\partial \mathcal{D}_k^i} \\ & + (\kappa_e \varphi, v)_{\partial \mathcal{D}_k^b} + \frac{1}{4} (\varphi, v)_{\partial \mathcal{D}_k^b} \end{aligned} \quad (140)$$

Method 3 is the Robin boundary condition we implemented in Section 2.6. An analytic one-dimensional diffusion equation solution with zero incident current boundary conditions was used to benchmark the solution to the diffusion equation using three proposed Robin boundary condition methods. The original MIP DSA method (Equation 79a) was also solved for comparison. The analytic solution to the 1-D diffusion equation with homogeneous Robin boundary conditions is

$$\phi(x) = c_1 e^{x/L} + c_2 e^{-x/L} + \frac{S_0}{\sigma_a} \quad (141)$$

$$c_1 = \frac{1}{4} \frac{S_0}{\sigma_a} \left[\left(\frac{1}{4} + \frac{1}{2} \frac{D}{L} \right) e^{1/L} - \left(\frac{1}{4} - \frac{1}{2} \frac{D}{L} \right) \right] \\ \cdot \left[\left(\frac{1}{4} - \frac{1}{2} \frac{D}{L} \right)^2 - \left(\frac{1}{4} + \frac{1}{2} \frac{D}{L} \right)^2 e^{2/L} \right]^{-1} \quad (142)$$

$$c_2 = \left[-c_1 \left(\frac{1}{4} + \frac{1}{2} \frac{D}{L} \right) e^{1/L} - \frac{1}{4} \frac{S_0}{\sigma_a} \right] e^{1/L} \left(\frac{1}{4} - \frac{1}{2} \frac{D}{L} \right)^{-1} \quad (143)$$

where $L^2 = D/\sigma_a$. The opacities and source values were $\sigma_t = 1/\varepsilon$, $\sigma_a = \varepsilon$, $S_0 = \varepsilon$, and $D = 1/(3\sigma_t)$. A first-order orthogonal mesh, 3rd order finite elements, S_8 level-symmetric angular quadrature, and convergence criteria (see Equation 38) $\varepsilon_{\text{conv}} = 10^{-10}$ were used. Table 9 summarizes the L_2 norm of the errors between the FEM diffusion equation solution and the analytic solution. Method 1 (Equation 139),

Table 9: L_2 norm of the errors between the diffusion equation using the given boundary condition method and the reference solution (1-D analytic solution) using 3rd-order elements, $C = 4$, on an orthogonal mesh with 2304 zones.

ε	Method 1	Method 2	Method 3	MIP DSA
10	0.722	0.722	4.05×10^{-11}	0.722
1	0.363	0.363	2.03×10^{-10}	0.363
0.1	0.0607	0.0606	3.39×10^{-10}	0.0607
0.01	0.00650	0.00647	3.63×10^{-10}	0.00650
1×10^{-3}	6.55×10^{-4}	6.21×10^{-4}	3.66×10^{-10}	6.55×10^{-4}
1×10^{-4}	6.56×10^{-5}	4.25×10^{-5}	3.66×10^{-10}	6.56×10^{-5}
1×10^{-5}	6.56×10^{-6}	2.19×10^{-6}	3.67×10^{-10}	6.54×10^{-6}
1×10^{-6}	6.56×10^{-7}	2.18×10^{-7}	4.08×10^{-10}	3.91×10^{-7}

Method 2 (Equation 140), and the MIP DSA method solve the problem with increas-

ing accuracy as the problem gets more optically thick (i.e. $\varepsilon \rightarrow 0$). The accuracy of Method 3 appears to be significantly less dependent on the optical thickness of the problem. However, we do observe the accuracy is slightly reduced as the problem becomes optically thick. Method 3 is the most accurate discretization in all the problems considered here.

C Mathematica Scripts

C.1 Mass Matrix Entries for RZ BLD Gauss-Legendre on Quadrilaterals

```
(*Mass matrix entry for RZ BLD Gauss-Legendre on quadrilaterals*)
\

Clear[r0, r1, r2, r3, z0, z1, z2, z3, mr0, mr1, mr2, mr3, mz0, mz1, \
mz2, mz3]

(*Define physical integration point coordinates to compare to MFEM \
output:r0=(1+(-Sqrt[1/3]))/(1-(-1))*(0.25-0);
r1=(1+(Sqrt[1/3]))/(1-(-1))*(0.25-0);
z0=(1+(-Sqrt[1/3]))/(1-(-1))*(0.25-0);
z3=(1+(Sqrt[1/3]))/(1-(-1))*(0.25-0);*)

(*These make the mesh \
rectangular:*)
z2 := z3
z1 := z0
r2 := r1
r3 := r0

(*Quadrilateral transformation back to reference square-more general \
than rectangle transformation-but NOT curved mesh*)

r[rho_, kappa_] := (r1 - r0) rho + (r3 - r0) kappa + (r2 + r0 - r1 - \
r3) rho kappa + r0
z[rho_, kappa_] := (z1 - z0) rho + (z3 - z0) kappa + (z2 + z0 - z1 - \
z3) rho kappa + z0
```

```

z3) rho kappa + z0

(*Mesh nodes are needed to conserve cell volume.Cannot define mr0=0 \
nor mz0=0 here.Perform integration and then set the values.*)

\

(*Comment out to get the general mesh element mr1=0.25;
mz3=0.25;*)

mr2 := mr1

mr3 := mr0

mz1 := mz0

mz2 := mz3

mr[rho_, kappa_] := (mr1 - mr0) rho + (mr3 - mr0) kappa + (mr2 + mr0 -
mr1 - mr3) rho kappa + mr0

mz[rho_, kappa_] := (mz1 - mz0) rho + (mz3 - mz0) kappa + (mz2 + mz0 -
mz1 - mz3) rho kappa + mz0

a = {mr[rho, kappa], mz[rho, kappa]};

b = {rho, kappa};

(*Determinant of the Jacobian-for determining area of the physical \
element.*)

j = Det[D[a, {b}]];

(*Basis functions.The coefficients are from MATLAB script \
"GaussLegendreQuadrilateral.m".*)

BLD1[rho_, kappa_] :=
3*rho*kappa - (3 + Sqrt[3])/2*rho - (3 + Sqrt[3])/2*
kappa + (1 + Sqrt[3]/2)

```

```

BLD2[rho_, kappa_] := -3*rho*kappa + (3 + Sqrt[3])/2*rho +
3/(3 + Sqrt[3])*kappa - 0.5

BLD3[rho_, kappa_] :=
3*rho*kappa - 3/(3 + Sqrt[3])*rho -
3/(3 + Sqrt[3])*kappa + (1 - Sqrt[3]/2)

BLD4[rho_, kappa_] := -3*rho*kappa +
3/(3 + Sqrt[3])*rho + (3 + Sqrt[3])/2*kappa - 0.5

(*Check for orthogonality.*)

BLD1[r0, z0]*BLD2[r0, z0];

(*The r variable gets transformed back to the reference element*)

M =

Integrate[
mr[rho, kappa]*BLD1[rho, kappa]*BLD1[rho, kappa]*j, {rho, 0,
1}, {kappa, 0, 1}]

mr0 = 0.25;
mz0 = 0.25;
mr1 = 0.5;
mz3 = 0.5;

M

```

C.2 Angular Redistribution Matrix Entries for RZ BLD Gauss-Legendre on Quadrilaterals

(*Angular Redistribution matrix for RZ BLD Gauss-Legendre on \

```

quadrilaterals*)Clear[r0, r1, r2, r3, z0, z1, z2, z3, mr0, mr1, mr2, \
mr3, mz0, mz1, mz2, mz3]

(*Define physical integration point coordinates to compare to MFEM \
output:r0=(1+(-Sqrt[1/3]))/(1-(-1))*(0.25-0);

r1=(1+(Sqrt[1/3]))/(1-(-1))*(0.25-0);

z0=(1+(-Sqrt[1/3]))/(1-(-1))*(0.25-0);

z3=(1+(Sqrt[1/3]))/(1-(-1))*(0.25-0);*)

(*These make the mesh \
rectangular:*)
z2 := z3

z1 := z0

r2 := r1

r3 := r0

(*Quadrilateral transformation back to reference square-more general \
than rectangle transformation-but NOT curved mesh*)

r[rho_, kappa_] := (r1 - r0) rho + (r3 - r0) kappa + (r2 + r0 - r1 - \
r3) rho kappa + r0

z[rho_, kappa_] := (z1 - z0) rho + (z3 - z0) kappa + (z2 + z0 - z1 - \
z3) rho kappa + z0

(*Mesh nodes are needed to conserve cell volume.Cannot define mr0=0 \
nor mz0=0 here.Perform integration and then set the values.*)

\
(*Comment out to get the general mesh element mr1=0.25; \
mz3=0.25;*)

```

```

mr2 := mr1
mr3 := mr0
mz1 := mz0
mz2 := mz3
mr[rho_, kappa_] := (mr1 - mr0) rho + (mr3 - mr0) kappa + (mr2 + mr0 -
mr1 - mr3) rho kappa + mr0
mz[rho_, kappa_] := (mz1 - mz0) rho + (mz3 - mz0) kappa + (mz2 + mz0 -
mz1 - mz3) rho kappa + mz0
a = {mr[rho, kappa], mz[rho, kappa]};
b = {rho, kappa};
(*Determinant of the Jacobian-for determining area of the physical \
element.*)
j = Det[D[a, {b}]];
(*Basis functions.The coefficients are from MATLAB script \
"GaussLegendreQuadrilateral.m".*)
BLD1[rho_, kappa_] :=
3*rho*kappa - (3 + Sqrt[3])/2*rho - (3 + Sqrt[3])/2*
kappa + (1 + Sqrt[3]/2)
BLD2[rho_, kappa_] := -3*rho*kappa + (3 + Sqrt[3])/2*rho +
3/(3 + Sqrt[3])*kappa - 1/2
BLD3[rho_, kappa_] :=
3*rho*kappa - 3/(3 + Sqrt[3])*rho -
3/(3 + Sqrt[3])*kappa + (1 - Sqrt[3]/2)
BLD4[rho_, kappa_] := -3*rho*kappa +
3/(3 + Sqrt[3])*rho + (3 + Sqrt[3])/2*kappa - 1/2

```

```

M = Integrate[
  BLD1[rho, kappa]*BLD1[rho, kappa]*j, {rho, 0, 1}, {kappa, 0, 1}]

mr0 = 0;
mz0 = 0;
mr1 = 0.25;
mz3 = 0.25;

thisalpha = 0.350021175;
w = 0.523598775598298;
M*thisalpha

```

C.3 r-Leakage Matrix Entries for RZ BLD Gauss-Legendre on Quadrilaterals

```

(*r-Leakage matrix for RZ BLD Gauss-Legendre on \
quadrilaterals*)Clear[r0, r1, r2, r3, z0, z1, z2, z3, mr0, mr1, mr2, \
mr3, mz0, mz1, mz2, mz3, mu, rho, kappa]

(*Define physical integration point coordinates to compare to MFEM \
output: *)

r0 = (1 + (-Sqrt[1/3]))/(1 - (-1))*(0.25 - 0);
r1 = (1 + (Sqrt[1/3]))/(1 - (-1))*(0.25 - 0);
z0 = (1 + (-Sqrt[1/3]))/(1 - (-1))*(0.25 - 0);
z3 = (1 + (Sqrt[1/3]))/(1 - (-1))*(0.25 - 0);

(*Use to define rectangular mesh:*)
r2 = r1;

```

```

r3 = r0;
z1 = z0;
z2 = z3;

(*Transform arbitrary quadrilateral to reference square*)

r[rho_, kappa_] := (r1 - r0) rho + (r3 - r0) kappa + (r2 + r0 - r1 -
r3) rho kappa + r0
z[rho_, kappa_] := (z1 - z0) rho + (z3 - z0) kappa + (z2 + z0 - z1 -
z3) rho kappa + z0

(*Mesh nodes are needed to conserve cell volume.Cannot define mr0=0 \
nor mz0=0 here.Perform integration and then set the values.*)

\

(*Comment out to get the general mesh element mr1=0.25;
mz3=0.25;*)

mr2 := mr1
mr3 := mr0
mz1 := mz0
mz2 := mz3

mr[rho_, kappa_] := (mr1 - mr0) rho + (mr3 - mr0) kappa + (mr2 + mr0 -
mr1 - mr3) rho kappa + mr0
mz[rho_, kappa_] := (mz1 - mz0) rho + (mz3 - mz0) kappa + (mz2 + mz0 -
mz1 - mz3) rho kappa + mz0
a = {mr[rho, kappa], mz[rho, kappa]};
b = {rho, kappa};

(*Determinant of the Jacobian-for determining area of the physical \
element.*)

```

```

j = Det[D[a, {b}]] ;

(*Basis functions.The coefficients are from MATLAB script \
"GaussLegendreQuadrilateral.m".*)

BLD1[rho_, kappa_] :=
3*rho*kappa - (3 + Sqrt[3])/2*rho - (3 + Sqrt[3])/2*
kappa + (1 + Sqrt[3]/2)

BLD2[rho_, kappa_] := -3*rho*kappa + (3 + Sqrt[3])/2*rho +
3/(3 + Sqrt[3])*kappa - 1/2

BLD3[rho_, kappa_] :=
3*rho*kappa - 3/(3 + Sqrt[3])*rho -
3/(3 + Sqrt[3])*kappa + (1 - Sqrt[3]/2)

BLD4[rho_, kappa_] := -3*rho*kappa +
3/(3 + Sqrt[3])*rho + (3 + Sqrt[3])/2*kappa - 1/2

(*The r value gets transformed back to the reference element*)

Kr = \
-mu*Integrate[
BLD1[rho, kappa]*D[BLD1[rho, kappa], rho]*j, {rho, 0, 1}, {kappa,
0, 1}]

mr0 = 0.0;

mr1 = 0.25;

mz0 = 0.0;

mz3 = 0.25;

mu = -0.495004692;

BLD1[r0, z0]

rho = r1;

```

```
D[BLD1[rho, kappa], kappa]
```

```
Kr
```

C.4 z-Leakage Matrix Entries for RZ BLD Gauss-Legendre on Quadrilaterals

```
(*z-Leakage matrix for RZ BLD Gauss-Legendre on \
quadrilaterals*)Clear[r0, r1, r2, r3, z0, z1, z2, z3, mr0, mr1, mr2, \
mr3, mz0, mz1, mz2, mz3, xi, rho, kappa]

(*Define physical integration point coordinates to compare to MFEM \
output:*)

r0 = (1 + (-Sqrt[1/3]))/(1 - (-1))*(0.25 - 0);
r1 = (1 + (Sqrt[1/3]))/(1 - (-1))*(0.25 - 0);
z0 = (1 + (-Sqrt[1/3]))/(1 - (-1))*(0.25 - 0);
z3 = (1 + (Sqrt[1/3]))/(1 - (-1))*(0.25 - 0);

(*Use to define rectangular mesh:*)
r2 = r1;
r3 = r0;
z1 = z0;
z2 = z3;

(*Transform arbitrary quadrilateral to reference square*)

r[rho_, kappa_] := (r1 - r0) rho + (r3 - r0) kappa + (r2 + r0 - r1 - \
r3) rho kappa + r0
z[rho_, kappa_] := (z1 - z0) rho + (z3 - z0) kappa + (z2 + z0 - z1 - \
z3) rho kappa + z0
```

```

z3) rho kappa + z0

(*Mesh nodes are needed to conserve cell volume.Cannot define mr0=0 \
nor mz0=0 here.Perform integration and then set the values.*)

\

(*Comment out to get the general mesh element mr1=0.25;
mz3=0.25;*)

mr2 := mr1

mr3 := mr0

mz1 := mz0

mz2 := mz3

mr[rho_, kappa_] := (mr1 - mr0) rho + (mr3 - mr0) kappa + (mr2 + mr0 -
mr1 - mr3) rho kappa + mr0

mz[rho_, kappa_] := (mz1 - mz0) rho + (mz3 - mz0) kappa + (mz2 + mz0 -
mz1 - mz3) rho kappa + mz0

a = {mr[rho, kappa], mz[rho, kappa]};

b = {rho, kappa};

(*Determinant of the Jacobian-for determining area of the physical \
element.*)

j = Det[D[a, {b}]];

(*Basis functions.The coefficients are from MATLAB script \
"GaussLegendreQuadrilateral.m".*)

BLD1[rho_, kappa_] :=
3*rho*kappa - (3 + Sqrt[3])/2*rho - (3 + Sqrt[3])/2*
kappa + (1 + Sqrt[3]/2)

BLD2[rho_, kappa_] := -3*rho*kappa + (3 + Sqrt[3])/2*rho +

```

```

3/(3 + Sqrt[3])*kappa - 1/2

BLD3[rho_, kappa_] :=

3*rho*kappa - 3/(3 + Sqrt[3])*rho -

3/(3 + Sqrt[3])*kappa + (1 - Sqrt[3]/2)

BLD4[rho_, kappa_] := -3*rho*kappa +

3/(3 + Sqrt[3])*rho + (3 + Sqrt[3])/2*kappa - 1/2

(*The r value gets transformed back to the reference element*)

Kz = \

-xi*Integrate[

BLD1[rho, kappa]*D[BLD1[rho, kappa], kappa]*j, {rho, 0, 1}, {kappa,
0, 1}]

mr0 = 0.0;

mr1 = 0.25;

mz0 = 0.0;

mz3 = 0.25;

xi = -0.868890301;

D[BLD1[rho, kappa], kappa]

xi*j

Kz

Kr + Kz

```

C.5 z-Leakage Matrix Entries for RZ BLD Gauss-Legendre on Quadrilaterals

```

(*z-Leakage matrix for RZ BLD Gauss-Legendre on \
quadrilaterals*)Clear[r0, r1, r2, r3, z0, z1, z2, z3, mr0, mr1, mr2, \

```

```

mr3, mz0, mz1, mz2, mz3, xi, rho, kappa]

(*Define physical integration point coordinates to compare to MFEM \
output:*)

r0 = (1 + (-Sqrt[1/3]))/(1 - (-1))*(0.25 - 0);
r1 = (1 + (Sqrt[1/3]))/(1 - (-1))*(0.25 - 0);
z0 = (1 + (-Sqrt[1/3]))/(1 - (-1))*(0.25 - 0);
z3 = (1 + (Sqrt[1/3]))/(1 - (-1))*(0.25 - 0);

(*Use to define rectangular mesh:*)

r2 = r1;
r3 = r0;
z1 = z0;
z2 = z3;

(*Transform arbitrary quadrilateral to reference square*)

r[rho_, kappa_] := (r1 - r0) rho + (r3 - r0) kappa + (r2 + r0 - r1 -
r3) rho kappa + r0
z[rho_, kappa_] := (z1 - z0) rho + (z3 - z0) kappa + (z2 + z0 - z1 -
z3) rho kappa + z0

(*Mesh nodes are needed to conserve cell volume.Cannot define mr0=0 \
nor mz0=0 here.Perform integration and then set the values.*)

\

(*Comment out to get the general mesh element mr1=0.25;
mz3=0.25;*)

mr2 := mr1
mr3 := mr0

```

```

mz1 := mz0

mz2 := mz3

mr[rho_, kappa_] := (mr1 - mr0) rho + (mr3 - mr0) kappa + (mr2 + mr0 -
mr1 - mr3) rho kappa + mr0

mz[rho_, kappa_] := (mz1 - mz0) rho + (mz3 - mz0) kappa + (mz2 + mz0 -
mz1 - mz3) rho kappa + mz0

a = {mr[rho, kappa], mz[rho, kappa]};

b = {rho, kappa};

(*Determinant of the Jacobian-for determining area of the physical \
element.*)

j = Det[D[a, {b}]];

(*Basis functions.The coefficients are from MATLAB script \
"GaussLegendreQuadrilateral.m".*)

BLD1[rho_, kappa_] :=
3*rho*kappa - (3 + Sqrt[3])/2*rho - (3 + Sqrt[3])/2*
kappa + (1 + Sqrt[3]/2)

BLD2[rho_, kappa_] := -3*rho*kappa + (3 + Sqrt[3])/2*rho +
3/(3 + Sqrt[3])*kappa - 1/2

BLD3[rho_, kappa_] :=
3*rho*kappa - 3/(3 + Sqrt[3])*rho -
3/(3 + Sqrt[3])*kappa + (1 - Sqrt[3]/2)

BLD4[rho_, kappa_] := -3*rho*kappa +
3/(3 + Sqrt[3])*rho + (3 + Sqrt[3])/2*kappa - 1/2

(*The r value gets transformed back to the reference element*)

Kz = \

```

```

-xi*Integrate[
  BLD1[rho, kappa]*D[BLD1[rho, kappa], kappa]*j, {rho, 0, 1}, {kappa,
  0, 1}]
mr0 = 0.0;
mr1 = 0.25;
mz0 = 0.0;
mz3 = 0.25;
xi = -0.868890301;
D[BLD1[rho, kappa], kappa]
xi*j
Kz
Kr + Kz

```

C.6 r Surface-Integral Matrix Entries for RZ BLD Gauss-Legendre on Quadrilaterals

```

(*r surface-integral matrix for RZ BLD Gauss-Legendre on \
quadrilaterals*)

Clear[r0, r1, r2, r3, z0, z1, z2, z3]

(*Define physical integration point coordinates to compare to MFEM \
output:

r0=(1+(-Sqrt[1/3]))/(1-(-1))*(0.25-0);
r1=(1+(Sqrt[1/3]))/(1-(-1))*(0.25-0);
z0=(1+(-Sqrt[1/3]))/(1-(-1))*(0.25-0);
z3=(1+(Sqrt[1/3]))/(1-(-1))*(0.25-0);*)
(*Use to define rectangular \

```

```

mesh:*)
r2 = r1;
r3 = r0;
z1 = z0;
z2 = z3;
(*Transform arbitrary quadrilateral to reference square*)

r[rho_, kappa_] := (r1 - r0) rho + (r3 - r0) kappa + (r2 + r0 - r1 -
r3) rho kappa + r0
z[rho_, kappa_] := (z1 - z0) rho + (z3 - z0) kappa + (z2 + z0 - z1 -
z3) rho kappa + z0
a = {r[rho, kappa], z[rho, kappa]};
b = {rho, kappa};
(*Determinant of the Jacobian-for determining area of the physical \
element.*)
j = Det[D[a, {b}]];
(*Basis functions.The coefficients are from MATLAB script \
"GaussLegendreQuadrilateral.m".*)
BLD1[rho_, kappa_] :=
3*rho*kappa - (3 + Sqrt[3])/2*rho - (3 + Sqrt[3])/2*
kappa + (1 + Sqrt[3]/2)
BLD2[rho_, kappa_] := -3*rho*kappa + (3 + Sqrt[3])/2*rho +
3/(3 + Sqrt[3])*kappa - 1/2
BLD3[rho_, kappa_] :=
3*rho*kappa - 3/(3 + Sqrt[3])*rho -

```

```

3/(3 + Sqrt[3])*kappa + (1 - Sqrt[3]/2)

BLD4[rho_, kappa_] := -3*rho*kappa +
3/(3 + Sqrt[3])*rho + (3 + Sqrt[3])/2*kappa - 1/2

(*The r value gets transformed back to the reference element*)

Lr =
Integrate[r1*BLD1[1, kappa]*BLD1[1, kappa]*j, {kappa, 0, 1}] -
Integrate[r0*BLD1[0, kappa]*BLD1[0, kappa]*j, {kappa, 0, 1}]

r0 = 0.0;
r1 = 0.25;
z0 = 0.0;
z3 = 0.25;

```

C.7 z Surface-Integral Matrix Entries for RZ BLD Gauss-Legendre on Quadrilaterals

```

(*z surface-integral matrix for RZ BLD Gauss-Legendre on \
quadrilaterals*)

Clear[r0, r1, r2, r3, z0, z1, z2, z3]

(*Define physical integration point coordinates to compare to MFEM \
output:

r0=(1+(-Sqrt[1/3]))/(1-(-1))*(0.25-0);
r1=(1+(Sqrt[1/3]))/(1-(-1))*(0.25-0);
z0=(1+(-Sqrt[1/3]))/(1-(-1))*(0.25-0);
z3=(1+(Sqrt[1/3]))/(1-(-1))*(0.25-0);*)
(*Use to define rectangular \
mesh:*)

```

```

r2 = r1;
r3 = r0;
z1 = z0;
z2 = z3;

(*Transform arbitrary quadrilateral to reference square*)

r[rho_, kappa_] := (r1 - r0) rho + (r3 - r0) kappa + (r2 + r0 - r1 -
r3) rho kappa + r0
z[rho_, kappa_] := (z1 - z0) rho + (z3 - z0) kappa + (z2 + z0 - z1 -
z3) rho kappa + z0
a = {r[rho, kappa], z[rho, kappa]};
b = {rho, kappa};
(*Determinant of the Jacobian-for determining area of the physical \
element.*)
j = Det[D[a, {b}]];
(*Basis functions.The coefficients are from MATLAB script \
"GaussLegendreQuadrilateral.m".*)
BLD1[rho_, kappa_] :=
3*rho*kappa - (3 + Sqrt[3])/2*rho - (3 + Sqrt[3])/2*
kappa + (1 + Sqrt[3]/2)
BLD2[rho_, kappa_] := -3*rho*kappa + (3 + Sqrt[3])/2*rho +
3/(3 + Sqrt[3])*kappa - 1/2
BLD3[rho_, kappa_] :=
3*rho*kappa - 3/(3 + Sqrt[3])*rho -
3/(3 + Sqrt[3])*kappa + (1 - Sqrt[3]/2)

```

```

BLD4[rho_, kappa_] := -3*rho*kappa +
3/(3 + Sqrt[3])*rho + (3 + Sqrt[3])/2*kappa - 1/2
(*The r value gets transformed back to the reference element*)

Lz =
Integrate[r[rho, 1]*BLD1[rho, 1]*BLD1[rho, 1]*j, {rho, 0, 1}] -
Integrate[r[rho, 0]*BLD1[rho, 0]*BLD1[rho, 0]*j, {rho, 0, 1}]

r0 = 0.0;
r1 = 0.25;
z0 = 0.0;
z3 = 0.25;

Lz
Lr + Lz

```

C.8 Linear Form Angular Redistribution Matrix Entries for RZ BLD Gauss-Legendre on Quadrilaterals

```

(*Linear Form Angular Redistribution matrix for RZ BLD Gauss-Legendre \
on quadrilaterals*)Clear[r0, r1, r2, r3, z0, z1, z2, z3, mr0, mr1, \
mr2, mr3, mz0, mz1, mz2, mz3]

(*Define physical integration point coordinates to compare to MFEM \
output:r0=(1+(-Sqrt[1/3]))/(1-(-1))*(0.25-0);
r1=(1+(Sqrt[1/3]))/(1-(-1))*(0.25-0);
z0=(1+(-Sqrt[1/3]))/(1-(-1))*(0.25-0);
z3=(1+(Sqrt[1/3]))/(1-(-1))*(0.25-0);*)

(*These make the mesh \
rectangular:*)

```

```

z2 := z3
z1 := z0
r2 := r1
r3 := r0
(*Quadrilateral transformation back to reference square-more general \
than rectangle transformation-but NOT curved mesh*)

r[rho_, kappa_] := (r1 - r0) rho + (r3 - r0) kappa + (r2 + r0 - r1 -
r3) rho kappa + r0
z[rho_, kappa_] := (z1 - z0) rho + (z3 - z0) kappa + (z2 + z0 - z1 -
z3) rho kappa + z0

(*Mesh nodes are needed to conserve cell volume.Cannot define mr0=0 \
nor mz0=0 here.Perform integration and then set the values.*)
\
(*Comment out to get the general mesh element mr1=0.25;
mz3=0.25;*)

mr2 := mr1
mr3 := mr0
mz1 := mz0
mz2 := mz3
mr[rho_, kappa_] := (mr1 - mr0) rho + (mr3 - mr0) kappa + (mr2 + mr0 -
mr1 - mr3) rho kappa + mr0
mz[rho_, kappa_] := (mz1 - mz0) rho + (mz3 - mz0) kappa + (mz2 + mz0 -
mz1 - mz3) rho kappa + mz0
a = {mr[rho, kappa], mz[rho, kappa]};
```

```

b = {rho, kappa};

(*Determinant of the Jacobian-for determining area of the physical \
element.*)

j = Det[D[a, {b}]];

(*Basis functions.The coefficients are from MATLAB script \
"GaussLegendreQuadrilateral.m".*)

BLD1[rho_, kappa_] :=
3*rho*kappa - (3 + Sqrt[3])/2*rho - (3 + Sqrt[3])/2*
kappa + (1 + Sqrt[3])/2

BLD2[rho_, kappa_] := -3*rho*kappa + (3 + Sqrt[3])/2*rho +
3/(3 + Sqrt[3])*kappa - 1/2

BLD3[rho_, kappa_] :=
3*rho*kappa - 3/(3 + Sqrt[3])*rho -
3/(3 + Sqrt[3])*kappa + (1 - Sqrt[3])/2

BLD4[rho_, kappa_] := -3*rho*kappa +
3/(3 + Sqrt[3])*rho + (3 + Sqrt[3])/2*kappa - 1/2

M = Integrate[
BLD2[rho, kappa]*BLD2[rho, kappa]*j, {rho, 0, 1}, {kappa, 0, 1}]

mr0 = 0;
mz0 = 0;
mr1 = 0.25;
mz3 = 0.25;

alphatau = 0.845025867;

```

```

psiMinusHalf = 0.1591549;
M*alphatau*psiMinusHalf

```

C.9 Linear Form Scattering/Fixed Source Matrix Entries for RZ BLD Gauss-Legendre on Quadrilaterals

```

(*Linear Form scattering/fixed sources for RZ BLD Gauss-Legendre on \
quadrilaterals*)Clear[r0, r1, r2, r3, z0, z1, z2, z3, mr0, mr1, mr2, \
mr3, mz0, mz1, mz2, mz3, Source]

(*Define physical integration point coordinates to compare to MFEM \
output:r0=(1+(-Sqrt[1/3]))/(1-(-1))*(0.25-0);
r1=(1+(Sqrt[1/3]))/(1-(-1))*(0.25-0);
z0=(1+(-Sqrt[1/3]))/(1-(-1))*(0.25-0);
z3=(1+(Sqrt[1/3]))/(1-(-1))*(0.25-0);*)

(*These make the mesh \
rectangular:*)
z2 := z3
z1 := z0
r2 := r1
r3 := r0

(*Quadrilateral transformation back to reference square-more general \
than rectangle transformation-but NOT curved mesh*)

r[rho_, kappa_] := (r1 - r0) rho + (r3 - r0) kappa + (r2 + r0 - r1 - 
r3) rho kappa + r0
z[rho_, kappa_] := (z1 - z0) rho + (z3 - z0) kappa + (z2 + z0 - z1 - 
z3) rho kappa + z0

```

```

z3) rho kappa + z0

(*Mesh nodes are needed to conserve cell volume.Cannot define mr0=0 \
nor mz0=0 here.Perform integration and then set the values.*)

\

(*Comment out to get the general mesh element mr1=0.25;
mz3=0.25;*)

mr2 := mr1

mr3 := mr0

mz1 := mz0

mz2 := mz3

mr[rho_, kappa_] := (mr1 - mr0) rho + (mr3 - mr0) kappa + (mr2 + mr0 -
mr1 - mr3) rho kappa + mr0

mz[rho_, kappa_] := (mz1 - mz0) rho + (mz3 - mz0) kappa + (mz2 + mz0 -
mz1 - mz3) rho kappa + mz0

a = {mr[rho, kappa], mz[rho, kappa]};

b = {rho, kappa};

(*Determinant of the Jacobian-for determining area of the physical \
element.*)

j = Det[D[a, {b}]];

(*Basis functions.The coefficients are from MATLAB script \
"GaussLegendreQuadrilateral.m".*)

BLD1[rho_, kappa_] :=
3*rho*kappa - (3 + Sqrt[3])/2*rho - (3 + Sqrt[3])/2*
kappa + (1 + Sqrt[3]/2)

```

```

BLD2[rho_, kappa_] := -3*rho*kappa + (3 + Sqrt[3])/2*rho +
3/(3 + Sqrt[3])*kappa - 1/2

BLD3[rho_, kappa_] :=
3*rho*kappa - 3/(3 + Sqrt[3])*rho -
3/(3 + Sqrt[3])*kappa + (1 - Sqrt[3])/2

BLD4[rho_, kappa_] := -3*rho*kappa +
3/(3 + Sqrt[3])*rho + (3 + Sqrt[3])/2*kappa - 1/2

M = Integrate[
Source*mr[rho, kappa]*BLD2[rho, kappa]*j, {rho, 0, 1}, {kappa, 0, 1}]
(*Source=0.7/(2*Pi);*)

Source = (0.3*1)/(2*Pi);

mr0 = 0;
mz0 = 0;
mr1 = 0.25;
mz3 = 0.25;

M

```